Inflationary non-Gaussianity : theoretical predictions and observational consequences

Gabriel Jung

université PARIS-SACLAY

NNT : 2018SACLS105

Thèse de doctorat

UNIVERSITÉ PARIS SUD

Comprendre le monde, construire l'avenir®

Non-gaussianités inflationnaires : prévisions théoriques et conséquences observationnelles

Thèse de doctorat de l'Université Paris-Saclay
préparée à l'Université Paris-Sud

Ecole doctorale n°564 Physique en Île-de-France (EDPIF)
Spécialité de doctorat: Physique

Thèse présentée et soutenue à Orsay, le 22 mai 2018, par

M. GABRIEL JUNG

Composition du Jury :

Christos Charmousis Directeur de recherche, *Université Paris-Sud (UMR 8627)*	Président du jury
Ana Achúcarro Professeure, *Université de Leiden*	Rapporteure
Sabino Matarrese Professeur, *Université de Padoue*	Rapporteur
Martin Bucher Directeur de recherche, *Université Paris Diderot (UMR 7164)*	Examinateur
Martin Kunz Professeur, *Université de Genève*	Examinateur
Bartjan van Tent Maître de conférences, *Université Paris-Sud (UMR 8627)*	Directeur de thèse

Abstract

A powerful probe of the physics at play in the early universe is the Cosmic Microwave Background (CMB). Its anisotropies have been measured recently with high precision by the Planck satellite. These measurements are in agreement with the predictions of inflation, a theory describing a period of fast and accelerated expansion in the early universe. To discriminate between the different inflation models, it is important to look for deviations from Gaussianity of the CMB anisotropies (i.e. non-Gaussianity). This thesis is devoted to the study of non-Gaussianity of the bispectral type (related to the three-point correlation functions) parametrized by its amplitude parameters $f_{\rm NL}$, both from the theoretical and observational points of view.

After an introductory part on standard cosmology, the second part of the thesis describes the method of the binned bispectrum estimator, used to extract information about non-Gaussianity from CMB measurements. In order to recover information about the primordial universe, one has to clean observational data from the contamination caused by galactic foregrounds. We verify the results at the bispectral level. Numerical templates for the temperature bispectra of several galactic foregrounds are determined using data from the 2015 Planck release. These templates are then used to perform joint analyses on raw sky and CMB temperature data maps, to improve the determination of the amount of primordial non-Gaussianity.

In the third part, the level of bispectral non-Gaussianity produced in two-field inflation models with standard kinetic terms is investigated using the long-wavelength formalism. It is important to better understand what regions of inflation model space have been ruled out by Planck. We apply a newly derived expression for $f_{\rm NL}$ to the case of a sum potential and show that it is very difficult to satisfy simultaneously the conditions for a large $f_{\rm NL}$ and the observational constraints on the spectral index n_s. In the case of the sum of two monomial potentials and a constant we explicitly show in which small region of parameter space this is possible, and we show how to construct such a model. Finally, we also use the new expression for $f_{\rm NL}$ to show that for the sum potential, the explicit expressions remain valid even beyond the slow-roll approximation.

Acknowledgments

This thesis is the result of several years of very intensive work and would not have been possible if I had not been so well supported. Here, I would like to express my gratitude to all those who have been involved.

I am very thankful to the members of my thesis committee who took some of their precious time to evaluate this work. In particular, I want to thank Ana Achúcarro and Sabino Matarrese for reviewing this manuscript, and Christos for accepting to be the president of the jury. I could not thank enough my advisor Bartjan here. We started to work together six years ago, a long time before the beginning of my PhD and I appreciated tremendously this collaboration, which, I think, has been very fruitful. I hope it can continue. My understanding of the physics at play in the CMB and in the primordial universe would not have been the same without his guidance and our numerous very useful discussions.

The Laboratoire de Physique Théorique, and especially the small cosmology group, has always been a very welcoming place and a very stimulating work environment. I am glad for the years I spent there. The administrative staff, but also its director Sébastien, have been very supportive when I needed help. Many members of the LPT have been my professors during my first years in Orsay. Among them, I have to thank Renaud for his general relativity and cosmology lectures which were a large influence on the path I followed, Damir and his many wise advices and also Asmaa, especially for the help to find the internship of my first year of master. This internship, which I did at Fermilab under the supervision of Patrick Fox (thank you!), has been one of the most important moments of my education. And of course I have to mention the PhD students, for all the good moments we spent together at the LPT, but also outside. Thanks in particular to Antoine and Florent, with whom we shared the same office during most of our respective PhDs, Andrei, Luca, Matias and Olcyr who started at the same time as me and are now in very different parts of the world, Hermès, Luiz and Renaud the "old" generation, but also the "young" ones Maíra, Mathias, Timothé.

I am also grateful to Benjamin Racine for the amazing opportunity to come to Oslo. Our collaboration has been a very great experience!

Je dois aussi remercier ici mes amis qui m'auront fait vivre des moments inoubliables pendant toutes ces années.

Je pense en particulier à mes amis de longue date Antoine (et notre parfaite synchronisation de calendrier), Yohan, Mikaël, Erwan et Tanguy, qui me connaissaient à l'époque où j'envisageais pour la première fois ces études ! Je remercie aussi mes amis de prépa, Gwen et JB, qui étaient présents le jour de ma soutenance !

Un énorme merci à mes amis du magistère, Steven et Guillaume pour tous les bons souvenirs depuis près de sept ans, Aurélien et Nicolas pour la régularité de nos séances de piscine, Baur pour tous nos lundis soir, mais aussi Anaïs, Nadia et Sébastien pour toutes nos soirées ensemble!

Je remercie aussi Gaëtan, JL, Jerem, Nathan et Flo, après tous ces moments sur Cryptocat (et pas que) ! Mais aussi Antoine, Johan et Rémi, ainsi que Laure et sa redéfinition du mot *flood*, et Mathieu pour nos longs débats en période de *keynote*.

Les nombreux concerts auxquels j'ai pu assister à Paris (mais pas seulement) ont été des moments d'évasion importants pour moi pendant cette période. Merci à Caroline, Lauriane, Michaël et Thibault de les avoir rendus encore plus mémorables !

Je ne peux pas m'arrêter là sans remercier (énormément) Mathilde, qui est arrivée dans ma vie à une période compliquée et sans qui ces derniers mois auraient été infiniment plus difficiles. Merci encore pour ton soutien et ta patience.

Le soutien de ma famille a aussi été primordial tout au long de mes études et je ne pourrai jamais assez les remercier. En particulier, je pense à Jules, Marie, Morgane et Anne-Françoise. Enfin, tout cela n'aurait pas été possible sans l'immense aide de mon père Jean-Luc et de mes grand-parents Pierre et Jeannette.

Contents

Contents iv

List of Tables vi

List of Figures vii

I Introduction 1

1 Introduction 2

2 Standard model of cosmology 5
2.1 Background theory . . . 6
2.2 The Big Bang theory . . . 8
2.3 Inflation . . . 15

3 Gaussianity in the primordial Universe 18
3.1 Some statistics . . . 19
3.2 Gaussian statistics for the CMB . . . 20
3.3 Primordial fluctuations from standard single-field inflation . . . 22
3.4 After inflation . . . 27

II Non-Gaussianity in CMB observations 31

4 Estimating non-Gaussianity 32
4.1 Angular and reduced bispectrum . . . 32
4.2 Theoretical shapes . . . 34
4.3 Non-Gaussian statistics for the CMB . . . 36
4.4 The binned bispectrum estimator . . . 38

5 Galactic foregrounds 47
5.1 Thermal dust . . . 48
5.2 Other foregrounds . . . 52
5.3 Noise and masks . . . 56

6 Data analysis using the galactic templates 61
6.1 Gaussian simulations . . . 62
6.2 CMB analyses . . . 67
6.3 Raw sky . . . 68

III Non-Gaussianity in two-field inflation 71

7 Definitions and set-up 72
7.1 Background dynamics . . . 72
7.2 Slow-roll parameters . . . 73
7.3 Perturbations . . . 75
7.4 Green's functions . . . 77
7.5 Observables . . . 79
7.6 The $g_{\rm int}$ equation . . . 83

8 Slow roll 85
8.1 General case . . . 85
8.2 Sum potential . . . 86
8.3 Product potential . . . 90
8.4 Monomial potentials . . . 91
8.5 Discussion . . . 95

9 Beyond the slow-roll regime 99
9.1 Two kinds of turns . . . 99
9.2 Green's functions . . . 102
9.3 The $g_{\rm int}$ equation during the turn . . . 103
9.4 Fate of the slow-roll homogeneous solution . . . 104
9.5 Fate of the slow-roll particular solution . . . 106
9.6 Solution of the $g_{\rm int}$ equation . . . 110
9.7 End of inflation and $f_{\rm NL}$ . . . 111

10 Numerical examples 113
10.1 Double quadratic potential . . . 113
10.2 How to build a monomial potential model that produces $f_{\rm NL}$ of order unity 115
10.3 First type of turn . . . 116
10.4 Second type of turn . . . 121

11 Conclusion 124

Appendices 129

A Weights of bispectral shapes 130

B Long-wavelength formalism 135

C Derivation of the $g_{\rm int}$ equation 136

D Start of the turn and value of $f_{\rm NL}$ 138

Résumé en français 140

Bibliography 146

Abstract 158

List of Tables

21 Standard results of Friedmann equations 8

41 Correlation coefficients between the most common bispectral shapes 45

51 Correlation coefficients of the most common bispectral shapes 52
52 Correlation coefficients between the foreground templates and the common shapes 54
53 Correlation coefficients between the cleaned synchrotron and the other shapes . . . 56
54 Correlation coefficients between the foreground templates determined with the common and Commander masks 58

61 Determination of $f_{\rm NL}$ in the dust map 61
62 Determination of $f_{\rm NL}$ using 100 Gaussian simulations of the CMB + dust with isotropic noise 63
63 Ratio of the observed variance over the theoretical prediction 66
64 Comparison of Fisher and observed error bars for 100 Gaussian maps + dust . . . 66
65 Determination of $f_{\rm NL}$ using 100 Gaussian simulations of the CMB + dust with anisotropic noise 67
66 Determination of $f_{\rm NL}$ using the CMB SMICA map and the Commander dust map 68
67 Determination of $f_{\rm NL}$ using the CMB SMICA map and the Commander dust map 68
68 Determination of $f_{\rm NL}$ in the raw 143 GHz map (high resolution) 70
69 Determination of $f_{\rm NL}$ in the raw 143 GHz map (low resolution) 70

81 Constraints from the spectral index on $\tilde{V}_{\sigma\sigma *}$ for different n with $N_\phi = 60$. 93
82 Upper bounds from the spectral index on $\left|-\frac{6}{5} f_{\rm NL} \eta_*^\perp\right|$ for different n with $N_\phi = 60$. 94

List of Figures

31 Map of the CMB anisotropies from the 2015 Planck release 18
32 CMB power spectrum from 2015 Planck release 29

51 Map of the thermal dust at 143 GHz from the 2015 Planck release 48
52 Dust power spectrum at 143 GHz from the 2015 Planck release 49
53 Dust bispectrum at 143 Ghz from the 2015 Planck release 50
54 Dust bispectrum (over noise) at 143 GHz from the 2015 Planck release 51
55 CMB and foregrounds brightness as a function of frequency from 2015 Planck release 52
56 Dust, free-free, AME and synchrotrons maps at 143 GHz from the 2015 Planck release 53
57 Dust, free-free, synchrotron and AME power spectra at 143 GHz 54
58 Dust, free-free, synchrotron and AME bispectra (over noise) at 143 GHz 55
59 Bispectral signal-to-noise of the synchrotron at 143 GHz 56
510 Noise power spectrum in the dust map at 143 GHz from the 2015 Planck release . 57
511 Common and Commander masks 57
512 Foregrounds power spectra for the two masks at 143 GHz 58
513 Foregrounds bispectra (over noise) with the Commander mask at 143 GHz 59
514 Zoom on the synchrotron map at 143 GHz with the Commander mask 60

61 Convergence of $f_{\rm NL}$ as a function of $\ell_{\rm min}$ or $\ell_{\rm max}$ 64
62 Ratio of the observed variance over the theoretical prediction 65
63 Hit-count map describing the scanning pattern of Planck 67
64 Power spectrum of the raw 143 GHz map 69

71 $\bar{v}_{12}/(1+\bar{v}_{12}^2)$ and $\bar{v}_{12}^2/(1+\bar{v}_{12}^2)$ as a function of $\bar{v}_{12}$. 81

81 $\frac{(\bar{v}_{12e})^3}{((1+(\bar{v}_{12e})^2)^2}$ as a function of $\bar{v}_{12e}$ and its two upper limits 0.325 and $1/\bar{v}_{12e}$. 88
82 Parameter space of m and n where the turn can occur before the end of slow-roll . 97

91 The two types of turn where the slow-roll approximation is broken 100
92 |r.h.s.|, |order1| and |order2| during the turn of the field trajectory 107

101 Quadratic potential 114
102 Monomial potential $n = 2$, $m = 4$ 118
103 Monomial potential $n = 4$, $m = 2$ 119
104 Quartic-axion potential 120
105 Monomial potential $n = 2$, $m = 2$ 122
106 Non-monomial potential 123

A1 Weights of the bispectral shapes (high resolution) 132
A2 Weights of the bispectral shapes (low resolution) 133
A3 Weights of the bispectral shapes (low resolution) 134

Part I

Introduction

Chapter 1

Introduction

A hundred years of observations and theoretical works have refined the standard model of cosmology describing our universe's history and content. In the very early universe, there is a period of rapid and accelerated expansion called inflation [179, 96, 132]. It solves several issues of the pre-inflationary standard cosmology like the horizon and the flatness problems. More remarkably, inflation gives an explanation for the origin of the primordial cosmological perturbations which are the seeds of the large-scale structure of the universe observed today.

There is an almost direct observational window on these tiny primordial fluctuations: the temperature and polarization anisotropies of the Cosmic Microwave Background (CMB), which is the oldest electromagnetic radiation in the universe emitted when the primordial plasma became transparent. Multiple missions have mapped the sky in the microwave range and the most recent results come from the Planck mission [13, 15]. Like its predecessors, Planck found no disagreement with the basic inflationary predictions: the distribution of primordial density perturbations is almost but not exactly scale-invariant and is consistent with Gaussianity. Moreover, the Planck satellite significantly improved the constraints on any potential deviations from a Gaussian distribution (i.e. on non-Gaussianity) [14].

When determining cosmological parameters of primordial origin using precise CMB measurements, one of the main issues is that several foregrounds of galactic (e.g. dust) or extra-galactic (e.g. radio point sources) origin also emit in the microwave range. This required the development of many techniques (see [8, 9, 16] and references therein) to clean the observational data from these different sources of contamination.

If the CMB were Gaussian, all the information would be encoded in the power spectrum, which is related to the two-point correlation function of the CMB temperature/polarization fluctuations. The power spectrum is parametrized by two important observables from the point of view of inflation: its amplitude A_s and the spectral index n_s that describes its slope, or in other words the deviation from exact scale invariance. Primordial non-Gaussianity is generally parametrized by the amplitude parameters $f_{\rm NL}$ of a number of specific bispectrum shapes that are produced in generic classes of inflation models. The bispectrum is related to the three-point correlator of the CMB anisotropies. It is known to be unobservably small [141] for the simplest inflationary model: standard single-field slow-roll inflation. However, this result is not general, meaning that current observations can in principle be used to constrain more complicated inflationary models. One popular extension of inflation which can produce non-Gaussianity is so-called multiple-field inflation, where the expansion is driven by several scalar fields.

In this thesis, the topic of primordial non-Gaussianity is studied from two different points of view. The first is the estimation of bispectral non-Gaussianity in observational data of the CMB anisotropies (Planck). It is a continuation of the work on the binned bispectrum estimator [43, 42], used for the official Planck analysis [11, 14]. We are interested in studying

the contamination of the primordial signal due to several galactic foregrounds (mainly the dust) and determining (numerical) bispectrum templates for them. Even if the bispectrum is not ideal to describe the non-Gaussianity of the galactic foregrounds because they are very anisotropic (it would be better to work in pixel space instead of harmonic space), it is exactly what we need to understand their impact on the determination of the primordial shapes. The main aim is to verify if it is possible to detect these foregrounds in raw sky observations or some residual of them in cleaned CMB maps.

The second and main work concerns multiple-field inflation, where local non-Gaussianity can be produced on super-horizon scales. Its aims are threefold. The first is a continuation of the work on the long-wavelength formalism [163, 162, 164, 191, 192, 189], used to compute the non-Gaussianity parameter f_{NL}. We derive a new formulation for the expression of f_{NL} and discuss its consequences for certain classes of potentials. Since Planck has excluded the possibility of large local non-Gaussianity (of order 10), the reader might wonder what the interest is of looking for models with large non-Gaussianity. However, it is very important in order to understand if Planck actually ruled out any significant parts of the multiple-field model space, or if these models generically predict small non-Gaussianity. Moreover, an f_{NL} of order 1, which we will consider as large, has not yet been ruled out by Planck but might be observable by the next generation of experiments.

The second aim is to understand if it is possible to have large non-Gaussianity while staying within the slow-roll approximation. We also take into account the constraints from Planck on the other inflationary observables, in particular n_s. And it turns out that satisfying the observational constraints on n_s while having a large f_{NL} and staying within the slow-roll approximation is very hard. In the case of a sum of two monomial potentials and a constant we explicitly work out the region of the parameter space (in terms of the powers of the two potentials) where this is possible. Note that we assume everywhere that the isocurvature mode has disappeared by the end of inflation. Otherwise it would be easy to get large non-Gaussianity by ending inflation in the middle of a turn of the field trajectory, but we feel that in that case the results at the end of inflation would be meaningless, since they could not be extrapolated to the time of recombination and the CMB without properly treating the end of inflation and the consecutive period of (p)reheating.

Finally, the third aim is to understand the, at first sight very surprising, numerical observation that even in the case where the slow-roll approximation is broken during the turn of the field trajectory, the analytical slow-roll expression for f_{NL} is often still a very good approximation of the final exact result. It turns out that we can understand this using the new formulation mentioned above. In that formulation f_{NL} is given by a differential equation and the solution can be written as the sum of a homogeneous and a particular solution. As we will show, the homogeneous solution can be given analytically in an exact form (without any need of the slow-roll approximation), while the particular solution is negligible exactly in the regions where slow roll is broken and we cannot compute it analytically.

The thesis is divided into three main parts. The first part introduces the cosmological concepts necessary for this thesis. In chapter 2, we review the standard model of cosmology, discussing the evolution of the homogeneous background and the thermal history of our universe in the context of the Big Bang theory. The historical motivations for a period of inflation in the early universe are discussed and finally the basic equations describing inflation are given. In chapter 3, small fluctuations are added to this homogeneous background. We recall some basic statistical concepts and we apply them to the Gaussian distribution of the CMB anisotropies (valid at first order) decomposed using spherical harmonics. We then recall the main inflationary results of first-order perturbation theory and we link them to the CMB observations.

The second part focuses on the estimation of bispectral non-Gaussianity using Planck ob-

servational data. Chapter 4 is an introduction to the topic. The quantities of interest (e.g. bispectrum) are defined. The derivation of the weakly non-Gaussian probability density function is discussed using the Edgeworth expansion. The method of the binned bispectrum estimator is also reviewed. In chapters 5 and 6, our data analysis results using the binned bispectrum estimator on data from the 2015 Planck release are presented. In chapter 5, several galactic foregrounds are studied at the bispectral level. The newly determined templates from these foregrounds are then applied to several CMB maps (Gaussian simulations and real data) in chapter 6.

The third part of this thesis concerns the generation of non-Gaussianity in two-field inflation. In chapter 7 we define the slow-roll parameters and other quantities used in the rest of the thesis. It also recalls the main steps of the long-wavelength formalism, in particular the expressions for the different observables. This chapter is also where we derive the new formulation mentioned above. In chapter 8, we treat the slow-roll results mentioned in aim two above. It uses increasing levels of approximation. First, the slow-roll approximation is discussed. Then we add the hypothesis that the potential is sum-separable to solve the Green's function equations and to obtain simple expressions for the observables. Then they are applied to the specific class of monomial potentials, where the effects of the spectral index constraint on the region of the parameter space where $f_{\rm NL}$ is large are computed. In chapter 9, we keep the sum-separable potential hypothesis to compute $f_{\rm NL}$ beyond the slow-roll approximation. Two different types of generic field trajectories with a turn are discussed. We show that in the end the slow-roll expression from the previous section also gives a very good approximation of the exact result for $f_{\rm NL}$ in this case. Chapter 10 contains several specific examples to illustrate the different results of this part of the thesis. The method to build a monomial potential that produces a large $f_{\rm NL}$ while satisfying all constraints is detailed, while some examples from the literature are also discussed. Each time we compare the exact numerical results in the long-wavelength formalism to the approximated analytic expressions derived in this thesis. Finally we conclude in chapter 11, while some additional details are treated in the appendices.

Chapter 2

Standard model of cosmology

At the foundations of modern cosmology, there are several important observations:

- The universe is homogeneous and isotropic when viewed on sufficiently large scales (> 100 Mpc).[1]
- The universe is not static, it is in expansion.
- The universe is filled by a thermal bath of photons at a temperature of around 3K.
- The matter is distributed in a structured way from stars to superclusters containing thousands of galaxies, each of these galaxies containing themselves billions (or more) stars. These structures were formed over time by gravitational collapse.
- In the past, the matter distribution was much more homogeneous and isotropic.

In this chapter, we will develop the three first points further to describe the behaviour of the universe as a whole. General relativity is the usual framework to study its evolution. We will start by reviewing the background theory of Friedmann-Lemaître-Roberston-Walker (FLRW) universes. This is followed by a discussion about the thermal history of our Universe in the context of the Big Bang theory motivated by the expansion, with a focus on the cosmic microwave background. This will provide several motivations for a period of exponential expansion in the very early universe, called inflation. In the last section, we recall the main elements of the theory of inflation with a focus on the background, using the basic equations of scalar-field cosmology and introducing the notion of slow-roll.

The two last points require to go beyond the description of the universe presented in this chapter, as they concern local fluctuations in the homogeneous background. The main goal of this thesis is to study the generation of the tiny primordial inhomogeneities and anisotropies and the methods to study their observations. This will be developed in detail starting in chapter 3. However, the formation of structures afterwards, a very rich domain of cosmology, is beyond the scope of this thesis.

Many lectures and textbooks are available to study modern cosmology. To cite only a few of them, a great introduction can be found in [128] while for more details, many recent textbooks like [64, 149, 198, 157] can be consulted by the reader.

[1] The megaparsec ($\approx 3 \times 10^6$ light-years $\approx 3.10^{19}$ km) is the standard unit of distance in cosmology.

2.1 Background theory

2.1.1 Some elements of general relativity

General relativity describes the link between the geometry of the universe and its content. We start by recalling a few formal definitions of geometric quantities.

The invariant square of an infinitesimal line element is given by

$$\mathrm{d}s^2 = g_{\mu\nu}\mathrm{d}x^\mu \mathrm{d}x^\nu, \tag{2.1}$$

where we use the standard summation convention and $g_{\mu\nu}$ is the metric tensor, the fundamental object of study in general relativity. It describes the geometric structure of space-time. We can then introduce the Christoffel symbols

$$\Gamma^\lambda_{\mu\nu} = \frac{1}{2} g^{\lambda\alpha} \left(\partial_\mu g_{\nu\alpha} + \partial_\nu g_{\mu\alpha} - \partial_\alpha g_{\mu\nu}\right). \tag{2.2}$$

They are needed to define the covariant derivative D_μ, the correct differentiation operator for parallel transport on a curved manifold

$$D_\mu A^\nu = \partial_\mu A^\nu + \Gamma^\nu_{\mu\lambda} A^\lambda. \tag{2.3}$$

Another key quantity to characterize a curved manifold is the Riemann tensor

$$R^\mu{}_{\nu\alpha\beta} = \partial_\alpha \Gamma^\mu_{\nu\beta} - \partial_\beta \Gamma^\mu_{\nu\alpha} + \Gamma^\mu_{\sigma\alpha}\Gamma^\alpha_{\nu\beta} - \Gamma^\mu_{\sigma\beta}\Gamma^\sigma_{\nu\alpha} \tag{2.4}$$

and in particular the tensor constructed by contraction of two indices

$$R_{\mu\nu} = R^\lambda{}_{\mu\lambda\nu}, \tag{2.5}$$

known as the Ricci tensor and its trace

$$R = R_{\mu\nu} g^{\mu\nu}, \tag{2.6}$$

called the Ricci scalar. They measure the curvature of the manifold, so in general relativity it corresponds to the change from Minkowski space.

Finally, it is convenient to combine these definitions to form the Einstein tensor

$$G_{\mu\nu} = R_{\mu\nu} - \frac{1}{2} R g_{\mu\nu}, \tag{2.7}$$

of which the covariant derivative is conserved (Bianchi identities)

$$D_\mu G^{\mu\nu} = 0. \tag{2.8}$$

We will now apply these few definitions to discuss the standard model of cosmology.

2.1.2 Cosmological background

An homogeneous and isotropic universe is described by the Friedmann-Lemaître-Roberston-Walker (FLRW) metric [87, 122, 166, 196]

$$\mathrm{d}s^2 = -N^2(t)\mathrm{d}t^2 + a^2(t)\left(\frac{\mathrm{d}r^2}{1-Kr^2} + r^2 \mathrm{d}\Omega^2\right), \tag{2.9}$$

where $a(t)$ is the scale factor of the universe, the lapse function $N(t)$ fixes the choice of time coordinate ($N = 1$ for the cosmic time, $N = a$ for the conformal time, etc.) and K is the

rescaled spatial curvature of the Universe (it can take the values +1, 0 or -1 for a closed, flat or open universe respectively).

The Einstein equation, which describes the interactions between the geometry (so how a evolves in (2.9)) and the matter content [68, 69], follows from applying the action principle to

$$S = \int \mathrm{d}^4x \left(\kappa^{-2}\sqrt{-g}\left(\frac{R}{2} - \Lambda\right) + \mathcal{L}_m \right), \tag{2.10}$$

where κ is the inverse Planck mass defined by $\kappa^2 \equiv 8\pi G = 8\pi/M_p^2$, g is the determinant of the metric, $\mathcal{L}_m$ is the matter Lagrangian and Λ is the cosmological constant. The Einstein equation has the usual form

$$G_{\mu\nu} + \Lambda g_{\mu\nu} = \kappa^2 T_{\mu\nu} \quad \text{with} \quad T^\mu_\nu \equiv -\frac{2g^{\mu\lambda}}{\sqrt{-g}}\frac{\delta \mathcal{L}_m}{\delta g^{\lambda\nu}}. \tag{2.11}$$

More can be said about the form of the energy-momentum-stress tensor $T_{\mu\nu}$ from the properties of isotropy and homogeneity of the matter content. One can show that the most general expression has to be diagonal

$$T_{00} = \rho(t), \quad T_{ij} = p(t) g_{ij} \quad \text{and} \quad T_{0i} = 0, \tag{2.12}$$

where ρ and p are the energy density and the pressure of the matter field.

Substituting this energy-momentum tensor and the metric (2.9) in the Einstein equation (2.11), one obtains the Friedmann equation [87, 88] from the (00) component

$$H^2 \equiv \frac{\dot{a}^2}{N^2 a^2} = \frac{\kappa^2}{3}\rho + \frac{\Lambda}{3} - \frac{K}{a^2}, \tag{2.13}$$

where we introduced the Hubble parameter H. From the spatial components, we find

$$\frac{1}{a}\frac{\mathrm{d}}{\mathrm{d}t}\left(\frac{\dot{a}}{N}\right) = -\frac{\kappa^2}{6}(\rho + 3p) + \frac{\Lambda}{3} \quad \Longleftrightarrow \quad \frac{\dot{H}}{N} = -\frac{\kappa^2}{2}(p+\rho) + \frac{K}{a^2}. \tag{2.14}$$

Another important equation, not independent from the previous ones, is hidden in the Einstein equations. It follows from the Bianchi identities (2.8) which imply the conservation of the energy-momentum tensor $D_\mu T^\mu_\nu = 0$. In our case it takes the form

$$\dot{\rho} + 3HN(\rho + p) = 0. \tag{2.15}$$

As we have only two independent equations for three unknowns (the scale factor, the energy density and the pressure), it is standard to assume the following equation of state

$$p = w\rho. \tag{2.16}$$

In the case of a constant w, it is then easy to solve (2.15) to obtain the evolution of the energy density as a function of the scale factor

$$\rho \propto a^{-3(1+w)}. \tag{2.17}$$

The solution of the Friedmann equation (2.13) (with $K = 0$ and $\Lambda = 0$) is then given by

$$a(t) \propto \begin{cases} e^{Ht}, & \text{if } w = -1, \\ t^{\frac{2}{3(1+w)}}, & \text{otherwise.} \end{cases} \tag{2.18}$$

	Equation of state	Energy density	Scale factor
Non-relativistic	$w = 0$	$\rho \propto a^{-3}$	$a \propto t^{2/3}$
Relativistic	$w = \frac{1}{3}$	$\rho \propto a^{-4}$	$a \propto t^{1/2}$
Cosmological constant	$w = -1$	$\rho \propto a^{0}$	$a \propto e^{Ht}$
Curvature	$w = -\frac{1}{3}$	$\rho \propto a^{-2}$	$a \propto t$

Table 21: Solutions of equations (2.15) and (2.13) in the case $K = 0$ and $\Lambda = 0$ for non-relativistic (or pressureless) matter, relativistic matter (radiation) and for fluids equivalent to a cosmological constant or the curvature term.

Table 21 recalls the standard values of w for different types of matter and the associated solutions for the energy density and the scale factor. As we will see in the next section, the first three values correspond to the different cosmological eras.

We end this section with a few more useful definitions. Instead of working with the energy density ρ, it is common to use the dimensionless density parameters Ω defined by

$$\Omega \equiv \frac{\rho}{\rho_{\text{crit}}}, \qquad \text{with} \quad \rho_{\text{crit}} \equiv \frac{3H^2}{\kappa^2}. \tag{2.19}$$

It is then straightforward to define an Ω_X for each type of matter (e.g. baryons, photons, etc.). Following the same method on the other terms of Friedmann equation (2.13), we can define similar parameters for the cosmological constant and the curvature

$$\Omega_\Lambda \equiv \frac{\Lambda}{3H^2}, \qquad \Omega_K \equiv \frac{K}{(aH)^2}, \tag{2.20}$$

and the Friedmann equation can be rewritten as

$$\sum_X \Omega_X + \Omega_\Lambda = 1 + \Omega_K. \tag{2.21}$$

2.2 The Big Bang theory

In the previous section we reviewed the general equations describing the dynamics of FLRW universes and the link with their matter content. Here we discuss how several different observations lead to the Big Bang theory.

2.2.1 Expansion and redshift

While the possibility of a universe in expansion was foreseen by Friedmann in the early 1920's, it was a few years later that both Lemaître [122] and Hubble [105] deduced from observations that indeed our universe is expanding. They showed that in average other galaxies are moving away from us with a recessional velocity obeying a simple law. It is proportional to the distance, and known as Hubble's law

$$\boldsymbol{v}_r = H_0 \boldsymbol{d}, \tag{2.22}$$

where H_0 is the current value of the Hubble parameter as indicated by the subscript 0. The Hubble constant is now measured to be around 70 km s^{-1} Mpc^{-1}. Different types of observations can give us constraints on the exact value of H_0, but there are currently tensions between them.

Observing that galaxies are receding from us was done by measuring the shift of the characteristic lines of their spectra to larger wavelengths. The standard parameter to describe this effect is the redshift z defined by

$$z = \frac{\lambda_{\text{obs}} - \lambda_{\text{em}}}{\lambda_{\text{em}}}, \tag{2.23}$$

where λ_{em} and λ_{obs} are the wavelengths at emission and observation. The redshift is related to the scale factor by

$$z + 1 = \frac{a_0}{a}. \tag{2.24}$$

Because of the expansion, the further away an observed object is, the more redshifted it will be. Hence if the redshift is a good scale of distance (except for nearby objects which also have a non-negligible peculiar velocity compared to their recessional one), it is also a good scale of time. In cosmology it is common to use z as the time scale of the past events of our universe as we will see in the next section.

2.2.2 Thermal history of the universe

Extrapolating the current expansion of our universe leads to the idea that in the past everything was much closer so the universe was much denser and hotter up to a point where the scale factor is zero and the temperature and the density are infinite. This singularity is called the Big Bang. The Big bang theory is then the study of the cooling of the universe from that point until now. In this section, we recall the main events, giving approximate time and energy scales, which have occurred in the last 13.8 billions years (the estimated time that has elapsed since the Big Bang). We focus on the early universe whose description is based on our understanding of the physics at high energy scales, so the standard model of particle physics (for a complete and recent review see [154]).

Beyond the standard model

Times before the Planck scale (10^{-43} s, 10^{19} GeV), are far beyond our scope because they require a quantum theory of gravity. However, even at the end of the Planck era, the energy was still orders of magnitude larger than the ones which are produced in the LHC ($\sim 10^4$ GeV). This leaves plenty of time for new physics, like a period of inflation (see section 2.3) which could have occurred around the GUT scale (10^{-37} s, 10^{16} GeV) when the strong interaction is believed to have decoupled from the electroweak.

Quark era

It is only much later, a few picoseconds after the Big Bang, that we arrive at energy scales which have been explored in particle accelerators. Heavy leptons and gauge bosons were disappearing by decaying and annihilating. An important event of that epoch (around 100 GeV) is the separation of the electroweak interaction into the weak interaction and electromagnetism. At that time the universe is mostly filled by a quark-gluon plasma where the quarks are asymptotically free.

Hadron and lepton eras

When the universe was 10^{-6} s old (~ 1 GeV), the quarks and the gluons finally bound together thanks to the strong interaction to form hadrons. Those made up of three quarks like the protons and the neutrons are called baryons. There were also mesons, which are constituted of a quark and an antiquark. Most of the hadrons disappeared by annihilation with anti-hadrons

or by decay and could not be reformed as the universe was still cooling down (the lightest mesons are pions and have a mass of more than 100 MeV). The leptons started to dominate.

Another important event around that time was the decoupling of the neutrinos which occurred ~ 1 s after the Big Bang (1 MeV). This notion of decoupling is very important in the early universe. Basically, it means that the energy scale of the universe became low enough for the neutrinos to stop interacting with the rest of the primordial content (the rate of interaction became smaller than the rate of expansion H). Since that time the neutrino density only evolved with the expansion. Unfortunately this cosmic neutrino background, with a predicted temperature of 1.95 K is far beyond the reach of our detectors (the solar neutrinos which have an energy $\sim 10^{10}$ larger are already extremely hard to detect).

After that, the main reactions keeping the other species in equilibrium were the electron-positron annihilation to and creation from photons. However, ~ 6 s after the Big Bang (500 keV), the universe became to cold for the creation reaction to occur. Most of the lepton energy was then transferred to photons and only $1/10^9$ of the electrons survived.

Photon era

After 3 minutes (100 keV), the temperature was finally low enough for the first nuclei to form from the remaining protons and neutrons. Even if free neutrons are unstable, their mean lifetime of 900 seconds was several times larger than the age of the universe at that time, so many neutrons produced during the hadron era were still present. Only light nuclei were produced, starting with deuterium (1 proton + 1 neutron) and then helium with nothing heavier than lithium and beryllium. This period is called primordial nucleosynthesis and the first estimations of the distribution of the different nuclei were given by Gamow [89]. The fact that we observe the predicted ratio of helium and hydrogen with an homogeneous distribution on cosmological scales is one of the strong arguments for the Big Bang theory.

For all these energy scales we described (except maybe those beyond the standard model of particle physics), it was relativistic matter that dominated. This is usually called the radiation domination era. However, as we have seen in table 21, its energy density decreases like a^{-4}. Hence after some time, non-relativistic matter for which the energy density is evolving as a^{-3} will start to dominate.

Matter domination era

Indeed, there is much later a transition to the matter domination era which occurs at the redshift $z_{\rm eq} \sim 3400$, so around 50000 years after the Big Bang.

After that for many thousands of years, the photons were still in thermal equilibrium with the plasma of ionized matter (light nuclei). This changed when the temperature was low enough to form neutral atoms of hydrogen. This process is called recombination. Then the scattering of photons by the free electrons (the main reaction keeping the photons in equilibrium with the rest) became inefficient. This is called the decoupling of the photons and as the neutrinos earlier they have since then traveled freely, only affected by the expansion (and also a little by the different structures of matter that will appear later, as the universe is not fully transparent). We can now observe these photons in the cosmic microwave background (see section 2.2.3) which was emitted 380000 years after the Big Bang ($z_{\rm dec} \sim 1100$). The surface defined by $z_{\rm dec}$ is often called the last scattering surface.

At recombination, the universe was still very homogeneous (relative fluctuations of order 10^{-5}). It then took many millions of years to form observable structures by gravitational collapse. It is in the core of the first stars that heavier elements started to be created by nuclear fusion reactions (stellar nucleosynthesis). The oldest observed galaxies were formed

only a few hundred million years after the Big Bang, at a redshift of more than 10. The structures which are familiar to everyone appeared much later. Our own galaxy, the Milky Way, acquired its characteristic form less than 10 billion years ago. The solar system was formed around 4.6 billion years ago hence around the time the universe entered into another era.

Dark energy domination era

One of the most surprising results of modern cosmology was the observation in 1998 by two teams [156, 160] that the expansion of our universe is accelerating. The matter domination era (during which the expansion was slowing) ended when the universe was around 9 billion years old, at a redshift $z \sim 0.4$. The dominant contribution comes from an unknown form of energy called dark energy, with a negative pressure which could be a cosmological constant.

2.2.3 The Cosmic Microwave Background (CMB)

One of the main predictions of the Big Bang theory, which was first claimed by Alpher and Herman in 1948 [21], is the presence of a thermal bath of photons at a temperature of a few Kelvin. It was indeed detected in 1965 by Penzias and Wilson at 3.5 K [155] and they were helped to make the link with the Big Bang theory [62]. This signal was then called the cosmic microwave background (CMB). A recent review can be found in [41].

At the time of decoupling, the photons were in thermal equilibrium. That means that they were distributed according to a Planck or blackbody spectrum whose intensity is given by

$$I_\nu = \frac{4\pi}{c^2} \frac{\nu^3}{e^{\frac{h\nu}{k_B T_\gamma}} - 1}, \tag{2.25}$$

where h is Planck's constant and k_B is Boltzmann's constant. An important property of this distribution is that it remains a blackbody spectrum in a universe in expansion, with the difference that the temperature is redshifted so $a(t)T_\gamma(t) = T_{\gamma_{\text{dec}}} a_{\text{dec}}$, meaning that the current temperature is $T_{\gamma_0} \approx T_{\gamma_{\text{dec}}}/1100$. Many other observations followed to refine the CMB temperature measurement. They also found that the CMB is isotropic to a large extent, at the exception of the dipole due to our relative velocity with respect to the last scattering surface.

Among the most important past missions, we have to mention the COBE satellite which was launched in 1989, which gave us the most accurate measurements of the CMB blackbody spectrum [144] characterized by the temperature

$$T_{\gamma_0} = 2.725 \pm 0.001 \text{ K}. \tag{2.26}$$

More importantly, COBE went a step further with the first detection of temperature anisotropies (see section 3.2 for their description) beyond the dipole [178], on large scales. Many models of the primordial universe were ruled out at that time for predicting the wrong amount of primordial fluctuations.

The satellite WMAP, which took data for nine years after being launched in 2001, brought the precision of the measurements to another level by including many more scales [35, 34]. It also measured the E-polarization of the CMB (more explanations later). WMAP observed the sky in five different frequency channels (23, 33, 41, 61 and 94 GHz) using detectors passively cooled. One of the main results of the mission was the detection of a small but statistically significant deviation from scale-invariance for the spectrum of the anisotropies which was another strong argument for inflation as we will see in section 3.3.

The most recent and accurate results for temperature and polarization anisotropies come from the Planck mission [185, 7]. The satellite was launched in 2009, with a two times better

angular resolution and ten times better sensitivity than WMAP. Planck observed the sky in nine frequency channels (30, 44, 70, 100, 143, 217, 353, 545 and 857 GHz) with two different instruments (LFI and HFI). LFI (Low Frequency Instrument) mapped the sky for four years in the three lowest frequency bands, with a technology similar to WMAP. But HFI (High Frequency Instrument) used cryogenically cooled (at 0.1 K) bolometers to observe the six other frequency channels during two and a half years. All the Planck data is now public after the two releases of 2013 and 2015. A new analysis should arrive soon with a better understanding of the polarization systematics.

A successor to Planck has been proposed, called CORE (Cosmic Origins Explorer) [40, 83]. In part III, we will use forecasts of error bars on some parameters expected from this type of experiment.

We mentioned previously the polarization of the CMB and this deserves a few clarifications. While it appeared unpolarized during the first observations, it also contains very small fluctuations of polarization (in a similar way to the temperature anisotropies). The physical origin of the CMB polarization is Thomson scattering of the photons on free electrons still present before decoupling. There is a standard decomposition of the spin 1 field describing polarization into the so-called E- and B-modes [110], similarly to the electric and magnetic fields of electrodynamics. E-polarization is now well-mapped thanks to WMAP and Planck, however primordial B-modes have not yet been detected and that will be one of the main objectives of future CMB missions, like LiteBIRD [145] and CORE. In this thesis, we will not use polarization data in the data analysis part II. Hence, we will not develop it further.

2.2.4 Λ-CDM

The Planck CMB observations, coupled to many other observations of more late-time effects which we do not have the time to describe here, have refined our knowledge of the current and past energy content of our universe. In this section, we will briefly describe the different density parameters given in [13] (error bars correspond to the 68% limits).

Dark energy: $\Omega_{\Lambda_0} = 0.6911 \pm 0.0062$

As mentioned at the end of section 2.2.2, observations of the recent acceleration of the expansion of the universe (for a few billion years) indicates that the universe is dominated by dark energy, which now represents nearly 70 % of its content.

Determining the nature of this unknown form of energy, which has a negative pressure $p \simeq -\rho$, is one of the main challenges of modern physics. At the level of precision of the observations, it is well described by the cosmological constant Λ (so $p = -\rho$) of the Einstein equation (2.11). Quantum field theory even gives an explanation of its origin, it could be the vacuum energy. However, computations show that the vacuum energy is 10^{120} times too large to be the observed cosmological constant.

Several possibilities have been considered to solve the issue like proposing modifications of general relativity (see the review [56] for example).

Non-relativistic matter: $\Omega_{m_0} = 0.3089 \pm 0.0062$

The remaining 30 % are mostly non-relativistic (pressureless matter), which can themselves be described into two components: Ω_b and Ω_c:

- **Baryons:** $\Omega_{b_0} h^2 = 0.02230 \pm 0.00014$[2]
  All the observable structures of our universe are made of baryons (protons and neutrons,

[2] h is the reduced Hubble parameter: $H_0 = 100h$ km s^{-1} Mpc^{-1}.

but we usually consider the electrons, which are a lot lighter, with them). They only represent ~ 5 % of the universe content.

- **Cold dark matter:** $\Omega_{c_0}h^2 = 0.1188 \pm 0.0010$
  Plenty of evidence for the existence of an unknown form of matter called dark matter has been found over the last decades. In 1933, Zwicky observed rapid motions of galaxies which can not be explained by the luminous matter, he then proposed the existence of dark matter to solve the problem of missing mass [206]. At the scale of a galaxy, anomalies were observed in the galactic rotation curves [22, 167]. Dark matter plays a very important role in the formation of the structures and comparison between the ones observed today and N-body simulations favors cold dark matter (non-relativistic). Many possibilities have been studied. For example there is the WIMP (Weakly Interacting Massive Particle), a heavy particle that would interact with standard matter only via gravity and weak interaction. Many experiments tried to detect them in the previous decade, without success (see [85] for example, one of my previous works).

Relativistic Matter $\Omega_{r_0} < 10^{-4}$

- **Photons:** $\Omega_{\gamma_0} \simeq 5.35 \times 10^{-5}$
  The photons which dominate the energy content in the early universe and we can now observe in the CMB (see previous section) only constitute a tiny fraction of the total energy density (and those emitted later, by stars for example, even less).

- **Neutrinos:** $\Omega_{\nu_0} = 1.25 N_\nu \times 10^{-5}$ (for massless neutrinos and $N_\nu = 3$)
  As for the photons, the three known families of neutrinos which constitute the cosmic neutrino background represent a very small fraction of the content of the universe. The exact value is unknown as it depends on their mass which has not yet been measured (it is known to be of order 0.1 eV at most). They have a measurable effect on the CMB spectrum and on the formation of structures later (see [125, 33] for example).

The results presented in this section constitute the standard model of cosmology, often called Λ-CDM as these two components contribute 95 % of the energy density of the universe.

2.2.5 Cosmological puzzles

While the Big Bang theory is extremely successful to describe and understand most of the ~ 14 billion years of evolution of our universe, there are still a few problems. For example, the nature of dark matter and dark energy, which together constitute most of the content of the universe, is still unknown. However, here, we will focus on those which provide strong motivations for inflation, the main topic of this thesis which we will define properly in the next section.

The horizon problem

Since our universe is only 14 billions years old, information from distant places had only a limited amount of time to travel to us. However, because of the expansion it is not trivial to find how remote two regions of space can be for causal contact to still have been possible. The answer to this question is called the particle horizon which is given by

$$d_H(t) = a(t) \int_0^t \frac{\mathrm{d}t'}{a(t')}. \tag{2.27}$$

Substituting into this the scale factor expressions given in table 21, one can show that in a flat matter dominated universe we have $d_H(t) = \frac{2}{H(t)}$ and in a a flat radiation dominated universe

$d_H(t) = \frac{1}{H(t)}$. Hence, the quantity H^{-1}, which is often called the Hubble scale (or length or radius) is related to the notion of horizon for these universes. It is a good indication of the current size of the observable universe.

During the radiation and matter dominated eras, the radius of a part of the universe increases like a ($\propto t^{1/2}$ or $\propto t^{2/3}$ for radiation and matter domination respectively), while the particle horizon increases like H^{-1} ($\propto t$). So going backwards in time, the size of the now-observable universe was larger than the particle horizon. There is then no apparent reason for the universe to be homogeneous on the largest scales because causal contact was established only recently. This is the horizon problem. At the time of the emission of the CMB, the particle horizon was much smaller than the size of our now-observable part of the universe was at that time. To illustrate the horizon problem, it is standard to compute the angular size of the particle horizon on the last scattering surface, which is given by

$$\theta_{\text{hor,CMB}} = \frac{\int_0^{t_{\text{rec}}} \frac{\mathrm{d}t'}{a(t')}}{\int_{t_{\text{rec}}}^{t_0} \frac{\mathrm{d}t'}{a(t')}}, \tag{2.28}$$

where the numerator is the comoving particle horizon at the time of the emission of the CMB and the denominator is the comoving distance from the last scattering surface to us. Including the different matter contents we discussed in the previous section and the observed values of their density parameters, it is possible to solve the integrals numerically. The well-known answer is that $\theta_{\text{hor,CMB}} \sim 1°$, so the CMB is made of 10^4 causally disconnected patches. The Big Bang theory does not provide an explanation for the homogeneity of the CMB on larger scales.

A good indication of the solution to the horizon problem is that the numerator integral is divergent if there is a period of accelerated expansion induced by a fluid with $w < -\frac{1}{3}$ before the radiation domination epoch[3], so in principle it is possible to have the particle horizon as large as necessary to solve the horizon problem. This period of accelerated expansion, called inflation, only lasts for a finite amount of time and usually does not start before the energy scale is below the GUT scale, so we are not concerned with the divergence. In section 2.3.2, we will compute explicitly the minimum required amount of inflation.

The flatness problem

Observations have shown that the contribution from curvature to the total energy density is small today: $|\Omega_{K_0}| < 0.005$ [13], so the universe is very flat. Moreover, as we have seen in table 21, the curvature energy density decreases less rapidly than the radiation and matter ones. This means that in the past, its contribution was even smaller. At the transition from the radiation to the matter dominated era when non-relativistic matter becomes the main component, we had $|\Omega_K(z_{\text{eq}})| = \left|\frac{\Omega_{K_0}}{\Omega_{\text{m}_0}} \frac{1}{z_{\text{eq}}}\right| \lesssim 5.10^{-6}$. Even earlier at the time of primordial nucleosynthesis when relativistic matter (radiation) dominates, it was $|\Omega_K(z_{\text{PNS}})| = \left|\frac{\Omega_{K_0}}{\Omega_{\text{r}_0}} \left(\frac{1}{z_{\text{PNS}}}\right)^2\right| \lesssim 10^{-18}$. At the Planck scale, it should be even smaller than 10^{-63}.

An obvious but fine-tuned solution would be to have a perfectly flat universe. However, one can show that having a sufficiently long period where the matter content has an equation of state with $w < -\frac{1}{3}$ also works. The idea is to have a period of the early universe where the expansion is accelerated to flatten out any initial curvature of the universe.

[3] Note that in the case $w = -1$ (cosmological constant dominated cosmology), the lower bound of the integral should be $-\infty$ and not 0 to have $a = 0$ initially.

Other problems

One other historic issue that led to the theory of inflation is the monopole problem. Grand unified theories predict phase transitions in the very early universe that produce topological defects like magnetic monopoles. These topological defects should now dominate the energy content of our universe (their density evolves like a^{-3}), yet they have never been observed. A period of accelerated expansion after their production would dilute their distribution and could explain why we have not detected them.

Another question in the Big Bang theory is how our universe can both be so homogeneous and isotropic on the largest scales (with relative fluctuations of order 10^{-5}) and still have structures like galaxies and clusters on smaller scales. Again, the first issue is obviously solved by a period of inflation that will erase any initial inhomogeneity. But more surprisingly, inflation also provides an explanation for the origin of the small fluctuations on top of this homogeneous background (see chapter 3).

As we have seen, many important issues of the Big Bang theory can be solved by a period of accelerated expansion in the early universe. We will see how to describe inflation in the next section.

2.3 Inflation

The basic concept of inflation is very simple, it is a period of very fast and very accelerated expansion occurring in the very early universe. During such a period, the universe's energy content is dominated by one (or several) scalar field(s) with an almost constant potential energy that has the effect of a cosmological constant. Inflation leaves the universe very cold and empty. It has to be followed by a period of reheating during which standard matter is created from the potential energy of the scalar field (see [114]).

The cosmology textbooks cited at the beginning of the chapter all contain detailed chapters about inflation. There are also plenty of other materials purely focused on inflation, see for example [32, 165, 123, 129, 173, 197].

2.3.1 History

Before recalling the basic equations of inflation, we start by doing a short review of historic inflationary models.

The first cosmological model describing a period of exponential expansion in the very early universe was rather complicated and used one-loop quantum corrections to the Einstein equations. It was proposed by Starobinsky [179] in 1979-1980. In 1981, Guth [96] proposed a simpler model in which the scalar field is trapped in a local minimum of the potential provoking an exponential expansion until it reaches the global minimum by quantum tunneling. He also invented the term inflation and noticed that such a period would solve several remaining issues of the Big Bang theory (i.e. flatness, horizon, etc., see section 2.2.5). His model known today as "old inflation" did not provide enough reheating. Hence other models soon followed.

The "new inflation" model due to Linde [131], Albrecht and Steinhardt [19] introduced the idea of a field slowly rolling down a potential hill inducing a nearly exponential expansion, the basic idea for many other inflationary models developed later. However, their specific model based on the SU(5) Coleman-Weinberg potential [57] was shown not to be compatible with observational constraints. Then Linde noticed that an inflationary period could be produced with simpler models (for example a quadratic potential) and called it chaotic inflation because the scalar field has almost arbitrary initial conditions. Many usual standard single-field models are included in this class of potentials.

Different possibilities were later introduced like power-law inflation [134] or natural inflation [86]. In hybrid inflation [133], there are two scalar fields, one responsible for inflation while the other one plays a role at the end of inflation only.

In this thesis, we focus on two-field potentials and several examples will be provided in chapter 10. But for now we will keep the simple case of one scalar field to discuss the basics of inflation.

2.3.2 Scalar-field cosmology

To derive the equations describing inflation, we use again the FLRW metric (2.9) and the action (2.10), but in a simple case. As inflation has the effect to make the universe flat and the scalar field dominates the energy content, we can consider that the cosmological constant Λ and the spatial curvature K are zero. Then the background equations of single-field inflation can be obtained using the following matter Lagrangean

$$\mathcal{L}_m = \sqrt{-g}\left(-\frac{1}{2}g^{\mu\nu}\partial_\mu\partial_\nu\phi - V(\phi)\right), \tag{2.29}$$

where ϕ is the scalar field responsible for inflation (inflaton) and V is its potential. The energy-momentum-stress tensor is then given by

$$T^\mu_\nu = \partial^\mu\phi\partial_\nu\phi - \delta^\mu_\nu\left(\frac{1}{2}\partial^\lambda\phi\partial_\lambda\phi + V(\phi)\right). \tag{2.30}$$

Here we are discussing the background evolution of the universe, so we consider a scalar field depending only on time (we will include spatial dependence later in chapter 3.3). In that case, one can see that the energy density and pressure introduced in (2.12) are

$$\rho = \frac{1}{2}\left(\frac{\dot\phi}{N}\right)^2 + V(\phi), \qquad p = \frac{1}{2}\left(\frac{\dot\phi}{N}\right)^2 - V(\phi), \tag{2.31}$$

and it is straightforward to rewrite the Friedmann equations (2.13) and (2.14)

$$H^2 = \frac{\kappa^2}{3}\left[\frac{1}{2}\left(\frac{\dot\phi}{N}\right)^2 + V(\phi)\right], \qquad \dot H = -\frac{1}{2}\kappa^2\left(\frac{\dot\phi}{N}\right)^2. \tag{2.32}$$

The energy-momentum conservation equation (2.15) gives us the field equation

$$\ddot\phi + \left(3HN - \frac{\dot N}{N}\right)\dot\phi + N^2\frac{\partial V}{\partial\phi} = 0. \tag{2.33}$$

In general, these equations cannot be solved analytically and this will require using several approximations as we will detail in part III.

We finish this section by showing how inflation can be used to solve the cosmological issues introduced in section 2.2.5. For the horizon problem, it is required that a causal region at the start of inflation is now at least as large as the observable universe so using comoving particle horizons we have

$$\frac{1}{a_0 H_0} < \frac{1}{a_{\text{begin}} H_{\text{begin}}}. \tag{2.34}$$

Then the minimal amount of inflation is given by

$$\frac{a_{\text{end}}}{a_{\text{begin}}} = \frac{a_{\text{end}}}{a_0}\frac{H_{\text{begin}}}{H_0} = \frac{T_0}{T_{\text{end}}}\frac{H_{\text{begin}}}{H_0}, \tag{2.35}$$

where the first equality follows from (2.34) and the second one use the fact that the temperature scales as the inverse of the scale factor. To evaluate this expression, some assumptions have to be made. The typical energy scale for inflation is a bit below the GUT scale so we can use $M \sim 10^{16}$ GeV with $H_{\text{begin}} \sim \kappa M^2$. Moreover, we suppose that all the scalar field energy is used for reheating so $T_{\text{end}} \sim M$. Then using the observed values of H_0 and T_0 given in the previous section, one obtains

$$\frac{a_{\text{end}}}{a_{\text{begin}}} \sim 10^{29} \kappa M \sim e^{60}. \tag{2.36}$$

The minimum amount of inflation needed to solve the horizon problem is around 60 e-folds. However, if the reheating temperature is lower, this value will vary between 50 - 60 e-folds [130].

Moreover, the amount of inflation solving the horizon problem is also sufficient for the flatness problem because $\Omega_K \propto (aH)^{-2}$ so having $|\Omega_{K_{\text{begin}}}| > |\Omega_{K_0}|$ gives the same condition for the minimal amount of inflation

$$\frac{1}{(a_{\text{begin}} H_{\text{begin}})^2} > \frac{1}{(a_0 H_0)^2}. \tag{2.37}$$

2.3.3 Slow roll

If the potential is almost flat and the field slowly rolls down, the kinetic terms are very small. This means that certain terms in the equations can be neglected. To quantify this we can introduce a set of slow-roll parameters.

The first parameter we will use is [58]

$$\epsilon \equiv -\frac{\dot{H}}{NH^2} = \frac{\kappa^2 \dot{\phi}^2}{2(NH)^2}. \tag{2.38}$$

It is simply a comparison of the kinetic terms with the potential, hence it has to be very small compared to one for the slow-roll approximation to be valid. However, it is not sufficient because the field acceleration should also be small compared to the field velocity for the slow-roll approximation to stay valid. For this, one can introduce the slow-roll parameters [94]

$$\eta^{(n)} \equiv \frac{N}{H^{n-1}\dot{\phi}} \left(\frac{1}{N}\frac{\mathrm{d}}{\mathrm{d}t}\right)^{n-1} \left(\frac{\dot{\phi}}{N}\right), \quad \text{with} \quad n > 1. \tag{2.39}$$

We are particularly interested in the function $\eta \equiv \eta^{(2)}$ which in the case of cosmic time ($N = 1$) takes the more familiar form $\eta = \ddot{\phi}/(H\dot{\phi})$. It compares the field acceleration to the field velocity, and in the slow-roll approximation it also has to be very small compared to one.

The parameters η and ϵ are first-order slow-roll parameters. We will also use later the second-order parameter $\xi \equiv \eta^{(3)}$ (depending on $\dddot{\phi}$) which is expected to be a lot smaller than the first-order terms. This will be used to perform slow-roll expansions of several equations, in order to be able to solve them analytically.

One can also take a derivative (2.38) and (2.39) to find

$$\dot{\epsilon} = 2NH\epsilon(\epsilon + \eta), \qquad \dot{\eta}^{(n)} = NH\left[(\epsilon - \eta)\eta^{(n)} + \eta^{(n+1)}\right], \tag{2.40}$$

where we can see that the time derivatives of the slow-roll parameters are one order higher than the parameters themselves.

These definitions will be used in the next chapter, when we go beyond the description of the homogeneous background during inflation and we add to it the small fluctuations which are the seeds of the large scale structures we observe today.

Chapter 3

Gaussianity in the primordial Universe

We observe that the Universe has structure. These structures have been formed over time by gravitational collapse. This is confirmed by observations of the CMB which show that the early universe was much more homogeneous and isotropic. More importantly, the very tiny fluctuations of the CMB have been measured with a great accuracy (see figure 31). Their statistical study is a gold mine of information about the primordial universe. One of the main characteristics of these perturbations is that they follow a Gaussian distribution at first order. Hence, we start the chapter by a short review of some basic elements of statistics which can describe this property. Then, we apply them to the CMB, recalling its usual expansion in spherical harmonics. We also explain how these small fluctuations have been generated during a period of single-field inflation. We end the chapter by discussing the relation between inflationary perturbations and CMB anisotropies.

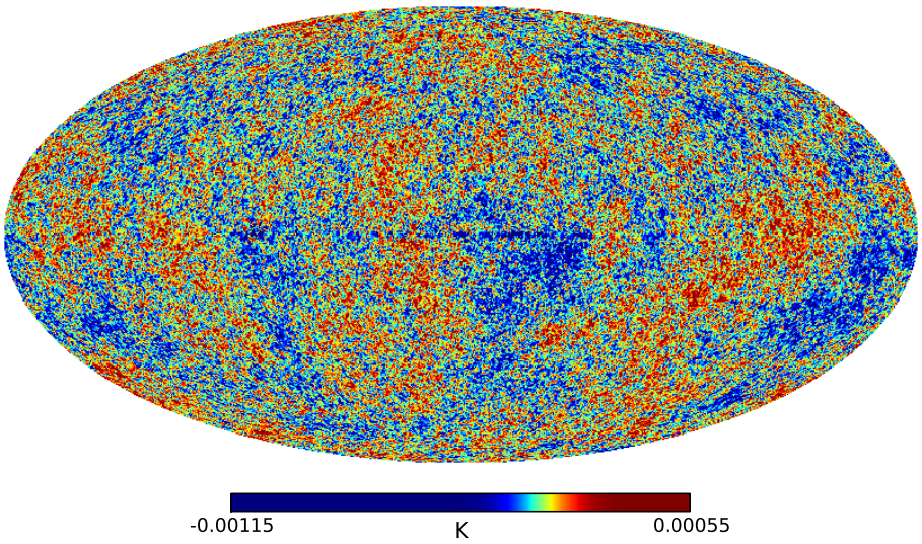

Figure 31: Map of the CMB anisotropies from the 2015 Planck release.

3.1 Some statistics

Statistics are the tool to extract information about a parent population from the properties of an observed sample. That is why to deduce physical quantities from CMB observations, some notions of statistics and estimation theory are needed. In this section, we provide the strict minimum mandatory to follow the next chapters. For those who wish to go further, the book [137] provides a very nice and complete introduction on the topic.

A random field $\boldsymbol{\phi}$ is a set of N real or complex random variables ϕ_i, like for example the harmonic coefficients $a_{\ell m}$ of the CMB (see section 3.2). With an observed sample, it is important to have an estimate of the likelihood to get this exact sample. The tool for this job is the probability density function $p(\boldsymbol{\phi})$ (PDF) of the parent random field. It gives the probability for the random variables to be in a particular range of values and obviously satisfies

$$\int p(\boldsymbol{\phi})\ \mathrm{d}^N\boldsymbol{\phi} = 1, \tag{3.1}$$

where the integration is over all possible values of $\boldsymbol{\phi}$ ($\mathrm{d}^N\boldsymbol{\phi}$ is the Lebesgue measure). The PDF is a positive function which plays an important role to find the expectation value of any quantity $f(\boldsymbol{\phi})$

$$\langle f(\boldsymbol{\phi})\rangle = \int f(\boldsymbol{\phi})p(\boldsymbol{\phi})\ \mathrm{d}^N\boldsymbol{\phi}. \tag{3.2}$$

In particular, $\langle\phi_1\rangle$ is the mean of the random variable ϕ_1. It is also possible to define correlation functions between two or more variables, for example the second-order correlation functions between the components of a random field is called its covariance matrix

$$C_{ij} = \langle(\phi_1 - \langle\phi_1\rangle)(\phi_2 - \langle\phi_2\rangle)\rangle. \tag{3.3}$$

In the one-dimensional case, this is simply the well-known variance of the random variable.

A very important PDF, in general but also especially in this thesis, is the Gaussian distribution which takes the following form for a single random variable ϕ

$$p(\phi) = \frac{1}{\sqrt{2\pi\sigma^2}} e^{-\frac{(\phi-\mu)^2}{2\sigma^2}}. \tag{3.4}$$

It is pretty easy to verify that μ is the mean and σ^2 the variance.

Higher order correlations functions are defined similarly to (3.3). However, in the context of the CMB, we are only really interested in second and third-order correlation functions for the simple reason that for a Gaussian distribution, every odd order correlation function is zero while higher even orders can be expressed by the two-point correlation function. The third-order correlation function is then useful to describe a possible small deviation from Gaussianity, this will be discussed in section 4.3.1.

In the case of the CMB, we have a lot of observational data and we also have a good idea of the form of the PDF (close to a Gaussian distribution). We now need the tools to extract unknown quantities characterizing the PDF. For this we introduce the likelihood $p(\boldsymbol{\phi}, \theta)$ which is the probability to get $\boldsymbol{\phi}$ for a certain value of the parameter θ. Estimation theory is the method to deduce the value of θ from observational data and to determine the minimum reachable error bars.

A first step is to define $\hat{\theta}$, an unbiased estimator of the unknown parameter θ, meaning that $\hat{\theta}$ is a function of the experimental data set used to determine θ and that its expectation value is the parameter itself $\langle\hat{\theta}\rangle = \int \hat{\theta}\, p(\boldsymbol{\phi}, \theta)\ \mathrm{d}^N\boldsymbol{\phi} = \theta$. One can then derive this equation with respect to θ, and after interchanging the order of integration and differentiation one obtains

$$\int \hat{\theta}\frac{\partial p(\boldsymbol{\phi},\theta)}{\partial\theta}\ \mathrm{d}^N\boldsymbol{\phi} = \int \hat{\theta}\frac{1}{p}\frac{\partial p}{\partial\theta}\, p\ \mathrm{d}^N\boldsymbol{\phi} = \int \hat{\theta}\frac{\partial \ln p}{\partial\theta}\, p\ \mathrm{d}^N\boldsymbol{\phi} = 1. \tag{3.5}$$

We also need the very similar computation using the normalization condition (3.1)

$$\theta\frac{\partial}{\partial\theta}\left[\int p(\boldsymbol{\phi})\ \mathrm{d}^N\boldsymbol{\phi}\right] = \theta\int\frac{1}{p}\frac{\partial p}{\partial\theta}\,p\ \mathrm{d}^N\boldsymbol{\phi} = \int\theta\frac{\partial\ln p}{\partial\theta}\,p\ \mathrm{d}^N\boldsymbol{\phi} = 0. \tag{3.6}$$

Combining these two results gives

$$\int(\hat{\theta}-\theta)\frac{\partial\ln p}{\partial\theta}\,p\ \mathrm{d}^N\boldsymbol{\phi} = 1. \tag{3.7}$$

One can then apply the Cauchy-Schwarz inequality $(u\cdot v)^2 \leq u^2v^2$ where the inner product is $u.v = \int uv\,p\ \mathrm{d}^N\boldsymbol{\phi}$ (and $u^2 = u\cdot u$) to verify that

$$1 \leq \left(\int(\hat{\theta}-\theta)^2\,p\ \mathrm{d}^N\boldsymbol{\phi}\right)\times\left(\int\left(\frac{\partial\ln p}{\partial\theta}\right)^2\,p\ \mathrm{d}^N\boldsymbol{\phi}\right). \tag{3.8}$$

It is easy to see that the first term inside parentheses is the variance of $\hat{\theta}$ noted $\mathrm{Var}(\hat{\theta})$. The second term is called the Fisher information $F(\theta)$ and is a very important notion of estimation theory because it gives us a bound on the lower value of the variance possible for an estimator with a certain PDF. (3.8) can be rewritten as

$$\mathrm{Var}(\hat{\theta}) \geq \frac{1}{F(\theta)}, \tag{3.9}$$

and is known as the Cramér-Rao bound. For the optimal estimator (in the sense that it has the smallest error bars) this inequality becomes an equality.

For example, the Fisher information when determining the variance of a Gaussian distribution is

$$F(\sigma^2) = \int\left[\frac{\partial}{\partial\theta}\left(-\frac{1}{2}\ln(2\pi)-\frac{1}{2}\ln(\sigma^2)-\frac{(\phi-\mu)^2}{2\sigma^2}\right)\right]^2\,p\ \mathrm{d}^N\boldsymbol{\phi} = \frac{1}{2\sigma^4}. \tag{3.10}$$

If the variance is determined from a sample of n independent random variables following the same Gaussian distribution, this Fisher information becomes $\frac{n}{2\sigma^4}$.

In the next section, we will apply these notions to the CMB in the simple case of a Gaussian distribution of the perturbations.

3.2 Gaussian statistics for the CMB

After this short section on the basics of estimation theory, it is important to introduce the notation generally used to analyze observed CMB maps. These dimensionless maps gives the fluctuations of physical quantities like temperature ($\Delta T/T_0$) or polarization as functions of the position $\hat{\Omega}$ on the celestial sphere S^2. These functions can be decomposed using the spherical harmonics $Y_{\ell m}$

$$M^p(\hat{\Omega}) = \sum_{\ell=0}^{+\infty}\sum_{m=-\ell}^{\ell} a^p_{\ell m}Y_{\ell m}(\hat{\Omega}), \qquad \text{with } \hat{\Omega} = (\theta,\varphi), \tag{3.11}$$

which can be inverted to

$$a^p_{\ell m} = \int_{S^2}\mathrm{d}\hat{\Omega}\,M^p(\hat{\Omega})Y^*_{\ell m}(\hat{\Omega}). \tag{3.12}$$

The multipole ℓ is a positive integer while m can take the $(2\ell+1)$ values between $-\ell$ and ℓ. The index p corresponds to either temperature T or polarization E and B. However, in this

thesis we do not study the polarization, hence in the following pages we will omit this label to lighten the notation. However, most analytical expressions given in this thesis concerning observations of the temperature anisotropies could be at least generalized to E-polarization.

The spherical harmonics $Y_{\ell m}$ form a set of orthonormal functions on the 2D-sphere and are given by

$$Y_{\ell m}(\theta,\varphi) = (-1)^m \sqrt{\frac{2\ell+1}{4\pi}\frac{(\ell-m)!}{(\ell+m)!}} P_{\ell m}(\cos\theta) e^{im\varphi}, \tag{3.13}$$

where $P_{\ell m}$ are associated Legendre polynomials.

Orthonormality is described by the relation

$$\int_{\theta=0}^{\pi}\int_{\varphi=0}^{2\pi} Y_{\ell m}(\theta,\phi) Y^*_{\ell' m'}(\theta,\phi)\sin\theta \; \mathrm{d}\varphi \; \mathrm{d}\theta = \delta_{\ell\ell'}\delta_{mm'}. \tag{3.14}$$

The addition theorem of spherical harmonics states that

$$\sum_{m=-\ell}^{\ell} Y_{\ell m}(\hat{\Omega}) Y^*_{\ell m}(\hat{\Omega}') = \frac{2\ell+1}{4\pi} P_\ell(\hat{\Omega}\cdot\hat{\Omega}'), \tag{3.15}$$

where P_ℓ is a Legendre polynomial (they are linked with associated Legendre polynomials $P_\ell = P_{\ell 0}$) and $\hat{\Omega}.\hat{\Omega}'$ is a scalar product.

It can be shown that the complex conjugation of spherical harmonics is $Y^*_{\ell m} = (-1)^m Y_{\ell -m}$. As maps are real quantities, using (3.12) the same relation applies to the $a_{\ell m}$ coefficients

$$a^*_{\ell m} = (-1)^m a_{\ell -m}. \tag{3.16}$$

This means in particular that even if there are N different complex $a_{\ell m}$ (with N the number of m and ℓ summed over), the number of independent real variables is only N. It is then straightforward to use the general equations for PDF with real random variables.

Another expression will play an important role in part II, it is the Gaunt integral

$$\mathcal{G}^{m_1 m_2 m_3}_{\ell_1\ell_2\ell_3} = \int_{S^2} \mathrm{d}\hat{\Omega}\, Y_{\ell_1 m_1}(\hat{\Omega})\, Y_{\ell_2 m_2}(\hat{\Omega})\, Y_{\ell_3 m_3}(\hat{\Omega}) = h_{\ell_1\ell_2\ell_3} \begin{pmatrix} \ell_1 & \ell_2 & \ell_3 \\ m_1 & m_2 & m_3 \end{pmatrix}, \tag{3.17}$$

with

$$h^2_{\ell_1\ell_2\ell_3} = \frac{(2\ell_1+1)(2\ell_2+1)(2\ell_3+1)}{4\pi} \begin{pmatrix} \ell_1 & \ell_2 & \ell_3 \\ 0 & 0 & 0 \end{pmatrix}^2, \tag{3.18}$$

where the terms inside parentheses are Wigner $3j$-symbols. Because of them, the Gaunt integral is non-zero only if the following conditions are respected

- $m_1 + m_2 + m_3 = 0$,
- Parity condition: $\ell_1 + \ell_2 + \ell_3$ is even, (3.19)
- Triangle inequality: $|\ell_1 - \ell_2| \leq \ell_3 \leq \ell_1 + \ell_2$.

Other useful properties of the Wigner $3j$-symbols are the identity relation

$$\sum_{m_1 m_2 m_3} \begin{pmatrix} \ell_1 & \ell_2 & \ell_3 \\ m_1 & m_2 & m_3 \end{pmatrix}^2 = 1. \tag{3.20}$$

and

$$\sum_m (-1)^{\ell - m} \begin{pmatrix} \ell & \ell & L \\ m & -m & 0 \end{pmatrix} = \sqrt{2\ell+1}\,\delta_{\ell,0}. \tag{3.21}$$

A main result of CMB observations is that fluctuations follow a Gaussian distribution (multivariate case of (3.4)) at first order. Hence, the probability density function of the harmonic coefficients is

$$P(a) = \frac{e^{-\frac{1}{2}\sum_{\ell m,\ell' m'} a^*_{\ell m} C^{-1}_{\ell m,\ell' m'} a_{\ell' m'}}}{\sqrt{(2\pi)^N \det C}}, \tag{3.22}$$

where $C_{\ell m,\ell' m'} = \langle a_{\ell m} a^*_{\ell' m'} \rangle$ is the covariance matrix. If we add the hypothesis of statistical isotropy, which is valid for the CMB itself, the covariance matrix becomes diagonal and the PDF simplifies to

$$P(a) = \prod_{\ell,m} \frac{1}{\sqrt{2\pi C_\ell}} e^{-\frac{1}{2}\frac{|a_{\ell m}|^2}{C_\ell}}, \tag{3.23}$$

where C_ℓ is the angular power spectrum is given by

$$C_\ell = \langle a_{\ell m} a^*_{\ell m} \rangle, \qquad C_{\ell m,\ell' m'} = C_\ell \, \delta_{\ell \ell'} \delta_{m m'}. \tag{3.24}$$

Measuring CMB temperature anisotropies can then be used to determine unknown parameters in this PDF. One can show that the optimal estimator for the power spectrum is

$$\hat{C}_\ell = \frac{1}{2\ell + 1} \sum_{m=-\ell}^{\ell} a_{\ell m} a^*_{\ell m}. \tag{3.25}$$

It is obviously unbiased, $\langle \hat{C}_\ell \rangle = C_\ell$ (sum of $2\ell + 1$ independent variables) and one can show that it saturates the Cramér-Rao bound (3.9) because the inverse of the Fisher information is indeed equal to the variance[1]

$$\mathrm{Var}(\hat{C}_\ell) = \frac{2}{2\ell + 1} C_\ell^2. \tag{3.26}$$

This is called the cosmic variance as it is a fundamental uncertainty which limits strongly the precision to which the power spectrum can be measured. It is due to the fact that we only have one realization of the sky and its effect is stronger for low ℓ as there are fewer m.

Just describing the Gaussian nature of CMB anisotropies is not sufficient, it is also important to understand from where comes this feature of primordial fluctuations. In the following section, we discuss the standard scenario of single-field inflation which gives an explanation for their origin.

3.3 Primordial fluctuations from standard single-field inflation

The theory of inflation does not only solve the different cosmological puzzles described in section 2.2.5, it also gives an explanation for the origin of the small fluctuations present in the CMB. These are in fact quantum fluctuations of the scalar field(s) stretched to macroscopic scales by the enormous amount of expansion. It is important to verify how they evolve during inflation and after, until recombination.

A key quantity to discuss the evolution of perturbations is the Hubble scale H^{-1}, describing the size of the observable universe in later periods, but roughly constant during inflation.

[1] Following (3.10), the Fisher information is $F(C_\ell) = \frac{2\ell+1}{2C_\ell^2}$. For the computation of the variance, a simple proof is to use the fact that $\frac{2\ell+1}{C_\ell}\hat{C}_\ell = \sum_{m=-\ell}^{\ell} \left| \frac{a_{\ell m}}{\sqrt{C_\ell}} \right|^2$ has a χ^2 distribution with $2\ell+1$ degrees of freedom (it is the sum of the squares of $2\ell+1$ Gaussian independent variables with a unit variance). The variance of this distribution is a well-known result and is $2(2\ell+1)$. Therefore, the variance of $\hat{C}_\ell$ is $\mathrm{Var}(\hat{C}_\ell) = 2(2\ell+1)(\frac{C_\ell}{2\ell+1})^2 = \frac{2}{2\ell+1} C_\ell^2$ and indeed $\mathrm{Var}(\hat{C}_\ell) = F(C_\ell)^{-1}$.

Perturbations are generated on very small scales, with a wavelength $\frac{a}{k}$ where k is the comoving scale of the perturbation, initially a lot smaller than the Hubble length. The scale factor a grows almost exponentially during inflation, which means that after some time, the wavelength becomes larger than the Hubble scale when $k = aH$, this is called horizon-crossing. Then, on super-Hubble scales (also called super-horizon), perturbations become frozen (under some conditions fulfilled in standard single-field inflation), i.e. they stop to evolve. At later times, during the radiation and matter dominated eras, it is the opposite situation and progressively these frozen modes re-enter the horizon. This is why we can observe today these primordial fluctuations almost directly in the CMB.

In this section, we will detail the generation of perturbations during a period of standard single-field inflation, linking them with observable parameters. There is a large amount of work on the topic in the literature, for earlier works see [180, 100, 97, 27] for example. More precise computations can also be found in [182, 143, 171].

Observing only very small temperature and polarization fluctuations is the CMB is a very good indication that the perturbations generated during inflation were small. Hence, the method to study them is perturbation theory.

Fluctuations of the inflaton also have an influence on the metric, that is why one important step is to find the perturbed version of the metric (3.27). In the literature, many different formulations can be found. Here, we recall the basics of perturbation theory and give only the terms we are interested in. The metric being a symmetric 4×4 matrix, it has ten degrees of freedom, corresponding to four scalar functions (4 degrees), two divergenceless vectors (4 degrees) and a symmetric transverse traceless tensor (2 degrees). However, four are in fact gauge degrees of freedom which are unphysical because they are related to the choice of coordinates. An important property of this perturbed metric, is that scalar, vector and tensor modes can be treated separately at linear order. The two degrees of freedom of the tensor perturbations correspond to the two polarizations of the graviton and thus are present even in an empty universe, we will discuss them briefly at the end of the section. However, vector and scalar modes need a source to become physical. In the models of inflation we are interested in there is no source for the vector modes, thus they will not be further discussed in this thesis (and even if they were present they would be diluted away by the enormous expansion). That leaves us with the scalar perturbations as the main focus of the section and they are the main contribution to the CMB fluctuations.

Keeping only the scalar part of the metric (and the homogeneous background), it is sufficient to consider the following metric

$$\mathrm{d}s^2 = -N^2(t, \boldsymbol{x})\mathrm{d}t^2 + a^2 e^{2\alpha(t,\boldsymbol{x})}\mathrm{d}\boldsymbol{x}^2. \tag{3.27}$$

where we made the gauge choice $g_{0i} = 0$ (there is only one gauge degree of freedom remaining) and α is the scalar curvature perturbation.

Scalar perturbations during inflation are sourced by the small quantum fluctuations of the scalar field. In this section, we want to study the power spectrum of these perturbations. This only requires perturbation theory at first-order, so we write the scalar field as

$$\phi(t, \boldsymbol{x}) = \phi(t) + \delta\phi(t, \boldsymbol{x}), \tag{3.28}$$

where $\phi(t)$ is the homogeneous background quantity studied in section 2.3.

The remaining scalar degree of freedom indicates that there is only one scalar quantity to compute. It is customary to use a gauge-invariant variable [25, 151] like

$$\zeta \equiv \alpha - HN\frac{\delta\rho}{\rho} = \alpha - HN\frac{\delta\phi}{\dot{\phi}} \tag{3.29}$$

which is the first-order adiabatic curvature perturbation. It is a combination of the scalar curvature perturbation and the variation of energy density (this last part can also be written as the variation of the scalar field).

The main set-up being fixed, the remaining part is to find the evolution equation of ζ. This is achieved by perturbing the field equation (2.33) and the Einstein equations (2.11) at first order. After combining them, one finds

$$\ddot{\zeta} + HN\left(3 + 2\epsilon + 2\eta - \frac{\dot{N}}{HN^2}\right) - \frac{N^2}{a^2}\partial^2\zeta = 0, \tag{3.30}$$

where $\partial^2 \equiv \partial^i\partial_i$. In the rest of the section, we choose to work with the conformal time τ, so the lapse function is $N = a$. We use the notation prime for a time derivative with respect to τ.

This equation is easier to study in Fourier space, which is why we will use the Fourier components ζ_k defined by

$$\zeta(\tau, \boldsymbol{x}) = \int \frac{\mathrm{d}^3\boldsymbol{k}}{(2\pi)^{3/2}}\zeta_k(\tau)e^{i\boldsymbol{k}.\boldsymbol{x}}. \tag{3.31}$$

Finally it is possible to rewrite the perturbation equation without its first-order derivative term using the Mukhanov-Sasaki variable originally introduced in [169, 150]

$$q_k = z\zeta_k \qquad \text{with} \qquad z = -\frac{a\sqrt{2\epsilon}}{\kappa}. \tag{3.32}$$

A direct computation gives

$$\frac{z'}{z} = aH\left(1 + \epsilon + \eta\right), \qquad \frac{z''}{z} = (aH)^2\left(2 + 2\epsilon + 3\eta + 2\epsilon^2 + 4\epsilon\eta + \xi\right). \tag{3.33}$$

Then substituting ζ_k by q in (3.30), one obtains the well-known Mukhanov-Sasaki equation

$$q_k'' + \left(k^2 - \frac{z''}{z}\right)q_k = 0. \tag{3.34}$$

That is the usual equation for an harmonic oscillator, with a mass depending on time. Solving analytically this equation is not possible in the general case, but under some approximations it is possible to obtain the well-known properties of standard inflationary perturbations.

For this, it is helpful to separate the different regimes of interest when studying this equation:

- Sub-horizon regime: $aH \ll k$
- Super-horizon regime: $aH \gg k$
- Transition: $aH \sim k$

Neglecting the slow-roll parameters, it is possible to solve (3.34) in de Sitter space where z is proportional to the scale factor a and the expansion is exponential so $a = -(H\tau)^{-1}$ (with H constant). The equation becomes

$$q_k'' + (k^2 - \frac{2}{\tau^2})q_k = 0, \tag{3.35}$$

which can be solved exactly

$$q_k = c_-\frac{e^{-ik\tau}}{\sqrt{2k}}\left(1 - \frac{i}{k\tau}\right) + c_+\frac{e^{ik\tau}}{\sqrt{2k}}\left(1 + \frac{i}{k\tau}\right). \tag{3.36}$$

Well inside the horizon, where (3.34) takes the simple form $q_k'' + k^2 q_k = 0$, the perturbations should behave like free field fluctuations in Minkowski space-time (with the Bunch Davies vacuum as initial condition)

$$\lim_{\tau\to-\infty} = \frac{1}{\sqrt{2k}} e^{-ik\tau}, \tag{3.37}$$

which imposes $c_+ = 0$ and $c_- = 1$.

Well outside the horizon, we obtain

$$\lim_{k\tau\to-\infty} q_k = \frac{-i}{\sqrt{2k^3\tau}} = \frac{iaH}{\sqrt{2k^3}} \propto \tau^{-1}. \tag{3.38}$$

Hence, the curvature perturbation $\zeta_k \propto \tau q_k$ is constant on super-Hubble scales and one usually says it is frozen outside the horizon.

As we have a simple solution for q_k on super-horizon scales, it is also possible to compute its two-point correlation function and the power spectrum. However, there is one subtlety, because we have to take into account the quantum nature of the perturbations here. This is done with the standard quantization procedure for an harmonic oscillator

$$\hat{q}_{\boldsymbol{k}}(\tau) = q_k(\tau)\hat{a}_{\boldsymbol{k}} + q_k^*(\tau)\hat{a}_{\boldsymbol{k}}^\dagger \tag{3.39}$$

where $\hat{a}_{\boldsymbol{k}}$ and $\hat{a}_{\boldsymbol{k}}^\dagger$ are the creation and annihilation operators satisfying the usual commutation relations

$$[\hat{a}_{\boldsymbol{k}}, \hat{a}_{\boldsymbol{k'}}] = 0, \qquad [\hat{a}_{\boldsymbol{k}}^\dagger, \hat{a}_{\boldsymbol{k'}}^\dagger] = 0 \qquad \text{and} \qquad [\hat{a}_{\boldsymbol{k}}, \hat{a}_{\boldsymbol{k'}}^\dagger] = \delta^{(3)}(\boldsymbol{k} - \boldsymbol{k'}). \tag{3.40}$$

Note that in the super-horizon limit, the quantum operators $\hat{q}_{\boldsymbol{k}}$ becomes proportional to $\left(\hat{a}_{\boldsymbol{k}} + \hat{a}_{\boldsymbol{k}}^\dagger\right)$ so they commute. Hence the quantum field $\hat{q} = \int \frac{\mathrm{d}^3\boldsymbol{k}}{(2\pi)^{3/2}} \hat{q}_k e^{i\boldsymbol{k}.\boldsymbol{x}}$ corresponds to a stochastic field with Gaussian statistics (for more details, see [159]). To describe a Gaussian field, the two-point correlation function is sufficient. One can compute it using the commutation relations (3.40) and show it is given by

$$\langle \hat{q}_{\boldsymbol{k}} \hat{q}_{\boldsymbol{k}}^* \rangle = q_{\boldsymbol{k}} q_{\boldsymbol{k}}^* \delta^{(3)}(\boldsymbol{k} - \boldsymbol{k'}) \equiv \frac{2\pi^2}{k^3} \mathcal{P}_q(k) \delta^{(3)}(\boldsymbol{k} - \boldsymbol{k'}). \tag{3.41}$$

Hence the power spectra of q and ζ are

$$\mathcal{P}_q = \frac{(aH)^2}{4\pi^2} \propto z^2 \qquad \text{and} \qquad \mathcal{P}_\zeta = \frac{1}{z^2}\mathcal{P}_q, \tag{3.42}$$

which are scale-invariant quantities.

In slow-roll inflation, there is a small change from de Sitter space, characterized by ϵ. This plays an important role in the transition regime in particular, when perturbations take their frozen super-horizon value. This means it is important to study carefully the transition regime, which can be done analytically in the slow-roll approximation. Indeed a is growing almost exponentially fast while H is roughly a constant and that means that the transition lasts a very small amount of time. One can then assume that slow-roll parameters like ϵ and η are constant during the transition and we denote their values evaluated at horizon-crossing by the subscript $*$. The main effect on the perturbations is a deviation from scale invariance, which at leading order is described by the spectral index

$$n_\zeta - 1 = \frac{\mathrm{d}\ln\mathcal{P}_\zeta}{\mathrm{d}\ln k}, \tag{3.43}$$

which is equivalent to write

$$\mathcal{P}_s = A_s \left(\frac{k}{k_*}\right)^{n_s - 1}. \tag{3.44}$$

Here we replaced the subscript ζ by the subscript s (for scalar perturbations) and A_s is the amplitude of scalar perturbations, which means it is the scale-invariant power spectrum we computed above (evaluated at horizon-crossing)

$$A_s = \frac{\kappa^2 H_*^2}{8\pi^2 \epsilon_*}. \tag{3.45}$$

The first step is then to write (3.34) at first-order in a slow-roll function expansion. It is easy to integrate $\epsilon = -H'/(aH^2)$ substituting ϵ by the small and constant ϵ_* determined at horizon-crossing to get

$$aH = -\frac{1+\epsilon_*}{\tau}. \tag{3.46}$$

Then, one can rewrite (3.33).

$$\frac{z'}{z} = -\frac{(1+2\epsilon_* + \eta_*)}{\tau} = -\frac{\nu - \frac{1}{2}}{\tau} \qquad \text{and} \qquad \frac{z''}{z} = \frac{2+3(2\epsilon_* + \eta_*)}{\tau^2} = \frac{\nu^2 - \frac{1}{4}}{\tau^2}, \tag{3.47}$$

with

$$\nu \equiv \frac{3}{2} + 2\epsilon_* + \eta_*. \tag{3.48}$$

Integrating the first equation gives that $z \propto \tau^{\frac{1}{2}-\nu}$. Using the second one in (3.34), one obtains

$$q_k'' + \left(k^2 - \frac{\nu^2 - \frac{1}{4}}{\tau^2}\right) q_k = 0, \tag{3.49}$$

This can be solved analytically and using the Bunch-Davies (3.37) vacuum initial condition, one can show that the solution is

$$q_k = \sqrt{\frac{\pi}{2}} \sqrt{-\tau} H_\nu^{(1)}(-k\tau), \tag{3.50}$$

where $H_\nu^{(1)}$ is a Hankel function of the first type, which has the super-horizon limit

$$\lim_{k\tau \to 0} H_\nu^{(1)}(-k\tau) = \frac{i}{\pi}\Gamma(\nu)\left(\frac{-k\tau}{2}\right)^{-\nu}. \tag{3.51}$$

Following the same method as in the de Sitter case, it is then easy to determine the k and τ dependence of the power spectra

$$\mathcal{P}_q \propto (-\tau)^{2-\nu} k^{3-2\nu} \quad \text{so} \quad \mathcal{P}_s = \frac{1}{z^2}\mathcal{P}_q \propto k^{3-2\nu} \tag{3.52}$$

and to compute the spectral index of scalar perturbations

$$n_s - 1 = 3 - 2\nu = -4\epsilon_* - 2\eta_*. \tag{3.53}$$

In the slow-roll approximation where ϵ_* and η_* are small compared to 1, it is clear that the difference from scale-invariance is small. The current Planck measurement is $n_s = 0.968 \pm 0.006$ [15] which confirms that this difference is small. The possibility to use this observable to constrain some types of inflation models will be discussed in detail in the last part of the thesis III.

The tensor perturbations, representing gravity waves, can be studied using the same method. First, the tensor term in the perturbed metric which should be added to (3.27) has the form $a^2 h_{ij} \mathrm{d}x^i \mathrm{d}x^j$, where h_{ij} is traceless and divergence-free (it has two degrees of freedom). Moreover, the tensor perturbations and the scalar field(s) are not coupled, meaning that the results

recalled here in the context of single-field inflation will hold in the case of multiple-field inflation which is the focus of part III. One interesting property of h_{ij} is that it is already a gauge-invariant quantity, which simplifies the situation compared to the scalar perturbations. Then, expanding in plane waves, one can find that the polarization mode Γ_k obeys

$$\Gamma_k'' + \left(k^2 - \frac{a''}{a}\right) = 0 \tag{3.54}$$

which is in fact (3.34) in de Sitter space (see [189] for example for the details). The power spectrum of the tensor perturbations has then a similar form

$$\mathcal{P}_t = \frac{2\kappa^2 H_*^2}{\pi^2}. \tag{3.55}$$

It depends only on H_*, meaning that a measurement of $\mathcal{P}_t$ would give us the energy scale of inflation. That could be done by detecting the B-polarization of the CMB, as it depends only on the tensor primordial fluctuations (and later-time effects). Moreover, it does not depend on ϵ_* like $\mathcal{P}_s$, indicating that its amplitude is a lot smaller because of slow-roll at the time of horizon-crossing. This is usually expressed into an observable called the tensor-to-scalar ratio r, simply defined by

$$r \equiv \frac{\mathcal{P}_t}{\mathcal{P}_s} = 16\epsilon_*. \tag{3.56}$$

The current observational bound is $r < 0.07$ at 95% CL assuming a pivot scale $k_* = 0.05$ Mpc^{-1} [12] and is already very constraining for some single-field inflation models (which are not the topic of this thesis).

The spectral index of the tensor perturbations has not exactly the same definition as the scalar perturbations. Instead of being the shift from 1 in the case of scale-independence, it is now very close to 0

$$n_t \equiv \frac{\mathrm{d}\ln \mathcal{P}_t}{\mathrm{d}\ln k} = -2\epsilon_*, \tag{3.57}$$

which gives the well-known consistency relation

$$r = -8n_t. \tag{3.58}$$

Verifying observationally this relation is an important objective because it would eliminate many types of more complicated inflation models (like multiple-field inflation, where the prediction for the power spectrum is not the same as we will see).

3.4 After inflation

We have seen how adiabatic perturbations are generated during standard slow-roll single-field inflation. Before that we have discussed how to describe the CMB temperatures anisotropies. In this section we will briefly discuss about the missing step which is how to relate the primordial fluctuations to observable CMB anisotropies.

One of the most important conclusions of the previous section was that the gauge-invariant quantity ζ describing the adiabatic mode of the scalar perturbations is frozen on super-horizon scales during inflation. This is also true at later times if there is no isocurvature mode on these scales, at least until they re-enter the horizon during the radiation and matter dominated eras.

Then relating the temperature fluctuations ΔT to ζ is not straightforward because many effects have to be taken into account. The evolution of density perturbations during the radiation and matter dominated eras (on sub-horizon scales) requires to study the interactions between

the different components of the content of the universe (photons, baryons, dark matter, etc.). This is usually done using the perturbed version of the Boltzmann equation in an expanding space-time. This can be described by introducing the radiation transfer functions Δ_ℓ defined by

$$\Delta_\ell(k) = \int_0^{\tau_0} \mathrm{d}\tau\, S(k,\tau) p_\ell(k[\tau_0 - \tau]). \tag{3.59}$$

In this expression, the function p_ℓ describes the geometric projection from Fourier space (k) to the multipole space (ℓ) while S is the source term corresponding to the different physical effects affecting the perturbations. Some early computations of these functions can be found in [39, 26]. The radiation transfer functions can also be computed numerically with freely available codes like CAMB[2] [127, 102] originally based on CMBFAST [172, 205] or CLASS[3] [124, 38]. Then the harmonic coefficients are given by

$$a_{\ell m} = 4\pi(-i)^\ell \int_0^\infty \frac{\mathrm{d}^3 k}{(2\pi)^3}\, \Delta_\ell(k) \Phi_k Y^*_{\ell m}(\Omega_k), \tag{3.60}$$

where Φ is the gravitational potential, which is often used to describe the scalar perturbations. It takes its name from the fact it can be related to the potential of Newtonian gravity in the weak field approximation. It is linked to ζ by

$$\Phi = -\frac{3+3w}{5+3w}\zeta, \tag{3.61}$$

where we recall that $w = p/\rho$, therefore the proportionality factor changes at the transition from a radiation to a matter dominated universe. One can then show that the CMB temperature power spectrum is

$$C_\ell = \frac{2}{\pi}\int_0^\infty k^2 dk \left(\frac{2\pi^2}{k^3}\mathcal{P}_\Phi(k)\right) \Delta_\ell(k)^2, \tag{3.62}$$

where $\mathcal{P}_\Phi$ is the power spectrum of the gravitational potential.

One of the main contributions in the transfer functions comes from the Sachs-Wolfe effect [168] which dominates on large scales. The following equation is a simplified formulation of this effect

$$\frac{\Delta T}{T} = \frac{1}{3}\Phi - \boldsymbol{v}.\hat{\boldsymbol{\Omega}} + \mathrm{ISW}, \tag{3.63}$$

where there are three different terms to discuss. The term ISW is the integrated Sachs-Wolfe effect. It is related to the fact that the gravitational potential changes over time when not in matter domination. Therefore it has two contributions, the first one occurring at the matter-radiation transition (it only affects small scales). The second one is a late-time effect, when the cosmological constant (or dark energy) starts to dominate the energy density of the universe. Therefore, it operates only on the largest scales. The second term $\boldsymbol{v}.\hat{\boldsymbol{\Omega}}$ is simply the Doppler effect due to the velocity perturbations of the baryons of the last scattering surface. Finally the most important term (see [200] for a simple physical explanation) describes the influence of the gravitational potential on the temperature fluctuations at large scales. It combines the intrinsic temperature perturbations (denser regions are hotter) and the additional redshift of the photons emitted in gravitational wells.

Focusing on the largest scales which were super-horizon modes at the time of decoupling and considering only the first term of (3.63), we can directly link the primordial power spectrum

[2] http://camb.info/
[3] http://class-code.net/

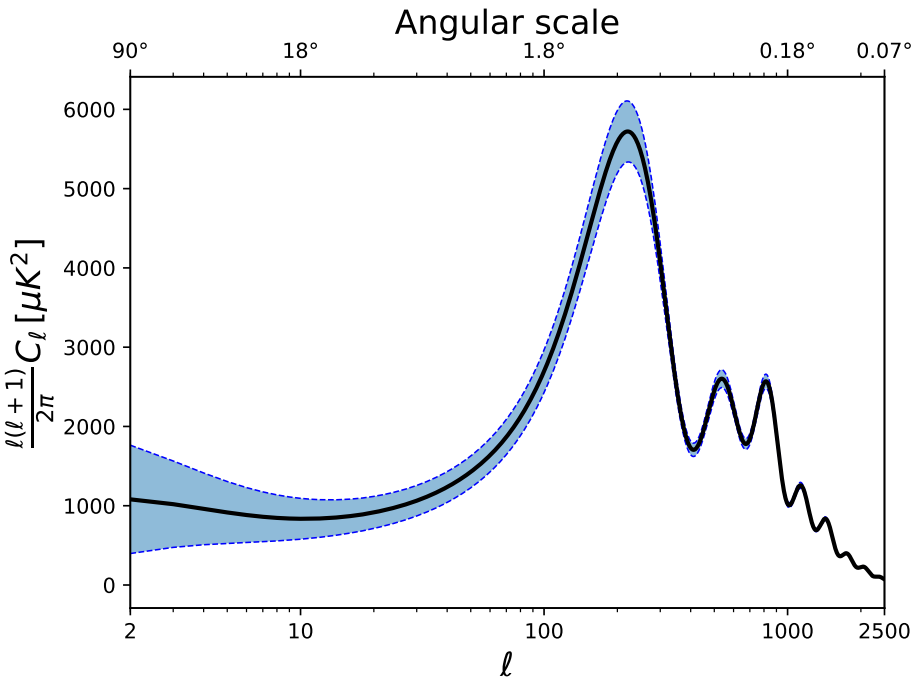

Figure 32: Planck CMB power spectrum with the best fit cosmological model [17] and its comic variance in units of μK^2 as function of the multipole ℓ and the angular scale $(180°/\ell)$.

with the CMB power spectrum. The geometric projection is a convolution with a spherical Bessel function j_ℓ and then using (3.63) one can show that the power spectrum takes the form

$$C_\ell \approx \frac{2}{9\pi}\int_0^\infty k^2 \mathrm{d}k \left(\frac{2\pi^2}{k^3}\mathcal{P}_\Phi(k)\right) j_\ell^2(k\tau_0). \tag{3.64}$$

During the matter-dominated era, we have $\mathcal{P}_\Phi = \frac{9}{25}\mathcal{P}_s$, hence we can substitute the gravitational potential power spectrum by the one we computed in the previous section (3.44) to write

$$C_\ell \approx \frac{4\pi}{25}A_s \int_0^\infty \frac{\mathrm{d}k}{k}\, j_\ell^2(k\tau_0)\left(\frac{k}{k_*}\right)^{n_s-1}. \tag{3.65}$$

Then choosing the pivot scale $k_* = 1/\tau_0$, the integral becomes the known result

$$\int_0^\infty \mathrm{d}x\, j_\ell^2(x)x^{n-2} = \frac{\pi}{2^{4-n}}\frac{\Gamma(3-n)\Gamma(\ell+\frac{n-1}{2})}{\Gamma^2(2-\frac{n}{2})\Gamma(\ell+\frac{5-n}{2})}, \tag{3.66}$$

expressed with Euler Γ functions. Then it is easy to derive the power spectrum of the CMB anisotropies in the scale-invariant case ($n_s = 1$) using $\Gamma(\ell)/\Gamma(\ell+2) = [\ell(\ell+1)]^{-1}$ and $\Gamma(2)/\Gamma^2(3/2) = 4/\pi$

$$C_\ell = \frac{2\pi}{\ell(\ell+1)}\frac{A_s}{25}. \tag{3.67}$$

It is related to the standard convention of plotting $\frac{\ell(\ell+1)}{2\pi}C_\ell$ (often called D_ℓ in the literature) instead of C_ℓ alone as in figure 32 which shows the Planck CMB power spectrum.

On this figure, we can see three different regions for which it is interesting to discuss the physical origin:

- At large scales ($\ell \lesssim 100$), the main contribution comes from the Sachs-Wolfe effect we just described. As expected from (3.67), the power spectrum (with its factor depending on ℓ) is nearly constant in the region, which is often called the Sachs-Wolfe plateau. Because these scales re-entered the horizon only after recombination and so were still super-horizon when the CMB was formed, it is the only part of the CMB power spectrum where we in fact observe directly the primordial power spectrum (except for the small changes due to the integrated Sachs-Wolfe effect). However, it is also the region where the cosmic variance is the strongest.

- At intermediate scales, we can observe several acoustic peaks (with the first around $\ell \approx 200$). These scales were already inside the horizon. At that time two effects had opposite influences on the baryon-photon plasma which led to oscillations of this fluid: matter was falling into gravity wells, while the photons, which were still coupled to the baryons, resisted (radiation pressure). The position of these peaks depends strongly on many cosmological parameters, so their measurement is one of the greatest tools for many aspects of modern cosmology. Hence it is also a long topic to discuss, which is beyond the scope of this thesis. The interested reader can find more information in [103, 104] for example.

- The smallest scales $\ell \gtrsim 1000$ constitute the region called Silk damping [175]. The decoupling of baryons and photons was not instantaneous and the mean free path of photons was not exactly zero before decoupling, so for the scales with a shorter wavelength than the mean free path of photons, anisotropies were erased (exponential decrease of the power spectrum).

In this chapter, we have used the theory of cosmological perturbations at first order to derive the standard predictions of slow-roll single-field inflation. We have also introduced the spherical harmonic decomposition of the CMB temperature anisotropies and we have recalled how these anisotropies are linked to the primordial fluctuations. The measurements of these anisotropies are now so precise thanks to Planck that it is important to go to the second order to better understand the primordial universe.

Part II

Non-Gaussianity in CMB observations

Chapter 4

Estimating non-Gaussianity

While the Gaussian nature of CMB anisotropies at first order is a well established observational result (with a simple theoretical explanation), it is necessary to go further by looking for so-called non-Gaussianity to better understand the physics at play in the primordial universe.

In the history of the universe, many different mechanisms can be sources of non-Gaussianity visible in the CMB. We can differentiate three main types:

- **Primordial non-Gaussianity**: they are predicted in several very early Universe theories which are alternatives to the standard single-field inflation of section 3.3 (many reviews exist [29, 52, 44]). Detecting them is our main objective when studying CMB non-Gaussianity as this could be used to constrain physics at a very high energy scale.
- **Intrinsic non-Gaussianity**: they arise from the non-linearities of the equations describing the evolution of perturbations after horizon reentry when going beyond the first order. However their effect is small at the Planck accuracy level, so we will not discuss them further in this thesis (see [158] and references therein for recent works).
- **Late-time non-Gaussianity**: Every structure present in our observable Universe has an influence on the CMB we observe today. The closer they are, the more important are non-linear effects. When the goal is to observe primordial non-Gaussianity, these effects are contamination we need to deal with. In particular, those of galactic origin are the main topic of chapter 5.

This chapter summarizes well-known results concerning the estimation of non-Gaussianity in the CMB anisotropies. In the first part, we recall the definition of the CMB bispectrum, the non-Gaussian quantity of interest here. Then, we discuss the predictions for different bispectral configurations, recalling the most common shapes (some of primordial origin, other being late-time effects). In the next part, we detail the procedure called the Edgeworth expansion, used to find the probability density function (PDF) describing weakly non-Gaussian statistics. From this PDF, we discuss the form of the best estimator for non-Gaussianity in the case of CMB observations in an ideal situation. Finally, we discuss the different issues arising in an actual experiment and how to adapt this estimator to the kind of data that is available using the method of the binned bispectrum estimator.

4.1 Angular and reduced bispectrum

The Gaussian distribution of the temperature fluctuations of the CMB is perfectly described by the angular power spectrum (3.24) (two-point correlation function of the spherical harmonic coefficients). The first step to investigate non-Gaussianity is therefore to go one order higher,

and to examine triangles in the sky. The equivalent function for the three-point correlation function is called the bispectrum. In this thesis, we study only non-Gaussianity of the bispectral type (which is in general the dominant contribution).

Quite similarly to the angular power spectrum defined in (3.24), the angular bispectrum [136] is given by

$$B_{\ell_1\ell_2\ell_3}^{m_1m_2m_3} = \langle a_{\ell_1m_1} a_{\ell_2m_2} a_{\ell_3m_3} \rangle. \tag{4.1}$$

This function contains all the information about the bispectral non-Gaussianity. However, it is also easy to understand that in practice, manipulating it is difficult, and not really useful in the context of our study. Indeed, an experience like Planck has a precision up to $\ell = 2500$, so $\mathcal{O}(10^9)$ triplets of ℓ and for each of these ℓ there are $2\ell + 1$ values of m, ending up with an array far too large to be computed.

It is then very useful to find a quantity which can replace the angular bispectrum $B_{\ell_1\ell_2\ell_3}^{m_1m_2m_3}$ in the role of describing the small deviations from Gaussianity of the CMB temperature anisotropies and there is a perfect candidate. It is the angle-averaged bispectrum which is rotationally invariant

$$B_{\ell_1\ell_2\ell_3} \equiv \left\langle \int_{S^2} \mathrm{d}\hat{\Omega}\, M_{\ell_1}(\hat{\Omega}) M_{\ell_2}(\hat{\Omega}) M_{\ell_3}(\hat{\Omega}) \right\rangle, \tag{4.2}$$

where $M_\ell = \Delta T_\ell / T_0$ is a map of the temperature fluctuations[1] as function of the position on the sky $\hat{\Omega}$, filtered at the multipole ℓ in the spherical harmonic decomposition

$$M_\ell(\hat{\Omega}) = \sum_{m=-\ell}^{\ell} a_{\ell m} Y_{\ell m}(\hat{\Omega}). \tag{4.4}$$

As we will see, this angle-averaged bispectrum is sufficient to study important properties of the non-Gaussianity (see section 4.2). However, information about the localization of non-Gaussianity in the sky is not kept. This is not an issue when considering primordial non-Gaussianity introduced in section 4.2 because of the isotropic nature of the CMB. Moreover, many late-time non-Gaussianity sources also have an isotropic effect. However, to study galactic non-Gaussianity (which is localized in the sky), a non-Gaussianity estimator in pixel space would be better because of the non-isotropic character of these foregrounds, but again we are only interested in the impact of these galactic shapes on the primordial ones.

It is straightforward to rewrite the angle-averaged bispectrum as:

$$B_{\ell_1\ell_2\ell_3} = \sum_{m_1m_2m_3} \langle a_{\ell_1m_1} a_{\ell_2m_2} a_{\ell_3m_3} \rangle \int_{S^2} \mathrm{d}\hat{\Omega}\, Y_{\ell_1m_1}(\hat{\Omega})\, Y_{\ell_2m_2}(\hat{\Omega})\, Y_{\ell_3m_3}(\hat{\Omega}), \tag{4.5}$$

where one can recognize the Gaunt integral introduced in section 3.2 for which the solution is given in (3.17). Then we immediately have a useful relation between the bispectrum and the reduced bispectrum which can be inverted

$$\begin{aligned} B_{\ell_1\ell_2\ell_3} &= h_{\ell_1\ell_2\ell_3} \sum_{m_1m_2m_3} \begin{pmatrix} \ell_1 & \ell_2 & \ell_3 \\ m_1 & m_2 & m_3 \end{pmatrix} B_{\ell_1\ell_2\ell_3}^{m_1m_2m_3}, \\ B_{\ell_1\ell_2\ell_3}^{m_1m_2m_3} &= \frac{1}{h_{\ell_1\ell_2\ell_3}} \begin{pmatrix} \ell_1 & \ell_2 & \ell_3 \\ m_1 & m_2 & m_3 \end{pmatrix} B_{\ell_1\ell_2\ell_3}, \end{aligned} \tag{4.6}$$

[1] Similarly, the observed angle-averaged bispectrum of a given map M^{obs} is

$$B_{\ell_1\ell_2\ell_3}^{\mathrm{obs}} \equiv \int_{S^2} \mathrm{d}\hat{\Omega}\, M_{\ell_1}^{\mathrm{obs}}(\hat{\Omega}) M_{\ell_2}^{\mathrm{obs}}(\hat{\Omega}) M_{\ell_3}^{\mathrm{obs}}(\hat{\Omega}). \tag{4.3}$$

where $h_{\ell_1\ell_2\ell_3}$ is defined in (3.18).

Because of the Wigner $3j$-symbols, $B_{\ell_1\ell_2\ell_3}$ vanishes if both the parity condition ($\ell_1+\ell_2+\ell_3$ even) and the triangle condition ($|\ell_1-\ell_2| \leq \ell_3 \leq \ell_1+\ell_2$) are not satisfied (as mentioned in section 3.2). The quantity $B_{\ell_1\ell_2\ell_3}/h^2_{\ell_1\ell_2\ell_3}$ is called the reduced bispectrum in the literature.

After defining the bispectrum, it is important to discuss in detail the different sources of non-Gaussianity and their known contribution to the CMB signal.

4.2 Theoretical shapes

In this section, we recall the analytical expressions for several common theoretical bispectra.

Very early universe theories like inflation give an explanation for the origin of the CMB temperature anisotropies. We have seen in section 3.4 the link between the gravitational potential power spectrum produced during inflation and the angular power spectrum we observe in the CMB. The same method can be used to express the contribution of the primordial bispectrum $B(k_1,k_2,k_3)$ of the gravitational potential Φ to the CMB power spectrum and bispectrum [115]:

$$B^{\text{th}}_{\ell_1\ell_2\ell_3} = h^2_{\ell_1\ell_2\ell_3}\left(\frac{2}{\pi}\right)^3 \int_0^\infty k_1^2 dk_1 \int_0^\infty k_2^2 dk_2 \int_0^\infty k_3^2 dk_3 \Big[\Delta_{\ell_1}(k_1)\Delta_{\ell_2}(k_2)\Delta_{\ell_3}(k_3)B(k_1,k_2,k_3) \times \int_0^\infty r^2 dr\, j_{\ell_1}(k_1 r) j_{\ell_2}(k_2 r) j_{\ell_3}(k_3 r)\Big], \tag{4.7}$$

where the j_ℓ are the spherical Bessel functions and the Δ_ℓ are the radiation transfer functions introduced in (3.59).

Several distinct shapes, or a combination of them, corresponding to the predictions of early universe models can be considered [24, 82]. The most common ones are:

- **Local shape**

$$B^{\text{local}}(k_1,k_2,k_3) = 2[P(k_1)P(k_2)+P(k_1)P(k_3)+P(k_2)P(k_3)]. \tag{4.8}$$

  It is related to the local relation $\Phi(\boldsymbol{x}) = \Phi_G(\boldsymbol{x}) + f^{\text{local}}_{\text{NL}}(\Phi_G(\boldsymbol{x})^2 - \langle\Phi\rangle^2)$ (where G indicates the Gaussian part of the gravitational potential). In Fourier space, the correlations are between modes of very different k (or ℓ in multipole space), in particular this bispectrum peaks in the limit of squeezed triangles, where one of the k is very small compared to the others.

  Local non-Gaussianity can arise from different mechanisms operating on super-horizon scales, like in multiple-field inflation where isocurvature and adiabatic perturbations interact on these scales.

- **Equilateral shape** [59]

$$\begin{aligned} B^{\text{equi}}(k_1,k_2,k_3) = &-6[P(k_1)P(k_2) + (2 \text{ perms})] - 12\,P^{2/3}(k_1)P^{2/3}(k_2)P^{2/3}(k_3) \\ &+ 6[P(k_1)P^{2/3}(k_2)P^{1/3}(k_3) + (5 \text{ perms})]. \end{aligned} \tag{4.9}$$

  As its name indicates, this bispectrum peaks in the limit of three equal momenta. Equilateral non-Gaussianity can be produced by adding higher derivative kinetic terms to the usual inflaton Lagrangian.

- **Orthogonal shape** [174]

$$B^{\rm ortho}(k_1,k_2,k_3) = -18[P(k_1)P(k_2) + (2\text{ perms})] - 48\,P^{2/3}(k_1)P^{2/3}(k_2)P^{2/3}(k_3) + 18[P(k_1)P^{2/3}(k_2)P^{1/3}(k_3) + (5\text{ perms})]. \tag{4.10}$$

  It is produced in the same conditions as the equilateral shape. The general bispectrum (approximated) produced in single-field inflation with non-canonical kinetic terms is a linear combination of these two shapes, which are by definition orthogonal (hence uncorrelated).[2]

Among the other primordial shapes that are often studied, we can cite bispectra with localized features or oscillations (see [14] for an overview of several examples). This kind of bispectrum is produced by inflationary models with a resonance or a step in the potential [53], for a review see [54] and for recent observational constraints [14, 187].

It is important to take into account that the CMB bispectrum is not entirely of primordial origin and one has to study the different contaminants. Some late time mechanisms producing non-Gaussianity can be described by analytical expressions as a function of ℓ.

The matter gravitational potential affects the CMB in several ways, and this becomes important at low redshift. There is lensing of the CMB due to the structures along the line of sight, which induces a small-scale shift of the CMB anisotropies. This small-scale effect is coupled to the integrated-Sachs-Wolfe effect ISW sourced by large-scale gravitational potential fluctuations. Like for the local shape, correlations between small and large scales induce a squeezed bispectral signal. In that case, it is strong enough to be detected. The following **lensing-ISW** template describes it entirely [90, 177, 126]

$$B^{\rm lensISW}_{\ell_1\ell_2\ell_3} = h^2_{\ell_1\ell_2\ell_3}\left[\frac{\ell_1(\ell_1+1)-\ell_2(\ell_2+1)+\ell_3(\ell_3+1)}{2}C^{TT}_{\ell_1}C^{T\phi}_{\ell_3} + (5\text{ perms})\right], \tag{4.11}$$

where C^{TT}_ℓ is the *lensed* temperature power spectrum, while $C^{T\phi}_\ell$ is the temperature-lensing potential cross power spectrum. There is no unknown amplitude to determine for this template, which is why it should be considered as a bias in the estimator, see (4.60).

In addition to these secondary anisotropies, different foregrounds also add their own contribution to the observed CMB bispectrum. Some of those of extra-galactic origin admit simple templates:

- Unclustered **point sources** (radio and late-type infrared galaxies) can be assumed to be Poisson distributed which implies a white noise spectrum [115] and hence a very simple theoretical shape

$$B^{\rm unclust}_{\ell_1\ell_2\ell_3} = h^2_{\ell_1\ell_2\ell_3}\, b_{\rm ps}. \tag{4.12}$$

  Here $b_{\rm ps}$ plays the role of the unknown parameter to determine (similar to $f_{\rm NL}$ for primordial shapes).

- **Cosmic Infrared Background** (constituted of dusty star-forming galaxies) admits the following template [118]

$$B^{\rm CIB}_{\ell_1\ell_2\ell_3} = h^2_{\ell_1\ell_2\ell_3}\, b_{\rm CIB}\left[\frac{(1+\ell_1/\ell_{\rm break})(1+\ell_2/\ell_{\rm break})(1+\ell_3/\ell_{\rm break})}{(1+\ell_0/\ell_{\rm break})^3}\right]^q, \tag{4.13}$$

  where $q = 0.85$, $\ell_{\rm break} = 70$ and $\ell_0 = 320$.

It is also possible to examine the correlations between some of these foregrounds. For example, the bispectrum describing the CIB-lensing correlations has been investigated in [60] where it has been shown to be small but inducing a bias to detect the orthogonal shape in Planck data.

[2] However, the local and orthogonal shapes are correlated at the Planck resolution (see Table 41).

4.3 Non-Gaussian statistics for the CMB

4.3.1 General PDF with weak non-Gaussianity

In this section, we are interested in finding the multivariate probability distribution function for a random N-dimensional field $\boldsymbol{\phi}$, with the only assumption that non-Gaussianity is small. For this, we follow the same method as in [186]. First, we recall the link between the PDF and its characteristic function (Fourier transform) which is expressed as a series of the cumulants of the PDF. In the general case, it is not possible to to solve these equations. However, with the approximation of weak non-Gaussianity, we can write the characteristic function as the Gaussian one with a small correction which can be computed. Then, after a few steps we obtain a nice expression for the PDF. This procedure is called the Edgeworth expansion and has been used first in the context of cosmological data in [109, 36].

Writing the previous steps in equation, we first have the general expression for the PDF $p(\boldsymbol{\phi})$ as the Fourier transform (where we use a capital K to avoid confusions with the k-indices used below) of the cumulant generating function G also known as the second characteristic function

$$p(\boldsymbol{\phi}) = \int \frac{\mathrm{d}^N \boldsymbol{K}}{(2\pi)^N} G(\boldsymbol{K}) e^{-i\boldsymbol{K}.\boldsymbol{\phi}}. \tag{4.14}$$

The cumulant generating function is defined by

$$\ln G(\boldsymbol{K}) = \sum_n \frac{i^n}{n!} \langle \phi_{j_1} ... \phi_{j_n} \rangle_{\mathrm{c}} \; K_{j_1} ... K_{j_n}, \tag{4.15}$$

where $\langle \phi_{j_1} ... \phi_{j_n} \rangle_{\mathrm{c}}$ is the cumulant of order n and with an implicit summation over the j_i indices, running from 1 to N. Note that the cumulants of order 2 and order 3 are equal to the more familiar correlation functions of the PDF introduced in section 3.1, but for higher order they are not the same. In particular, the Gaussian distribution is the only one where cumulants of order three and higher vanish. Hence, the term $n = 2$ of the series is the one associated with the Gaussian distribution, to study deviations we then need to study higher order terms. In the case of weak non-Gaussianity, a natural assumption is that it will be well described by the $n = 3$ term which is small. Expanding the corresponding exponential, the characteristic function at first order is

$$G(\boldsymbol{K}) = \left(1 - \frac{i}{6} B_{ijk} K_i K_j K_k\right) e^{-\frac{1}{2} K_i C_{ij} K_j} \tag{4.16}$$

with $C_{ij} = \langle \phi_i \phi_j \rangle$ and $B_{ijk} = \langle \phi_i \phi_j \phi_k \rangle$. Then we inject this expression into (4.14) and we use the following equality

$$(-i)^3 K_i K_j K_k \, e^{iK_m \phi_m} = \frac{\partial^3}{\partial \phi_i \partial \phi_j \partial \phi_k} e^{-iK_m \phi_m}, \tag{4.17}$$

to rewrite (4.14) as

$$p(\boldsymbol{\phi}) = \int \frac{\mathrm{d}^N \boldsymbol{K}}{(2\pi)^N} \, e^{-\frac{1}{2} K_i C_{ij} K_j} \left(1 - \frac{1}{6} B_{ijk} \frac{\partial^3}{\partial \phi_i \partial \phi_j \partial \phi_k}\right) e^{-iK_m \phi_m}. \tag{4.18}$$

It is then possible to compute this Gaussian integral

$$p(\boldsymbol{\phi}) = \frac{1}{\sqrt{(2\pi)^N \det C}} \left(1 - \frac{1}{6} B_{ijk} \frac{\partial^3}{\partial \phi_i \partial \phi_j \partial \phi_k}\right) e^{-\frac{1}{2} \phi_a C^{-1}_{ab} \phi_b}. \tag{4.19}$$

The remaining step is to perform the derivation in this expression. Going step by step and using the shorthand notation $g[\phi] = e^{-\frac{1}{2}\phi_a C^{-1}_{ab}\phi_b}$ we have

$$\begin{aligned}
\frac{\partial g(\boldsymbol{\phi})}{\partial \phi_k} &= -C^{-1}_{ka}\phi_a g(\boldsymbol{\phi}),\\
\frac{\partial^2 g(\boldsymbol{\phi})}{\partial \phi_j \phi_k} &= \left(-C^{-1}_{jk} + C^{-1}_{ja}C^{-1}_{kb}\phi_a\phi_b\right) g(\boldsymbol{\phi}),\\
\frac{\partial^3 g(\boldsymbol{\phi})}{\partial \phi_i \phi_j \phi_k} &= \left[\left(C^{-1}_{ij}C^{-1}_{ka} + C^{-1}_{ik}C^{-1}_{ja} + C^{-1}_{jk}C^{-1}_{ia}\right)\phi_a - C^{-1}_{ia}C^{-1}_{jb}C^{-1}_{kc}\phi_a\phi_b\phi_c\right] g(\boldsymbol{\phi}).
\end{aligned} \tag{4.20}$$

This gives the final result

$$p(\boldsymbol{\phi}) = \left[1 - \frac{B_{ijk}}{6}\left(\left(C^{-1}_{ij}C^{-1}_{ka} + C^{-1}_{ik}C^{-1}_{ja} + C^{-1}_{jk}C^{-1}_{ia}\right)\phi_a - C^{-1}_{ia}C^{-1}_{jb}C^{-1}_{kc}\phi_a\phi_b\phi_c\right)\right]\frac{e^{-\frac{1}{2}\phi_a C^{-1}_{ab}\phi_b}}{\sqrt{(2\pi)^N \det C}}, \tag{4.21}$$

which contains both linear and cubic terms in ϕ.

4.3.2 Applying this to the CMB

Using the CMB notations introduced in section 3.2, it is possible to apply the same method of Edgeworth expansion to find the PDF for the harmonic coefficients, which is

$$p(a) = \left(1 - \frac{1}{6}\sum_{\ell_i m_j}\langle a_{\ell_1 m_1} a_{\ell_2 m_2} a_{\ell_3 m_3}\rangle \frac{\partial^3}{\partial a_{\ell_1 m_1}\partial a_{\ell_2 m_2}\partial a_{\ell_3 m_3}}\right)\frac{e^{-\frac{1}{2}\sum\limits_{\ell m,\ell' m'} a^*_{\ell m} C^{-1}_{\ell m,\ell' m'} a_{\ell' m'}}}{\sqrt{(2\pi)^N \det C}}. \tag{4.22}$$

To compute the derivatives, it is possible to use (3.16), which also implies similar relations for the covariance matrix and its inverse

$$\begin{aligned}
C_{\ell -m,\ell' -m'} &= (-1)^{m+m'} C_{\ell' m',\ell m},\\
\left(C_{\ell m,\ell' m'}\right)^* &= C_{\ell' m',\ell m},\\
C^{-1}_{\ell -m,\ell' -m'} &= (-1)^{m+m'} C^{-1}_{\ell' m',\ell m},\\
\left(C^{-1}_{\ell -m,\ell' -m'}\right)^* &= C^{-1}_{\ell' m',\ell m}.
\end{aligned} \tag{4.23}$$

Then, one can obtain the derivative of the Gaussian

$$\frac{\partial}{\partial a_{\ell_1 m_1}}\left[e^{-\frac{1}{2}\sum\limits_{\ell m,\ell' m'} a^*_{\ell m} C^{-1}_{\ell m,\ell' m'} a_{\ell' m'}}\right] = -(-1)^{m_1} C^{-1}_{\ell_1 -m_1,\ell m} a_{\ell m}\, e^{-\frac{1}{2}\sum\limits_{\ell m,\ell' m'} a^*_{\ell m} C^{-1}_{\ell m,\ell' m'} a_{\ell' m'}}, \tag{4.24}$$

which substitued into (4.22) gives

$$\begin{aligned}
p(a) =& \frac{e^{-\frac{1}{2}\sum\limits_{\ell m,\ell' m'} a^*_{\ell m} C^{-1}_{\ell m,\ell' m'} a_{\ell' m'}}}{\sqrt{(2\pi)^N \det C}}\left\{1 + \frac{1}{6}\sum_{\ell_i m_j}\langle a_{\ell_1 m_1} a_{\ell_2 m_2} a_{\ell_3 m_3}\rangle\left[(-1)^{m_1+m_2+m_3} C^{-1}_{\ell_1 -m_1,l_4 m_4} a_{l_4 m_4}\right.\right.\\
&\times C^{-1}_{\ell_2 -m_2,l_5 m_5} a_{l_5 m_5} C^{-1}_{\ell_3 -m_3,l_6 m_6} a_{l_6 m_6} - (-1)^{m_1+m_3} C^{-1}_{\ell_1 -m_1,\ell_2 m_2} C^{-1}_{\ell_3 -m_3,l_4 m_4} a_{l_4 m_4}\\
&\left.\left. - (-1)^{m_2+m_3} C^{-1}_{\ell_3 -m_3,\ell_1 m_1} C^{-1}_{\ell_2 -m_2,l_4 m_4} a_{l_4 m_4} - (-1)^{m_1+m_2} C^{-1}_{\ell_2 -m_2,\ell_3 m_3} C^{-1}_{\ell_1 -m_1,l_4 m_4} a_{l_4 m_4}\right)\right]\right\}.
\end{aligned} \tag{4.25}$$

The main correction to the Gaussian distribution in the case of weak non-Gaussianity directly depends on the expectation value of the angular bispectrum $\langle B^{m_1 m_2 m_3}_{\ell_1 \ell_2 \ell_3}\rangle$ defined in (4.1). In an

actual experiment, one would want to compare observed data to predictions of his theoretical model. This transcribes by using the different theoretical bispectrum shapes, described in section 4.2 and normalized to the case $f_{\rm NL} = 1$, as the bispectrum expectation value

$$\langle a_{\ell_1 m_1} a_{\ell_2 m_2} a_{\ell_3 m_3} \rangle = f_{\rm NL} (B^{\rm th})^{m_1 m_2 m_3}_{\ell_1 \ell_2 \ell_3}. \tag{4.26}$$

Note that in section 4.2, the introduced theoretical shapes are angle-average bispectra (so no m) because as it will be clear later, they are those we use in this thesis. However, it is possible to compute the angular bispectral shapes using (4.6).

Inside the sum of (4.25), the expression above is in factor of the rest which can be decomposed into two terms. The first one is cubic in a_{lm} (so it has also the form of the bispectrum). The other one is linear in a_{lm} and plays the role of a correction to take into account the different anisotropies of the observed sky. This will be discussed more clearly in section 4.4.

Unfortunately, equation (4.25) is computationally challenging because of the presence of the inverse of the covariance matrix. Note that the covariance matrix is also a theoretical quantity, which does not depend on the bispectral shape of course, but is does depend on the cosmological parameters. Nevertheless, one can determine the optimal estimator for $f_{\rm NL}$ from this PDF.

In the case of weak non-Gaussianity, the best estimator for $f_{\rm NL}$ has been introduced in [59]. Using the PDF (4.25), it is possible to show that it saturates the Cramér-Rao bound. This standard result takes the form

$$\begin{aligned}\hat{f}_{\rm NL} = & \frac{1}{N} \sum_{\ell_i m_j} (B^{\rm th})^{m_1 m_2 m_3}_{\ell_1 \ell_2 \ell_3} \Big[(-1)^{m_1+m_2+m_3} C^{-1}_{\ell_1 -m_1, l_4 m_4} a_{l_4 m_4} C^{-1}_{\ell_2 -m_2, l_5 m_5} a_{l_5 m_5} C^{-1}_{\ell_3 -m_3, l_6 m_6} a_{l_6 m_6} \\ & - (-1)^{m_1+m_3} C^{-1}_{\ell_1 -m_1, \ell_2 m_2} C^{-1}_{\ell_3 -m_3, l_4 m_4} a_{l_4 m_4} - (-1)^{m_2+m_3} C^{-1}_{\ell_3 -m_3, \ell_1 m_1} C^{-1}_{\ell_2 -m_2, l_4 m_4} a_{l_4 m_4} \\ & - (-1)^{m_1+m_2} C^{-1}_{\ell_2 -m_2, \ell_3 m_3} C^{-1}_{\ell_1 -m_1, l_4 m_4} a_{l_4 m_4}) \Big],\end{aligned} \tag{4.27}$$

where N is the normalization factor:

$$N = \sum_{\ell_i m_j} (B^{\rm th})^{m_1 m_2 m_3}_{\ell_1 \ell_2 \ell_3} C^{-1}_{\ell_1 m_1, l_4 m_4} C^{-1}_{\ell_2 m_2, l_5 m_5} C^{-1}_{\ell_3 m_3, l_6 m_6} (B^{\rm th})^{m_4 m_5 m_6}_{l_4 l_5 l_6}. \tag{4.28}$$

Unfortunately, using this optimal estimator directly is computationally too heavy. One would have to inverse the covariance matrix (which can be achieved through Wiener filtering [74], but is challenging) and the number of ℓ and m is too large (ℓ is up to 2500 for Planck data). In the next section, we show how one can deal with these issues and we introduce the binned bispectrum estimator.

4.4 The binned bispectrum estimator

This section provides the steps to simplify the previous results to a usable tool to study bispectral non-Gaussianity and to evaluate the parameter $f_{\rm NL}$. We start by the isotropic case and then we generalize the result. Finally, we recall the method of the binned bispectrum estimator.

4.4.1 Isotropic case

While the general formulation of the best estimator of $f_{\rm NL}$ is extremely complicated to implement, it simplifies greatly in the case of an isotropic observed sky.

As written at the end of section 3.2, the covariance matrix is diagonal $C_{\ell m,\ell' m'} = C_l \delta_{\ell\ell'}\delta_{mm'}$ in that case and simplifications go even further because there is no m-dependence as we will check. One can substitute this into (4.27), with the angle-averaged bispectrum defined in the previous section to obtain a shorter expression for $\hat{f}_{\rm NL}$.

Going step by step, the normalization factor N after summing over the indices ℓ_i and m_i with $i = 4, 5, 6$ becomes

$$N = \sum_{\ell_1\ell_2\ell_3} \frac{(B^{\rm th}_{\ell_1\ell_2\ell_3})^2}{h^2_{\ell_1\ell_2\ell_3} C_{\ell_1} C_{\ell_2} C_{\ell_3}} \sum_{m_1 m_2 m_3} \begin{pmatrix} \ell_1 & \ell_2 & \ell_3 \\ m_1 & m_2 & m_3 \end{pmatrix}^2 = \sum_{\ell_1\ell_2\ell_3} \frac{(B^{\rm th}_{\ell_1\ell_2\ell_3})^2}{h^2_{\ell_1\ell_2\ell_3} C_{\ell_1} C_{\ell_2} C_{\ell_3}}, \tag{4.29}$$

where we used the Wigner $3j$-symbol identity (3.20). Similarly, the estimator is

$$\begin{aligned} \hat{f}_{\rm NL} =& \frac{1}{N} \sum_{\ell_i m_j} h^{-1}_{\ell_1\ell_2\ell_3} \begin{pmatrix} \ell_1 & \ell_2 & \ell_3 \\ m_1 & m_2 & m_3 \end{pmatrix} B^{\rm th}_{\ell_1\ell_2\ell_3} \times \\ & \Bigg[(-1)^{m_1+m_2+m_3} \frac{a_{\ell_1 -m_1} a_{\ell_2 -m_2} a_{\ell_3 -m_3}}{C_{\ell_1} C_{\ell_2} C_{\ell_3}} - (-1)^{m_1+m_3} \frac{\delta_{\ell_1\ell_2}\delta_{-m_1 m_2}}{C_{\ell_1} C_{\ell_3}} a_{\ell_3 -m_3} \\ & - (-1)^{m_2+m_3} \frac{\delta_{\ell_3\ell_1}\delta_{-m_3 m_1}}{C_{\ell_3} C_{\ell_2}} a_{\ell_2 -m_2} - (-1)^{m_1+m_2} \frac{\delta_{\ell_2\ell_3}\delta_{-m_2 m_3}}{C_{\ell_2} C_{\ell_1}} a_{\ell_1 -m_1} \Bigg]. \end{aligned} \tag{4.30}$$

In this expression, the cubic term in $a_{\ell m}$ corresponds to the observed angular bispectrum, using (3.16) to eliminate the factor $(-1)^{m_1+m_2+m_3}$ and the fact the bispectrum is a real quantity. Then, it can be substituted by the angle-averaged observed bispectrum. Concerning the linear terms, they are proportional to the monopole because of the different selection rules of the Gaunt integral (3.19). Combining the rule $m_1+m_2+m_3 = 0$ with the delta functions, each linear term is proportional to $\sum_m \begin{pmatrix} l & l & L \\ m & -m & 0 \end{pmatrix} a_{L0}$ where we can recognize an expression similar to (3.21). This implies the only remaining harmonic coefficient is a_{00} and the contribution of the linear terms is zero as we subtract the monopole from the maps.

Finally, performing the same steps as for the normalization factor N, the estimator takes the form

$$\hat{f}_{\rm NL} = \frac{1}{N} \sum_{\ell_1\ell_2\ell_3} \frac{B^{\rm th}_{\ell_1\ell_2\ell_3} B^{\rm obs}_{\ell_1\ell_2\ell_3}}{h^2_{\ell_1\ell_2\ell_3} C_{\ell_1} C_{\ell_2} C_{\ell_3}}, \tag{4.31}$$

which has been shown to be optimal for general theoretical bispectra [23] (in the isotropic case).

We also need to recall the standard computation [135] of the variance of the bispectrum which is important to evaluate the statistical error of our measurements

$$\mathrm{Var}(B^{\rm obs}_{\ell_1\ell_2\ell_3}) = \langle (B^{\rm obs}_{\ell_1\ell_2\ell_3})^2 \rangle - \langle B^{\rm obs}_{\ell_1\ell_2\ell_3} \rangle^2 \equiv V_{\ell_1\ell_2\ell_3}. \tag{4.32}$$

In the weak non-Gaussianity regime, the average value of the bispectrum is negligible. This leaves us with computing the mean value of the product of two bispectra

$$\langle B_{\ell_1\ell_2\ell_3}(\hat{\Omega}) B_{\ell_4\ell_5\ell_6}(\hat{\Omega}') \rangle = \int_{S^2\times S^2} \mathrm{d}\hat{\Omega}\, \mathrm{d}\hat{\Omega}'\, \langle M_{\ell_1}(\hat{\Omega}) M_{\ell_2}(\hat{\Omega}) M_{\ell_3}(\hat{\Omega}) M_{\ell_4}(\hat{\Omega}') M_{\ell_5}(\hat{\Omega}') M_{\ell_6}(\hat{\Omega}') \rangle. \tag{4.33}$$

One can use Wick's theorem for Gaussian fields to reduce the six-point correlation function to the sum of fifteen products of two-point correlation functions

- 6 terms: each ℓ is paired with an element of the other triplet like in $\langle M_{\ell_1}(\hat{\Omega}) M_{\ell_4}(\hat{\Omega}') \rangle \langle M_{\ell_2}(\hat{\Omega}) M_{\ell_5}(\hat{\Omega}') \rangle \langle M_{\ell_3}(\hat{\Omega}) M_{\ell_6}(\hat{\Omega}') \rangle$.

- 9 terms: the rest (example: $\langle M_{\ell_1}(\hat{\Omega})M_{\ell_2}(\hat{\Omega})\rangle\langle M_{\ell_3}(\hat{\Omega})M_{\ell_4}(\hat{\Omega}')\rangle\langle M_{\ell_5}(\hat{\Omega}')M_{\ell_6}(\hat{\Omega}')\rangle$)

We will explicitly compute the contribution of the 6 first terms below. But first, we show that in the isotropic case, the 9 last terms are zero. For this, we use the addition theorem (3.15) and the fact that the maps are real to compute the two-point correlation functions

$$\begin{aligned}\langle M_\ell(\hat{\Omega})M_{\ell'}(\hat{\Omega}')\rangle &= \sum_{m=-\ell}^{\ell}\sum_{m'=-\ell'}^{\ell'}\langle a_{\ell m}a^*_{\ell' m'}\rangle Y_{\ell m}(\hat{\Omega})Y^*_{\ell' m'}(\hat{\Omega}') \\ &= C_\ell\delta_{\ell\ell'}\frac{2\ell+1}{4\pi}P_\ell(\hat{\Omega}\cdot\hat{\Omega}').\end{aligned} \tag{4.34}$$

Then we can perform the integration on our example term (and the eight others follow the same computation)

$$\begin{aligned}&\int_{S^2\times S^2}\mathrm{d}\hat{\Omega}\,\mathrm{d}\hat{\Omega}'\,\langle M_{\ell_1}(\hat{\Omega})M_{\ell_2}(\hat{\Omega})\rangle\langle M_{\ell_3}(\hat{\Omega})M_{\ell_4}(\hat{\Omega}')\rangle\langle M_{\ell_5}(\hat{\Omega}')M_{\ell_6}(\hat{\Omega}')\rangle \\ &= \frac{(2\ell_1+1)(2\ell_3+1)(2\ell_5+1)}{(4\pi)^3}C_{\ell_1}C_{\ell_3}C_{\ell_5}\delta_{\ell_1\ell_2}\delta_{\ell_3\ell_4}\delta_{\ell_5\ell_6}\int_{S^2\times S^2}\mathrm{d}\hat{\Omega}\,\mathrm{d}\hat{\Omega}'\,P_{\ell_1}(1)P_{\ell_3}(\hat{\Omega}\cdot\hat{\Omega}')P_{\ell_5}(1)\end{aligned} \tag{4.35}$$

This integral can be solved using well-known properties of Legendre polynomials. First, we have $P_\ell(1)=1$ and then we can use the integral

$$\int_{S^2\times S^2}\mathrm{d}\hat{\Omega}\,\mathrm{d}\hat{\Omega}'\,P_\ell(\hat{\Omega}\cdot\hat{\Omega}')=0, \tag{4.36}$$

and we find the announced result.

Concerning the six first terms, we will also explicitely compute only the given example, but the correct permutations to obtain the five other terms will be in the final result. Substituting (4.4) into the integral and using the fact that the maps are real, one obtains

$$\begin{aligned}&\int_{S^2\times S^2}\mathrm{d}\hat{\Omega}\,\mathrm{d}\hat{\Omega}'\,\langle M_{\ell_1}(\hat{\Omega})M_{\ell_4}(\hat{\Omega}')\rangle\langle M_{\ell_2}(\hat{\Omega})M_{\ell_5}(\hat{\Omega}')\rangle\langle M_{\ell_3}(\hat{\Omega})M_{\ell_6}(\hat{\Omega}')\rangle \\ &\qquad= C_{\ell_1}C_{\ell_2}C_{\ell_3}\delta_{\ell_1\ell_4}\delta_{\ell_2\ell_5}\delta_{\ell_3\ell_6}\sum_{m_1,m_2,m_3}\left(\int_{S^2}\mathrm{d}\hat{\Omega}Y_{\ell_1 m_1}(\hat{\Omega})\,Y_{\ell_2 m_2}(\hat{\Omega})Y_{\ell_3 m_3}(\hat{\Omega})\right) \\ &\qquad\times\left(\int_{S^2}\mathrm{d}\hat{\Omega}'\,Y^*_{\ell_1 m_1}(\hat{\Omega}')Y^*_{\ell_2 m_2}(\hat{\Omega}')Y^*_{\ell_3 m_3}(\hat{\Omega}')\right).\end{aligned} \tag{4.37}$$

where one can recognize the Gaunt integral (3.17). Substituting it here and using the identity relation (3.20) and the fact that the columns of Wigner $3j$-symbols can be permuted when the parity condition is respected, one can find that the 6 terms give

$$\begin{aligned}\langle B_{\ell_1\ell_2\ell_3}B_{\ell_4\ell_5\ell_6}\rangle = h^2_{\ell_1\ell_2\ell_3}C_{\ell_1}C_{\ell_2}C_{\ell_3}\Big[&\delta_{\ell_1\ell_4}\delta_{\ell_2\ell_5}\delta_{\ell_3\ell_6}+\delta_{\ell_1\ell_4}\delta_{\ell_2\ell_6}\delta_{\ell_3\ell_5}+\delta_{\ell_1\ell_5}\delta_{\ell_2\ell_4}\delta_{\ell_3\ell_6} \\ &+\delta_{\ell_1\ell_5}\delta_{\ell_2\ell_6}\delta_{\ell_3\ell_4}+\delta_{\ell_1\ell_6}\delta_{\ell_2\ell_4}\delta_{\ell_3\ell_5}+\delta_{\ell_1\ell_6}\delta_{\ell_2\ell_5}\delta_{\ell_3\ell_4}\Big].\end{aligned} \tag{4.38}$$

Hence the variance is

$$V_{\ell_1\ell_2\ell_3}=g_{\ell_1\ell_2\ell_3}h^2_{\ell_1\ell_2\ell_3}C_{\ell_1}C_{\ell_2}C_{\ell_3} \tag{4.39}$$

We introduced here the combinatorial factor $g_{\ell_1\ell_2\ell_3}$ which takes the value 6, 2 or 1 depending on whether 3, 2 or no ℓ's are equal respectively.

This same factor also has another important use because in the temperature only case, the bispectrum $B_{\ell_1\ell_2\ell_3}$ is symmetric under the permutations of ℓ's (the situation would require more care with the polarization). Hence it is possible to decrease the number of operations by a factor around 6 by substituting the sum over all ℓ_1, ℓ_2 and ℓ_3 by

$$\frac{1}{6}\sum_{\ell_1\ell_2\ell_3} = \sum_{\ell_1\leq\ell_2\leq\ell_3} \frac{1}{g_{\ell_1\ell_2\ell_3}}. \tag{4.40}$$

Substituting this into (4.31), one can then notice that the denominator of each term is in fact the theoretical prediction for the variance of the bispectrum $V_{\ell_1\ell_2\ell_3}$. The optimal estimator is inverse variance weighted, which is very important in a real experiment where several effects have to be taken into account (we will discuss this in the following section).

A very convenient notation is the bispectral inner product defined by

$$\langle B^A, B^B\rangle = \sum_{\ell_1\leq\ell_2\leq\ell_3} \frac{B^A_{\ell_1\ell_2\ell_3} B^B_{\ell_1\ell_2\ell_3}}{V_{\ell_1\ell_2\ell_3}} \tag{4.41}$$

where B^A and B^B are both theoretical bispectral templates, or one theoretical and one observational bispectra.

Then, one can rewrite the estimator (4.31) in a nice form

$$\hat{f}_{\rm NL} = \frac{\langle B^{\rm th}, B^{\rm obs}\rangle}{\langle B^{\rm th}, B^{\rm th}\rangle}. \tag{4.42}$$

A previous demonstration for the form of this estimator using different arguments was proposed in [115]. The main idea of the demonstration is simple, so we recall it here. One has to assume that the different bispectrum configurations follow a Gaussian distribution. Then, finding the estimator requires only to minimize the following χ^2 with respect to $f_{\rm NL}$

$$\chi^2 = \sum_{\ell_1\leq\ell_2\leq\ell_3} \frac{\left(f_{\rm NL}B^{\rm th}_{\ell_1\ell_2\ell_3} - B^{\rm obs}_{\ell_1\ell_2\ell_3}\right)^2}{V_{\ell_1\ell_2\ell_3}}, \tag{4.43}$$

which straightforwardly gives the wanted form for $\hat{f}_{\rm NL}$.

4.4.2 General case

With actual data from a real experiment, several issues arise from different sources and the previous equations need to be rewritten to take them properly into account.

One of these sources is simply the instrument itself. We model its angular response by a beam window function, which is often well approximated by a Gaussian beam

$$b_\ell = \exp\left[-\frac{1}{2}\frac{\ell(\ell+1)\theta^2_{\rm FWHM}}{8\ln 2}\right], \tag{4.44}$$

which is entirely characterized by the full width at half maximum $\theta_{\rm FWHM}$ (in radians). Moreover, the instrument noise can be described by the noise power spectrum N_ℓ. This means that one has to substitute the CMB power spectrum C_ℓ by the one measured by a real experiment in the previous equations

$$C_\ell \longrightarrow b^2_\ell C_\ell + N_\ell. \tag{4.45}$$

When comparing the observed bispectrum to a theoretical template, we also need to take the beam into account

$$B^{\rm th}_{\ell_1\ell_2\ell_3} \longrightarrow b_{\ell_1} b_{\ell_2} b_{\ell_3} B^{\rm th}_{\ell_1\ell_2\ell_3}. \tag{4.46}$$

While the equations from the previous section assume rotational invariance, real data have two major sources of anisotropy: the mask and the anisotropic noise. Bright objects in the microwave domain, of galactic or extragalactic origins, prevent observations of the CMB over the whole sky. It is often necessary to mask the galactic plane and the strongest point sources in the sky. Besides the anisotropy induced by the mask, different effects have then to be taken into account. First, there is a multiplicative bias that needs to be included in the power spectrum and the bispectrum using the factor $f_{\rm sky}$ where $f_{\rm sky}$ is the unmasked fraction of the sky

$$C_\ell^{\rm masked} \simeq f_{\rm sky} C_\ell^{\rm unmasked}, \qquad B_{\ell_1\ell_2\ell_3}^{\rm masked} \simeq f_{\rm sky} B_{\ell_1\ell_2\ell_3}^{\rm unmasked}. \tag{4.47}$$

It is called the $f_{\rm sky}$ approximation [117] and it is valid for small enough masks. In addition to that, one has to be careful of different edge effects induced by the mask (see section 4 of [42] for a discussion of these issues). One effect that is easy to see is the fact that the mask acts as a step function in real space, so it has an influence over a large range of multipoles in harmonic space. Here, we will use the standard technique of inpainting: the masked region is filled in before being filtered in multipole space. For a complete description of the inpainting approach and a comparison to other possibilities, see [95]. The simplest method to fill in the masked regions of the map is diffusive filling in and it was used for the Planck non-Gaussianity results [11, 14]. After filling in the masked part by the average value of the map, diffusive filling in simply consists in giving to each masked pixel the average value of its neighbouring pixels and iterating this procedure (2000 times in the case of Planck).

Another source of anisotropy comes from the scanning pattern of the satellite which makes the noise anisotropic, because some parts of the sky are observed more often than others. This makes the estimator (4.30) unsuited to describe the non-Gaussianity of the CMB temperature fluctuations and leads to large error bars. This is easy to see if you go back to the computation of the bispectrum variance of the previous section. We had nine terms which cancel because of the integral (4.36) performed over the whole celestial sphere, but now we have to integrate only over the unmasked part of the sky. Hence, these nine terms give an important contribution to the variance and so to the error bars too.

We cannot use the general optimal formulation of the estimator (4.27) determined using an Edgeworth expansion. However, it contains the main ingredient for a simple solution which is to add a linear correction to the observed bispectrum

$$B_{\ell_1\ell_2\ell_3}^{\rm obs} \equiv \int_{S^2\setminus\mathcal{M}} {\rm d}\hat{\Omega}\, \left[M_{\ell_1}M_{\ell_2}M_{\ell_3} - M_{\ell_1}\langle M_{\ell_2}M_{\ell_3}\rangle - M_{\ell_2}\langle M_{\ell_1}M_{\ell_3}\rangle - M_{\ell_3}\langle M_{\ell_1}M_{\ell_2}\rangle\right], \tag{4.48}$$

where the integration is performed on the celestial sphere with the masked part denoted by $\mathcal{M}$ excluded. This is in fact the third order Wick product of the maps, and it is a known result that for a Gaussian variable, it is the cubic statistic with the smallest variance [65]. This solution was introduced in [59] where it was assumed that the covariance matrix $C_{\ell m,\ell' m'}$ is still diagonal in the estimator (and it has been verified that this approximation works well for the CMB) to find the usual cubic term (4.31). Then, the idea was to determine from this cubic term which linear correction would minimize the variance. Hence, to verify that the bispectrum (4.48) has the right form, we will derive its variance similarly to the previous section, the main difference being that integrations are performed over $S^2\setminus\mathcal{M}$ instead of S^2. Again, in the weak non-Gaussianity regime, we only have to compute the average of the product of two bispectra $\langle B_{\ell_1\ell_2\ell_3}^{\rm obs}(\hat{\Omega}) B_{\ell_4\ell_5\ell_6}^{\rm obs}(\hat{\Omega}')\rangle$ and there are three types of terms

- 1 term: product of the two cubic terms: $\langle M_{\ell_1}M_{\ell_2}M_{\ell_3}M_{\ell_4}M_{\ell_5}M_{\ell_6}\rangle$ (this is the only term present in the isotropic case).
- 6 terms: product of a linear term with a cubic term, e.g. $\langle -M_{\ell_1}M_{\ell_2}M_{\ell_3}M_{\ell_4}\rangle\langle M_{\ell_5}M_{\ell_6}\rangle$.

- 9 terms: product of two linear terms, e.g. $\langle M_{\ell_1} M_{\ell_4}\rangle\langle M_{\ell_2} M_{\ell_3}\rangle\langle M_{\ell_5} M_{\ell_6}\rangle$.

We have seen how the first term gives 15 contributions if we use Wick's theorem to transform the six-point correlation function into a combination of products of three two-point correlation functions. We have also seen that in the isotropic case, only the six terms where each multipole among $(\ell_1,\ \ell_2,\ \ell_3)$ is coupled with an element of the other triplet $(\ell_4,\ \ell_5,\ \ell_6)$ are non-zero. The same can be done for the four-point correlation function and each combination of a linear contribution with a cubic term will give three terms, hence a total of eighteen terms. Note also that each term derived from the linear correction contains necessarily two ℓ's of the same triplet that are coupled (it is in the definition of the linear term). Hence, it means that they cannot cancel the six terms of the isotropic case. The new terms (i.e. the terms that are not present in the isotropic case) are nine from the six-point correlation function, nine from the product of two linear terms, and eighteen from the terms with the four-point correlation functions (with a minus sign) and it is then easy to check that they cancel each other. So finally

$$\begin{aligned}\langle B^{\rm obs}_{\ell_1\ell_2\ell_3} B^{\rm obs}_{\ell_4\ell_5\ell_6}\rangle = \int_{(S^2\setminus\mathcal{M})\times(S^2\setminus\mathcal{M})} \mathrm{d}\hat{\Omega}\,\mathrm{d}\hat{\Omega}'\ [&\langle M_{\ell_1} M_{\ell_4}\rangle\langle M_{\ell_2} M_{\ell_5}\rangle\langle M_{\ell_3} M_{\ell_6}\rangle + (14)(26)(35)\\ &+(15)(24)(36) + (15)(26)(34) + (16)(24)(35) + (16)(25)(34)]\,,\end{aligned} \tag{4.49}$$

where we use an obvious shorthand notation to indicate the other permutations of filtered maps. It is important to note that we recover the same variance as in the isotropic case without a linear term (except for the integration interval). This proves that the estimator with this linear correction is optimal (with the assumption that $C_{\ell m,\ell' m'}$ is diagonal). Then, performing the same last steps of the calculation as before, the variance is given by

$$V_{\ell_1\ell_2\ell_3} = g_{\ell_1\ell_2\ell_3}\frac{h^2_{\ell_1\ell_2\ell_3}}{f_{\rm sky}}(b^2_{\ell_1}C_{\ell_1}+N_{\ell_1})(b^2_{\ell_2}C_{\ell_2}+N_{\ell_2})(b^2_{\ell_3}C_{\ell_3}+N_{\ell_3}), \tag{4.50}$$

when including the effect of the beam and the noise as explained previously. It is immediate to see that masking a larger part of the sky, which decreases the multiplicative bias $f_{\rm sky}$, makes the variance become larger.

In conclusion, we have shown that under the assumption that the covariance matrix $C_{\ell m,\ell' m'}$ is diagonal, the optimal estimator for $f_{\rm NL}$ is given by (4.42) where the inner product is computed with the variance (4.50). Hence it is evaluated from the theoretical power spectrum taking into account the characteristics of the experiment, like its beam and noise. Hence, the product of the two bispectra is weighted by the variance, meaning that for example a very noisy ℓ-triplet (inducing a large variance) cannot play an important role.

While the original estimator (4.27) has been greatly simplified, some more work is still required.

4.4.3 Binning

One of the main issues with the different equations above when used with WMAP or Planck temperature maps is the very high number of valid triplets (up to $\mathcal{O}(10^9)$ in the case of Planck). Different techniques have been developed to deal with the enormous amount of computations required, like the KSW [116, 201, 202] and skew-C_ℓ [152] estimators using factorisable templates or the modal estimator [80, 81, 79] decomposing the bispectrum into a sum of uncorrelated templates. Here we adopt the binned bispectrum estimator, originally introduced in [43] and further developed in [42]. It relies on the simple idea that the variation with ℓ of many physically

motivated bispectral templates is smooth. In that case, instead of having $(\ell_{\rm max} - \ell_{\rm min} + 1)$ maximally filtered maps M_ℓ with ℓ in $[\ell_{\rm min}, \ell_{\rm max}]$, it is possible to use broader filters:

$$M_i(\hat{\Omega}) = \sum_{\ell \in \Delta_i} M_\ell(\hat{\Omega}), \tag{4.51}$$

where $\Delta_i = [\ell_i,\ \ell_{i+1} - 1]$ with $i = 0, ..., (N_{\rm bins} - 1)$ and $\ell_{N_{\rm bins}} = \ell_{\rm max} + 1$ define the binning of the multipole space.

Similar to (4.48), the binned bispectrum is

$$B^{\rm obs}_{i_1 i_2 i_3} \equiv \frac{1}{\Xi_{i_1 i_2 i_3}} \int_{S^2 \setminus \mathcal{M}} {\rm d}\hat{\Omega}\, \left[M_{i_1} M_{i_2} M_{i_3} - M_{i_1} \langle M_{i_2} M_{i_3} \rangle - M_{i_2} \langle M_{i_1} M_{i_3} \rangle - M_{i_3} \langle M_{i_1} M_{i_2} \rangle \right], \tag{4.52}$$

where the normalization factor $\Xi_{i_1 i_2 i_3}$ is the number of ℓ triplets within the $(i_1,\ i_2,\ i_3)$ bin triplet satisfying the two selection rules (triangle inequality and parity condition). When it comes to binning the multipole space, it was shown in [42] that another rule of selection is necessary to avoid numerical inaccuracies when computing the observed bispectrum due to the pixelization of the celestial sphere. We use here the same selection criterion that the ratio of valid ℓ-triplets to the ones satisfying only the parity condition (but not the triangle inequality) in a bin triplet should be at least 1 % It has been shown (see [42]) that the variance has the same form as (4.50), with an extra factor $1/(\Xi_{i_1 i_2 i_3})^2$

$$V_{i_1 i_2 i_3} = \frac{1}{f_{\rm sky}} \frac{g_{i_1 i_2 i_3}}{(\Xi_{i_1 i_2 i_3})^2} \sum_{\ell_1 \in \Delta_1} \sum_{\ell_2 \in \Delta_2} \sum_{\ell_3 \in \Delta_3} h^2_{\ell_1 \ell_2 \ell_3} (b^2_{\ell_1} C_{\ell_1} + N_{\ell_1})(b^2_{\ell_2} C_{\ell_2} + N_{\ell_2})(b^2_{\ell_3} C_{\ell_3} + N_{\ell_3}). \tag{4.53}$$

The same definition of the bispectral inner product (4.41) can be used with i-triplets instead of multipole parameters so

$$\langle B^A, B^B \rangle = \sum_{i_1 \le i_2 \le i_3} \frac{B^A_{i_1 i_2 i_3} B^B_{i_1 i_2 i_3}}{V_{i_1 i_2 i_3}}. \tag{4.54}$$

Hence, the binned bispectrum estimator can be written in the usual form

$$\hat{f}_{\rm NL} = \frac{\langle B^{\rm th}, B^{\rm obs} \rangle}{\langle B^{\rm th}, B^{\rm th} \rangle}, \tag{4.55}$$

where every bispectrum is taken in its binned form, and we take into account all the experiment characteristics as described in section 4.4.2 (beam, noise, mask, linear correction). Note that the error on $\hat{f}_{\rm NL}$ is then given by ${\rm Var}(\hat{f}_{\rm NL}) = 1/\langle B^{\rm th}, B^{\rm th} \rangle$.

We also use the shorthand notation of the bispectral inner product in several other important quantities. We need it to define a simple criterion to verify how optimal the choice of binning is. As the product takes the same form for i-triplets or ℓ-triplets, it is easy to compare ideal and binned estimators using the relation

$$R \equiv \frac{{\rm Var}(\hat{f}^{\rm ideal}_{\rm NL})}{{\rm Var}(\hat{f}^{\rm binned}_{\rm NL})} = \frac{\langle B^{\rm th}, B^{\rm th} \rangle^{\rm binned}}{\langle B^{\rm th}, B^{\rm th} \rangle^{\rm no\ binning}}. \tag{4.56}$$

This ratio shows by how much binning the multipole space has increased the variance. It has been proven in [42] that R is a number between 0 and 1. Obviously, R is closer to 1 if the binning better describes the considered theoretical shape. We have at our disposal several types of theoretical bispectra to which the binned bispectrum of a map can be compared, see section 4.2. The binning we used has been optimized for the primordial shapes (local (4.8), equilateral (4.9) and orthogonal (4.10)).

	Local	Equil	Ortho	LensISW	UnclustPS	CIB
Local	1	0.21	-0.44	0.28	0.002	0.006
Equilateral		1	-0.05	0.003	0.008	0.03
Orthogonal			1	-0.15	-0.003	-0.001
Lensing-ISW				1	-0.005	-0.03
Unclustered point sources					1	0.93
CIB point sources						1

Table 41: Correlation coefficients from [42] between the theoretical templates defined in section 4.2 computed using the characteristics of the Planck experiment (temperature). We see a correlation between local and orthogonal and between local and lensing-ISW. Equilateral and orthogonal are mostly uncorrelated, and the correlation between the point source templates and the primordial ones is negligible.

One issue with these theoretical shapes is that they are not necessarily independent from each other. Hence it is important to evaluate if one can distinguish them in an experiment. A natural definition for their correlator is

$$C_{IJ} = \frac{\langle B^I, B^J \rangle}{\sqrt{\langle B^I, B^I \rangle \langle B^J, B^J \rangle}}. \tag{4.57}$$

The indices I and J label the theoretical shapes. C_{IJ} is between -1 and 1, a value close to 0 indicates that the theoretical bispectra I and J are almost uncorrelated. Note that because the bispectral inner product depends on the characteristics of the experiment, the shape correlators do too. In Table 41, we reported those computed in [42] from CMB data maps from the 2015 Planck release.

The formula (4.55) for the estimator $\hat{f}_{\rm NL}$ is used for each shape independently (giving each time a parameter $f^I_{\rm NL}$ describing a unique shape). However, in the case where some shapes are correlated and multiple shapes are present in the data, it means that some part of the bispectral signal is taken into account several times. It is possible to improve the result using the inverse of the matrix F_{IJ}[3]

$$F_{IJ} = \langle B^I, B^J \rangle \tag{4.58}$$

to define the joint estimator

$$\hat{f}^I_{\rm NL} = \sum_J (F^{-1})_{IJ} \langle B^J, B^{\rm obs} \rangle. \tag{4.59}$$

The variance of $\hat{f}^I_{\rm NL}$ goes from $1/F_{II}$ for a fully independent estimation to $(F^{-1})_{II}$ in the case of a joint analysis. One can show that the variance increases if there are several correlated templates. However, it is also possible that one of the $f^I_{\rm NL}$ parameters (or more) is already known, for example the lensing-ISW template including its amplitude (i.e. $f_{\rm NL}$ parameter) for the CMB is entirely determined by theory. It is then possible to avoid the increase of variance due to the joint analysis, treating such a shape as a known bias. In the case of two shapes, subtracting the known $f^{(2)}_{\rm NL}$ from the unknown $f^{(1)}_{\rm NL}$ is as simple as

$$f^{(1)}_{\rm NL} = \frac{1}{F_{11}} \langle B^{(1)}, B^{\rm obs} \rangle - \frac{F_{12}}{F_{11}} f^{(2)}_{\rm NL}. \tag{4.60}$$

[3] F_{IJ} is the Fisher matrix, a crucial quantity in estimation theory, and the multivariate generalization of the Fisher information introduced in (3.9).

The demonstration is straightforward, it is sufficient to use (4.59) for the shapes (1) and (2) to substitute $\langle B^{(2)}, B^{\rm obs}\rangle$ by $\langle B^{(1)}, B^{\rm obs}\rangle$ and $f_{\rm NL}^{(2)}$.

We have recalled all the analytical equations concerning the binned bispectrum estimator. In the next section, we will discuss briefly some numerical aspects.

4.4.4 Binned bispectrum estimator code

The binned bispectrum estimator was implemented numerically in Python and C by Van Tent, Bucher and Racine (see section 5 of [42] for a complete description). This code was used for the official 2013 and 2015 Planck releases [11, 14]. We also used it for the different data analyses presented in this thesis (see chapters 5 and 6).

The maps are read and represented (in Mollweide view) using the package Healpy[4]. This a Python wrapper to Healpix[5] [92], a code developed to standardize the spherical decomposition of pixelized CMB data maps. In this thesis, we will use maps with two different resolutions. The best resolution with Planck data corresponds to maps with $n_{\rm side} = 2048$ where the number of pixels is given by $N_{pix} = 12 n_{\rm side}^2$. We will also have a few low resolution maps $n_{\rm side} = 256$.

With the binned bispectrum estimator, it is possible to separate the computations into several independent modules

- **Theoretical** ($<$ 2 hours)[6]: this part adapts the theoretical shapes introduced in section 4.2 to the analyzed map(s). This means it applies the binning and the beam to the theoretical templates. Moreover, it computes the theoretical variance where the noise power spectrum is included.

- **Observational - cubic** ($<$ 4 hours): this part computes the binned bispectrum (4.2) of the analyzed map(s) (for example: 1 observed CMB data map + 100 Gaussian CMB simulations to determine the error bars).

- **Observational - linear** ($<$ 2 days): this part computes the linear correction to the binned bispectrum in (4.48). The two-point correlation functions $\langle M_{\ell_1} M_{\ell_2}\rangle$ are computed using Gaussian simulations of the observed data.

- **Estimator** ($<$ 1 min, after the rest): this part applies the estimator (4.55) and/or the joint-estimator (4.59) to the results of the previous modules to compute $f_{\rm NL}$ for the different bispectral shapes, and the associated error bars.

Thanks to this separability of the code, it is then easy and fast to test new theoretical shapes when the rest has already been computed. This is interesting for a new functionality we added for the work presented in this thesis, which is to be able to use the binned bispectrum of a given map (computed by the observational part) as a numerical template for the analysis of another map. To be more precise, we will use maps of galactic foregrounds and determine their binned bispectrum (for which there is no analytical expression) in the next chapter. Then, we will apply these templates to different maps (like the CMB) in chapter 6.

[4] https://github.com/healpy/healpy

[5] http://healpix.sf.net

[6] Estimated runtime at the Planck resolution for temperature only using computers of the Centre de Calcul de l'Institut de Physique Nucléaire et de Physique des Particules (CC-IN2P3) in Lyon, France https://cc.in2p3.fr/.

Chapter 5

Galactic foregrounds

In this chapter, we study several galactic foregrounds with the binned bispectrum estimator. As discussed previously, when studying non-Gaussianity in CMB data maps, the usual method is to compare the observed bispectrum to different theoretical shapes using the inner product (4.54). The determined parameters $f_{\rm NL}$ simply indicate to what extent these shapes are present in the data. Section 4.2 recalled some analytical expressions for the main shapes describing primordial non-Gaussianity (generated during inflation) but also late-time bispectra (generated after recombination) like extra-galactic foregrounds. However, when observing the CMB, the main source of contamination is our own galaxy and there is no equivalent theoretical expression to describe the non-Gaussianity of galactic foregrounds yet. There are many techniques to clean the maps from the presence of different galactic foregrounds (see [8, 9, 16] for a review) and CMB analyses at the bispectral level are generally performed on these cleaned maps. In this chapter, we use the fact that an analytical formulation of theoretical shapes is not mandatory, allowing us to examine these foregrounds too. Indeed, to use the inner product (4.54), one only needs the numerical binned theoretical bispectrum.[1] This means that in principle, the binned bispectrum of any map determined numerically could be used as theoretical template for the analysis of another map under the condition that the binning is the same. In this way we determine templates using the maps of different galactic foregrounds from the 2015 Planck release obtained by the Commander separation technique [78, 77].[2,3]

Before doing so, it is necessary to give a little more context for the different analyses of this chapter, by keeping in mind their end goal (see chapter 6) which is to use these new numerical templates on the CMB cleaned maps studied in [14]. To be more precise, we will use the SMICA [51] CMB map from the 2015 Planck release. We will also study the raw 143 GHz map, which is the dominant frequency channel in the SMICA map [8]. While it is the best channel to observe the CMB (best combination of a low noise level and a good resolution), that is not the case for the different foregrounds (at least if the goal was to study the physics of these foregrounds). Nevertheless, here we only need to estimate their eventual contamination to the CMB signal. At that frequency, the CMB dominates the sky after masking the brightest parts (galactic plane and strong point sources). For this, we use the temperature common mask of the Planck 2015 release, which is a combination of the masks of the different component separation methods [9]. In section 5.3, we will discuss the influence of the mask on the different foregrounds by using a smaller one (Commander mask). Finally, another important choice is

[1] With the shapes presented in section 4.2, one of the first steps of the binned bispectrum estimator code is to determine these numerical binned bispectra by summing all values of the analytical expressions for each valid ℓ-triplet inside the bin-triplets.

[2] https://pla.esac.esa.int

[3] Thanks to Ingunn Kathrine Wehus for providing the Commander maps of the different foregrounds at 143 GHz.

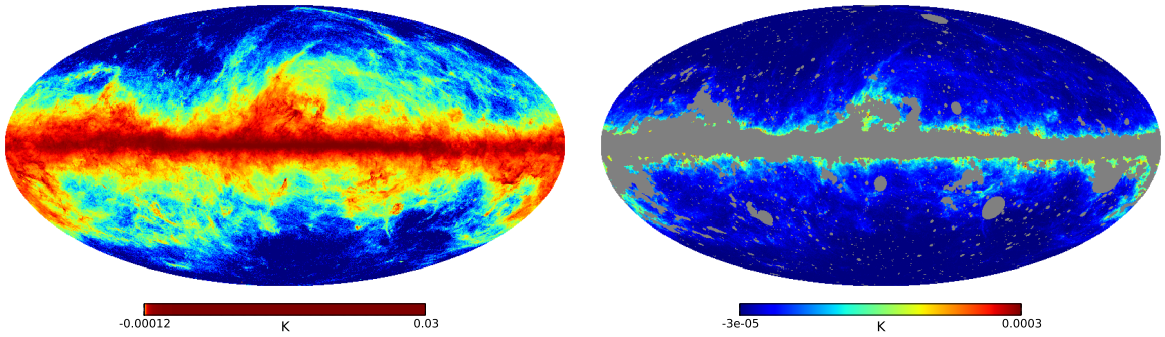

Figure 51: Unmasked (left) and masked (right) maps of thermal dust at 143 GHz from Commander (Planck 2015), using the common mask. On the left, the map is normalized using histogram equalization to highlight all the regions containing dust. On the right, the scale is linear, this shows that most of the signal is coming from the galactic plane near the mask. The range of the scale is also different.

the binning which was determined using the ratio R defined in (4.56) to be optimal for the primordial shapes. It is true that this criterion has nothing to do with the galactic foregrounds, but our ultimate goal is to determine the primordial shapes optimally, not the galactic ones. To illustrate the method, we start by studying the case of thermal dust.

The work presented in this chapter and the following can be found in [107].

5.1 Thermal dust

Above 100 GHz, the strongest contamination from galactic foregrounds is due to small dust grains (~ 1 μm or smaller) present in the interstellar medium. This dust plays an important role in galactic evolution (chemistry of interstellar gas, etc., see the textbook [67] for example), but it also has a large influence on astrophysical observations. Indeed dust grains are heated by the UV starlight they absorb, so they emit a thermal radiation (infrared) in the frequency range of CMB experiments. This emission is well described by a modified blackbody model also called greybody (see [10, 2, 9])

$$I(\nu) = A\nu^{\beta_d} B_\nu(T_d), \tag{5.1}$$

where B_ν describes Planck's law, $T_d \sim 20K$ is the mean temperature and $\beta_d \sim 1.5$ is the free emissivity spectral index.

Figure 51 shows the map of the galactic thermal dust at 143 GHz, before and after applying the common mask. As mentioned before, we are interested in the contribution of the foregrounds in a CMB analysis (where a mask is always used to hide the galactic plane). Hence, the map on the right is the most important here because it is the actual contribution of dust that could be seen in a CMB analysis. In the following, we will be interested in the power spectrum and the bispectrum of this map. As expected, most of the signal comes from the galactic plane, and it is strongest close to the mask. Because of the dust localization, this emission is very non-Gaussian [146] and anisotropic (and this is also the case for the other galactic foregrounds studied in section 5.2). As we mentioned in section 4.1, the bispectrum is not the best tool to describe such a localized non-Gaussianity (an estimator in pixel space would be better). However, we are only interested in the impact of this galactic foreground on the primordial shapes. This requires us to be careful with the different expressions of chapter

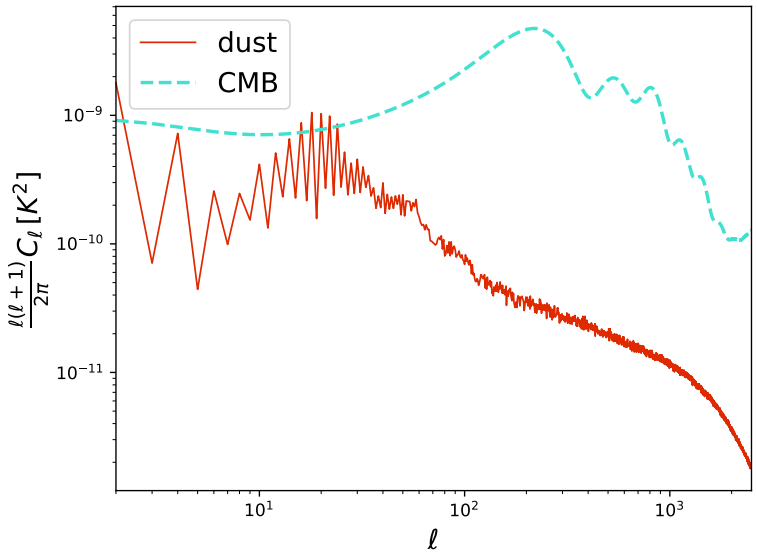

Figure 52: This figure shows the dust (at 143 GHz) and the CMB (Planck 2015 best fit) power spectra (including the beam and the noise for both) as a function of the multipole ℓ.

4.4.2, mostly derived using the weak non-Gaussianity approximation. Concerning the observed bispectrum of the dust map, which is exactly what we need to make a dust template, it is still defined by (4.52), but without the linear correction terms which are not justified here.

Before describing the dust bispectrum, it is interesting to examine the power spectra of the dust and CMB maps shown in figure 52. It is clear that at 143 GHz, the CMB dominates except for the largest scales (smallest ℓ) where the dust power spectrum has a sawtooth pattern. We can see that it is smaller (up to an order of magnitude) for each odd ℓ up to $\ell \sim \mathcal{O}(20)$. This is in fact due to the symmetry of the masked map in figure 51 around the galactic plane when viewed on the largest scales. Because of this symmetry, the temperature is an even function of the angle θ (with the usual $\hat{\Omega} = (\theta, \varphi)$, where θ describes the latitude position), using the simple approximation that the mask can be seen as a band with all the dust signal on the border. The spherical harmonics $Y_{\ell 0}$ also have a similar symmetry around the galactic plane so they are the main contribution when decomposing in harmonic space. However, the $Y_{\ell 0}$ are even in θ only for ℓ even and they are odd for ℓ odd, so the odd terms have to be small. For the same reasons similar effects are expected in the dust bispectrum as far as large scales are concerned.

As expected, the situation is different concerning the binned bispectrum. In order to make it easy to visualize, we use 2D-slices where the multipoles ℓ_1 and ℓ_2 go from 2 to 2500 but ℓ_3 is in a chosen bin. Figure 53 shows a slice ($\ell_3 \in [1092, 1149]$) of the binned dust bispectrum compared to the local shape in the case $f_{\rm NL}^{\rm local} = 1$.[4] If we compare the bispectrum amplitudes, it is clear that the dust is several orders of magnitude larger than the local shape. Moreover, acoustic oscillations present in both the CMB power spectrum and the local theoretical bispectrum are not there in the case of thermal dust (as expected).

However, the plots of figure 53 are not well suited to describe quantitatively the non-Gaussian nature of these shapes. As in the case of the power spectrum, which peaks at low ℓ if we do not multiply by the factor $\ell(\ell+1)$, the CMB bispectrum as well as the dust bispectrum

[4] $f_{\rm NL}^{\rm local} = 1$ is still well within the observational bounds. In part III, we will call it large non-Gaussianity because it is very large compared to the predictions of standard slow-roll single-field inflation $f_{\rm NL}^{\rm local} \sim \mathcal{O}(10^{-2})$.

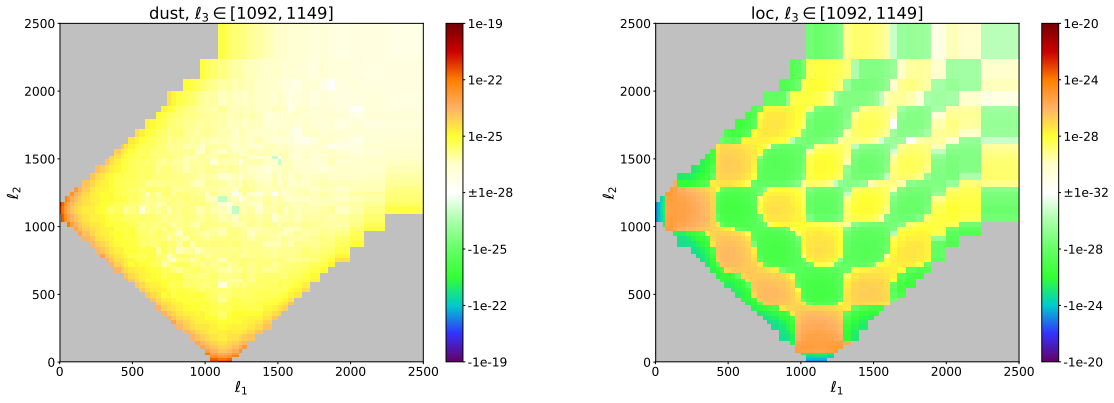

Figure 53: Left: observed binned bispectrum of the thermal dust as a function of the multipoles ℓ_1 and ℓ_2 for $\ell_3 \in [1092, 1149]$. Right: theoretical bispectrum for the local shape in the case $f_{\mathrm{NL}}^{\mathrm{local}} = 1$ for the same bin of ℓ_3. Note the difference of colour scale (both for maximal and minimal values).

have a strong ℓ dependence. This means that we should use an adapted function of ℓ to highlight the true nature of a bispectral signal. A good choice is to use signal-to-noise plots [42] as shown in figure 54: the bispectrum is divided by the square root of the variance of the map computed using (4.50). It is important to note that this is different from the correlation coefficients (4.57) that we discuss later in this chapter where the variance of the CMB map (the map shown in 31) is used. In this kind of plots, non-Gaussianity is simply represented by values large compared to $\mathcal{O}(1)$.

Figure 54 shows the bispectral signal-to-noise ratio for three different slices of the dust template (on the left), but also for a cleaned CMB map which we will study in detail in chapter 6 (on the right). It is now obvious that the dust map is very non-Gaussian and that indeed its bispectrum peaks in the squeezed configuration. This effect can be seen in the top plot (low ℓ_3) but also on the left (low ℓ_1) and on the bottom (low ℓ_2) of the other plots. A squeezed configuration is expected when there are correlations between small-scale and large-scale effects. There is a simple physical explanation for the origin of these correlations. The large clouds of dust (i.e. large-scale fluctuations) have the highest intensity where they are the thickest along the line of sight. Moreover, the brightest parts have stronger fluctuations (small-scale), see [146] for a discussion, so the small-scale fluctuations are modulated by the large-scale ones which corresponds to a squeezed bispectrum.

The squeezed signal present in both the dust and the local shapes is a good indication that they are correlated. This can be verified in table 51 which gives the correlation coefficients between the dust and the usual shapes of section 4.2 computed using (4.57) in the context of a CMB analysis (more details in next chapter), so the denominator of the inner product is the CMB bispectrum variance. There is an anti-correlation between the dust and local shapes (60 %) because they have opposite signs (this anti-correlation was pointed out in [203]). The local shape is itself correlated to the other primordial shapes (see table 41). However, this does not mean that the dust template has to be correlated to them too. And indeed, the dust and equilateral shapes are uncorrelated because the latter does not peak in the squeezed configuration. The correlations between local and dust (squeezed) do not come from the same multipole triplets as the correlations between local and equilateral (acoustic peaks). However, the orthogonal and dust shapes are a little correlated (around 15 %), because the orthogonal bispectrum in the squeezed limit is large. The dust bispectrum template is very weakly

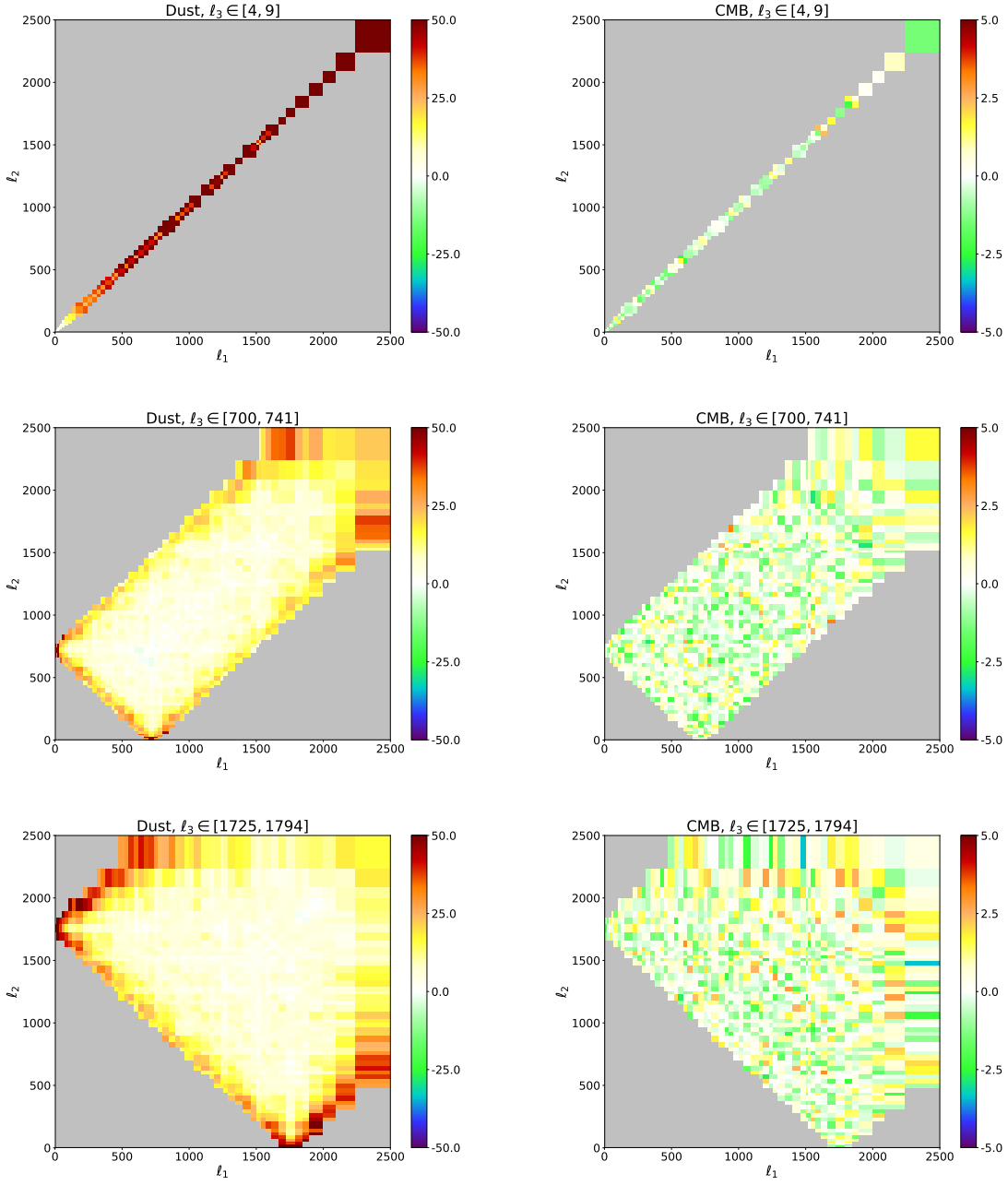

Figure 54: Left: bispectral signal-to-noise of the thermal dust as a function of the multipoles ℓ_1 and ℓ_2 for three different bins of ℓ_3. Right: same for the CMB map studied later in section 6.2 for the same bins of ℓ_3. Note the factor 10 difference in colour scale.

	Local	Equilateral	Orthogonal	Lensing-ISW	Point sources	CIB
Dust	-0.6	0.004	0.15	-0.34	0.054	0.083

Table 51: Correlation coefficients between the theoretical templates defined in section 4.2 and the observed dust bispectrum computed using the characteristics of the Planck experiment (temperature).

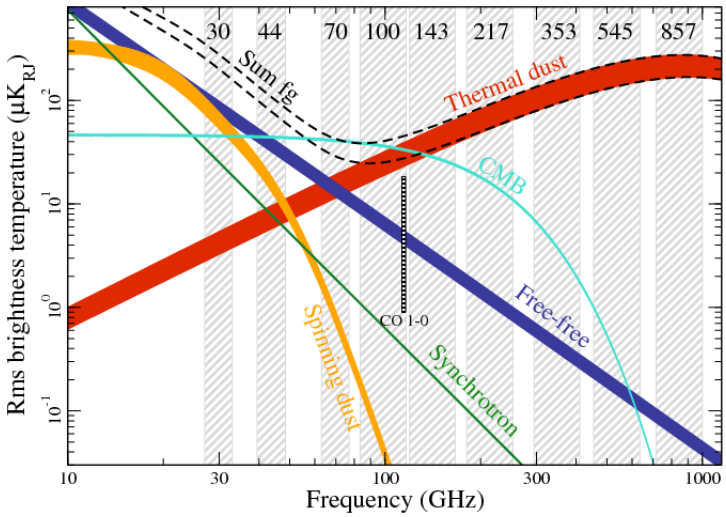

Figure 55: Brightness temperature rms of the CMB and the four galactic foregrounds studied in this chapter (dust, synchrotron, AME called spinning dust here, free-free) as a function of frequency. This figure is borrowed from [9] which should be consulted for the details of the exact parameters used (e.g. masks). The nine frequency channels of Planck are indicated.

correlated to extra-galactic foreground templates like unclustered point sources and CIB, but anti-correlated to lensing-ISW (which is known to be highly correlated to the local shape). An alternative representation of the bispectra of the different shapes, which shows in which regions of multipole space they dominate, is given in appendix A.

5.2 Other foregrounds

Apart from dust, there exist other foregrounds which have a greater effect at low frequencies, of which we will study three here. In this section we use maps produced by the Commander method to separate foregrounds, but this time in addition to the Planck data, observations from WMAP between 23 and 94 GHz [35] and a 408 MHz survey map [99] were also used to determine them. They have a lower resolution ($n_{\rm side} = 256$) and a larger beam (60' FWHM Gaussian beam). For the sake of comparison of these foregrounds with the dust we discussed in the previous section, we will also use here a dust map with the same characteristics.

In the case the dust grains rotate rapidly (in addition to their thermal vibrations), they can produce a microwave emission which probably corresponds to the anomalous microwave emission (**AME**) [121, 66], large at low frequencies.

Dust is not the only component responsible for the contamination of the CMB signal; some interactions of electrons with the interstellar medium can also generate emissions. On the one hand, ultra-relativistic electrons (cosmic rays) spiraling in the galactic magnetic fields radiate.

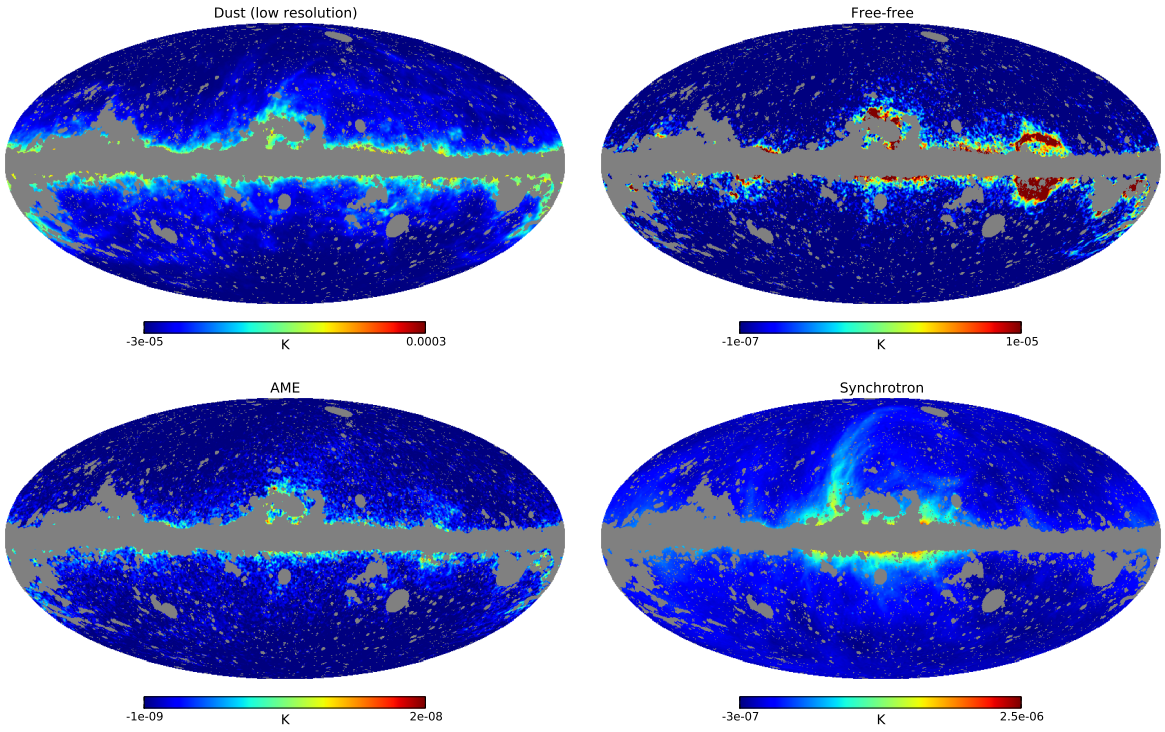

Figure 56: Masked maps of the different galactic foregrounds we consider in this thesis (dust, free-free, AME, synchrotron) at 143 GHz derived using the Commander method. Note the different colour scales.

This **synchrotron** emission can be described by a power law ν^β with $\beta \simeq -3$ indicating that indeed, this radiation is significant at low frequencies [99]. On the other hand, electrons can be slowed down by scattering off ions. This generates the **free-free** emission [63], also called bremsstrahlung.

Figure 55 shows the frequency dependence of the foregrounds and the CMB signals. As discussed, the synchrotron, the free-free and the spinning dust (AME) emissions dominate at low frequencies. The dust thermal emission is the main contribution at high frequencies and is of the same order as the CMB at 143 GHz (this of course depends on the choice of mask).

Figure 56 shows the contributions of all these foregrounds at 143 GHz. Similarly to the dust in the previous section, they are all localized in the galactic plane. Moreover, we can see that the dust signal has a higher intensity and therefore is the dominant foreground contribution at 143 GHz, as expected from figure 55. The same hierarchy can be seen in the power spectra, as shown in figure 57. It is clear that at 143 GHz, the contributions of AME, synchrotron and free-free are negligible compared to the CMB (remember that the brightest parts of the sky are masked). Note that because of the low resolution of the map and the 60 arcmin beam, the range of multipoles is a lot smaller than in the previous section ($\ell_{\max} = 300$ here). This also means that we were able to use smaller bins for the binned bispectrum estimator. We simply took the usual binning, with each bin split into three when possible (two otherwise).

The same behaviour is of course present in the bispectra (i.e. the templates) where the dust dominates everything. However, as discussed in the previous section, it is more interesting to study the bispectral signal-to-noise to study the form of these bispectra. Figure 58 shows these bispectra for three different slices of ℓ_3. Free-free, dust and AME peak in the squeezed configuration (but for AME, the signal is so low that it could be only noise). An argument similar to the dust case described in the previous section can explain this bispectral configuration. We can

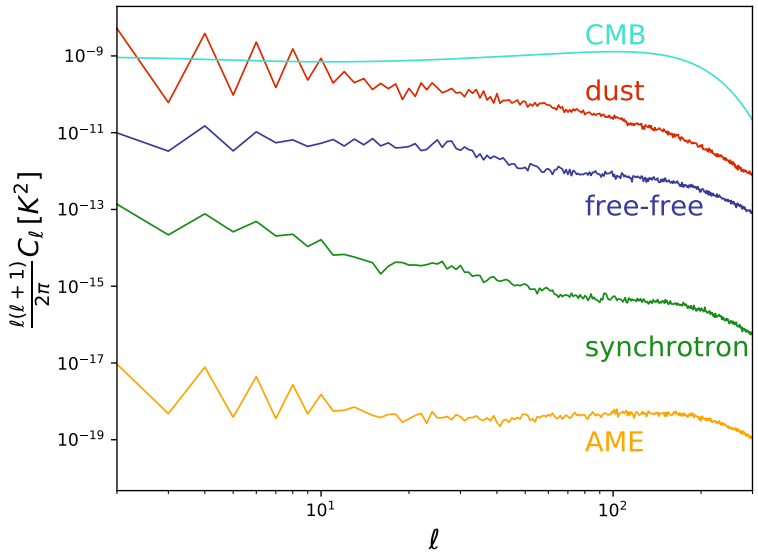

Figure 57: The different foregrounds (dust, free-free, synchrotron and AME) and the CMB power spectra at 143 GHz (including the 60 arcmin beam and the noise) as a function of the multipole ℓ.

	Local	Equilateral	Orthogonal	Lensing-ISW	Point sources	CIB
Dust (low resolution)	-0.14	0.0097	0.087	-0.036	0.0083	0.012
Free-free	-0.44	-0.045	0.43	0.043	0.069	0.11
AME	-0.23	0.032	0.052	-0.051	0.033	0.037
Synchrotron	-0.057	0.33	0.29	0.051	0.44	0.38

	Dust (low resolution)	Free-free	AME	Synchrotron
Dust (low resolution)	1	0.24	0.28	0.56
Free-free		1	0.37	0.32
AME			1	0.32
Synchrotron				1

Table 52: Correlation coefficients between the theoretical templates defined in section 4.2 and the observed foreground templates (low resolution) computed using the characteristics of the Planck experiment (temperature).

also verify this in table 52 where we have computed the correlation coefficients of these shapes with the ones previously introduced. As expected, the dust, free-free and AME bispectra are anti-correlated to the local shape (and for the other shapes see the previous section, the discussion is similar) and are correlated between themselves (they share the squeezed configuration). For a visual representation that helps to understand the correlations, see appendix A.

The case of synchrotron is different. The signal seems to be larger for three "high" values of ℓ, so it is similar to the equilateral shape. This is also the typical shape produced by unresolved point sources and by the CIB. Indeed, the synchrotron is correlated (around 40 %) to the point sources and CIB shapes as well as to equilateral and orthogonal (around 30 %). However, it

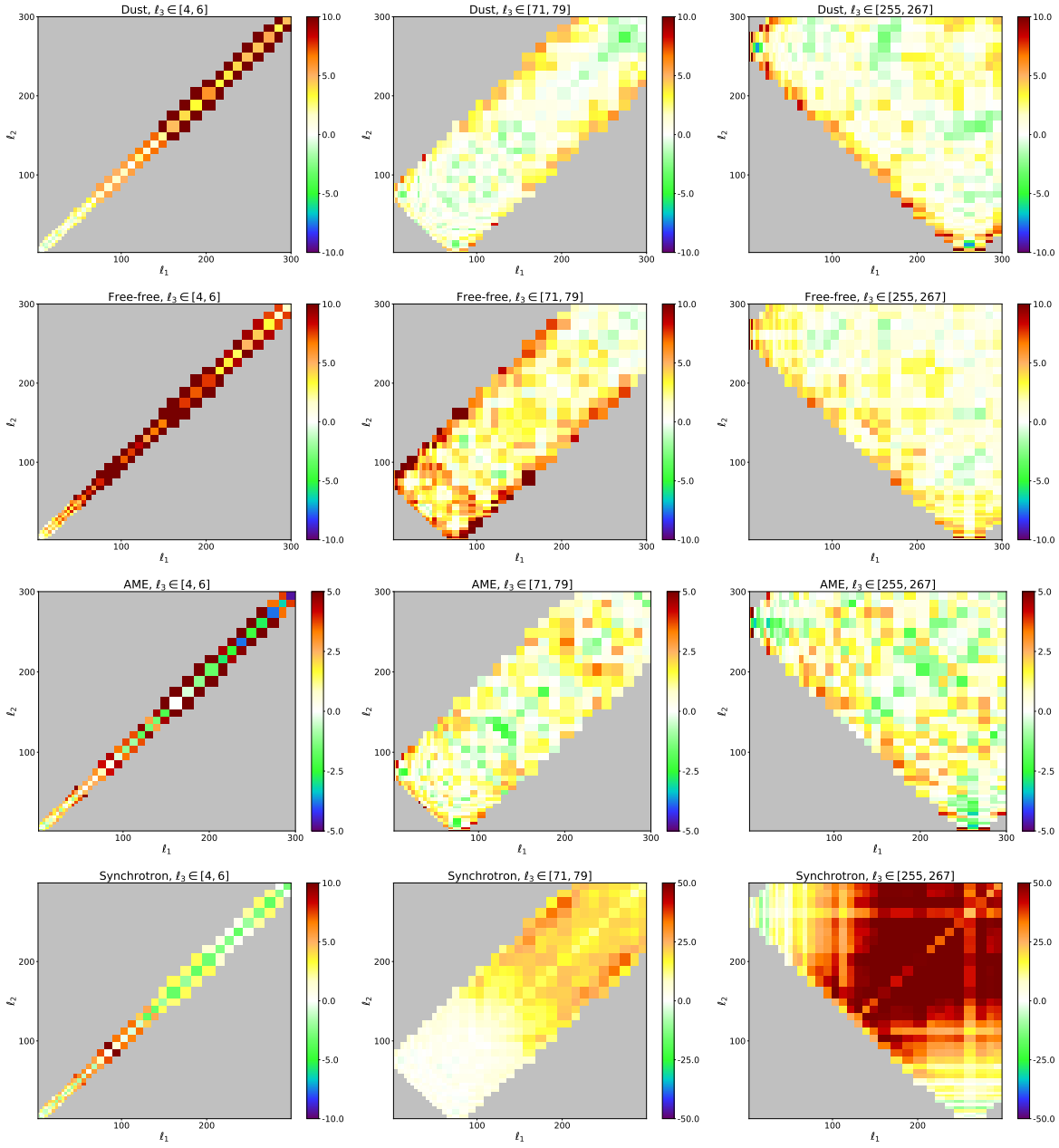

Figure 58: Bispectral signal-to-noise of the different foregrounds for $\ell_3 \in [4, 6]$, $\ell_3 \in [71, 79]$ and $\ell_3 \in [255, 267]$. Note the different color scales

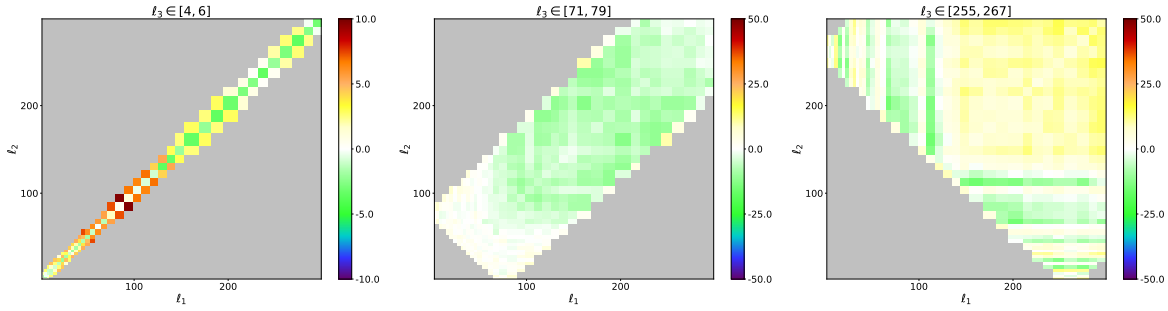

Figure 59: Bispectral signal-to-noise of the synchrotron after subtracting the unresolved point sources contamination for $\ell_3 \in [4, 6]$, $\ell_3 \in [71, 79]$ and $\ell_3 \in [255, 267]$. Note the different colour scales.

	Local	Equilateral	Orthogonal	Lensing-ISW	Point sources	CIB
Cleaned synchrotron	-0.14	0.025	0.13	-0.022	0.059	0.033

	Dust (low resolution)	Free-free	AME	Synchrotron
Cleaned synchrotron	0.62	0.32	0.34	0.92

Table 53: Correlation coefficients between the synchrotron bispectrum cleaned from the point sources contamination and the templates of table 52 computed using the characteristics of the Planck experiment (temperature).

is also correlated to the other foregrounds (more than 30 %), meaning that the synchrotron bispectrum also peaks in the squeezed limit, as shown in the bottom left plot of figure 58, even if it is not at all its dominant part. Physically that makes sense because we expect a squeezed signal for similar reasons as the other foregrounds. The simplest explanation for the equilateral shape is a contamination of the map by point sources and this possibility is mentioned in [9]. To verify it, we performed the simple test of subtracting the unresolved point sources bispectral template (of which the amplitude was determined using the estimator (4.55)) from the bispectrum of the synchrotron map. The cleaned bispectrum is shown in figure 59 where one can see that the left plot (showing the squeezed part of the bispectrum) has not changed from the one of figure 58, while the other two are much less non-Gaussian (but not perfectly cleaned either). This is also illustrated in table 53, where the correlation of the synchrotron bispectrum with the local shape increases (to around 15 %) and becomes of the same order as for the other foreground bispectra, while the anomalous correlation with the equilateral, point sources and CIB templates vanishes. From now on, when we mention the synchrotron bispectrum, it will be the one cleaned from the unresolved point sources contamination.

5.3 Noise and masks

The main source of anisotropy in the foreground maps are the foregrounds themselves as they are mostly present in the galactic plane, but we still need to examine the influence of the other sources discussed in section 4.4.2.

We start by the noise, which for the CMB has a large effect at high ℓ. Hence, it is sufficient to look at the best resolution dust map studied in section 5.1. Figure 510 shows the noise power spectrum of the dust map evaluated using half-mission maps. Even at high ℓ, it seems

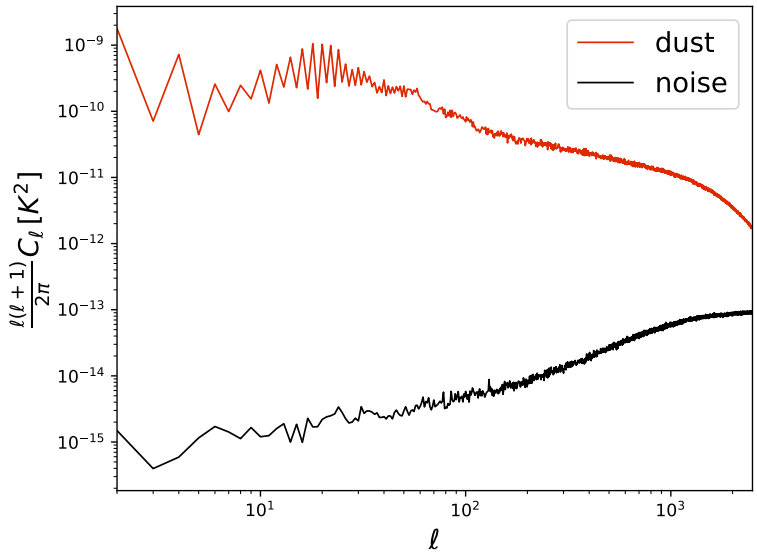

Figure 510: Dust and noise power spectra for the map studied in section 5.1 as a function of ℓ.

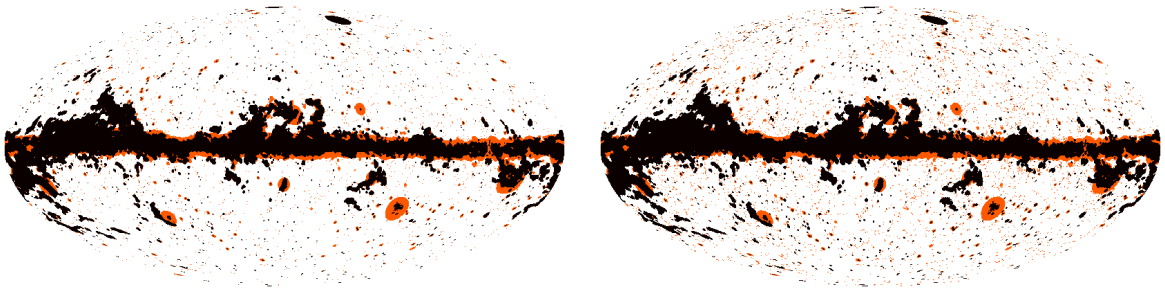

Figure 511: The different masks used in chapters 5 and 6. On the left, the high resolution versions ($n_{\text{side}} = 2048$) of the Commander mask ($f_{\text{sky}} = 0.822$) in black only and of the common mask ($f_{\text{sky}} = 0.776$) in black and orange. On the right, the masks have a low resolution ($n_{\text{side}} = 256$) and have been obtained by degrading the resolution of the masks on the left, in the process their size has slightly increased ($f_{\text{sky}} = 0.804$ and $f_{\text{sky}} = 0.745$). This effect is easily visible for the point sources.

that it is small compared to the signal. Hence, we will not discuss it further in this thesis.

The choice of mask should also be examined more carefully. That is why here we compare our previous results obtained with the common mask ($f_{\text{sky}} = 0.776$) to those obtained with the Commander mask which is slightly smaller ($f_{\text{sky}} = 0.822$) and of course fully included in the common mask. Figure 511 shows these two masks in the high and low resolution cases.

Figure 512 shows the power spectra of the different foregrounds with these two masks and highlights the large difference between the two cases. The reason for this difference is quite obvious because the masks have been constructed to hide most of the foregrounds, so with a smaller mask, there is a lot more of the foregrounds to detect. Moreover, as they are anisotropic, both the amplitude and the form are different depending on the mask, this is especially true for the synchrotron signal (as we will explain below).

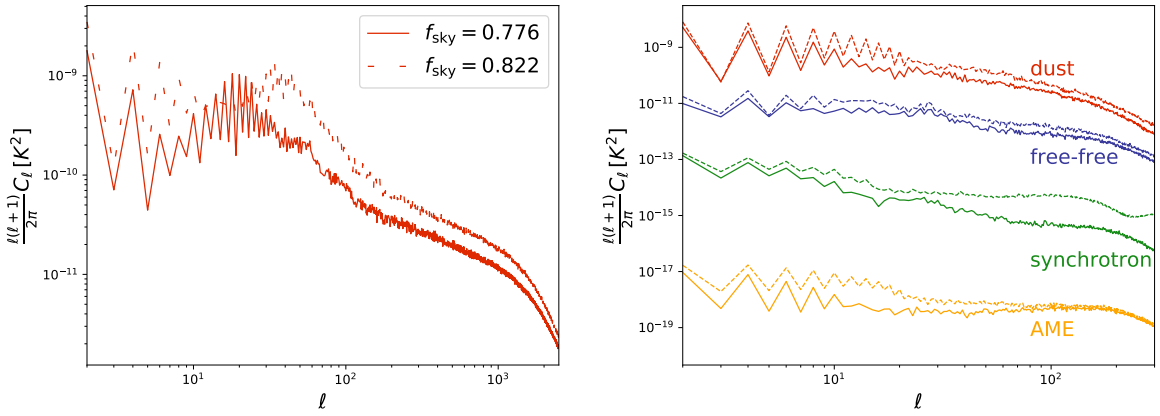

Figure 512: Power spectra of the different foregrounds using the common mask (solid line, $f_{\text{sky}} = 0.776$) and the Commander mask (dashed line, $f_{\text{sky}} = 0.822$). On the left, the high resolution dust map ($n_{\text{side}} = 2048$) and on the right, the low resolution foreground maps ($n_{\text{side}} = 256$).

Dust	Dust (low resolution)	Free-free	AME	Synchrotron
0.90	0.85	0.88	0.91	0.11

Table 54: Correlation coefficients between the bispectral templates determined using the common mask and the Commander mask for each foreground.

This is also checked for the bispectra as shown in figure 513. With the Commander mask (the smallest one), all the signals are a lot more non-Gaussian. To verify that is not only a difference of amplitude, we have at our disposal the perfect tool: the correlation coefficients defined in (4.57). For each foreground, we have computed the correlation between the templates determined using the two masks. The results are given in table 54. For the dust, free-free and AME emissions, the templates are correlated (above 80 %) and indeed we can see that the bispectra peak in the squeezed configuration as discussed previously. However, the fact that the correlation is not 100 % shows that the difference is not only the amplitude.

However, for synchrotron the situation is more complicated, like in the power spectrum case. Indeed the new template is very different from the one in figure 59, and it is confirmed by the low correlation between the two synchrotron templates determined with the two different masks. To understand this result, it is interesting to examine directly the data map with the Commander mask in figure 514. One can see that there are a few pixels where the intensity is ten times larger than with the common mask (where they are hidden). The influence of this very small region dominates the power spectrum and the bispectrum because the transition is so important. It could be modelized as a Heaviside step function, the Fourier transform of which is a sinc function, meaning that these two pixels have a large influence over the whole multipole space and we can see oscillations as expected in both the power spectrum (there is a minimum at $\ell \approx 240$) and the bispectrum (there are three regions of negative bispectrum with positive bispectrum around them on the plot for $\ell_3 \in [255, 267]$).

In conclusion, the choice of mask has a large influence on the templates we are determining because of the localization of the foregrounds in the galactic plane. This means that when we apply these templates to other maps in the next chapter, it is mandatory to use the same mask at every step. From now on, we will exclusively use the common mask.

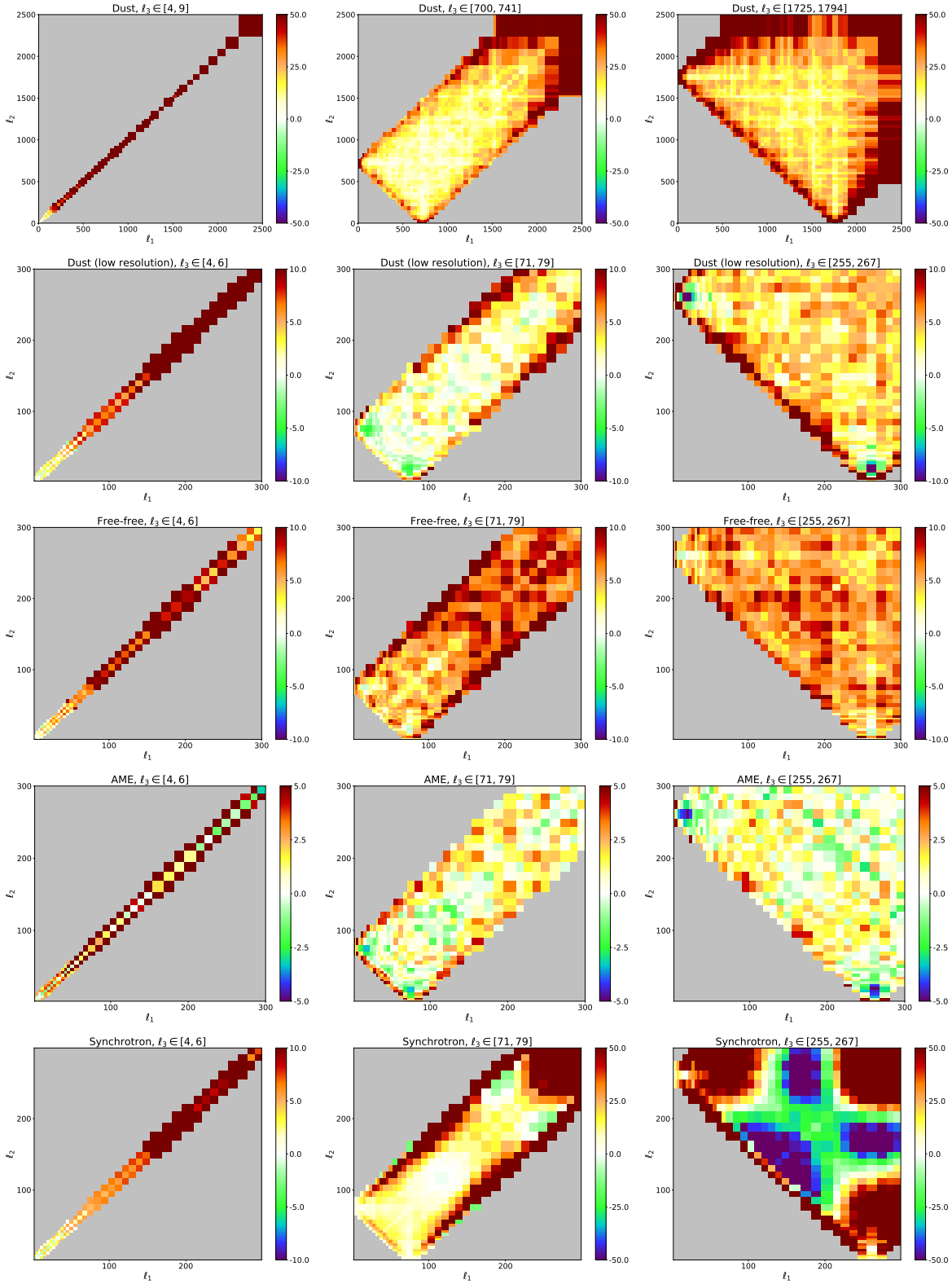

Figure 513: Bispectral signal-to-noise of the different foregrounds for the same three bins of ℓ_3 as figures 53 and 58 using the Commander mask. Note the different colour scales.

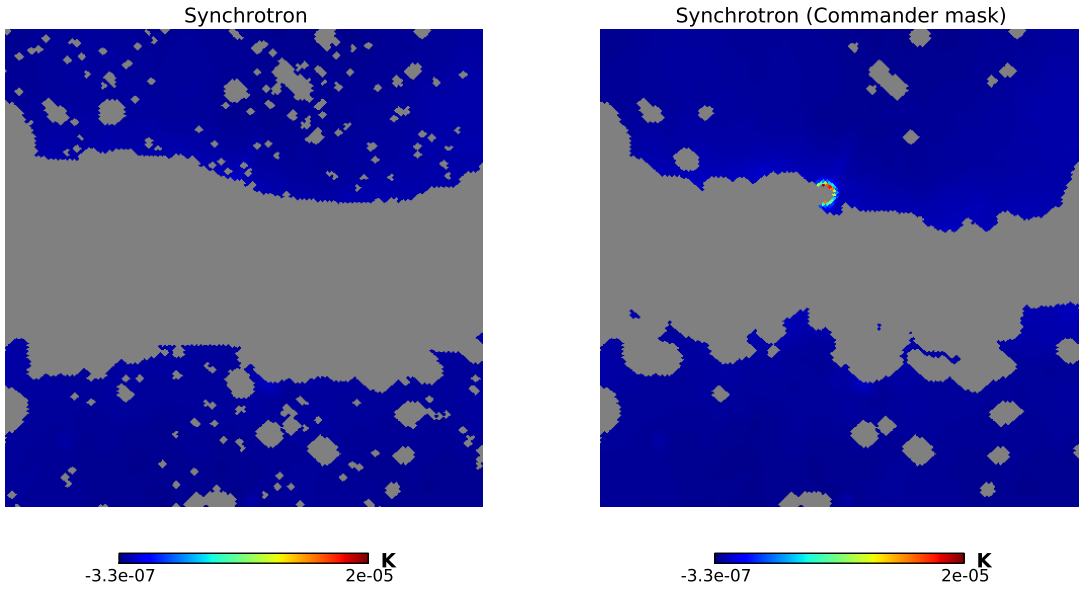

Figure 514: Zoom on the synchrotron map at 143 GHz after application of the masks (left: common mask, right: Commander mask).

Chapter 6

Data analysis using the galactic templates

The aims of this chapter are twofold. First, we want to verify that the numerical templates we just determined can be used in the context of a CMB data analysis. A large part of my work was to implement this possibility into the binned bispectrum estimator code (see section 4.4.4 for a description of the code). The first basic test to check this is to apply the template to the map it comes from. The expected answer for the amplitude parameter of this specific shape is then obviously $f_{\rm NL} = 1$. Moreover, if we perform a correlated analysis with other shapes like the primordial ones, their own $f_{\rm NL}$ has to be negligible. Indeed, that is what we observe (see table 61) and we can now discuss more interesting tests based on CMB maps. It is important to recall that the galactic foregrounds are highly anisotropic while the shapes introduced in section 4.2 have an isotropic origin (primordial, lensing-ISW or extra-galactic foregrounds). These galactic numerical templates also contain mask and noise effects, but we will show that it is not an issue. For this, we ran a series of tests with the simple idea of artificially adding dust to the maps containing CMB realizations (simulations, but also the observed data) to check that we indeed detect the right amount of dust and that it has no impact on the other shapes.

Then, we will focus on the second aim which is to analyze the CMB map from the 2015 Planck data. We will apply the numerical templates to the cleaned SMICA CMB map [8], both at low and high resolutions, for which we expect not to detect any galactic foregrounds. Finally we will perform a similar analysis on raw sky observations at 143 GHz.

	Local	Equilateral	Orthogonal	P.S./10^{-29}	CIB/10^{-27}	Dust
Indep	-5.3	16.5	15.4	1.76	1.32	1.0
Joint	-7×10^{-11}	2×10^{-10}	-2×10^{-11}	-1×10^{-13}	7×10^{-14}	1

Table 61: Determination of $f_{\rm NL}$ for the local, equilateral, orthogonal, point sources, CIB and dust shapes using the dust map studied in section 5.1. The only error bars at our disposal are Fisher forecasts; they are not indicated because for every case given here, they are several (at least three) orders of magnitude smaller than the determined values for $f_{\rm NL}$ in the independent case, which makes them many orders of magnitude larger than the non-dust values in the joint analysis.

6.1 Gaussian simulations

For the first tests, we constructed a set of 100 Gaussian simulations of the CMB obtained using the best fit of the CMB power spectrum from the 2015 Planck release [17] (see figure 32) at the resolution $n_{\text{side}} = 2048$. There are several reasons to use these simulations instead of the observed CMB map. First, it is important to check the validity of this new use of the binned bispectrum estimator with a large number of maps. Moreover, even the cleaned CMB map still contains contamination from extra-galactic foregrounds and the ISW-lensing. Here, these effects are not present. However, we need the Gaussian realizations of the CMB to have the characteristics of the SMICA CMB map. Hence, we smoothed the maps using a 5 arcmin FWHM Gaussian beam and we added noise based on the noise power spectrum of the SMICA CMB map (moreover, our choice of bins is optimal only if this noise is present in the maps, because it diminishes the weights of the bins at high ℓ following (4.50)). In this section, we will discuss two different cases for the noise. First, we will assume it has an isotropic distribution in pixel space. In the second case we will make it anisotropic by modulating it in pixel space using the hit-count map corresponding to the scanning pattern of the Planck satellite. Finally, we add some dust to these maps using the dust map at 143 GHz discussed in section 5.1. Every analysis presented in this chapter uses the common mask introduced in the previous chapter, see figure 511.

The determination of the amplitude parameters is performed using the binned bispectrum estimator, including a linear correction term to the bispectrum as discussed in section 4.4.2. In practice, the linear correction term is computed using Gaussian simulations of the analyzed maps with the same characteristics (beam, noise, mask). We use the average power spectrum of our 100 maps (CMB + dust) to generate the maps necessary for the computation of the linear correction. Here we use 80 maps for the linear correction. We have verified that this number is sufficient to detect squeezed bispectra like the local and the dust shapes to high precision. However, to measure the equilateral shape (which has no reason to be detected here) with a high precision, it would require more maps. The first analysis is performed with the same choice of 57 bins as in the 2015 Planck analysis [14] which was shown to be optimal to determine the primordial shapes, using multipoles from $\ell_{\text{min}} = 2$ to $\ell_{\text{max}} = 2500$ (remember that our analysis is temperature only). We add one times the dust map to the simulations of the CMB, thus the expected value of the f_{NL} for the dust template is 1. We also determine the amplitude parameters f_{NL} for the primordial shapes, the point sources and CIB bispectra in both the independent and the joint case.

Results are given in table 62. First, we see that we detect the expected amount of dust with a good accuracy. We also observe that the shapes correlated to the dust template (see table 51), because they also peak in the squeezed configuration, are strongly detected in the independent case. However, in the joint analysis all the non-Gaussianity of the maps is attributed to the dust, with only a small impact on the error bars of the primordial shapes, meaning that this test is successful. However, this choice of bins is only optimized to detect the primordial bispectra and not the dust. Then, it is important to verify if the results can be improved by adding a few bins at very low ℓ (below 30) to better measure the dust contribution. This can be seen in appendix A where we observe that only the very low ℓ_1 are important for the template (it is more squeezed than the local shape). Figure 61 can also be used to highlight this effect. It shows the convergence of f_{NL} when using a smaller multipole interval to determine f_{NL}. In the two top plots, we can see that if we exclude the very low ℓ (below 30) both the local and orthogonal f_{NL} are consistent with 0. If we exclude the region of multipole space where the dust template is the strongest, there is no detection of the primordial shapes, even in an independent analysis. The two bottom plots are interesting as they show that the determination of f_{NL} for the dust template is very stable when increasing ℓ_{min} or decreasing ℓ_{max}. Note however that

	Local	Equilateral	Orthogonal	P.S./10^{-29}	CIB/10^{-27}	Dust
Dust 100%, 57 bins (expected $f_{\rm NL}^{\rm dust} = 1$)						
Indep	-86 ± 14	27 ± 67	103 ± 38	1.4 ± 0.9	1.1 ± 0.5	1.03 ± 0.20
Joint	-6 ± 14	16 ± 77	-10 ± 45	0.1 ± 2.6	0.0 ± 1.5	1.00 ± 0.24
Dust 100%, 70 bins (expected $f_{\rm NL}^{\rm dust} = 1$)						
Indep	-67 ± 11	20 ± 68	92 ± 34	1.4 ± 1.0	1.0 ± 0.5	1.00 ± 0.20
Joint	0 ± 14	-5 ± 75	-1 ± 39	0.0 ± 2.6	0.0 ± 1.4	1.01 ± 0.24
Dust 75%, 70 bins (expected $f_{\rm NL}^{\rm dust} = 0.42$)						
Indep	-30 ± 8	11 ± 66	41 ± 36	0.6 ± 0.9	0.4 ± 0.5	0.42 ± 0.12
Joint	0 ± 9	1 ± 70	-2 ± 42	0.0 ± 2.6	0.0 ± 1.4	0.42 ± 0.13
Dust 0%, 70 bins (expected $f_{\rm NL}^{\rm dust} = 0$)						
Indep	-0.1 ± 0.5	-1.7 ± 6.1	-3.1 ± 3.4	-0.03 ± 0.09	-0.01 ± 0.05	0.001 ± 0.003
Joint	-0.3 ± 0.7	-1.6 ± 6.4	-4.2 ± 4.1	-0.15 ± 0.26	0.06 ± 0.13	0.001 ± 0.003

Table 62: Determination of $f_{\rm NL}$ for the local, equilateral, orthogonal, point sources, CIB and dust shapes using a set of 100 Gaussian simulations of the CMB with isotropic noise to which we added a known amount of dust (the dust map of section 5.1 multiplied by a factor 1 or 0.75, or no dust at all). The analysis is performed using 57 bins or 70 bins and the error bars are given at 1σ. For the reason behind the much smaller error bars in the 0 % dust case, see the main text.

the error bars on $f_{\rm NL}^{\rm dust}$ increase a lot if we use $\ell_{\rm min} > 30$. This is visible with the dashed blue lines which correspond to the 68% confidence intervals.

There is another important effect in the dust template when a very large scale (small ℓ) is concerned: the sawtooth pattern in the dust power spectrum (see figure 52) is also expected in the dust bispectrum for the same reason (the only large harmonic coefficients describing the dust at low ℓ are the $a_{\ell 0}$ with ℓ even). In principle, it could be used to differentiate between the dust and the local shapes, but this effect is hidden if the bins are large because it is averaged over several ℓ's, thus providing another motivation to add some bins at low ℓ. One issue when adding bins is that the memory constraints on the computer system we use limit us to a number of bins between 50 and 60 at most at the Planck resolution when including the polarization too. Here we can use 70 bins, because we only look at the temperature data and because we only add bins for the largest scales, where it is possible to downgrade the resolution of the filtered maps. With this new binning, the correlation coefficient between the local and dust shapes becomes -0.48 (instead of -0.60 for 57 bins, see table 51). So indeed adding a few bins at low ℓ helps to differentiate these squeezed shapes. The results of the same test with 70 bins are also given in table 62. In the independent analysis, the amount of local non-Gaussianity and its error bar decreases which is consistent with the fact that the dust and the local templates are easier to differentiate with the new binning. However, in the joint analysis there is no clear difference, except that the different central values are now very close to the expected values.

We also have to note that the approximation of weak non-Gaussianity, which is needed for the validity of the linear correction of the bispectrum to take into account the effects of the mask here, starts to break down when we observe a local shape at more than 6σ (independent case). This is why it is important to verify how a similar analysis works with a smaller amount of dust in the map. Hence, with the same choice of 70 bins, we perform two other tests with the 100 CMB simulations. For one we multiply the dust map by a factor 0.75 before adding it to the CMB realizations and the expected value of $f_{\rm NL}$ is then $0.75^3 \approx 0.42$. For the other

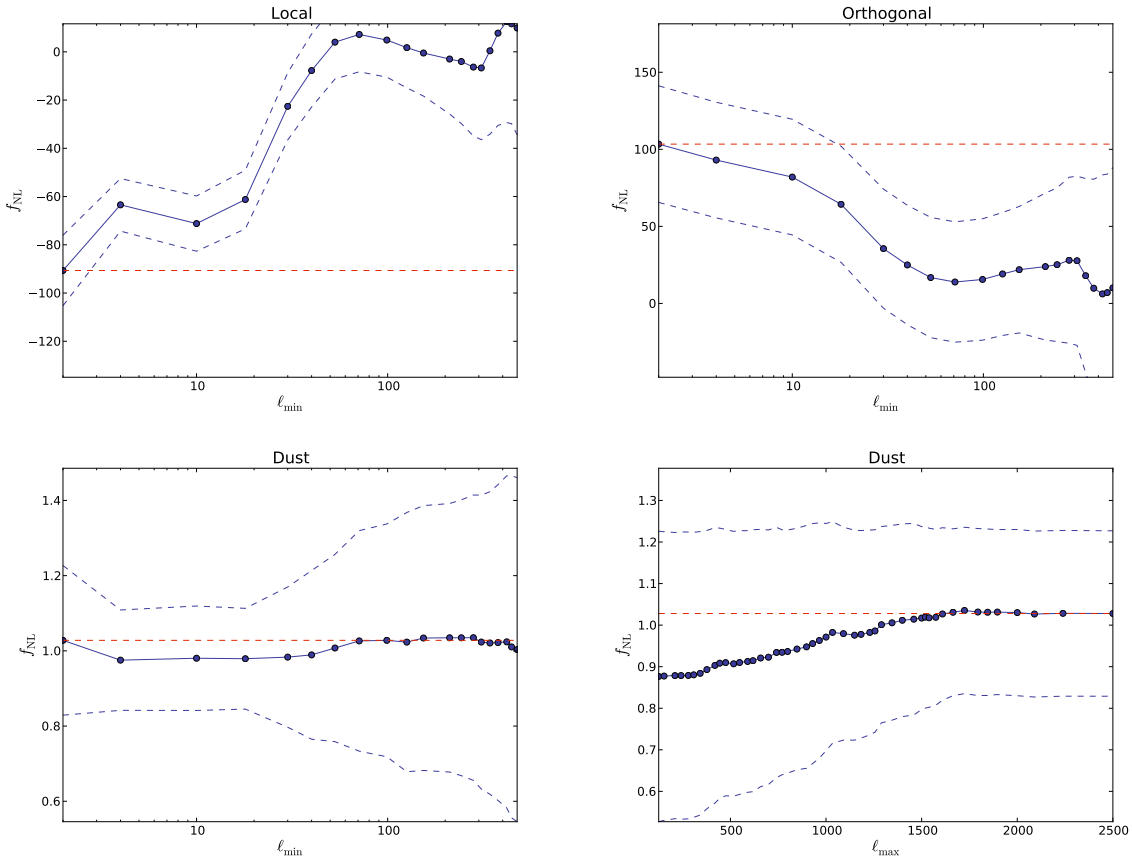

Figure 61: Convergence of f_{NL} in the independent analysis of the 100 Gaussian CMB simulations + dust map as a function of ℓ_{min} for the local (top left), orthogonal (top right) and dust (bottom left) shapes, and as a function of ℓ_{max} for the dust shape (bottom right). The blue dots correspond to the values determined by the binned bispectrum estimator when ℓ_{min} (or ℓ_{max} for the fourth plot) is inside the corresponding bin. The 68% confidence interval is given by the blue dashed lines. The horizontal red dashed line corresponds to the determined value of f_{NL} using the whole multipole interval (from 2 to 2500 with 57 bins).

test, we use the the Gaussian CMB maps without adding dust, to verify that we do not detect any bispectral shape. These results are also given in table 62 and are exactly as expected.

Note that the error bars for the case of the CMB only are roughly one order of magnitude smaller than for the rest. The reason is that we made a distinction between the standard deviation (square root of the variance) and the standard error (standard deviation divided by the square root of the number of maps, so divided by 10 here). The standard error gives the expected error on the determination of the mean value of f_{NL} with our sample of 100 Gaussian maps. The standard deviation gives the 1σ interval in which we would detect f_{NL} if we study one map. It is clear that the standard error has to be used in the CMB-only analyses because we determine the mean value of each f_{NL} from a sample of 100 maps. However, when we add dust to these maps, the situation is different because we only have one realization of the dust so the standard error cannot be used. We are however very conservative by using the standard deviation, the real error bars on the mean values of the different f_{NL} are probably between the standard error and the standard deviation (the more dust in the map, the closer to the standard deviation it will be). However, the fact that for the two amounts of dust with 70 bins the central values in the joint analysis are so close to the expected values is an indication that

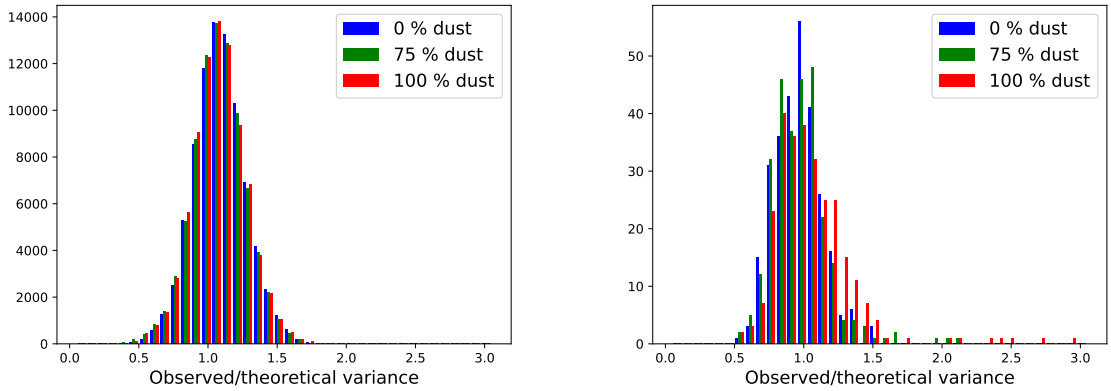

Figure 62: Distribution of the ratio of the observed variance over the theoretical prediction for the three different amounts of dust (0 % in blue, 75 % in green and 100 % in red). On the left, all the valid ℓ-triplets are included while on the right only very squeezed ℓ-triplets are shown (one small multipole $\ell_1 \leq 13$ and two large ones $\ell_{2,3} \geq 742$).

the error bars are likely overestimated for these two cases (the results with dust would still be correct if we divided the standard deviation by 10 to obtain the standard error, which is not true with 57 bins).

We can illustrate the breakdown of the weak non-Gaussianity approximation using the variance of the bispectrum. Indeed, we have at our disposal a theoretical prediction for the variance, given in (4.50), that scales as the power spectrum cubed and for which the derivation relies on the weak non-Gaussianity approximation. However, we can also directly compute the variance of the bispectrum from our 100 maps, which we call here observed variance. Figure 62 shows the distribution of the ratio of the observed variance over the theoretical variance for the three different amounts of dust in two different configurations. First, we examine this ratio over the whole triplet space (on the left) where there is no difference between the three cases and the values are distributed around 1 as expected. That is logical because the non-Gaussianity of the dust is very localized in multipole space; the bispectrum is large only in the very squeezed configuration. This is why on the right we consider only the triplets where one ℓ is very small (in the first five bins i.e. $\ell \leq 13$) and the two others large (in the last 30 bins, i.e. $\ell \geq 742$). Adding or removing a few bin triplets here does not change the results. Here we can see that if there is more dust (in red), there are several values which strongly deviate from one. This effect is even more obvious when we examine the mean and the standard deviation of these distributions, which are given in table 63. When considering the full space of multipole triplets, there is no significant difference between the three cases. However, when we examine only the squeezed part of the bispectrum, the standard deviation increases slightly with a small amount of dust (75 %), and is three times larger for 100 % dust compared to the CMB-only case. Hence, the weak non-Gaussianity approximation stops being valid, but not enough to invalidate the results (only a few bin-triplets deviate strongly). However, if we were to add even more dust, we would have to take this effect into account.

In addition to looking at the variance of the bispectrum itself, we can also investigate the variance of the $f_{\rm NL}$ parameters with regard to the validity of the weak non-Gaussianity approximation. Every error bar given in table 62 was computed from the observed variance of the set of 100 maps. However, we can also compute Fisher error bars from the theoretical prediction of the variance and they are given in table 64 for the three cases studied in this section for the local and dust shapes. We can see that for both, the more non-Gaussian the

	0 % dust		75 % dust		100 % dust	
	Full	Squeezed	Full	Squeezed	Full	Squeezed
Mean	1.09	0.97	1.08	0.97	1.08	1.11
Standard deviation	0.19	0.16	0.19	0.21	0.20	0.51

Table 63: Means and standard deviations of the distributions of the ratio of the observed variance over the theoretical prediction, shown in figure 62, for the three amounts of dust, including the full bispectrum or only a very squeezed part of it.

	100 % dust	75 % dust	0 % dust
Local			
Fisher	6.6	6.4	5.6
Observed	14	7.7	5.2
Dust			
Fisher	0.05	0.04	0.031
Observed	0.20	0.12	0.030

Table 64: Fisher and observed standard deviations on $f_{\rm NL}^{\rm local}$ and $f_{\rm NL}^{\rm dust}$ (independent analysis) determined from 100 Gaussian simulations of the CMB with isotropic noise to which we added a known amount of dust (100 %, 75 % or 0 % of the dust map of figure 51) using 70 bins.

map is, the more important is the difference between Fisher and observed error bars. This is related to the breakdown of the weak non-Gaussianity approximation. For a local $|f_{\rm NL}|$ of around 70 (corresponding to 100 % dust), the difference is a factor 2 between the two kinds of error bars. The difference is larger for the dust template, where for this case the observed error bars are four times larger than the Fisher forecasts. For both templates, when there is no dust (so purely Gaussian maps), the observed error bars agree with the Fisher forecasts up to the expected precision (the relative error in the standard deviation is $1/\sqrt{2(N-1)}$, which is 7 % for 100 maps).

As explained before, adding noise realizations with the correct power spectrum to the CMB simulations is necessary for the optimization of the binning and to make the simulations more realistic. However, the real instrument noise does not have an isotropic distribution in pixel space because some parts of the sky are observed more often than others, as shown in figure 63. Without a linear correction, the anisotropic noise also gives a large squeezed contribution to the bispectrum for the usual reason: small-scale fluctuations are larger (more noise) in the large-scale regions which are less observed and vice versa. This is why we also verify the previous results with an anisotropic distribution of the noise following the scanning pattern of the Planck satellite. The results are given in table 65. Here we use only the best choice of bins (70 bins) and the results are given for the same three amounts of dust as in table 62. Results are very similar with isotropic and with anisotropic noise for the three cases; each time

With these different tests, we have proven that the binned bispectrum estimator can be used to detect a galactic foreground shape that we determined numerically. It works well with the amount of dust that is expected at 143 GHz, the dominant frequency channel in the cleaned CMB map. So the next logical step is to use the template on real data.

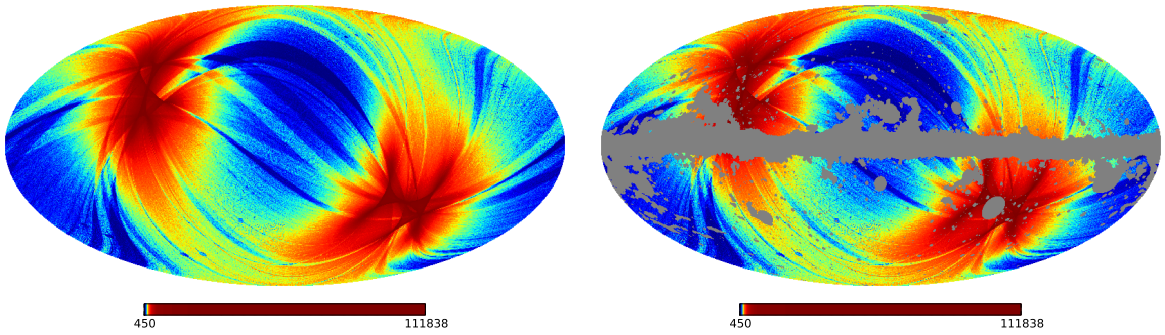

Figure 63: Unmasked (left) and masked (right) hit-count map of Planck (number of observation samples per pixel).

	Local	Equilateral	Orthogonal	P.S./10^{-29}	CIB/10^{-27}	Dust
Dust 100% (expected $f_{\rm NL}^{\rm dust} = 1$)						
Indep	-67 ± 11	24 ± 65	93 ± 34	1.5 ± 1.1	1.1 ± 0.5	1.00 ± 0.20
Joint	-1 ± 14	4 ± 73	-4 ± 40	0.2 ± 2.8	0.0 ± 1.4	1.00 ± 0.24
Dust 75% (expected $f_{\rm NL}^{\rm dust} = 0.42$)						
Indep	-30 ± 7	4 ± 62	44 ± 33	0.5 ± 1.1	0.4 ± 0.5	0.42 ± 0.12
Joint	0 ± 10	-5 ± 69	1 ± 38	-0.1 ± 2.8	0.0 ± 1.4	0.42 ± 0.14
Dust 0% (expected $f_{\rm NL}^{\rm dust} = 0$)						
Indep	-0.15 ± 0.50	0.3 ± 6.6	-1.4 ± 3.8	-0.08 ± 0.10	-0.05 ± 0.05	0.000 ± 0.003
Joint	-0.30 ± 0.64	1.2 ± 6.8	-2.2 ± 4.3	0.08 ± 0.23	-0.08 ± 0.11	0.000 ± 0.004

Table 65: Determination of $f_{\rm NL}$ for the local, equilateral, orthogonal, point sources, CIB and dust shapes using a set of 100 Gaussian simulations of the CMB with anisotropic noise to which we added a known amount of dust (the dust map of section 5.1 multiplied by a factor 1 or 0.75, or no dust at all). The analysis is performed using 70 bins and the error bars are given at 1σ.

6.2 CMB analyses

The previous tests have shown that detecting the dust is possible when there is a large amount of it. We can now apply the dust template to a real CMB analysis. Here, we follow the analysis of the Planck 2015 paper [14] (note that we only study the temperature bispectrum, while for Planck the polarization was also taken into account). We use a set of 160 simulation maps for the computation of the error bars and the linear correction. The power spectrum is the best fit cosmological model from the 2015 Planck analysis represented in figure 32. This time, we also include the ISW-lensing shape in the analysis because it is present in the data. As discussed in section 4.2, the amplitude of this template is known, so it can be used to subtract the bias (see equation (4.60)) from the bispectral non-Gaussianity of the map. Results are given in table 66.[1] We include the results with and without taking into account the ISW-lensing bias, and we perform two different joint analyses for comparison, with and without the dust. As expected, there is no detection of the primordial shapes or the dust. However, it is important to note that

[1] The difference between the values in this table and those in the Planck paper [14], in particular for equilateral, is mainly due to our use here of a slightly different mask (the preferred temperature mask from [8] instead of the slightly extended mask used in [14]).

	Local	Equilateral	Orthogonal	P.S./10^{-29}	CIB/10^{-27}	Dust/10^{-2}	Lensing-ISW
No ISW-lensing bias subtraction							
Indep	8.7 ± 5.5	8 ± 67	-34 ± 33	9.6 ± 1.0	4.6 ± 0.5	-0.8 ± 3.8	0.59 ± 0.29
Joint	6 ± 8	-21 ± 69	-3 ± 38	7.3 ± 2.7	1.2 ± 1.4	-2.2 ± 5.2	0.57 ± 0.31
Joint \ *dust*	4.2 ± 6.7	-15 ± 68	-6.6 ± 37	7.2 ± 2.7	1.3 ± 1.4		0.55 ± 0.31
ISW-lensing bias subtracted							
Indep	1.2 ± 5.5	6 ± 67	-8 ± 33	9.6 ± 1.0	4.6 ± 0.5	-4.0 ± 3.8	
Joint	-5 ± 8	-16 ± 69	1 ± 38	7.1 ± 2.7	1.3 ± 1.4	-3.5 ± 5.1	
Joint \ *dust*	1.0 ± 6.3	-7 ± 68	-5 ± 37	7.0 ± 2.7	1.4 ± 1.4		

Table 66: Determination of $f_{\rm NL}$ for the local, equilateral, orthogonal, point sources, CIB, dust and ISW-lensing shapes in the cleaned SMICA CMB map from the 2015 Planck release. In the three first lines, the ISW-lensing shape is considered as the others. In the last three, the ISW-lensing bias is subtracted. The joint analysis is performed with and without the dust template. The binning consists of 57 bins.

	Local	Equilateral	Orthogonal	Dust	Free-free	Synch/10^5	AME/10^{10}
Indep	13 ± 30	49 ± 155	66 ± 130	-0.01 ± 0.07	-1 ± 32	-0.1 ± 4.4	-10 ± 7
Joint	17 ± 51	281 ± 406	50 ± 287	-0.01 ± 0.10	22 ± 43	2 ± 6	-12 ± 8

Table 67: Determination of $f_{\rm NL}$ of some primordial and all galactic templates in the cleaned SMICA CMB map at low resolution $n_{\rm side} = 256$ with a 60 arcmin FWHM Gaussian beam from the 2015 Planck release. Because of the low $\ell_{\rm max} = 300$, the analysis is performed using 39 bins.

the error bars of the local and dust shapes in the joint analysis increase because these shapes are correlated. Similarly to the previous section, one way to improve the situation would be to find a binning that is optimal for both shapes.

We also performed a similar analysis on a low resolution cleaned CMB map ($n_{\rm side} = 256$) with a 60 arcmin FWHM Gaussian beam to look for the other foreground templates with the usual choice of bins. Results are given in table 67. Because of the resolution and the beam, we only analyze multipoles in the interval $[2, 300]$, which is the reason for the very large error bars. As that would leave only few bins from the original binning, we split all the bins below $\ell = 300$ into three (where possible, two otherwise), which gives 39 bins in total. Moreover, we did not subtract the ISW-lensing bias as its contribution is small compared to the error bars. The point sources and the CIB are not given in the table because they were not observed here. The results are consistent with zero non-Gaussianity in the map. But the new foreground shapes (AME, free-free and synchrotron) have very large error bars and even if they were present in the map, it would not be possible to detect them.

6.3 Raw sky

After applying the foreground templates to the cleaned CMB map that is not supposed to contain any galactic foreground (which we confirmed), it is also interesting to study the raw 143 GHz Planck map. Again, we had to generate Gaussian simulations of this map to compute the linear correction. For this, we used the power spectrum of the map and we determined the noise power spectrum using the half-mission maps. The power spectra are shown in figure 64.

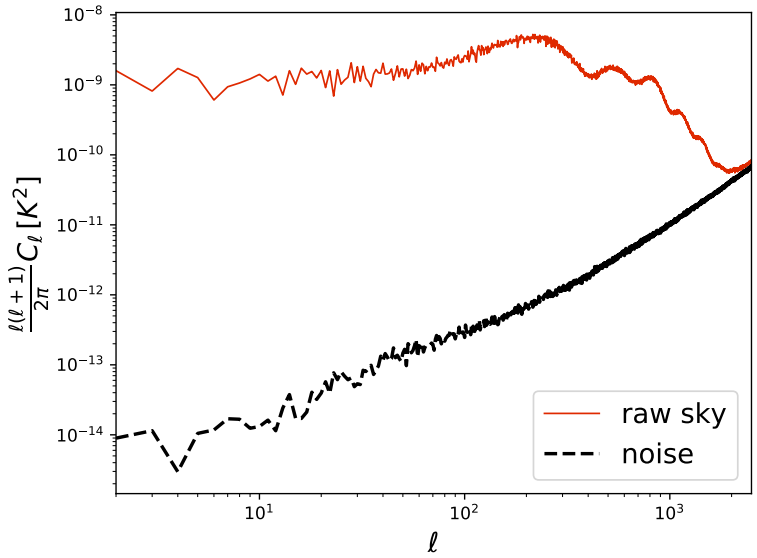

Figure 64: Power spectrum of the raw 143 Ghz map as well as the estimated noise power spectrum.

The noise is modulated in pixel space using the hit-count map of figure 63 to make it anisotropic. The beam of this map can be approximated by a 7.3 arcmin FWHM Gaussian beam.

Results are given in tables 68 and 69. We detected the expected amount of dust since $f_{\rm NL}^{\rm dust} = 1$ is within the 1σ error bars in both the independent and joint analyses. For the other foregrounds, the situation is similar to the previous section: the error bars are far too large for a detection (the synchrotron and AME shapes are not given here because the error bars are many orders of magnitude larger than the expected quantity in the map). To determine error bars, we did not have good simulations of the data map but we had of course Fisher forecasts. We made the simple but reasonable hypothesis that the factor between the real error bars and the Fisher ones due to the breakdown of the weak non-Gaussianity approximation is the same as for the anisotropic case in section 6.1. Then it was easy to determine error bars for the primordial and the dust shapes that are a bit larger than in table 65. However, for the CIB and the point sources, which are not the main object of study here, the situation is different because they were not present in the Gaussian simulations, so we could not apply this method. Hence we only give Fisher error bars for those two shapes, but because of the strong detection we know that they are underestimated. This is not an issue because they are uncorrelated to the local and the dust shapes. For the low-resolution case in table 69 we only have Fisher error bars for all shapes. In conclusion, the method also works correctly when applied to a raw sky map.

Here, we have proven that we have successfully implemented the possibility to use numerical bispectral templates of the galactic foregrounds with the method of the binned bispectrum estimator using Gaussian simulations of the CMB containing a known amount of dust. Then we have verified the consistency of the results with observational data of the 2015 Planck release, both a cleaned CMB map where we observe no dust and the raw sky map where we detect the full template of the dust.

	Local	Equilateral	Orthogonal	P.S./10^{-29}	CIB/10^{-27}	Dust
Indep	-61 ± 13	22 ± 71	-12 ± 39	90 ± 4	28 ± 1	1.09 ± 0.25
Joint	13 ± 18	-37 ± 81	-81 ± 47	115 ± 9	-11 ± 3	1.08 ± 0.32

Table 68: Determination of $f_{\rm NL}$ in the raw 143 GHz map at high resolution $n_{\rm side} = 2048$ from the 2015 Planck release. The analysis is performed with the usual choice of 57 bins. For the details on the error bars for the primordial and the dust shapes, see the main text. The CIB and point sources error bars are Fisher forecasts.

	Local	Equilateral	Orthogonal	Dust	Free-free
Indep	-41 ± 54	232 ± 198	277 ± 177	0.88 ± 0.28	39 ± 50
Joint	-33 ± 94	543 ± 536	112 ± 388	0.85 ± 0.39	-9 ± 69

Table 69: Determination of $f_{\rm NL}$ in the raw 143 GHz map at low resolution $n_{\rm side} = 256$ from the 2015 Planck release. The analysis is performed with 39 bins. The error bars are all Fisher forecasts.

Part III

Non-Gaussianity in two-field inflation

Chapter 7

Definitions and set-up

The Planck satellite significantly improved the constraints on any potential deviation from a Gaussian distribution of primordial density perturbations generated during inflation (i.e. Non-Gaussianity) [11, 14]. Is is then important to better understand what regions of inflation model space have been ruled out. However, it is well-known that the bispectrum produced during a phase of standard single-field slow-roll inflation is unobservably small [6, 141]. This result does not hold in more general situations and many extensions of that simple case have been proposed with different predictions for non-Gaussianity, meaning that observations can in principle be used to constrain them.[1] For example, models with higher derivative operators based on the Dirac-Born-Infeld action [20, 176, 147, 148, 190] can produce large non-Gaussianity of the so-called equilateral type. Another possibility is to consider multiple fields during inflation, which adds isocurvature perturbations to the usual adiabatic perturbation. The isocurvature perturbations can interact with the adiabatic one on super-Hubble scales (while in single-field inflation the adiabatic perturbation is constant on super-Hubble scales) which can lead to so-called local non-Gaussianity. In this case non-Gaussianity can be generated long after inflation as in the curvaton scenario [140, 30, 113, 76, 46, 194, 98], or directly after inflation during (p)reheating [204, 138, 37, 28, 75, 106, 73]. However, in this thesis we will be interested in the case where this local non-Gaussianity is produced on super-Hubble scales during inflation. Since we will only talk about local non-Gaussianity in this part of the thesis, $f_{\rm NL}$ should always be understood as $f_{\rm NL}^{\rm local}$.

This chapter sets up the basic equations and definitions used in the rest of the thesis, which is based on our paper [108]. Most of this chapter summarizes results derived in previous papers, but several new useful relations are given in section 7.4 and the final section 7.6 contains an important new result.

7.1 Background dynamics

The models we will consider are two-field inflation models with standard kinetic terms and a potential $W(\phi,\sigma)$ in the framework of general relativity. Here $\phi(t,\boldsymbol{x})$ and $\sigma(t,\boldsymbol{x})$ denote the two fields, which we will often combine into the vector ϕ^A with $A=1$ for ϕ and $A=2$ for σ. Since we have standard kinetic terms (trivial field metric), there is no difference between upper and lower field indices. For the moment we keep W completely general, although in the later

[1] It has been pointed out [184, 153] that the finite size of the observable universe leads to gauge corrections, which have to be taken into account to convert the inflationary bispectrum to actual observations. Indeed in single-field inflation the squeezed limit of the bispectrum vanishes identically for a local observer today. In multiple-field inflation, on the other hand, these corrections are also of order $1-n_s$ [183] and hence are expected to be negligible in the case of large $f_{\rm NL}$.

chapters we will often have to assume some specific form of the potential in order to solve the equations. The matter Lagrangian takes the form

$$\mathcal{L}_m = \sqrt{-g}\left(-\frac{1}{2}g^{\mu\nu}\partial_\mu\phi_A\partial_\nu\phi^A - W(\phi^A)\right). \tag{7.1}$$

As time coordinate t we will use the number of e-folds $t \equiv \ln a$, where $a(t)$ is the scale factor of the universe, and we denote derivatives with respect to this time coordinate by overdots. The Hubble parameter of the universe is denoted by $H(t)$. Unlike in the case of cosmic time, where the expansion information of the universe is encoded in a and H is directly derived from it, when using the number of e-folds as time coordinate, a is a trivial function, and the expansion information is encoded in H, which can in this case not be derived from a.

In terms of the number of e-folds the background field equation for ϕ^A and the Friedmann equations for H take the following form:

$$\ddot{\phi}^A + (3-\epsilon)\dot{\phi}^A + \frac{W_A}{H^2} = 0, \qquad H^2 = \frac{\kappa^2 W}{3-\epsilon}, \qquad \frac{\dot{H}}{H} = -\frac{\kappa^2}{2}\left(\dot{\phi}^2 + \dot{\sigma}^2\right). \tag{7.2}$$

Here $\kappa^2 \equiv 8\pi G$ and the index on W denotes a derivative with respect to the fields: we define $W_{A_1\ldots A_n} \equiv \partial^n W/(\partial\phi^{A_1}\cdots\partial\phi^{A_n})$. The quantity ϵ is a short-hand notation of which the physical interpretation will be discussed in the next section. It is defined as

$$\epsilon \equiv -\frac{\dot{H}}{H} = \frac{\kappa^2}{2}\left(\dot{\phi}^2 + \dot{\sigma}^2\right) \tag{7.3}$$

(where the second equality follows from the Friedmann equation for $\dot{H}$).

As we have a two-dimensional field space, we need a basis, and as usual we will define the basis vectors with respect to the field trajectory [93, 94, 91]:

$$e_1^A = (e_{1\phi}, e_{1\sigma}), \qquad e_2^A = (e_{1\sigma}, -e_{1\phi}), \qquad e_{1\phi} = \frac{\dot{\phi}}{\sqrt{\dot{\phi}^2+\dot{\sigma}^2}}, \qquad e_{1\sigma} = \frac{\dot{\sigma}}{\sqrt{\dot{\phi}^2+\dot{\sigma}^2}}. \tag{7.4}$$

So the first basis vector is always along the field trajectory as it is defined as the direction of the field velocity. The second basis vector is perpendicular to the first, and since we have only two dimensions it can be completely expressed in terms of the components of the first basis vector (see appendix A of [191] for some refinements of this basis originally introduced in [93]).

For later use we will define the following quantities:

$$\tilde{W}_{A_1\ldots A_n} = \left(\frac{\sqrt{2\epsilon}}{\kappa}\right)^{n-2}\frac{W_{A_1\ldots A_n}}{3H^2}, \qquad \tilde{W}_{m_1\ldots m_n} = \tilde{W}_{A_1\ldots A_n}e_{m_1}^{A_1}\cdots e_{m_n}^{A_n}, \tag{7.5}$$

where the m indices denote the components of the basis and the Einstein summation convention is implied. In order to distinguish explicit components of these two different quantities, indices 1 and 2 will indicate components in the basis (7.4) (e.g. $\tilde{W}_{21}$), while indices ϕ and σ will be used to indicate components in terms of the original fields (e.g. $\tilde{W}_{\sigma\sigma}$).

7.2 Slow-roll parameters

Similarly to section 2.3.3, we introduce a set of slow-roll parameters. It is important to keep in mind that the introduction of these parameters is not yet an approximation: the equations are still completely exact and the slow-roll parameters can be considered as just a short-hand

notation. It only becomes an approximation (the slow-roll approximation) if we then say that some of these parameters are small and start neglecting certain terms. We will do that in certain later sections, but not here.

The first slow-roll parameter is ϵ defined in (7.3). It will be small if the kinetic energy of the fields is small compared to their potential energy. The other slow-roll parameters are vectors in field space and can be defined as follows with $n \geq 2$ [94, 191]:

$$\eta^{(n)A} \equiv \frac{1}{H^n\sqrt{\dot\phi^2+\dot\sigma^2}}\left(H\frac{\mathrm{d}}{\mathrm{d}t}\right)^{n-1}\left(H\dot\phi^A\right). \tag{7.6}$$

As usual the most important ones are for $n=2$ (simply called η^A) and $n=3$ (called ξ^A). For example, for η^A the expression above becomes

$$\eta^A = \frac{1}{\sqrt{\dot\phi^2+\dot\sigma^2}}\left(\ddot\phi^A - \epsilon\dot\phi^A\right). \tag{7.7}$$

We will usually consider the parallel and perpendicular components of these as defined in the basis (7.4):

$$\eta^\parallel \equiv \eta^A e_{1A}, \qquad \eta^\perp \equiv \eta^A e_{2A}, \qquad \xi^\parallel \equiv \xi^A e_{1A}, \qquad \xi^\perp \equiv \xi^A e_{2A}. \tag{7.8}$$

The parameters $\eta^\parallel$ and $\eta^\perp$ will be small if the components of the field acceleration parallel and perpendicular to the field velocity, respectively, are small compared to the field velocity.[2] The parameter $\eta^\perp$ is quite fundamental to anything concerning multiple-field inflation: as long as it is negligible we are in an effectively single-field situation, but as soon as it becomes significant we have true multiple-field effects. This will be illustrated quite clearly by the results of this thesis. The parameters ϵ and $\eta^\parallel$ are the direct generalizations of the ϵ and η introduced in section 2.3.3 and describe effectively single-field effects.

In the context of the slow-roll approximation, $\epsilon, \eta^\parallel, \eta^\perp$ are called first-order slow-roll parameters, while $\xi^\parallel, \xi^\perp$ are second-order slow-roll parameters. Now one might wonder about the fact that we call $\eta^\perp$ a slow-roll parameter, given that the actual slow-roll approximation (in the spirit of a field slowly rolling along its trajectory) would only require ϵ, $\eta^\parallel$ and higher-order parallel slow-roll parameters to be small, and say nothing about the perpendicular parameters. However, in order to be able to derive the analytical expressions in chapter 8, where we treat the slow-roll regime, we need to assume a stronger version of the standard slow-roll approximation where all parameters, including $\eta^\perp$ and even χ (defined in (7.11)) are small. And as we will later see, in the models considered in this thesis it is anyway not possible to have a large $\eta^\perp$ while $\eta^\parallel$ stays small. Hence we will call all these parameters slow-roll parameters, and assume all of them to be small in the slow-roll approximation (sometimes adding the word "strong" to be explicit). On the other hand, when talking about breaking the slow-roll regime in chapter 9, we consider situations where ϵ or $\eta^\parallel$ becomes large during inflation (in addition to $\eta^\perp$), which breaks slow roll according to anyone's definition. In the current section, however, we are not assuming anything to be small and not making any approximations.

From their definition and using the field equation (7.2) and its derivative, one can show that

$$\eta^\parallel = -3 - 3\tilde W_1, \qquad \eta^\perp = -3\tilde W_2, \tag{7.9}$$

$$\xi^\parallel = -3\tilde W_{11} + 3\epsilon - 3\eta^\parallel, \qquad \xi^\perp = -3\tilde W_{21} - 3\eta^\perp. \tag{7.10}$$

[2] This remark is exact when acceleration in terms of cosmic time is considered. When using the number of e-folds as time coordinate, as we do here, there is a correction term as seen in (7.7). However, that correction disappears for $\eta^\perp$.

We also introduce the parameter

$$\chi \equiv \tilde{W}_{22} + \epsilon + \eta^{\parallel}. \tag{7.11}$$

Despite its similarity to the expressions for $\xi^{\parallel}$ and $\xi^{\perp}$, the parameter χ is a first-order slow-roll parameter and not a second-order one. The reason is that within the slow-roll approximation cancellations occur in the right-hand sides of (7.9), making the slow-roll parameters on the left-hand side one order smaller than the individual terms on the right-hand side. However, no such cancellation occurs in (7.11).

We can compute the time derivatives of the basis vectors and the slow-roll parameters and find:

$$\begin{aligned}
&\dot{e}_{1\phi} = \eta^{\perp} e_{1\sigma}, \qquad \dot{e}_{1\sigma} = -\eta^{\perp} e_{1\phi}, \qquad \dot{\epsilon} = 2\epsilon(\epsilon + \eta^{\parallel}),\\
&\dot{\eta}^{\parallel} = \xi^{\parallel} + (\eta^{\perp})^2 + (\epsilon - \eta^{\parallel})\eta^{\parallel}, \qquad \dot{\eta}^{\perp} = \xi^{\perp} + (\epsilon - 2\eta^{\parallel})\eta^{\perp},\\
&\dot{\chi} = \epsilon\eta^{\parallel} + 2\epsilon\chi - (\eta^{\parallel})^2 + 3(\eta^{\perp})^2 + \xi^{\parallel} + \frac{2}{3}\eta^{\perp}\xi^{\perp} + \tilde{W}_{221},\\
&\dot{\xi}^{\parallel} = -3\tilde{W}_{111} + 2\eta^{\perp}\xi^{\perp} + (2\epsilon - 3)\xi^{\parallel} + 9\epsilon\eta^{\parallel} + 3(\eta^{\parallel})^2 + 3(\eta^{\perp})^2,\\
&\dot{\xi}^{\perp} = -3\tilde{W}_{211} - \eta^{\perp}\xi^{\parallel} + (2\epsilon - 3)\xi^{\perp} + 9\epsilon\eta^{\perp} + 6\eta^{\parallel}\eta^{\perp} - 3\eta^{\perp}\chi.
\end{aligned} \tag{7.12}$$

7.3 Perturbations

We are in this thesis interested in predictions of non-Gaussianity from two-field inflation and this requires going further than in section 3.3. Concerning non-Gaussianity, we need to consider not only first-order but also second-order perturbations on top of the homogeneous background. Moreover, the presence of two scalar fields implies that there are now two scalar perturbation degrees of freedom. In addition to the adiabatic curvature mode ζ (denoted ζ_1 in the following) that describes the fluctuations of the total energy density (depends on gauge), there is also an isocurvature mode ζ_2 that corresponds to the relative fluctuations between the components. For their computation we will use the long-wavelength formalism developed in [163, 162, 164, 191, 192, 189], for which we will now recall the main steps.[3] To be more precise, in this section we review the set-up and define the main variable ζ_m^i to compute. We then write its evolution equation and we discuss the different terms of this equation perturbed at first and second-order. In the next section, we will introduce the method to solve it using Green's functions, which will in fact be the main quantities we discuss in this thesis. Finally, in another section we will use these Green's functions to compute the observable parameters discussed throughout the thesis. To lighten the content of these sections, several second-order quantities will be given explicitly only in appendix B, while their first-order equivalent will be discussed here.

As its name indicates, the long-wavelength formalism is used to study the perturbations on super-horizon scales. On those scales spatial gradients are typically much smaller than time derivatives[4], meaning that second-order spatial gradient terms will be ignored (like the one in (3.30)). One additional assumption is required, the slow-roll approximation has to be valid at the time of horizon-crossing (which is in agreement with observations) for at least a few e-folds, but can be broken at later times as will be discussed.

The long-wavelength metric has the simple form

$$\mathrm{d}s^2 = -N^2(t, \boldsymbol{x})\mathrm{d}t^2 + a^2(t, \boldsymbol{x})\mathrm{d}\boldsymbol{x}^2. \tag{7.13}$$

[3] The δN formalism is a popular alternative [181, 170, 139] to the long-wavelength formalism.

[4] It is an expansion in terms of the small parameter $\mathcal{O}(1/(HL))$ where L is the length scale of the perturbation (so $L \gg 1/H$).

But as we specified in the previous section, we have chosen the number of e-folds as the time coordinate, meaning that we work in the flat gauge $NH = 1$ (where $H = \partial_t \ln a/N$) in this part of the thesis.

A consistent definition of gauge-invariant perturbations has been worked out in [142, 161, 119] and corresponds to a generalization of the ζ variable of section 3.3. But in the context of the long-wavelength formalism, it is better to work with a related gradient quantity [163]. In this thesis, the key variable for the perturbations is

$$\zeta_i^m = \delta_{m1}\partial_i \ln a - \frac{\kappa}{\sqrt{2\epsilon}} e_{mA}\partial_i \phi^A, \tag{7.14}$$

where the subscript m corresponds either to the adiabatic mode $m = 1$ or the isocurvature mode $m = 2$. Taken at first-order and in the case of single-field inflation, it is simply the spatial gradient of ζ defined in (3.29). It is important to note that this quantity is not gauge-invariant at second order. Moreover, in the uniform energy gauge (which we are not using for the moment), it can be related easily to the proper gauge-invariant quantity, which is needed to compute observables. This will be an important step of the computation, after solving the evolution equation of this ζ_i^m in the flat gauge, which can be written in matrix form [164]

$$\dot{v}_{ia}(t, \boldsymbol{x}) + A_{ab}(t, \boldsymbol{x}) v_{ib}(t, \boldsymbol{x}) = 0, \tag{7.15}$$

where $v_{ia} \equiv (\zeta_i^1, \zeta_i^2, \dot{\zeta}_i^2)$ (so a, b can be 1, 2, 3). The matrix $\mathbf{A}$ is given by

$$\begin{pmatrix} 0 & -2\eta^\perp & 0 \\ 0 & 0 & -1 \\ 0 & 3\chi + 2\epsilon^2 + 4\epsilon\eta^\parallel + 4(\eta^\perp)^2 + \xi^\perp & 3 + \epsilon + 2\eta^\parallel \end{pmatrix}. \tag{7.16}$$

There is one simple equation not included in this system, which illustrates one of the most important differences between multiple-field and single-field inflation: the curvature perturbation ζ_1 is not necessarily frozen on super-horizon scales, but can evolve under the influence of the isocurvature mode ζ_2. In fact this is described by the very simple but exact equation (that is why we do not need to include $\dot{\zeta}_i^1$ in the previous system)

$$\dot{\zeta}_i^1 = 2\eta^\perp \zeta_i^2. \tag{7.17}$$

See [193] for the proof that it is valid at all orders on super-horizon scales. If we have both a non-zero $\eta^\perp$ and a non-zero isocurvature mode, then the adiabatic perturbation will still evolve on super-horizon scales, and not be fully determined at horizon-crossing.

Perturbing (7.15), we find the following equations at first and second-order

$$\begin{aligned} \dot{v}_{ia}^{(1)} + A_{ab}^{(0)}(t) v_{ib}^{(1)} &= b_{ia}^{(1)(t,\boldsymbol{x})}, \\ \dot{v}_{ia}^{(2)} + A_{ab}^{(0)}(t) v_{ib}^{(2)} &= -A_{ab}^{(1)}(t, \boldsymbol{x}) v_{ib}^{(1)} + b_{ia}^{(2)}(t, \boldsymbol{x}). \end{aligned} \tag{7.18}$$

Here $A_{ab}^{(0)}$ corresponds to the background version of the matrix $\boldsymbol{A}$, while $A_{ab}^{(1)}$ is obtained by perturbing it at first-order, so $A_{ab}^{(1)} = \bar{A}_{abc}^{(0)} v_c^{(1)}(t, \boldsymbol{x})$ with $v_c^{(1)}(t, \boldsymbol{x}) = \partial^{-2}\partial^i v_{ic}^{(1)}$. We also added the source terms $b^{(1)}$ and $b^{(2)}$ to take into account sub-horizon effects in our super-horizon equations.

In section 3.3, the continuous generation of perturbations at small scales was seen as an initial condition for the variable ζ. Here, we work with the long-wavelength variable v_{ab} which should be zero initially. Then the influx of perturbations crossing the horizon has to be incorporated. This is achieved using a source term following the perturbations from their generation

until a short time after they cross the horizon, when they become super-horizon and can be considered as stochastic classical variables. The source term $b^{(1)}$ can be written as

$$b_{ia}^{(1)} = \int \frac{\mathrm{d}^3\boldsymbol{k}}{(2\pi)^{3/2}} \dot{\mathcal{W}}(k) X_{am}^{(1)}(k) \hat{a}_m^\dagger(\boldsymbol{k}) i k_i e^{i\boldsymbol{k}.\boldsymbol{x}} + c.c.. \tag{7.19}$$

where we used the linear mode function solutions $X^{(am)}(k)$ (more about them later) and $\mathcal{W}(k)$ is a window function separating short and long wavelengths. As in section 3.3, $\hat{a}_m$ and $\hat{a}_m^\dagger$ are the quantum annihilation and creation operators satisfying the usual commutation relations.

The second-order source term $b^{(2)}$ is given explicitly in appendix B. Its contribution to non-Gaussianity is small but can be computed and will be included.

7.4 Green's functions

To solve the first-order perturbation equations, we introduce several Green's functions [164, 162]. They satisfy the following differential equations:

$$\begin{aligned}
\frac{\mathrm{d}}{\mathrm{d}t} G_{1y}(t,t') &= 2\eta^\perp(t) G_{2y}(t,t'), \\
\frac{\mathrm{d}}{\mathrm{d}t} G_{2y}(t,t') &= G_{3y}(t,t'), \\
\frac{\mathrm{d}}{\mathrm{d}t} G_{3y}(t,t') &= -A_{32}(t) G_{2y}(t,t') - A_{33}(t) G_{3y}(t,t'),
\end{aligned} \tag{7.20}$$

with

$$A_{32} = 3\chi + 2\epsilon^2 + 4\epsilon\eta^\parallel + 4(\eta^\perp)^2 + \xi^\parallel, \qquad A_{33} = 3 + \epsilon + 2\eta^\parallel, \tag{7.21}$$

as well as the following differential equations in terms of the time t':

$$\begin{aligned}
\frac{\mathrm{d}}{\mathrm{d}t'} G_{x2}(t,t') &= -2\eta^\perp(t')\delta_{x1} + A_{32}(t') G_{x3}(t,t'), \\
\frac{\mathrm{d}}{\mathrm{d}t'} G_{x3}(t,t') &= -G_{x2}(t,t') + A_{33}(t') G_{x3}(t,t').
\end{aligned} \tag{7.22}$$

The initial conditions are $G_{xy}(t,t) = \delta_{xy}$. For $y = 1$, the solutions are: $G_{11} = 1$, $G_{21} = G_{31} = 0$. For $y = 2, 3$ we need to make some approximations to solve the equations analytically.

We can also combine the equations (7.20) into a second-order differential equation for G_{2y} in closed form:

$$\frac{\mathrm{d}^2}{\mathrm{d}t^2} G_{2y}(t,t') + A_{33}(t) \frac{\mathrm{d}}{\mathrm{d}t} G_{2y}(t,t') + A_{32}(t) G_{2y}(t,t') = 0. \tag{7.23}$$

The first-order solution of (7.18) is

$$v_{ia}^{(1)}(t,\boldsymbol{x}) = \int \frac{\mathrm{d}^3\boldsymbol{k}}{(2\pi)^{3/2}} v_{am}(k,t) \hat{a}_m^\dagger(\boldsymbol{k}) i k_i e^{i\boldsymbol{k}.\boldsymbol{x}} + c.c., \tag{7.24}$$

with

$$v_{am}(k,t) = \int_{-\infty}^{t} \mathrm{d}t' G_{ab}(t,t') \dot{\mathcal{W}}(k,t') X_{bm}^{(1)}(k,t'). \tag{7.25}$$

Moreover, the same functions also serve to determine the second-order solution

$$v_{ia}^{(2)}(t,\boldsymbol{x}) = -\int_{-\infty}^{t} \mathrm{d}t' G_{ab}(t,t') \bar{A}_{bcd}(t') v_{ic}^{(1)}(t',\boldsymbol{x}) v_d^{(1)}(t',\boldsymbol{x}) + \int_{-\infty}^{t} \mathrm{d}t' G_{ab}(t,t') b_{ib}^{(2)}(t',\boldsymbol{x}). \tag{7.26}$$

As discussed previously, the long-wavelength formalism separates the perturbations in short and long-wavelength modes, the transition occurring a few e-folds after horizon-crossing (denoted t_*). As in section 3.3, we suppose that the slow-roll approximation is a good approximation at that time as motivated by observational results. Hence, at the time of the transition to super-horizon mode, a few e-folds after horizon-crossing, we can consider that quantities have changed very little, so that we can use their horizon-crossing values for the following computations.

Analytical solutions for the linear mode $X^{(1)}_{bm}$ at horizon-crossing have been determined in [94] using the slow-roll approximation. While we will not detail the computation here, it is quite similar to the one in section 3.3, with the additional equation (7.17) and it also includes perpendicular slow-roll parameters. The only non-zero components are [164]

$$X^{(1)}_{11}(t_*) = X^{(1)}_{22}(t_*) = \gamma_*, \qquad X^{(1)}_{32}(t_*) = -\chi_*\gamma_* \qquad \text{with} \quad \gamma_* \equiv \frac{-\kappa H_*}{2k^{3/2}\sqrt{\epsilon_*}}. \tag{7.27}$$

We recall that the asterisk subscript indicates that quantities are evaluated at the time of horizon crossing t_*.

A good choice of window function is simply a step function [164, 163], so

$$\dot{\mathcal{W}} = \delta\left(\frac{kc}{aH\sqrt{2}} - 1\right), \tag{7.28}$$

where c is of order of a few (this defines a time slightly after horizon-crossing, but as we are in slow-roll, the exact choice of c is not important). Then one can obtain

$$\begin{aligned} v_{11}(t) &= \gamma_*\Theta(t - t_*), \\ v_{21}(t) &= v_{31}(t) = 0, \\ v_{x2}(t) &= \gamma_*\Theta(t - t_*)\bar{v}_{x2}(t), \end{aligned} \tag{7.29}$$

introducing the short-hand notation

$$\bar{v}_{x2}(t) \equiv G_{x2}(t, t_*) - \chi_* G_{x3}(t, t_*). \tag{7.30}$$

This means that $\bar{v}_{12*} = 0$, $\bar{v}_{22*} = 1$ and $\bar{v}_{32*} = -\chi_*$. The functions $\bar{v}_{x2}$ satisfy the same differential equation (7.20) in terms of t as the G_{x2}. We will use these solutions for the computation of observables in the next section.

For now, it is interesting to further discuss the behaviour of these Green's functions. In the general case, these equations cannot be solved analytically. Hence, we will focus on the case $t' = t_*$ and we assume again that at horizon-crossing the slow-roll approximation is valid for at least a few e-folds. This means that during these few e-folds, the different slow-roll parameters, which evolve slowly, can be considered as constants at the lowest order. Under these conditions, the differential equation (7.23) takes the form:

$$\ddot{g}(t) + A_{33}\dot{g}(t) + A_{32}g(t) = 0, \tag{7.31}$$

where g can be either G_{22}, G_{23} or $\bar{v}_{22}$, differing only in initial condition. Here, A_{32} and A_{33} are now constants. The solution of this equation is:

$$g(t) = \frac{1}{\lambda_- - \lambda_+}\left[(\lambda_- g_0 - \dot{g}_0)e^{\lambda_+ t} + (-\lambda_+ g_0 + \dot{g}_0)e^{\lambda_- t}\right], \tag{7.32}$$

where $\lambda_+ = \frac{1}{2}\left(-A_{33} + \sqrt{(A_{33})^2 - 4A_{32}}\right)$, $\lambda_- = \frac{1}{2}\left(-A_{33} - \sqrt{(A_{33})^2 - 4A_{32}}\right)$ and g_0, $\dot{g}_0$ are the initial values of g and $\dot{g}$. In the slow-roll regime, $|A_{32}| \ll 1$ while $A_{33} \approx 3$. The direct

consequence is that $|\lambda_+| \ll 1$, which implies that the $e^{\lambda_+ t}$ mode does not change much in a few e-folds, while $\lambda_- \approx -3$, which means that the other mode decays exponentially and can be neglected after a few e-folds (three is sufficient).

For two different sets of initial conditions, the ratio between the solutions becomes:

$$\frac{g_1}{g_2} = \frac{\dot{g}_1}{\dot{g}_2} = \frac{\lambda_- g_{1_0} - \dot{g}_{1_0}}{\lambda_- g_{2_0} - \dot{g}_{2_0}}, \tag{7.33}$$

which is a constant. Hence, G_{22*} (defined as $G_{22}(t, t_*)$), G_{23*} and $\bar{v}_{22}$ become proportional after a few e-folds of slow-roll. Then, after a few more e-folds of inflation, the approximation of constant slow-roll parameters stops to be valid and we can no longer consider A_{32} and A_{33} to be constants. However, by this time the proportionality between G_{22*}, G_{23*}, $\bar{v}_{22}$ and their derivatives G_{32*}, G_{33*}, $\bar{v}_{32}$ has been established, and because of the linearity of the differential equation (7.23), they will stay proportional until the end of inflation.

The case of G_{12}, G_{13} and $\bar{v}_{12}$ is a little trickier. With $\eta^\perp$ being a constant, these functions are the primitives of G_{22}, G_{23}, $\bar{v}_{22}$ according to (7.20). However, one does not obtain the same factor of proportionality (7.33) with a simple integration of (7.32) because of the constant of integration. On the other hand, from (7.20) we know these functions stay small compared to one before the turn of the field trajectory, because $\eta^\perp$ is negligible compared to other slow-roll parameters. During the turn, while $\eta^\perp$ is of the same order as other slow-roll parameters or even larger, they can become large. We will see later that typical and interesting values of $\bar{v}_{12}$ are larger than order unity. Hence, the only relevant part of the integral is after the beginning of the turn. To compute it, one can just integrate the first equation of (7.20) starting at the beginning of the turn instead of at horizon-crossing. Moreover, once the turn has started, we know that the relations of proportionality between G_{22*}, G_{23*} and $\bar{v}_{22}$ are already established, which means that from (7.20) the same relations exist between $\dot{G}_{12*}$, $\dot{G}_{13*}$ and $\dot{\bar{v}}_{12}$ on the only relevant part of the integration interval. Then the common factor is conserved by the integration. During the turn, (7.33) becomes valid for the Green's functions G_{12*}, G_{13*} and $\bar{v}_{12}$. In particular this is true for the final values of these functions, which will play an important role in the next sections. If these functions stay negligible during the turn, or vanish at the end, the result does not hold. However, as already mentioned, this case is not interesting as multiple-field effects will play no role. To summarize, the explicit proportionality relations are:

$$\frac{G_{12*}}{G_{13*}} = \frac{G_{22*}}{G_{23*}} = \frac{G_{32*}}{G_{33*}} = -\lambda_- \approx 3 \qquad \text{and} \qquad \frac{\bar{v}_{12}}{G_{12*}} = \frac{\bar{v}_{22}}{G_{22*}} = \frac{\bar{v}_{32}}{G_{32*}} = \frac{\lambda_- + \chi_*}{\lambda_-} \approx 1. \tag{7.34}$$

7.5 Observables

We almost have everything needed to compute and discuss observable parameters. But first one last subtlety must be discussed. The quantity ζ_i^m is not gauge-invariant at second-order and therefore cannot be linked directly to the proper gauge-invariant quantity ζ^m which will be used for the computation of correlation functions. This is investigated in detail in [192]. To summarize the results, one has to change the gauge from flat to uniform energy density ($\partial_i \rho = 0$) in which our key quantity is simply the gradient of the gauge-invariant perturbation. At first-order, there is no difference between the results in the two different gauges. However at second-order, a correction term is needed and we have to replace the second-order adiabatic term $\zeta_i^{1(2)}$ by

$$\zeta_i^{1(2)} \longrightarrow \zeta_i^{1(2)} + 2\eta^\perp \zeta^{1(1)} \zeta_i^{2(1)}, \tag{7.35}$$

where $\zeta^{1(1)} \equiv \partial^{-2} \partial^i \zeta_i^{1(1)}$.

We already introduced some observable parameters in previous chapters. Here we review the ones we will discuss in this part of the thesis. The most important (potential) observables predicted by inflation are the amplitude of the scalar power spectrum $\mathcal{P}_s$ of the adiabatic curvature perturbation ζ^1, its spectral index $n_s - 1 \equiv \frac{\mathrm{d}\ln\mathcal{P}_s}{\mathrm{d}\ln k}$, the tensor-to-scalar ratio $r \equiv \mathcal{P}_t/\mathcal{P}_s$ and the non-Gaussianity parameters f_{NL} of a few specific bispectrum shapes (local, equilateral, orthogonal). The first two have been measured quite accurately by the Planck satellite, while for the latter two we have so far only upper limits. Of course there are more predicted parameters, especially in the case of multiple-field inflation, for example the running of the power spectrum, the spectral index of the tensor power spectrum, the power spectrum of isocurvature modes, and non-Gaussianity parameters of many more bispectrum shapes, but none of these have been detected so far. In this thesis we will focus on the local non-Gaussianity parameter f_{NL} of certain quite general classes of two-field inflation models. We will in particular investigate if these models can give an f_{NL} of order unity (which is large compared to the prediction of standard single-field slow-roll inflation of $\mathcal{O}(10^{-2})$) or even larger. In other words, does the Planck constraint of $f_{\mathrm{NL}} = 0.8 \pm 5.0$ [14] rule out some of the parameter regions of these models, or is everything still allowed? The observational constraints on n_s will turn out to be an important ingredient of our considerations. The current Planck result is $n_s = 0.968 \pm 0.006$ [15], while the planned next-generation satellite experiment CORE expects to reach error bars that are about four times smaller, of about 0.0015. On the other hand, it turns out that the current observational constraint on r does not give any additional information compared to n_s for our purposes, so we will ignore it in the rest of the thesis.[5]

The explicit expressions for the first three quantities in the case of two-field inflation requires us to compute the two-point correlation function of the Fourier coefficients of $\zeta^{1(1)}(\boldsymbol{x}, t)$, recalling that its spatial gradient is given by (7.24). Hence the Fourier coefficients are

$$\zeta^{1(1)}_{\boldsymbol{k}} = v_{1m}(k,t)[\hat{a}^\dagger_m(\boldsymbol{k}) + \hat{a}_m(-\boldsymbol{k})]. \tag{7.36}$$

It is then straightforward to derive

$$\langle \zeta^{1(1)}_{\boldsymbol{k}_1} \zeta^{1(1)}_{\boldsymbol{k}_2} \rangle = \delta^3(\boldsymbol{k}_1 + \boldsymbol{k}_2) v_{1m}(k_1,t) v_{1m}(k_1,t). \tag{7.37}$$

Then, using (7.29) the power spectrum of the adiabatic mode defined in (3.41) takes the form

$$\mathcal{P}_s = \frac{\kappa^2 H_*^2}{8\pi^2 \epsilon_*} \left[1 + (\bar{v}_{12})^2\right], \tag{7.38}$$

and the spectral index up to second-order in slow-roll parameters is

$$\begin{aligned} n_s - 1 =& \frac{\mathrm{d}\ln\mathcal{P}_s}{\mathrm{d}t_*}\frac{\mathrm{d}t_*}{\mathrm{d}\ln k} = \frac{\mathrm{d}\ln\mathcal{P}_s}{\mathrm{d}t_*}\frac{1}{1-\epsilon_*} \\ =& \frac{1}{1-\epsilon_*}\left[-4\epsilon_* - 2\eta^{\parallel}_* + 2\frac{\bar{v}_{12}}{1+(\bar{v}_{12})^2}\left(-2\eta^{\perp}_* + \chi_* \bar{v}_{12}\right.\right. \\ & \left.\left. + G_{13}(t,t_*)\left(-\tilde{W}_{221*} + 2\epsilon_*^2 + (\eta^{\parallel}_*)^2 + (\eta^{\perp}_*)^2 + 3\epsilon_*(\eta^{\parallel}_* - \chi_*) - 2\eta^{\parallel}_*\chi_* + \chi_*^2\right)\right)\right], \end{aligned} \tag{7.39}$$

where we used $k = aH\sqrt{2}/c$, the first differential equation in (7.22) and the time derivatives of slow-roll parameters (7.12).

[5] The current upper bound $r < 0.07$ [12] is constraining for some models of single-field inflation. However, as explained later, we are interested in two-field models where the value of $\bar{v}_{12}$ in (7.40) is at least around 4, which makes r easily one order of magnitude smaller than in those single-field models.

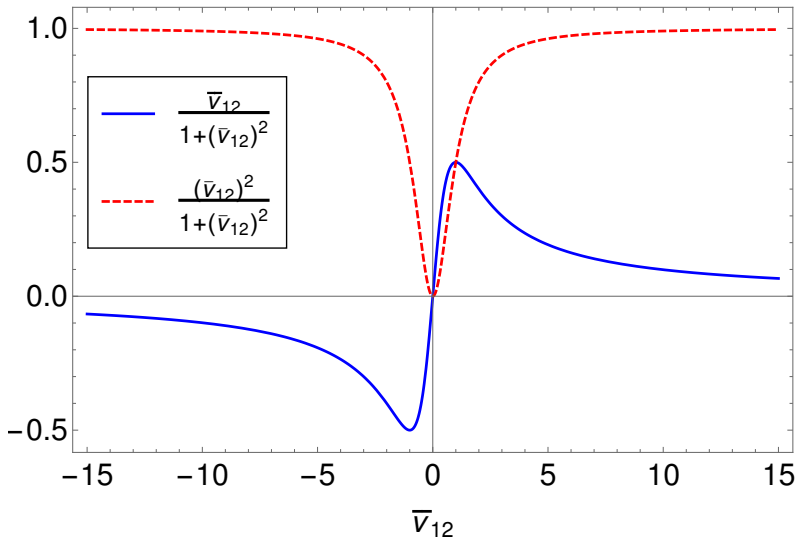

Figure 71: $\bar{v}_{12}/(1+\bar{v}_{12}^2)$ and $\bar{v}_{12}^2/(1+\bar{v}_{12}^2)$ as a function of $\bar{v}_{12}$.

Having two scalar-field degrees of freedom has no effect on the power spectrum of tensor perturbations (3.55) (there is no interaction between the isocurvature mode and the tensor modes on super-horizon scales), so the tensor-to-scalar ratio defined in (3.56) is given by

$$r = \frac{16\epsilon_*}{1+(\bar{v}_{12})^2}. \tag{7.40}$$

In the above expressions the influence of the isocurvature mode on the adiabatic mode on super-horizon scales is encoded in $\bar{v}_{12}$ and $G_{13}(t,t_*)$, which have been defined in section 7.4. Both these quantities still depend on time and in principle have to be evolved all the way to recombination in order to compute the CMB observables. However, we will impose on all our models that the isocurvature modes have disappeared by the end of inflation, so that we have returned to an effectively single-field situation by then and $\bar{v}_{12}$ and $G_{13}(t,t_*)$ have become constant and no longer evolve. In that case we can pick the end of inflation as the time to evaluate those two quantities and compute the observables without needing to know any details about the evolution of the universe after inflation.

An important conclusion can be drawn from the expression of the spectral index. Given that $G_{13}(t,t_*) \approx \bar{v}_{12}/3$ as proved in (7.34), the relevant factors to study are $\bar{v}_{12}/(1+\bar{v}_{12}^2)$ and $\bar{v}_{12}^2/(1+\bar{v}_{12}^2)$, which are shown in figure 71. We see that they are never larger than unity in absolute value and are in fact of order unity unless $\bar{v}_{12} \approx 0$, which is when multiple-field effects are negligible and which is not interesting from the point of view of this thesis.[6] So barring any fine-tuned cancellations between terms, the observed value of n_s allows us to conclude that slow roll is a good approximation at horizon crossing with all first-order slow-roll parameters at t_* at most of order 10^{-2}. However, it is certainly possible for slow roll to be broken afterwards.

The main observable we are interested in here is the local adiabatic bispectral non-Gaussianity parameter $f_{\rm NL}$. To be more precise, this is only the part of $f_{\rm NL}$ that comes from the three-point correlator of two first-order perturbations and one second-order perturbation (expressed as products of two first-order ones), sometimes called $f_{\rm NL}^{(4)}$ in the literature (see e.g. [195]), which is the only contribution on super-horizon scales. It does not include the so-called intrinsic non-Gaussianity $f_{\rm NL}^{(3)}$ due to interaction terms in the cubic action, which only play a role before and

[6] The factor $\bar{v}_{12}/(1+\bar{v}_{12}^2)$ also goes to zero for $|\bar{v}_{12}| \to \infty$. However, while this term in (7.39) would then be compatible with a large $\eta_*^\perp$, that is forbidden by the other terms.

at horizon crossing and are necessarily slow-roll suppressed in models with standard kinetic terms. Combining one Fourier coefficient of second-order perturbations with two first-order terms without forgetting the correction part introduced in (7.35), one obtains

$$\begin{aligned}\langle\zeta^1_{\boldsymbol{k}_1}\zeta^1_{\boldsymbol{k}_1}\zeta^1_{\boldsymbol{k}_1}\rangle^{(2)} &= (2\pi)^{-3/2}\delta^3(\sum_s \boldsymbol{k}_s)[f(k_1,k_2)+f(k_1,k_3)+f(k_2,k_3)]\\ &= (2\pi)^{-3/2}\delta^3(\sum_s \boldsymbol{k}_s)B_s(k_1,k_2,k_3),\end{aligned} \tag{7.41}$$

where B_s is the bispectrum of the adiabatic perturbations and

$$\begin{aligned}f(k,k') \equiv v_{1m}(k)v_{1n}(k')\left(\eta^{\perp}v_{2m}(k)v_{1n}(k') + F(b^{(2)}) - \frac{1}{2}\int_{-\infty}^{t}\mathrm{d}t'\, G_{1a}(t,t')\bar{A}_{abc}v_{bm}(k)v_{cn}(k')\right)\\ + k \longleftrightarrow k'.\end{aligned} \tag{7.42}$$

In this expression, $F(b^{(2)})$ is the small contribution of the second-order source term, not written explicitly to lighten the notation (its expression can be found in [191]). As mentioned in chapter 4.2, the $f_{\rm NL}$ parameter of the local shape is simply the bispectrum divided by the power spectrum squared

$$-\frac{6}{5}f_{\rm NL} \equiv \frac{B_s(k_1,k_2,k_3)}{\frac{2\pi^2}{k_1^3}\mathcal{P}_s(k_1)\frac{2\pi^2}{k_2^3}\mathcal{P}_s(k_2) + (k_1 \leftrightarrow k_3) + (k_2 \leftrightarrow k_3)} \tag{7.43}$$

The factor $-6/5$ in the definition is a historical artifact due to the way $f_{\rm NL}$ was originally defined in terms of the gravitational potential Φ and not the adiabatic curvature perturbation ζ^1, see equation (3.61).

Different aspects of the scale dependence of the bispectrum have been studied, like the computation of the bispectrum in the squeezed limit, the scale-dependence of $f_{\rm NL}$ or the possible observational effects [47, 48, 111, 49, 112]. Another related subject that has received much attention in recent years is the study of features in the effective inflaton potential or kinetic terms (like changes in the sound speed for the inflaton interactions), possibly due to the presence of massive fields, which lead to correlated oscillations in the power spectrum and the bispectrum [54, 4, 84, 5, 101, 3]. Here we make the assumption that the momentum dependence of $f_{\rm NL}$ can be neglected, to compute it in the limit of three equal momenta. The general case has been investigated in [191, 193] where it has been shown that indeed it is a small effect for the types of models we are interested in this thesis.

Using several integrations by parts detailed in [191] and the step functions solutions given in (7.29), the final result from the long-wavelength formalism for the local adiabatic bispectral non-Gaussianity parameter $f_{\rm NL}$ is

$$-\frac{6}{5}f_{\rm NL} = \frac{-2(\bar{v}_{12})^2}{(1+(\bar{v}_{12})^2)^2}\left(g_{\rm iso}+g_{\rm sr}+g_{\rm int}\right). \tag{7.44}$$

Here the only approximation (except the equal momenta assumption) made is that slow roll is a good approximation at horizon crossing (but can be broken afterwards), as we will assume throughout the thesis and which is motivated by the observed value of the spectral index as discussed above. The isocurvature, slow-roll, and integral contributions are given by

$$\begin{aligned}g_{\rm iso} &= (\epsilon+\eta^{\parallel})(\bar{v}_{22})^2 + \bar{v}_{22}\bar{v}_{32}, \qquad g_{\rm sr} = -\frac{\epsilon_*+\eta^{\parallel}_*}{2\bar{v}_{12}^2} + \frac{\eta^{\perp}_*\bar{v}_{12}}{2} - \frac{3}{2}\left(\epsilon_* + \eta^{\parallel}_* - \chi_* + \frac{\eta^{\perp}_*}{\bar{v}_{12}}\right),\\ g_{\rm int} &= -\int_{t_*}^{t}\mathrm{d}t'\left[2(\eta^{\perp})^2(\bar{v}_{22})^2 + (\epsilon+\eta^{\parallel})\bar{v}_{22}\bar{v}_{32} + (\bar{v}_{32})^2 - G_{13}(t,t')\bar{v}_{22}(\Xi\bar{v}_{22}+9\eta^{\perp}\bar{v}_{32})\right],\end{aligned} \tag{7.45}$$

where we have defined

$$\Xi \equiv 12\eta^{\perp}\chi - 6\eta^{\parallel}\eta^{\perp} + 6(\eta^{\parallel})^2\eta^{\perp} + 6(\eta^{\perp})^3 - 2\eta^{\perp}\xi^{\parallel} - 2\eta^{\parallel}\xi^{\perp} - \frac{3}{2}(\tilde{W}_{211} + \tilde{W}_{222}). \tag{7.46}$$

The explicit time dependence of all functions has been omitted, except for G_{13} since it depends on two times. $\bar{v}_{22}$ and $\bar{v}_{32}$ are proportional to the isocurvature mode and hence will go to zero at the end of inflation by our assumption, so that $g_{\rm iso}$ vanishes there. If we relaxed our assumption of the isocurvature mode going to zero by the end of inflation, it would be easy to get huge non-Gaussianity at the end of inflation from the $g_{\rm iso}$ term, but it would be meaningless since one would have to follow its evolution explicitly through the rest of the evolution of the universe to get a prediction for the observable. In the single-field limit, a small, slow-roll suppressed part of $g_{\rm sr}$ is all that survives and it gives back the $f_{\rm NL}^{(4)}$ part of the usual single-field result of Maldacena [141]. In the two-field case all terms of $g_{\rm sr}$ are also slow-roll suppressed since they are proportional to slow-roll parameters at horizon crossing. (It is easy to check that the various functions of $\bar{v}_{12}$ can never become large, independent of the value of $\bar{v}_{12}$.) Hence the only persistent large non-Gaussianity can come from the integrated contribution $g_{\rm int}$.

7.6 The $g_{\rm int}$ equation

As discussed at the end of the previous section, the only persistent large non-Gaussianity can come from the integral term $g_{\rm int}$ (7.45), first derived in [191]. So to answer our question if large non-Gaussianity is at all possible and if so in which models, we need to investigate this term. Unfortunately, the fact that it is an integral, and that the time dependence is not only in the upper limit of the integral but also in the t dependence of G_{13}, makes it rather hard to get a handle analytically on its behaviour in general.

However, as is shown in appendix C, by taking several derivatives of (7.45) it is possible to derive a second-order differential equation for the derivative of $g_{\rm int}(t)$ in closed form in terms of t only

$$\begin{aligned}
&(\eta^{\perp})^2\,\dddot{g}_{int} + \eta^{\perp}\left[3\eta^{\perp} - \epsilon\eta^{\perp} + 6\eta^{\parallel}\eta^{\perp} - 2\xi^{\perp}\right]\ddot{g}_{int} \\
&\quad + \left[(\eta^{\perp})^2\left(-12\epsilon + 6\chi + 6(\eta^{\parallel})^2 + 6(\eta^{\perp})^2 + 4\xi^{\parallel}\right) + \eta^{\perp}\left(3\tilde{W}_{211} - 8\eta^{\parallel}\xi^{\perp}\right) + 2(\xi^{\perp})^2\right]\dot{g}_{int} \\
&= K_{22}(\bar{v}_{22})^2 + K_{23}\bar{v}_{22}\bar{v}_{32} + K_{33}(\bar{v}_{32})^2,
\end{aligned} \tag{7.47}$$

where the K_{xy} are explicit (long) expressions in terms of products of slow-roll parameters and are defined in (C.2). This differential equation and its general solution discussed below is one of the central new results of this part of the thesis.

Despite its complicated looks, (7.47) actually admits a completely exact analytical homogeneous solution:

$$\dot{g}_{\rm int}(t) = 2A\,\eta^{\perp}(t)G_{22}(t,t_*) + 2B\,\eta^{\perp}(t)G_{23}(t,t_*) + P(t), \tag{7.48}$$

where A and B are integration constants to be determined from the initial conditions and $P(t)$ is a particular solution of the equation. This expression can then be integrated to give

$$g_{\rm int}(t) = A\,G_{12}(t,t_*) + B\,G_{13}(t,t_*) + \int_{t_*}^{t} {\rm d}t' P(t'). \tag{7.49}$$

Here we used the fact that $g_{\rm int}(t_*) = 0$ to eliminate the additional integration constant. Note that instead of $2\eta^{\perp}G_{22}$ we can also use $2\eta^{\perp}\bar{v}_{22}$ as independent homogeneous solution, which integrates to $\bar{v}_{12}$.

Now one might wonder if we have made any progress here, since in (7.49) $g_{\rm int}$ is still expressed in terms of an integral, and while there is only a single time now, it does involve an a priori unknown function $P(t)$. However, as we will show in the next section, for certain classes of potentials and within the slow-roll approximation, we can find an explicit analytical expression both for $P(t)$ and for its integral. Since slow roll is a good approximation at horizon crossing, as discussed before, where the initial conditions are given, this then allows us to determine the constants A and B for those models. Finally we will show in a later section that in the regions where the slow-roll approximation for $\eta^{\parallel}$ and $\eta^{\perp}$ breaks down (with the only condition that ϵ remains small) and we do not have an explicit analytical solution for $P(t)$, we do not actually need it since its contribution is negligible compared to the homogeneous solution. This will finally allow us to write down the exact analytical result for the observable $f_{\rm NL}$ in those models, even if slow roll is broken during some part of the inflationary evolution.

Chapter 8

Slow roll

In this chapter, we use several consecutive levels of approximations to simplify the expressions of the previous chapter. We start by applying only the (strong) slow-roll approximation to general two-field potentials. As discussed in section 7.2, this means that all slow-roll parameters, including $\eta^\perp$ and χ, are assumed to be small, which is a stronger approximation than the standard slow-roll approximation where only parallel slow-roll parameters are assumed to be small. Then, in the two next sections, we focus on product-separable and sum-separable potentials where the Green's functions can be computed as well as the different observables. Finally, in the last two sections, we specialize to the case of monomial sum potentials.

8.1 General case

We apply the slow-roll approximation to the equations of the previous chapter, starting by the slow-roll parameters. Using the field equation, we obtain explicit expressions for the basis components. We then perform a first-order slow-roll expansion on the second line of (7.9) to obtain $\eta^\parallel$ and $\eta^\perp$. For $\xi^\parallel$ and $\xi^\perp$ we proceed in a similar way on (7.12). The results are:

$$\begin{aligned} &e_{1A} = -\tilde{W}_A, \qquad \eta^\parallel = \epsilon - \tilde{W}_{11}, \qquad \eta^\perp = -\tilde{W}_{21}, \\ &\xi^\parallel = 3\epsilon\eta^\parallel + (\eta^\parallel)^2 + (\eta^\perp)^2 - \tilde{W}_{111}, \qquad \xi^\perp = 3\epsilon\eta^\perp + 2\eta^\parallel\eta^\perp - \eta^\perp\chi - \tilde{W}_{211}. \end{aligned} \tag{8.1}$$

The same slow-roll expansion applied to the differential equations for the Green's functions (7.20) and (7.22) gives:

$$\frac{\mathrm{d}}{\mathrm{d}t}G_{22}(t,t') + \chi(t)G_{22}(t,t') = 0, \tag{8.2}$$

$$G_{32}(t,t') = -\chi(t)G_{22}(t,t'), \qquad G_{x3}(t,t') = \frac{1}{3}G_{x2}(t,t'). \tag{8.3}$$

For the observables, from (7.39) we get:

$$n_s - 1 = -4\epsilon_* - 2\eta_*^\parallel + 2\frac{\bar{v}_{12}}{1+\bar{v}_{12}^2}\left(-2\eta_*^\perp + \bar{v}_{12}\chi_*\right) \tag{8.4}$$

and for the different terms of f_{NL} in (7.44):

$$g_{\mathrm{iso}} = (\epsilon + \eta^\parallel - \chi)\bar{v}_{22}^2, \qquad g_{\mathrm{sr}} = -\frac{\epsilon_* + \eta_*^\parallel}{2\bar{v}_{12}^2} + \frac{\eta_*^\perp\bar{v}_{12}}{2} - \frac{3}{2}\left(\epsilon_* + \eta_*^\parallel - \chi_* + \frac{\eta_*^\perp}{\bar{v}_{12}}\right). \tag{8.5}$$

For g_{int}, the slow-roll approximation is not sufficient to compute the integral. However, we can simplify the differential equation (7.47) to (see appendix C for the details of the computation):

$$\eta^\perp\,\ddot{g}_{\mathrm{int}} - \left[\eta^\perp(\epsilon - 2\eta^\parallel - \chi) + \xi^\perp\right]\dot{g}_{\mathrm{int}} = K_{\mathrm{sr}}(\bar{v}_{22})^2, \tag{8.6}$$

with

$$\begin{aligned} K_{\rm sr} = {} & \eta^{\parallel}\eta^{\perp}\xi^{\parallel} + 3(\eta^{\parallel})^2\eta^{\perp}\chi - 3\eta^{\parallel}\eta^{\perp}\chi^2 - (\eta^{\parallel})^3\eta^{\perp} + \eta^{\parallel}(\eta^{\perp})^3 - \eta^{\parallel}\xi^{\perp}\chi - \eta^{\perp}\xi^{\parallel}\chi - (\eta^{\perp})^2\xi^{\perp} \\ & + \xi^{\perp}\chi^2 + \eta^{\parallel}\eta^{\perp}\tilde{W}_{221} - 2\eta^{\perp}\chi\tilde{W}_{221} + \epsilon\eta^{\perp}\tilde{W}_{221} - (\eta^{\perp})^2\tilde{W}_{222} + 4\epsilon\eta^{\parallel}\eta^{\perp}\chi + \epsilon^2\eta^{\parallel}\eta^{\perp} \\ & - 4\epsilon\eta^{\perp}\chi^2 + 3\epsilon^2\eta^{\perp}\chi - 2\epsilon(\eta^{\perp})^3 - \epsilon\xi^{\perp}\chi + \eta^{\perp}\chi^3 + \epsilon\eta^{\perp}\xi^{\parallel}. \end{aligned} \tag{8.7}$$

This equation can be solved for certain classes of potentials. We will look at the simple case of a sum potential, which was solved initially in [195, 31] and discussed in detail in [45, 71, 72].

8.2 Sum potential

A sum potential has the form

$$W(\phi, \sigma) = U(\phi) + V(\sigma). \tag{8.8}$$

An immediate consequence of this form is that all mixed derivatives of the potential are zero. Using this and by writing out $\tilde{W}_{11}, \tilde{W}_{22}, \tilde{W}_{21}$ (defined in (7.5)) explicitly in terms of $\tilde{W}_{\phi\phi}, \tilde{W}_{\sigma\sigma}, \tilde{W}_{\phi\sigma}$ and using the normalization of the basis $e_{1\phi}^2 + e_{1\sigma}^2 = 1$, one can show that

$$e_{1\phi}e_{1\sigma}(\tilde{W}_{11} - \tilde{W}_{22}) = (e_{1\phi}^2 - e_{1\sigma}^2)\tilde{W}_{21}, \tag{8.9}$$

which using 7.9 and (7.11) is equivalent to

$$e_{1\phi}e_{1\sigma}(\xi^{\parallel} + 3\chi - 6\epsilon) = (e_{1\phi}^2 - e_{1\sigma}^2)(\xi^{\perp} + 3\eta^{\perp}). \tag{8.10}$$

Similarly for third-order derivatives, we can write:

$$\begin{aligned} e_{1\phi}e_{1\sigma}\tilde{W}_{221} &= e_{1\phi}e_{1\sigma}\tilde{W}_{111} + (e_{1\sigma}^2 - e_{1\phi}^2)\tilde{W}_{211}, \\ e_{1\phi}e_{1\sigma}\tilde{W}_{222} &= e_{1\phi}e_{1\sigma}\tilde{W}_{211} + (e_{1\sigma}^2 - e_{1\phi}^2)\tilde{W}_{221}. \end{aligned} \tag{8.11}$$

Using (8.10), they are equivalent to

$$\begin{aligned} (\xi^{\perp} + 3\eta^{\perp})\tilde{W}_{221} &= (\xi^{\perp} + 3\eta^{\perp})\tilde{W}_{111} - (\xi^{\parallel} + 3\chi - 6\epsilon)\tilde{W}_{211}, \\ (\xi^{\perp} + 3\eta^{\perp})\tilde{W}_{222} &= (\xi^{\perp} + 3\eta^{\perp})\tilde{W}_{211} - (\xi^{\parallel} + 3\chi - 6\epsilon)\tilde{W}_{221}. \end{aligned} \tag{8.12}$$

Note that these equations are general and not only slow-roll. After a first-order slow-roll expansion, they become:

$$\begin{aligned} \eta^{\perp}\tilde{W}_{221} &= \eta^{\perp}\tilde{W}_{111} - (\chi - 2\epsilon)\tilde{W}_{211}, \\ \eta^{\perp}\tilde{W}_{222} &= \eta^{\perp}\tilde{W}_{211} - (\chi - 2\epsilon)\tilde{W}_{221}. \end{aligned} \tag{8.13}$$

We use this to rewrite the right-hand term of (8.6) as

$$K_{\rm sr} = 2\epsilon\left(-3\epsilon^2\eta^{\perp} + 3(\eta^{\parallel})^2\eta^{\perp} - 3(\eta^{\perp})^3 + \epsilon\eta^{\perp}\chi - 3\eta^{\parallel}\eta^{\perp}\chi + \eta^{\perp}\xi^{\parallel} + \epsilon\xi^{\perp} - \eta^{\parallel}\xi^{\perp}\right). \tag{8.14}$$

Then, one can show that a particular solution of this equation is $\dot{g}_{\rm int} = 2\epsilon(\epsilon + \eta^{\parallel} - \chi)\bar{v}_{22}^2$, which can be integrated into $g_{\rm int} = \epsilon\bar{v}_{22}^2 - \epsilon_*$.

We also know that $\dot{g}_{{\rm int}*} = -2(\eta_*^{\perp})^2 + (\epsilon_* + \eta_*^{\parallel} - \chi_*)\chi_*$ from (C.1) and the initial conditions of the Green's functions. Combining this particular solution with the homogeneous solution,

we get the full solution for $\dot{g}_{\rm int}$ and then $g_{\rm int}$ after integration, in agreement with the known result from [191]:

$$\begin{aligned}
\dot{g}_{\rm int} &= 2\epsilon(\epsilon + \eta^{\parallel} - \chi)(\bar{v}_{22})^2 - \frac{e_{1\phi*}^2 \tilde{V}_{\sigma\sigma*} - e_{1\sigma*}^2 \tilde{U}_{\phi\phi*}}{e_{1\phi*} e_{1\sigma*}} \eta^{\perp} \bar{v}_{22}, \\
g_{\rm int} &= \epsilon \bar{v}_{22}^2 - \epsilon_* - \left[\eta_*^{\perp} - \frac{1}{2\eta_*^{\perp}}(\epsilon_* + \eta_*^{\parallel} - \chi_*)(\chi_* - 2\epsilon_*)\right] \bar{v}_{12}, \\
&= \epsilon \bar{v}_{22}^2 - \epsilon_* - \frac{e_{1\phi*}^2 \tilde{V}_{\sigma\sigma*} - e_{1\sigma*}^2 \tilde{U}_{\phi\phi*}}{2 e_{1\phi*} e_{1\sigma*}} \bar{v}_{12}.
\end{aligned} \tag{8.15}$$

Here the first two terms on the last line are the particular solution, and the last term the homogeneous solution. It is possible to show that the particular solution and the homogeneous solution are generally of the same order during inflation (this is discussed later in section 9.5). However, we are only interested in the final values of the observables n_s and $f_{\rm NL}$. As discussed before, the only large contribution in $f_{\rm NL}$ can come from $g_{\rm int}$, if we suppose isocurvature modes vanish before the end of inflation, which means in terms of Green's functions that $\bar{v}_{22}$ and $\bar{v}_{32}$ vanish while $\bar{v}_{12}$ becomes constant. Hence in that case, the integrated particular solution is also slow-roll suppressed and only the homogeneous solution matters at the end of inflation. From now on, the different expressions for the observables are only given at the end of inflation. For every other parameter (like the Green's functions and the slow-roll parameters), if they are evaluated at the end of inflation, it is indicated by the subscript e.

Using the result (8.15) with $\bar{v}_{22e} = 0$, we can write:

$$\begin{aligned}
-\frac{6}{5} f_{\rm NL} &= \left[\eta_*^{\perp} - \frac{1}{2\eta_*^{\perp}}(\epsilon_* + \eta_*^{\parallel} - \chi_*)(\chi_* - 2\epsilon_*)\right] \frac{2(\bar{v}_{12e})^3}{\left(1 + (\bar{v}_{12e})^2\right)^2} + \mathcal{O}(10^{-2}) \\
&= \frac{e_{1\phi*}^2 \tilde{V}_{\sigma\sigma*} - e_{1\sigma*}^2 \tilde{U}_{\phi\phi*}}{e_{1\phi*} e_{1\sigma*}} \frac{(\bar{v}_{12e})^3}{\left(1 + (\bar{v}_{12e})^2\right)^2} + \mathcal{O}(10^{-2}).
\end{aligned} \tag{8.16}$$

This depends on the final value of the Green's function $\bar{v}_{12}$, which describes the contribution of the isocurvature mode to the adiabatic mode. Without computing it, it is possible to determine a necessary condition for $f_{\rm NL}$ to be of order unity or larger. Indeed it is easy to show that, for any value of $\bar{v}_{12e}$:

$$\left| \frac{(\bar{v}_{12e})^3}{\left(1 + (\bar{v}_{12e})^2\right)^2} \right| \leq \frac{3^{3/2}}{16} \approx 0.325. \tag{8.17}$$

If the slow-roll approximation is valid at horizon-crossing, which is the main assumption in the computation of $f_{\rm NL}$, we expect that $\tilde{V}_{\sigma\sigma*}$ and $\tilde{U}_{\phi\phi*}$ are of order slow-roll (small compared to one). Then, the only possibility to get $f_{\rm NL}$ of order unity is that one of the basis components is negligible at horizon-crossing. This means one of the fields is dominating at that time, by definition we choose it to be ϕ. Hence, at horizon-crossing $e_{1\phi*}^2 \approx 1$ and $e_{1\sigma*}^2 \ll 1$. Using (8.1), this also implies that $|U_{\phi*}| \gg |V_{\sigma*}|$ and we can simplify:

$$\frac{e_{1\phi*}^2 \tilde{V}_{\sigma\sigma*} - e_{1\sigma*}^2 \tilde{U}_{\phi\phi*}}{e_{1\phi*} e_{1\sigma*}} = \frac{e_{1\phi*} \tilde{V}_{\sigma\sigma*}}{e_{1\sigma*}} = \frac{\sqrt{2\epsilon_*}}{\kappa} \frac{V_{\sigma\sigma*}}{V_{\sigma*}}. \tag{8.18}$$

This has to be large to have $f_{\rm NL}$ non-negligible, which means that the second-order derivative $V_{\sigma\sigma*}$ is large compared to the first-order derivative $V_{\sigma*}$. Hence around σ_*, the potential is very flat in the σ direction. In terms of slow-roll parameters, this means that $|\eta_*^{\perp}| \lesssim |(\epsilon_* + \eta_*^{\parallel} - \chi_*)(\chi_* - 2\epsilon_*)|$. For the usual slow-roll order values of 10^{-2}, $\eta_*^{\perp}$ is at most of order 10^{-4}.

Another useful limit is:

$$\left| \frac{\bar{v}_{12e}^3}{\left(1 + (\bar{v}_{12e})^2\right)^2} \right| < \left| \frac{1}{\bar{v}_{12e}} \right|, \tag{8.19}$$

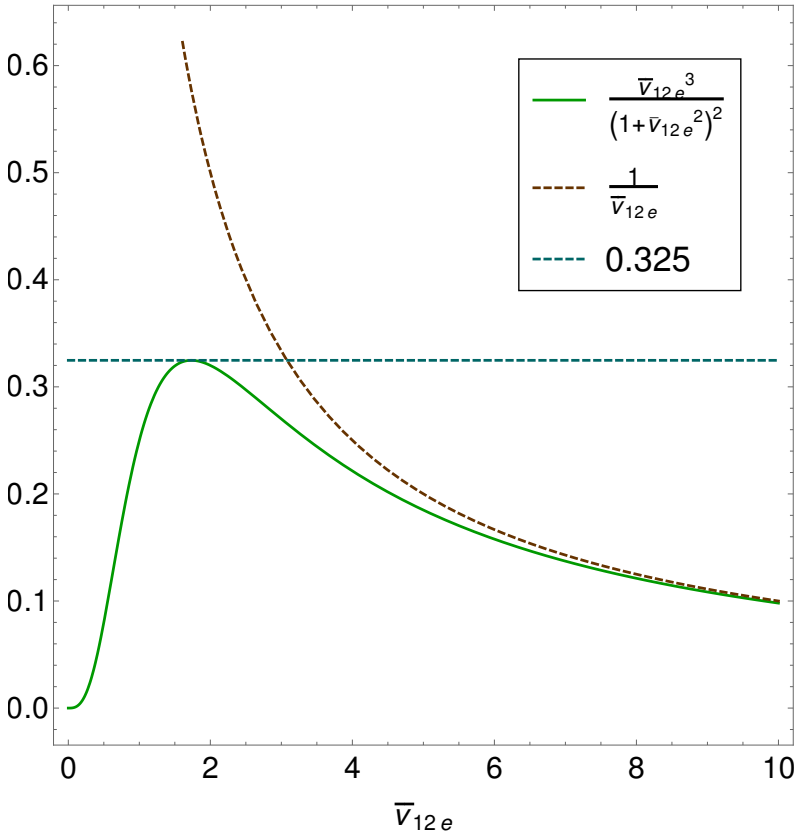

Figure 81: $\frac{(\bar{v}_{12e})^3}{((1+(\bar{v}_{12e})^2)^2}$ as a function of $\bar{v}_{12e}$ and its two upper limits 0.325 and $1/\bar{v}_{12e}$.

which becomes a very good approximation if $|\bar{v}_{12e}| > 4$. These two limits are shown explicitly in figure 81. From (7.20), if $\bar{v}_{12e}$ is of order unity, this implies that at some time there was a turn of the field trajectory where both the isocurvature mode and $\eta^{\perp}$ are non-negligible. This turn is then a necessary condition of large non-Gaussianity.

Still using the slow-roll approximation, we can go further by computing the Green's functions. From (8.10), we get:

$$\chi = 2\epsilon + \eta^{\perp}\frac{e_{1\phi}^2 - e_{1\sigma}^2}{e_{1\phi}e_{1\sigma}} = -\frac{\mathrm{d}}{\mathrm{d}t}\ln\left(H^2 e_{1\phi}e_{1\sigma}\right). \tag{8.20}$$

We can then solve (8.2):

$$G_{22}(t,t') = \frac{H(t)^2 e_{1\phi}(t)e_{1\sigma}(t)}{H(t')^2 e_{1\phi}(t')e_{1\sigma}(t')}. \tag{8.21}$$

Moreover, we have:

$$\eta^{\perp}H^2 e_{1\phi}e_{1\sigma} = \frac{\kappa^2}{6}\frac{\mathrm{d}Z}{\mathrm{d}t}, \tag{8.22}$$

with $Z \equiv Ve_{1\phi}^2 - Ue_{1\sigma}^2$ [195, 191], which gives us:

$$\bar{v}_{12} = \frac{Z - Z_*}{W_* e_{1\phi *}e_{1\sigma *}}, \qquad \bar{v}_{22} = \frac{We_{1\phi}e_{1\sigma}}{W_* e_{1\phi *}e_{1\sigma *}}. \tag{8.23}$$

At the end of inflation, when the fields reach the minimum of the potential, Z tends to zero. Obviously, this can only happen if there is a turn of the field trajectory at some time after

horizon-crossing to make both fields evolve. Moreover, if $e_{1\sigma*}^2 \ll 1$ (necessary condition for $f_{\rm NL}$ of order unity), $Z_* = V_* e_{1\phi*}^2$. We then obtain, using (8.1):

$$\bar{v}_{12e} = -\frac{V_* e_{1\phi*}}{W_* e_{1\sigma*}} = \text{sign}(e_{1\phi*})\sqrt{2\epsilon_*}\frac{\kappa V_*}{V_{\sigma*}}. \tag{8.24}$$

With a small enough $e_{1\sigma*}$, it is easy to obtain $\bar{v}_{12e}$ larger than four or five. In figure 81, this places us on the right where $\frac{(\bar{v}_{12e})^3}{(1+(\bar{v}_{12e})^2)^2} \approx \frac{1}{\bar{v}_{12e}}$. The consequence for the potential V is that $\kappa V_* \gg V_{\sigma*}$.

Substituted into (8.16), in the case where the slow-roll parameters factor is large, we obtain:

$$-\frac{6}{5} f_{\rm NL} \approx \frac{\tilde{V}_{\sigma\sigma*} e_{1\phi*}}{e_{1\sigma*}} \frac{1}{\bar{v}_{12e}} = \frac{\tilde{V}_{\sigma\sigma*} e_{1\phi*}}{e_{1\sigma*}} \frac{W_* e_{1\sigma*}}{-V_* e_{1\phi*}} = -\frac{V_{\sigma\sigma*}}{\kappa^2 V_*}. \tag{8.25}$$

This directly shows that $f_{\rm NL}$ is of order unity when the second derivative of V_* and V_* itself are of the same order, while its first-order derivative $V_{\sigma*}$ is small compared to the two previous quantities because of (8.18) and (8.24), a result already highlighted in [71, 72]. Larger $f_{\rm NL}$ is a priori possible, but requires a fine-tuning of the model. Moreover, the sign of $f_{\rm NL}$ is the sign of $V_{\sigma\sigma*}$. A negative $f_{\rm NL}$ corresponds to a potential in the form of a ridge at t_*, where σ_* is very close to the maximum for the potential to be flat enough in the σ_* direction, while a positive $f_{\rm NL}$ corresponds to a valley potential.

In the same limit of large $\bar{v}_{12e}$, the spectral index takes the form

$$n_s - 1 = -4\epsilon_* - 2\eta_*^{\parallel} + 2\chi_* = -2\epsilon_* + 2\tilde{V}_{\sigma\sigma*}. \tag{8.26}$$

The spectral index is close to 1, hence $\tilde{V}_{\sigma\sigma*} = \frac{V_{\sigma\sigma*}}{\kappa^2 W_*}$ is at most of order 10^{-2}. If it is smaller, this requires a fine-tuning of ϵ_*. If $f_{\rm NL}$ is of order unity, then $\frac{V_*}{W_*}$ is also of order 10^{-2}.

To summarize, at horizon-crossing, the conditions are $U_* \gg V_*$ and $|U_{\phi*}| \gg |V_{\sigma*}|$. The second-order derivative $V_{\sigma\sigma*}$ is not negligible and can be either smaller, equal or larger than $U_{\phi\phi*}$ but it is not hugely larger or smaller. To be precise, we make a quite general assumption that $|V_{\sigma\sigma*}U_{\phi*}^2| \gg |U_{\phi\phi*}V_{\sigma*}^2|$ and $|V_{\sigma\sigma*}V_{\sigma*}^2| \ll |U_{\phi\phi*}U_{\phi*}^2|$. With these different assumptions for the potential, the expressions for the slow-roll parameters and basis vectors become:

$$\begin{aligned}
&\epsilon = \frac{1}{2\kappa^2}\left(\frac{U_\phi}{U}\right)^2, \qquad \eta^{\parallel} = -\frac{U_{\phi\phi}}{\kappa^2 U} + \epsilon, \qquad \eta^{\perp} = -\frac{V_\sigma}{U_\phi}\frac{U_{\phi\phi} - V_{\sigma\sigma}}{\kappa^2 U}, \\
&e_{1\phi} = -\text{sign}(U_\phi), \qquad e_{1\sigma} = -\frac{V_\sigma}{\kappa\sqrt{2\epsilon}\, U}, \qquad \chi = \frac{V_{\sigma\sigma}}{\kappa^2 U} + \epsilon + \eta^{\parallel} = \frac{U_\phi}{V_\sigma}\eta^{\perp} + 2\epsilon.
\end{aligned} \tag{8.27}$$

At horizon-crossing, the situation is very close to single-field inflation. In the slow-roll regime, by definition everything evolves slowly, hence a legitimate question is to ask when these conditions will stop to be valid. In fact, they will break at the turn of the field trajectory. At that time V_σ stops to be negligible compared to U_ϕ (or equivalently, $e_{1\sigma}$ is not small compared to one). As already discussed, the turn is mandatory to have $\bar{v}_{12e}$ large enough. However, they will also break if V stops to be negligible compared to U, this happens when the field ϕ is near the minimum of its potential. In this second case, we know the slow-roll approximation will also stop to be valid because ϵ is becoming large (similarly to single-field inflation). Hence, if this happens before the turn, as the slow-roll approximation is not valid anymore, we lose the analytical results for the Green's functions and $f_{\rm NL}$. We have to check if the turn can occur before the first field reaches the minimum of its potential, or in simple terms, is it possible to have $f_{\rm NL}$ of order unity without breaking the slow-roll approximation? To be able to make progress in answering that question, we will consider a specific class of two-field sum potentials, where both U and V are monomial plus a possible constant in section 8.4.

8.3 Product potential

In this section, we study the case of product potentials, which take the form $W(\phi,\sigma) = U(\phi)V(\sigma)$. This case was solved analytically in [55]. Here, we show that the slow-roll version of the $g_{\rm int}$ equation (8.6) takes a simple and nice form which is easy to deal with.

As for the sum-separable case, we start by using the specific form of the potential to find some new relations concerning its derivatives without assuming any approximation. A simple one is $W_{\phi\sigma} = \frac{W_\phi W_\sigma}{W}$ which links the second-order mixed derivative of the potential to the first-order ones. Then using the field equation (7.2) and the definitions of ϵ, $\eta^\parallel$ and $\eta^\perp$ given in (7.3) and (7.6), this relation can be rewritten in terms of slow-roll parameters:

$$(3-\epsilon)\tilde{W}_{\phi\sigma} = \frac{2}{3}\epsilon\left[e_{1\phi}e_{1\sigma}\left((\eta^\parallel+3)^2-(\eta^\perp)^2\right)+\eta^\perp(\eta^\parallel+3)(e_{1\phi}^2-e_{1\sigma}^2)\right]. \tag{8.28}$$

We also need the generalized version of (8.9), valid for any two-field potential, which is:

$$e_{1\phi}e_{1\sigma}(\tilde{W}_{11}-\tilde{W}_{22}) = (e_{1\phi}^2-e_{1\sigma}^2)\tilde{W}_{21}+\tilde{W}_{\phi\sigma}. \tag{8.29}$$

Combining the two previous equations and using (7.9), we obtain:

$$\begin{aligned} &e_{1\phi}e_{1\sigma}\left[-3\chi-\xi^\parallel+\epsilon\chi-2\epsilon^2-4\epsilon\eta^\parallel+\frac{\epsilon}{3}\left(\xi^\parallel-2(\eta^\parallel)^2+2(\eta^\perp)^2\right)\right] \\ &=(e_{1\phi}^2-e_{1\sigma}^2)\left[3\eta^\perp+\xi^\perp+\epsilon\eta^\perp-\frac{\epsilon}{3}\left(\xi^\perp+2\eta^\parallel\eta^\perp\right)\right]. \end{aligned} \tag{8.30}$$

Similar computations can be done for the third-order derivatives $W_{\phi\phi\sigma} = \frac{W_{\phi\phi}W_\sigma}{W}$ and $W_{\phi\sigma\sigma} = \frac{W_{\sigma\sigma}W_\phi}{W}$ to show that:

$$\begin{aligned} (3-\epsilon)\tilde{W}_{\phi\phi\sigma} &= -2\epsilon\left[(\eta^\parallel+3)e_{1\sigma}-\eta^\perp e_{1\phi}\right]\tilde{W}_{\phi\phi}, \\ (3-\epsilon)\tilde{W}_{\phi\sigma\sigma} &= -2\epsilon\left[(\eta^\parallel+3)e_{1\phi}+\eta^\perp e_{1\sigma}\right]\tilde{W}_{\sigma\sigma}. \end{aligned} \tag{8.31}$$

Finally, using the definitions of $\tilde{W}_{221}$ and $\tilde{W}_{222}$ in terms of third-order derivatives and basis components, substituting them into (8.30) and (8.31) and performing a first-order expansion in terms of slow-roll parameters gives:

$$\begin{aligned} \tilde{W}_{221} =& -\epsilon\eta^\parallel-\epsilon\chi+(\eta^\parallel)^2-2\eta^\parallel\chi+\chi^2+(\eta^\perp)^2-\xi^\parallel+\frac{\chi}{\eta^\perp}\xi^\perp, \\ \tilde{W}_{222} =& -\xi^\perp-\eta^\perp(\epsilon-2\eta^\parallel+2\chi) \\ &-\frac{\chi}{\eta^\perp}\left(-2\epsilon^2-3\epsilon\eta^\parallel+(\eta^\parallel)^2-\xi^\parallel-\epsilon\chi-2\eta^\parallel\chi+\chi^2\right)-\left(\frac{\chi}{\eta^\perp}\right)^2\xi^\perp. \end{aligned} \tag{8.32}$$

These equations can then be used to simplify the right-hand side of (8.6), and one easily finds that in fact the right-hand side completely vanishes. Hence, the slow-roll solution consists only of the homogeneous solution and using the initial condition $\dot{g}_{\rm int*} = -2(\eta_*^\perp)^2+(\epsilon_*+\eta_*^\parallel-\chi_*)\chi_*$ (from the slow-roll approximation of (C.1)) we find:

$$g_{\rm int} = -\left[\eta_*^\perp-\frac{1}{2\eta_*^\perp}(\epsilon_*+\eta_*^\parallel-\chi_*)\chi_*\right]\bar{v}_{12} = -\frac{e_{1\phi*}^2\tilde{V}_{\sigma\sigma*}-e_{1\sigma*}^2\tilde{U}_{\phi\phi*}}{2e_{1\phi*}e_{1\sigma*}}\bar{v}_{12}. \tag{8.33}$$

The most important thing to note here is that the second expression has exactly the same form as the homogeneous part of the sum potential case in (8.15), without the particular solution. As discussed in section 8.2, it is that term which can give a large contribution to $f_{\rm NL}$. The

natural question is then if the situation is the same for the product potential. The similarity of the expressions makes it possible to use exactly the same method to answer this question as for the treatment of the sum potential.

First, we define:

$$\tilde{g}_{\rm int} = \frac{-2(\bar{v}_{12})^2}{(1+(\bar{v}_{12})^2)^2}\, g_{\rm int} = \frac{e_{1\phi*}^2 \tilde{V}_{\sigma\sigma*} - e_{1\sigma*}^2 \tilde{U}_{\phi\phi*}}{e_{1\phi*}e_{1\sigma*}} \frac{(\bar{v}_{12})^3}{(1+(\bar{v}_{12})^2)^2}, \tag{8.34}$$

which is the entire term depending on $g_{\rm int}$ in $f_{\rm NL}$ (7.44). As for the sum potential (see section 8.2), the only possibility of having this expression larger than order slow-roll is to have one field dominating at horizon crossing: $e_{1\phi*}^2 \approx 1 \gg e_{1\sigma*}^2$. But at the same time, it is required that $\bar{v}_{12}$ is at least of order unity (and at least four to obtain the largest $f_{\rm NL}$). The main difference with the sum potential case comes in fact from the expression for $\bar{v}_{12}$. In the slow-roll approximation, it is possible to solve the Green's function equations. The computation is similar to the sum potential case and is detailed in [191] where it is shown that:

$$\bar{v}_{12} = \frac{S - S_*}{2e_{1\sigma*}e_{1\phi*}}, \qquad \bar{v}_{22} = \frac{e_{1\phi}e_{1\sigma}}{e_{1\phi*}e_{1\sigma*}}, \tag{8.35}$$

with $S \equiv e_{1\phi}^2 - e_{1\sigma}^2$. These expressions are quite different from (8.23) for the sum potential.

At horizon crossing, $e_{1\phi*}^2 \approx 1$ meaning $S_* \approx 1$. For the value of S at the end of inflation there are two different situations. As discussed several times in this thesis, we want that $\bar{v}_{22}$ goes to zero at the end of inflation to get rid of the isocurvature mode, meaning that the situation is far closer to single-field inflation at the end of inflation than at horizon crossing. Hence, if at the end ϕ also dominates (same direction of the field trajectory), $|e_{1\sigma}| \ll |e_{1\sigma*}|$. This means that $S - S_* \approx e_{1\sigma*}^2$, which leads to the fact that $\bar{v}_{12}$ is small compared to 1. In that case $g_{\rm int}$ cannot give a large $f_{\rm NL}$. However, if σ dominates at the end of inflation (different direction of the field trajectory), we have:

$$\bar{v}_{12} = \frac{-1}{e_{1\phi*}e_{1\sigma*}}, \tag{8.36}$$

which is large compared to 1. We can then use that $\frac{(\bar{v}_{12})^3}{(1+(\bar{v}_{12})^2)^2} \approx \frac{1}{\bar{v}_{12}}$ if $|\bar{v}_{12}| \gg 1$ and (8.34) to write:

$$\tilde{g}_{\rm int} \approx \frac{e_{1\phi*}^2 \tilde{V}_{\sigma\sigma*} - e_{1\sigma*}^2 \tilde{U}_{\phi\phi*}}{e_{1\phi*}e_{1\sigma*}} \times \frac{e_{1\phi*}e_{1\sigma*}}{-1} \approx -\tilde{V}_{\sigma\sigma*}, \tag{8.37}$$

which is of order slow roll. Hence also in this case $f_{\rm NL}$ is small. This is in agreement with the known conclusion that a product potential cannot give a large $f_{\rm NL}$ in the slow-roll approximation with vanishing isocurvature mode at the end of inflation [45, 191].

8.4 Monomial potentials

Using the results of section 8.2, we want to analytically study inflation between horizon-crossing and the beginning of the turn of the field trajectory. The idea is that the slow-roll approximation is broken when the dominating field ϕ gets close to the minimum of its potential, and we want to verify if the turn can occur before that time. This means that the form of the potential does not need to describe the end of inflation.

We know that $V(\sigma)$ has to be very flat around σ_*, hence we can use an expansion in σ keeping only the largest term to write:

$$V(\sigma) = C + \beta(\kappa\sigma)^m, \tag{8.38}$$

where C, m and β are constants. Here $m > 1$, while β can be either positive or negative. Because of the expansion in σ, this potential is in fact quite general. Depending on the sign of β, the potential either corresponds to a ridge where σ_* is near the local maximum C ($\beta < 0$) or to a valley with σ_* near the minimum ($\beta > 0$). For the potential U, there are many possibilities, we choose to focus on a monomial potential:

$$U(\phi) = \alpha(\kappa\phi)^n, \tag{8.39}$$

with $\alpha > 0$ and $n > 1$.

We redefine the fields as being dimensionless: $\tilde{\phi} = \kappa\phi$ and $\tilde{\sigma} = \kappa\sigma$ and we will omit the tildes in the redefined fields. Using the expressions for the slow-roll parameters (8.27), we have:

$$\begin{aligned}
\epsilon &= \frac{n^2}{2}\frac{1}{\phi^2}, \qquad \eta^{\parallel} = -\frac{n(n-2)}{2}\frac{1}{\phi^2} = -\frac{n-2}{n}\epsilon, \\
\eta^{\perp} &= -\frac{m\beta}{n\alpha^2}\frac{\sigma^{m-1}}{\phi^{2n-1}}\left(n(n-1)\alpha\phi^{n-2} - m(m-1)\beta\sigma^{m-2}\right) \\
&= -\frac{m\beta}{n^{2n}\alpha^2}2^{n-\frac{1}{2}}\sigma^{m-1}\left(n^{n-1}(n-1)2^{1-\frac{n}{2}}\alpha\epsilon^{\frac{n}{2}+\frac{1}{2}} - m(m-1)\beta\sigma^{m-2}\epsilon^{n-\frac{1}{2}}\right), \\
\chi &= \frac{1}{\alpha}\frac{1}{\phi^n}\left(n\alpha\phi^{n-2} + m(m-1)\beta\sigma^{m-2}\right) = \frac{2\epsilon}{n} + \frac{m(m-1)\beta}{n^n\alpha}2^{n/2}\epsilon^{n/2}\sigma^{m-2}.
\end{aligned} \tag{8.40}$$

It is useful to express the slow-roll parameters as a function of ϵ instead of ϕ because ϵ increases after horizon-crossing, at least until the turn, and with ϵ we know exactly when the slow-roll approximation stops to be valid. ϵ and $\eta^{\parallel}$ are of the same order except in the case of $n = 2$ where $\eta^{\parallel}$ is of order ϵ^2 as can be checked with a second-order calculation.

The next step is to use the conditions that $f_{\rm NL}$ should be of order unity and n_s should be within the observational bounds to constrain the free parameters of this potential. With this form of V, we have the useful relation:

$$(m-1)V_\sigma = \sigma V_{\sigma\sigma}. \tag{8.41}$$

We know that $|e_{1\sigma *}| \ll 1$ and substituting (8.41) into the expression for $e_{1\sigma}$ in (8.27), we can write:

$$e_{1\sigma} = -\frac{\tilde{V}_{\sigma\sigma}}{\sqrt{2\epsilon}}\frac{\sigma}{m-1}. \tag{8.42}$$

Combining this with the constraints on the spectral index (8.26) which imply that ϵ_* and $\tilde{V}_{\sigma\sigma *}$ are both of order 10^{-2} at most, this imposes σ_* to be small compared to 1. Applying these constraints due to the observables to the potential gives:

$$\frac{V_{\sigma\sigma *}}{W_*} = \frac{m(m-1)\beta\sigma_*^{m-2}}{\alpha\phi_*^n + C + \beta\sigma_*^m} \sim \mathcal{O}(10^{-2}), \qquad \frac{V_{\sigma\sigma *}}{V_*} = \frac{m(m-1)\beta\sigma_*^{m-2}}{C + \beta\sigma_*^m} \sim \mathcal{O}(1). \tag{8.43}$$

Within the limit $\sigma_* \ll 1$, we learn from these equations that $\alpha\phi_*^n \gg m(m-1)\beta\sigma_*^{m-2} \sim C + \beta\sigma_*^m$.

We also need to determine the slow-roll parameters at t_*, which requires to know ϕ_*. One way to determine this is to know the amount of inflation due to each field between horizon-crossing and the end of inflation. We can start by solving the field equation:

$$\dot{\phi} = -\frac{n}{\phi}, \tag{8.44}$$

which integrates immediately to:

$$\phi(t) = \phi_*\sqrt{1 - \frac{t}{N_\phi}}, \tag{8.45}$$

n	2	3	4	5	6
$10^3\,\tilde{V}_{\sigma\sigma*}$	-7.7 ± 3	-3.5 ± 3	0.7 ± 3	4.8 ± 3	9 ± 3

Table 81: Constraints from the spectral index on $\tilde{V}_{\sigma\sigma*}$ for different n with $N_\phi = 60$.

with $N_\phi = \frac{\phi_*^2}{2n}$ the slow-roll approximation of the number of e-folds due to ϕ after horizon-crossing.

The potential is known only before the turn of the field trajectory, especially for V if it is an expansion of some more complicated function. This means that we do not know the value of N_ϕ, however it is in the range of a few to 60 e-folds. We will test different values. Nevertheless, in the simplest cases N_σ (number of e-folds due to σ) is small compared to N_ϕ. As a simple argument here, we consider the case where σ falls off a ridge, so that $V_* \approx C$. If V keeps the same form almost until the end of inflation, the minimum of the potential ($V = 0$) corresponds approximately to $\sigma_e = (-C/\beta)^{1/m} \sim [m(m-1)]^{1/m}\sigma_*^{1-2/m}$, using the second part of (8.43). For $m = 2$, this is of order 1, for larger m it becomes smaller (only m close to 1 is problematic). In a pure monomial potential like U without the constant term, having ϕ_* of order unity would imply that N_ϕ is itself of order unity. V is a bit different because of the constant term, however once σ starts to fall at a non-negligible pace (the turn), it becomes quite similar and σ goes from σ_* negligible to σ_e of order unity. Hence this also corresponds to N_σ of order unity which can be neglected in the total number of e-folds compared to N_ϕ. Note this is not a general proof, just a plausible argument to claim that N_ϕ is the dominant contribution. We can also see that σ_e becomes larger if $V_{\sigma\sigma*}/V_*$ in (8.43) becomes smaller. Hence the fact that N_σ is small is linked to having $f_{\rm NL}$ of order unity or more.

The parameter ϵ_* is related to the value of N_ϕ, hence for these models where $N_\sigma \ll N_\phi$, the value of ϵ_* is directly fixed by the total number of e-folds after horizon-crossing:

$$\epsilon_* = \frac{n}{4N_\phi}. \tag{8.46}$$

When ϵ_* is fixed, we can use the spectral index formula (8.26) to constrain $\tilde{V}_{\sigma\sigma*}$:

$$\tilde{V}_{\sigma\sigma*} = \frac{n_s - 1}{2} + \epsilon_*. \tag{8.47}$$

Using $n_s = 0.968 \pm 0.006$ from the Planck data, table 81 shows the constraints for integer values of n. Note that for $n \geq 5$, the second-order derivative has to be positive. According to (8.16), we also know that:

$$\left|-\frac{6}{5}f_{\rm NL}\right| < 0.65\left|\eta_*^\perp - \frac{1}{2\eta_*^\perp}(\epsilon_* + \eta_*^\parallel - \chi_*)(\chi_* - 2\epsilon_*)\right|, \tag{8.48}$$

which gave the estimation of $\eta_*^\perp$ of order 10^{-4} to get $f_{\rm NL}$ of order unity. We can neglect the first $\eta_*^\perp$ which is already a few orders of magnitude smaller than the single-field slow-roll typical value of $f_{\rm NL}$. Then we obtain:

$$\left|-\frac{6}{5}f_{\rm NL}\eta_*^\perp\right| < 0.325\left|(\epsilon_* + \eta_*^\parallel - \chi_*)(\chi_* - 2\epsilon_*)\right|. \tag{8.49}$$

We can rewrite the right-hand side term:

$$(\epsilon_* + \eta_*^\parallel - \chi_*)(\chi_* - 2\epsilon_*) = -\tilde{V}_{\sigma\sigma*}\frac{2(1-n)}{n}\epsilon_* - \tilde{V}_{\sigma\sigma*}^2. \tag{8.50}$$

n	2	3	4	5	6
$\left\lvert-\frac{6}{5}f_{\rm NL}\eta_*^\perp\right\rvert$	6.8×10^{-5}	5.0×10^{-5}	2.6×10^{-5}	6.7×10^{-5}	1.2×10^{-4}

Table 82: Upper bounds from the spectral index on $\left\lvert-\frac{6}{5}f_{\rm NL}\eta_*^\perp\right\rvert$ for different n with $N_\phi = 60$.

This is largest for $\tilde{V}_{\sigma\sigma*} = \frac{n-1}{n}\epsilon_*$, which corresponds to $n_s = 1 - \frac{1}{2N_\phi} \geq 0.992$ which is outside of the observed value. The maximum of the absolute value in (8.49) will then be given by the upper or the lower bound on n_s (because in the interval of the observed value for n_s it can change sign). Table 82 gives the numerical constraints on $\left\lvert-\frac{6}{5}f_{\rm NL}\eta_*^\perp\right\rvert$ for integer values of n. We observe that the maximum value for $\eta_*^\perp$ is two orders of magnitude smaller than ϵ_* for $f_{\rm NL}$ of order unity. Moreover this limit is quite strong since the factor 0.325 (8.17) is a limit which asks some fine tuning to be reached. This factor can easily be ten or a hundred times smaller. Hence, in most cases $\eta_*^\perp$ will be a lot smaller than this limit.

To summarize, we know ϵ_* once we fix N_ϕ. We then determine $\tilde{V}_{\sigma\sigma*}$ using ϵ_* and the observational constraints on n_s. This leads to an upper bound for $|\eta_*^\perp|$ by imposing a value for $f_{\rm NL}$. However, to see when the turn exactly happens, we need to know the full evolution of $\eta^\perp$, not just its initial value. For this, some work needs to be done on the expression for $\eta^\perp$ given in (8.40), where we can eliminate unknown quantities (like the parameters of the potential) by using the expressions for the slow-roll parameters at horizon crossing:

$$\epsilon_* = \frac{n^2}{2}\frac{1}{\phi_*^2}, \qquad \tilde{V}_{\sigma\sigma*} = \frac{m(m-1)\beta\sigma_*^{m-2}}{\alpha\phi_*^n}. \tag{8.51}$$

It is then straightforward to compute:

$$\begin{aligned}\tilde{V}_{\sigma\sigma} &= \frac{V_{\sigma\sigma}}{\kappa^2 U} = \tilde{V}_{\sigma\sigma*}\left(\frac{\sigma}{\sigma_*}\right)^{m-2}\left(\frac{\epsilon}{\epsilon_*}\right)^{n/2},\\ \eta^\perp &= \eta_*^\perp\left(\frac{\sigma}{\sigma_*}\right)^{m-1}\left(\frac{\epsilon}{\epsilon_*}\right)^{n/2}\frac{2\frac{n-1}{n}\epsilon^{1/2} - \tilde{V}_{\sigma\sigma}\epsilon^{-1/2}}{2\frac{n-1}{n}\epsilon_*^{1/2} - \tilde{V}_{\sigma\sigma*}\epsilon_*^{-1/2}}.\end{aligned} \tag{8.52}$$

As already discussed, we want to express the time dependence in terms of ϵ which is directly related to ϕ. However, the expression for $\eta^\perp$ also depends on σ, and while a bound for its initial value at horizon-crossing can be given using (8.40) and the bounds on $\tilde{V}_{\sigma\sigma*}$ and $\eta_*^\perp$, we need to know how it evolves with time. For this we solve the field equation:

$$\dot{\sigma} = -\frac{m\beta}{\alpha}\frac{\sigma^{m-1}}{\phi^n}. \tag{8.53}$$

Inserting the solution (8.45) for ϕ into the equation for σ we find the following differential equation:

$$\frac{\mathrm{d}\sigma}{\sigma^{m-1}} = -\frac{m\beta}{\alpha}\frac{1}{\phi_*^n}\frac{\mathrm{d}t}{(1-t/N_\phi)^{n/2}}. \tag{8.54}$$

We see that we need to consider the special cases $m = 2$ and $n = 2$ separately. We start with the most general case $m \neq 2$ and $n \neq 2$, where (with σ_* the initial value of σ):

$$\begin{aligned}\sigma &= \sigma_*\left[1 + \frac{m(2-m)}{n(2-n)}\frac{\beta}{\alpha}\frac{\sigma^{m-2}}{\phi_*^{n-2}}\left(\left(1-\frac{t}{N_\phi}\right)^{1-n/2} - 1\right)\right]^{\frac{1}{2-m}}\\ &= \sigma_*\left[1 + \frac{1}{2}\frac{m-2}{m-1}\frac{n}{n-2}\frac{\tilde{V}_{\sigma\sigma*}}{\epsilon_*^{n/2}}\left(\epsilon^{n/2-1} - \epsilon_*^{n/2-1}\right)\right]^{\frac{1}{2-m}}.\end{aligned} \tag{8.55}$$

In the case $m \neq 2$ and $n = 2$, we have:

$$\begin{aligned}\sigma &= \sigma_* \left[1 + \frac{m(2-m)}{4\sigma_*^{2-m}} \frac{\beta}{\alpha} \ln\left(1 - \frac{t}{N_\phi}\right)\right]^{\frac{1}{2-m}} \\ &= \sigma_* \left[1 + \frac{1}{2}\frac{2-m}{m-1}\frac{\tilde{V}_{\sigma\sigma*}}{\epsilon_*} \ln\left(\frac{\epsilon_*}{\epsilon}\right)\right]^{\frac{1}{2-m}},\end{aligned} \tag{8.56}$$

while for $m = 2$ and $n \neq 2$:

$$\begin{aligned}\sigma &= \sigma_* \exp\left[\frac{2\beta}{\alpha}\frac{\phi_*^{2-n}}{n(2-n)}\left(\left(1 - \frac{t}{N_\phi}\right)^{1-n/2} - 1\right)\right] \\ &= \sigma_* \exp\left[\frac{n}{2(2-n)}\frac{\tilde{V}_{\sigma\sigma*}}{\epsilon_*^{n/2}}\left(\epsilon^{n/2-1} - \epsilon_*^{n/2-1}\right)\right].\end{aligned} \tag{8.57}$$

Inserting these expressions into (8.52) gives the ratio $\eta^\perp/\eta_*^\perp$. In the last case $m = 2$ and $n = 2$, these equations take a nicer form:

$$\sigma = \sigma_*\left(1 - \frac{t}{N_\phi}\right)^{\frac{\beta}{2\alpha}} = \sigma_*\left(1 - \frac{t}{N_\phi}\right)^{\frac{\tilde{V}_{\sigma\sigma*}}{2\epsilon_*}} = \sigma_*\left(\frac{\epsilon}{\epsilon_*}\right)^{-\frac{\tilde{V}_{\sigma\sigma*}}{2\epsilon_*}}, \qquad \frac{\eta^\perp}{\eta_*^\perp} = \left(\frac{\epsilon}{\epsilon_*}\right)^{-\frac{\tilde{V}_{\sigma\sigma*}}{2\epsilon_*}+\frac{3}{2}}. \tag{8.58}$$

8.5 Discussion

In figure 82, we use the expressions of the previous section to determine the regions of the parameter space of m and n where a turn of the field trajectory might happen before the end of the slow-roll regime. For this we want to verify when multiple-field effects start to play a role or, in terms of slow-roll parameters, we want to find when $\eta^\perp$ becomes of the same order as ϵ. We choose ϵ and not $\eta^\parallel$ because $\eta^\parallel$ is of the same order as ϵ for most cases except if $n \approx 2$ when it is much smaller.

First, we choose the maximum value of $|\eta_*^\perp|$ possible for $|-\frac{6}{5}f_{\rm NL}| = 1$ using the range of values for $\tilde{V}_{\sigma\sigma*}$ determined from the spectral index. Then we compute the maximum value of $|\eta^\perp|$ when $\epsilon = 0.1$. We choose this value of ϵ because this is already close to the end of inflation and the slow-roll approximation starts to break down after that point. Moreover, if the turn starts after this time, it is possible that there is not enough time for the isocurvature modes to decay. Finally, we plot the regions of the parameter space of m and n where $\eta^\perp$ is at least as large as ϵ at that time, meaning there is a turn of the field trajectory. We also assume that $N_\phi = 60$. These are the default values for the parameters $f_{\rm NL}$, N_ϕ and ϵ. Next we vary them to test the validity of these choices. We also explore the effects of a future improvement of the spectral index measurements.

The main conclusion of figure 82 is that for most m and n, the turn cannot happen before the end of the slow-roll regime, except in the top left part of the figures (small n and large m). For example, the simple quadratic case $m = 2$ and $n = 2$ (indicated by a small cross) is excluded.

The first figure shows that obviously the space of allowed parameters decreases if we want $f_{\rm NL}$ to be larger. In fact, imposing a larger $f_{\rm NL}$ is the same as imposing a smaller $\eta_*^\perp$. This does not change the evolution of $\eta^\perp$, only its initial condition, so that it will be harder to reach a final value of order ϵ.

In the second figure, we explore the effects of an improvement of the measurements of the spectral index by comparing the Planck result at 1σ $n_s = 0.968 \pm 0.006$ and 2σ $n_s =$

0.968 ± 0.012[1], with the accuracy expected with a CORE-like experiment [83] where the error bar would be of order $\Delta n_s = 0.0015$. We also add the case where the error bar becomes negligible. We see that the region where $f_{\rm NL}$ is at least of order unity is strongly dependent on the spectral index. Decreasing the error bars on n_s decreases the parameter region where $f_{\rm NL}$ is of order unity. We will see later that in fact it is the lower bound of n_s which matters. If a more accurate measurement would shift the central value of n_s, so that its lower bound would be slightly smaller than for Planck, then the size of the top-left region in this plot would increase. This is not indicated in the figure to keep the plot from being too busy, but $n_s = 0.94$ is sufficient to allow most of the parameter region in the figure ($m > 2$ and $n < 7$).

The third plot shows the effect of the parameter N_ϕ. We do not know exactly the total duration of inflation; the usual value is between 50 and 60 e-folds. Moreover, we cannot be sure that N_σ can be neglected, which means that N_ϕ is not necessarily the full duration of inflation after horizon-crossing. In this figure, we observe that the surface of the top left region diminishes for smaller N_ϕ. In fact, for N_ϕ smaller than 45 e-folds, it vanishes completely. The smaller N_ϕ, the harder it will be to build a model where $f_{\rm NL}$ is large.

The last figure is here to help to determine at what time the turn can occur. In the other figures, the only condition was before the end of the slow-roll regime. However, this regime is valid for most of the time after horizon-crossing. We can see that simply reducing ϵ by a factor two reduces a lot the allowed parameter region. This means that having a turn a few e-folds after horizon-crossing is extremely hard to have or even impossible. Most of the time the turn will happen near the end of slow-roll.

To explain these different behaviours, we first need to discuss $\tilde{V}_{\sigma\sigma*}$. It is determined from the spectral index and ϵ_* using equation (8.47) which contains two terms: $\frac{1}{2}(n_s - 1)$ which is negative and larger in absolute value for the lower bound on the spectral index, and ϵ_* which is positive and can be either smaller or larger than the first term. A small ϵ_* corresponds to small n and/or large N_ϕ. This means that in each of the four figures, the left (small n) corresponds to a negative $\tilde{V}_{\sigma\sigma*}$, while $\tilde{V}_{\sigma\sigma*}$ is positive on the right (large n). The transition happens between $n = 4$ and $n = 5$ for $N_\phi = 60$ for example. If we decrease N_ϕ, this value decreases and the transition is shifted to the left. The same happens if we increase the lower bound on the spectral index. In every figure this transition is indicated by a dashed vertical line. The sign of $\tilde{V}_{\sigma\sigma*}$ is important because this corresponds to the form of the potential V at horizon-crossing. If it is positive we have a valley, while a negative value describes falling off a ridge.

Now that we have seen the role of the other parameters on $\tilde{V}_{\sigma\sigma}$, we have to explain the different regions by looking at the equations for the evolution of the ratio $\eta^\perp/\eta^\perp_*$ for the different cases. In the valley case ($\tilde{V}_{\sigma\sigma*} > 0$), σ has to decrease to the minimum at $\sigma = 0$. However, because the potential has to be very flat at horizon-crossing, we start close to the minimum. Even if σ reaches its minimum before ϕ, $\eta^\perp$ does not have the time to become large because in $\eta^\perp$, the decrease of σ is opposed by the increase of ϵ. Hence, there is no allowed parameter region to the right of the dashed vertical line in the figures.

In the region of negative $\tilde{V}_{\sigma\sigma*}$, the situation is the opposite: σ increases to fall from the almost flat ridge where it started. Hence in $\eta^\perp$ we have the effect of both ϵ and σ increasing. After inserting σ for the different cases into (8.52), the only dependence on m appears in the ratio $(m-2)/(m-1)$ which tends to 1 when m increases. This explains the asymptotic behaviour which appears on the right-hand side of the allowed region.

Looking at the different expressions for σ, we also see that the largest $\tilde{V}_{\sigma\sigma*}$ in absolute value makes σ increase the fastest. This implies that the lower bound on the spectral index is the

[1] We use the 1σ error bars on n_s everywhere else in this chapter because even if it change exact numerical values, the general conclusion remains the same.

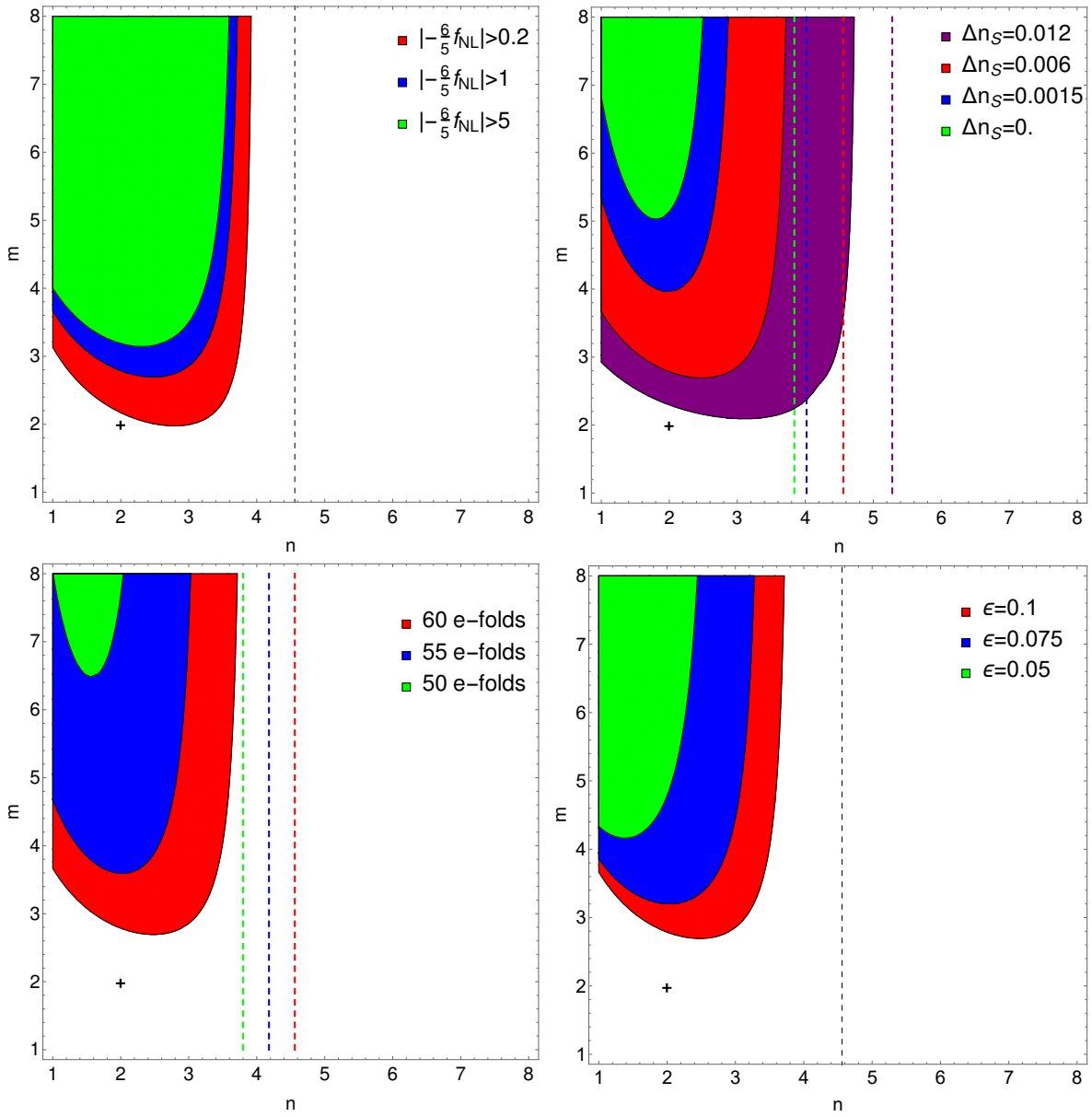

Figure 82: The regions of the parameter space of m and n where the turn of the field trajectory can occur before the end of the slow-roll regime. In the top left figure, these regions are determined for several values of $f_{\rm NL}$: $|-\frac{6}{5}f_{\rm NL}|$ larger than 5 (green), 1 (blue) or 0.2 (red). In the top right figure, we explore different error bars of the spectral index: the Planck constraint at 1σ $n_s = 0.968 \pm 0.006$ (red) and 2σ $n_s = 0.968 \pm 0.012$ (purple), $n_s = 0.968 \pm 0.0015$ in blue (CORE-like experiment [83]) and negligible error bars in green. On the bottom left, different values of N_ϕ are represented: 50 (green), 55 (blue) and 60 (red). The last plot changes the constraint on ϵ to check when the turn can occur: $\epsilon = 0.05$ (green), 0.075 (blue) and 0.1 (red). The dashed vertical lines indicate the change of sign of $\tilde{V}_{\sigma\sigma*}$, which depends on n, N_ϕ and n_s: it is necessarily positive on the right-hand side of this line. The small cross highlights that the double quadratic potential ($m = n = 2$) is excluded in all plots.

most important to obtain $\tilde{V}_{\sigma\sigma *}$. When n decreases, larger (in absolute value) $\tilde{V}_{\sigma\sigma *}$ are possible, which explains why smaller m are allowed. But in σ there are also terms which decrease when n becomes smaller and which compensate this effect, which is why for even smaller n the minimum required value of m starts to increase again.

At the end of section 8.2, the difficulty, or at least the high level of fine-tuning, needed for a model where $f_{\rm NL}$ is of order unity or more in slow-roll has been highlighted. Here, we showed explicitly that this is even impossible most of the time for simple monomial potentials. However, some examples exist, when $m > 4$ and $n < 4$ generally. We also showed that N_ϕ has to be close to the total number of e-folds after horizon-crossing which should be as large as possible given other constraints (around 60 e-folds), which implies that the turn of the field trajectory is quick. This also means that slow-roll parameters like ϵ_* and $\eta_*^{\parallel}$ are exactly the same as in the purely single-field case. However, the observables n_s and $f_{\rm NL}$ are different. Adding a second field which is responsible for the non-negligible $f_{\rm NL}$ can help some single-field models which were not working well given the Planck constraints on n_s to go back into the allowed range of parameters. However, this asks a lot of fine-tuning of the potential of the second field. For $f_{\rm NL}$ to be of order unity or more, this asks even more fine-tuning as only the lowest spectral index values will work. This also means that the improvement of the spectral index measurements expected with a satellite like CORE would seriously constrain the possibility of having a large $f_{\rm NL}$, especially if the central value of the spectral index moves closer to the upper bound from Planck.

We have also seen that in the cases that do work, most of the time the turn is near the end of the slow-roll period. This means that ϵ and the other parameters are already of order 0.1 at the start of the turn. Then parameters like $\eta^{\parallel}$ and $\eta^{\perp}$ can easily become of order 1 or more during the turn when things are getting more violent. The slow-roll approximation is then broken anyway. If the turn happens a bit later, we can expect that isocurvature modes will not have enough time to vanish before the end of inflation (this does not exclude the existence of some cases where they vanish in time, but only a numerical study of such examples is possible). Finally, we can imagine a case where the turn has not started when ϕ reaches the minimum of its potential. If this happens, there is a period of large ϵ (which would be the end of inflation in the single-field case). Again, during this period the slow-roll approximation is no longer valid. Therefore, these different situations show the need to understand what happens if the very useful slow-roll approximation is not sufficient. This is the topic of the next chapter.

Chapter 9

Beyond the slow-roll regime

The previous chapter showed that it is difficult to have $f_{\rm NL}$ not be slow-roll suppressed in the slow-roll regime. Is the situation the same if we leave this regime for a short period? The case of potentials with a separable Hubble parameter has been worked out in [50]. Here we discuss different cases of sum-separable potentials where this can happen and we will show that like in the slow-roll situation, only the homogeneous part of the solution of (7.47) is relevant once isocurvature modes have vanished. This means we will use the same quasi-single-field initial conditions at horizon-crossing as at the end of section 8.2: $V_* \ll U_*$ and $|V_{\sigma *}| \ll |U_{\phi *}|$ while $|V_{\sigma\sigma *}U_{\phi *}^2| \gg |U_{\phi\phi *}V_{\sigma *}^2|$ and $|V_{\sigma\sigma *}V_{\sigma *}^2| \ll |U_{\phi\phi *}U_{\phi *}^2|$.

9.1 Two kinds of turns

We identified two different cases, illustrated in figure 91, where the slow-roll approximation stops to be valid during the turn. In figure 91, the main differences of the two situations are shown. With potentials of a quite similar form, we have the possibility for two different trajectories depending on the direction before and after the turn. In the previous chapter, the importance of the parameters ϵ and $\eta^\perp$ to study the turn has been highlighted. Graphically they are useful to determine when the turn occurs and when the slow-roll regime is broken.

The first case is the one studied in the previous chapter. We determined that for a simple monomial potential, if the turn is possible before ϕ reaches the minimum of its potential, it is more likely to happen in the last few e-folds when slow-roll parameters are already of order 10^{-1}, at the limit of the slow-roll approximation. Then, during the turn, η parameters may become of order unity or more, which completely invalidates the idea of an expansion in terms of small slow-roll parameters. The turn is still early enough to have $\eta^\perp$ small again at the end of inflation to make the isocurvature mode vanish. In this case the direction of the field trajectory is the same before and after the turn. This is compatible with a monomial potential where we established that N_σ has to be small compared to N_ϕ and the turn is then short.

In the second case, perpendicular terms are still negligible when ϵ becomes of order 10^{-1}. Then, like in single-field inflation, ϵ continues to grow. This is the end of the slow-roll regime. From (7.12) we see that this makes $\eta^\parallel$ also become large (in absolute value) and a maximum of ϵ is reached when $\eta^\parallel = -\epsilon$. A short time after that point, ϵ starts to decrease very fast as the $\eta^\parallel$ term dominates in $\dot\epsilon$. A large $\eta^\parallel$ also has an effect on the perpendicular parameter $\eta^\perp$ which has been negligible until then. It is possible that $\eta^\perp$ becomes large and that the turn will occur after a few e-folds at most if $f_{\rm NL}$ is of order unity, see appendix D. Hence, it is possible to have the turn starting with $\epsilon \ll 1$. This is also motivated by the assumption of isocurvature modes vanishing before the end of inflation. Indeed, this requires a turn not too close to the end of inflation ($\epsilon = 1$) which is the case if ϵ is small compared to one during the turn. In this type of

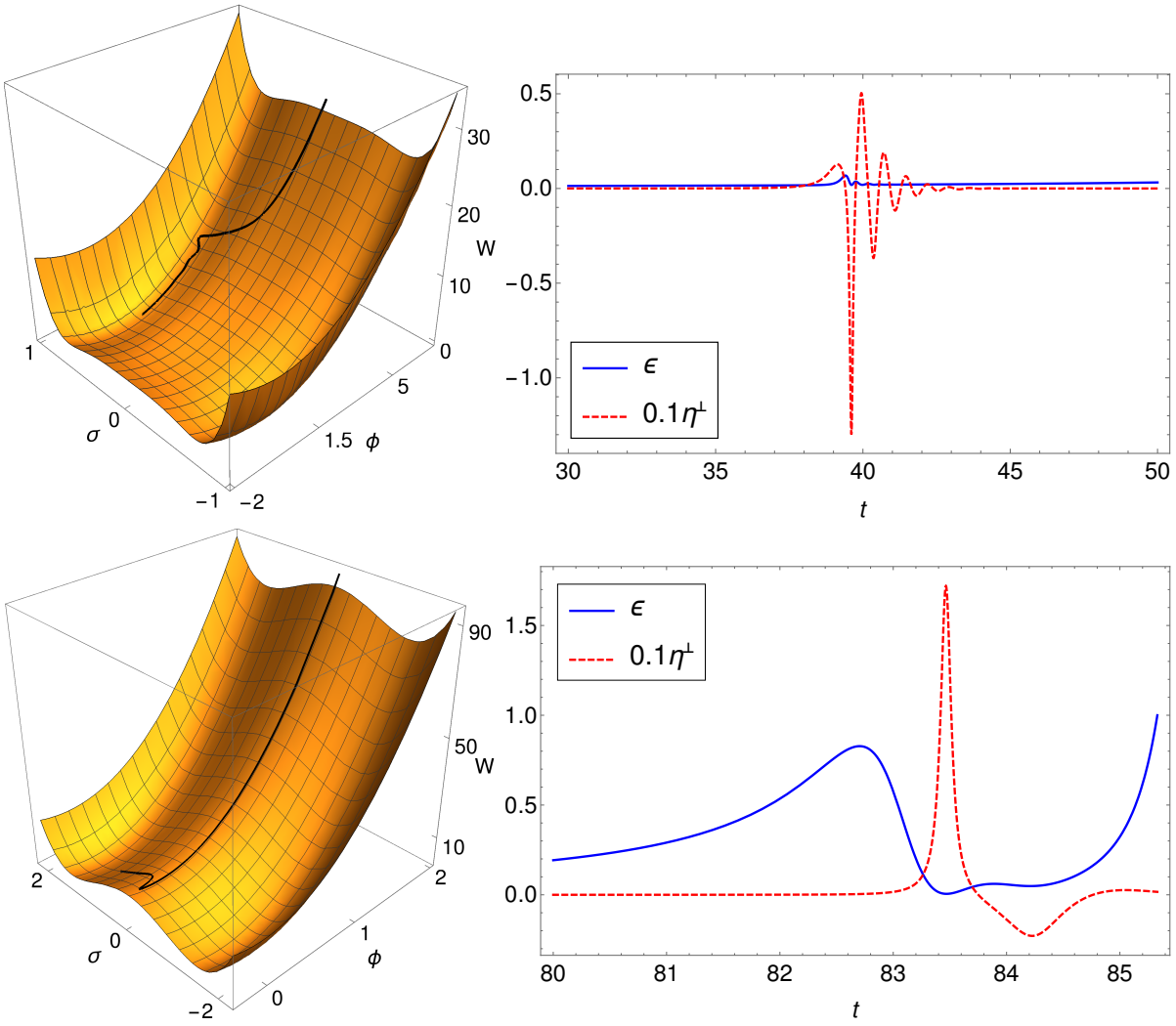

Figure 91: Illustrations of the two different types of turn where the slow-roll approximation is broken. On the left, the field trajectory is displayed in black on the potential while on the right the slow-roll parameters ϵ and $\eta^{\perp}$ are shown for a typical example. The top correspond to what we call the first type (see sections 10.3.1 and 10.3.2 for examples), while the plots at the bottom show the second type (see sections 10.1, 10.4.1 and 10.4.2 for examples).

turn, the direction is not the same before and after. Before the turn ϕ is dominating but also near the minimum of its potential, while σ is still at a local maximum. Inflation ends when ϕ is still near its minimum but σ is also evolving towards its own minimum.

In both theses cases, we established that the slow-roll approximation can be broken. We know that solving the equations without any approximation is not possible, even in the simple case of a sum potential. However, we have also seen that ϵ is small at the start of the turn simply because of the assumption of vanishing isocurvature modes. Moreover, in $\dot{\epsilon}$ (7.12), there is a factor ϵ in front. This means that when ϵ is small, ϵ cannot evolve very fast and will stay small during a short period like the turn, unless the turn is very sharp with η parameters becoming very large. Hence during the turn, except in the most extreme cases we do not treat, we still have that ϵ is small compared to one which will play an important role in this chapter.

In the first type of turn, this hypothesis of small ϵ has the important consequence that the slow-roll approximation is in fact broken only for the field σ. Indeed, in the field equation (7.2), each field can only affect the other through H which evolves slowly if $\epsilon \ll 1$. Hence, even if σ starts to evolve fast, it is only a small perturbation for ϕ which continues to evolve slowly during and after the turn until near the end of inflation when $\epsilon \approx \kappa^2\dot{\phi}^2/2$ becomes of order unity. Hence, the derivatives of ϕ of order two and more are negligible. This can be used to simplify the slow-roll parameter expressions from (7.6), keeping only the terms which are larger than order slow-roll:

$$\eta^{\parallel} = \frac{\ddot{\sigma}\dot{\sigma}}{\dot{\phi}^2+\dot{\sigma}^2}, \qquad \eta^{\perp} = -\frac{\ddot{\sigma}\dot{\phi}}{\dot{\phi}^2+\dot{\sigma}^2}, \qquad \xi^{\parallel} = \frac{\dddot{\sigma}\dot{\sigma}}{\dot{\phi}^2+\dot{\sigma}^2} \qquad \text{and} \qquad \xi^{\perp} = -\frac{\dddot{\sigma}\dot{\phi}}{\dot{\phi}^2+\dot{\sigma}^2}. \tag{9.1}$$

Using this, a direct computation gives useful relations between the parallel and perpendicular parameters of the same order:

$$e_{1\phi}\eta^{\parallel} = -e_{1\sigma}\eta^{\perp} \qquad \text{and} \qquad e_{1\phi}\xi^{\parallel} = -e_{1\sigma}\xi^{\perp}. \tag{9.2}$$

In the second type of turn, the slow-roll approximation is broken for the two fields, so that these relations are then not valid. However, there is also an important approximation we can make in this case. Before the turn, the slow-roll approximation is broken during the period of large ϵ. Having ϵ large for some time also means that H decreases a lot during that period. This means that during the turn, we have:

$$H^2 \ll H_*^2. \tag{9.3}$$

A brief remark about the end of inflation is necessary. We use the common definition that the period of inflation finishes when $\epsilon = 1$. However, in the second type of turn, ϵ can be larger than 1 for a very small number of e-folds before the turn. A more complete definition of the end of inflation is then that $\epsilon = 1$ with $U \ll U_*$ and $V \ll V_*$, which ensures that the second field as well had time to evolve.

The main tool in this chapter is the differential equation (7.47) which we will call the g_{int} equation. We have already solved it during the period of slow-roll which goes from horizon-crossing to the turn or to ϵ of order 1. We also know the exact homogeneous solution of the full equation. The only remaining work is to understand what happens to the particular solution beyond the slow-roll approximation. We will each time follow the same method. First we discuss each equation in the more general case, only supposing that $\eta^{\parallel}$ and $\eta^{\perp}$ are large while $\epsilon \ll 1$. Then, when needed to go further, we will study separately each case using (9.2) or (9.3) depending on the type of turn considered.

9.2 Green's functions

Beyond the slow-roll regime, we have to solve the second-order differential equation (7.23) to compute the Green's functions (recalling that $\bar{v}_{22}(t)$ and $G_{22}(t,t_*)$ obey the same equation). We assume that the solution has the form $\bar{v}_{22} \propto f e_{1\phi} e_{1\sigma}$, similar to the slow-roll case (8.23). One motivation is that, during the turn, the dominant term will be $(\eta^\perp)^2$ and this is canceled by this form of solution. Substituting this into (7.23), we find a differential equation for the function f:

$$\begin{aligned} e_{1\phi}e_{1\sigma}\,\ddot{f} + \left[2\eta^\perp(e_{1\sigma}^2 - e_{1\phi}^2) + (3+\epsilon+2\eta^\parallel)e_{1\phi}e_{1\sigma}\right]\dot{f} \\ + \left[2\epsilon\eta^\perp(e_{1\sigma}^2 - e_{1\phi}^2) + (6\epsilon + 2\epsilon^2 + 4\epsilon\eta^\parallel)e_{1\phi}e_{1\sigma}\right] f = 0. \end{aligned} \tag{9.4}$$

In the slow-roll regime, a first-order expansion of this equation gives

$$e_{1\phi}e_{1\sigma}\,\dot{f} + 2\epsilon\, e_{1\phi}e_{1\sigma} f = 0, \tag{9.5}$$

and then it is easy to show that $f = H^2$ to find the slow-roll result (8.23). During this initial period of slow roll, having a first-order equation as a very good approximation means that the second mode needed to solve the full equation rapidly becomes negligible. Once slow roll is broken, we only need to study how the remaining mode evolves.

In the general case, an analytical solution cannot be found. However, if we take a solution of the form $f = H^\alpha$ by inspiration from the slow-roll solution (because that is the form of the solution until the moment when the slow-roll regime is broken), (9.4) becomes:

$$\begin{aligned} &e_{1\phi}e_{1\sigma}\left[\ddot{\alpha}\ln H + \dot{\alpha}^2(\ln H)^2 - \alpha\dot{\alpha}\ln H + \dot{\alpha}\left(-2\epsilon + (3+\epsilon+2\eta^\parallel)\ln H\right)\right. \\ &\left.+(\alpha-2)(\alpha-1)\epsilon^2 - 4(\alpha-1)\epsilon\eta^\parallel - 3(\alpha-2)\epsilon\right] + 2\eta^\perp(e_{1\sigma}^2 - e_{1\phi}^2)\left[\dot{\alpha}\ln H + (1-\alpha)\epsilon\right] = 0. \end{aligned} \tag{9.6}$$

There are two interesting values for α which are 1 and 2. They can be linked to the two regimes already discussed previously where the slow-roll approximation is not valid.

We can see directly that the lowest order term in slow-roll is canceled by $\alpha = 2$ as expected. Moreover, the ϵ^2 term also vanishes with this value. This means that when ϵ becomes larger while the other parameters are still small compared to 1, $f = H^2$ is still a good approximation. This is exactly what happens at the end of the slow-roll regime just before the second type of turn, when the first field is near the minimum of its potential. Then, the complete solutions for the Green's functions are:

$$\bar{v}_{22} = \frac{H^2 e_{1\phi}e_{1\sigma}}{H_*^2 e_{1\phi*}e_{1\sigma*}}, \qquad \bar{v}_{32} = \frac{H^2}{H_*^2 e_{1\phi*}e_{1\sigma*}}\left(-2\epsilon e_{1\phi}e_{1\sigma} + \eta^\perp(e_{1\sigma}^2 - e_{1\phi}^2)\right). \tag{9.7}$$

The same integration as in the slow-roll case works to compute $\bar{v}_{12}$:

$$\bar{v}_{12} = \frac{Z - Z_*}{W_* e_{1\phi*}e_{1\sigma*}}, \tag{9.8}$$

with Z previously introduced in (8.22).

The other interesting value $\alpha = 1$ cancels every second-order term in the equation. Hence, this is a good solution when $\eta^\perp$ and $\eta^\parallel$ are large but ϵ is small compared to 1, hence during the turn. The solutions are then,

$$\bar{v}_{22} = \frac{H}{\mathcal{N}} e_{1\phi}e_{1\sigma}, \qquad \bar{v}_{32} = \frac{H}{\mathcal{N}}\left(-\epsilon e_{1\phi}e_{1\sigma} + \eta^\perp(e_{1\sigma}^2 - e_{1\phi}^2)\right), \tag{9.9}$$

where $\mathcal{N}$ is a constant used to satisfy the continuity of $\bar{v}_{22}$. If we call the time when this solution becomes better than the previous one t_0, we have $\mathcal{N} = \frac{H_*^2}{H(t_0)} e_{1\phi *} e_{1\sigma *}$.

We cannot directly compute $\bar{v}_{12}$ in this regime. However, ϵ is supposed to be very small compared to 1 which means that H is almost a constant. We can then write $H(t) = H_0 + \delta H(t)$ where $\delta H(t)$ is only a small correction. Taking the square of this expression and doing a first-order slow-roll expansion gives $\delta H(t) = \frac{1}{2}\frac{H^2 - H_0^2}{H_0}$. Then it is easy to deduce $H(t) = \frac{1}{2}\frac{H^2 + H_0^2}{H_0}$. Substituting this into (9.9), we can perform the integration and we get:

$$\bar{v}_{12} = -\frac{H_0^2}{H_*^2}\frac{S - S_0}{4 e_{1\phi *} e_{1\sigma *}} + \frac{Z/2 + Z_0/2 - Z_*}{W_* e_{1\phi *} e_{1\sigma *}}, \tag{9.10}$$

with $S \equiv e_{1\phi}^2 - e_{1\sigma}^2$.

9.3 The g_{int} equation during the turn

A first use of the Green's functions during the turn computed in the previous section is to insert them into (7.47) to simplify the right-hand side of the equation: r.h.s. $\equiv K_{22}(\bar{v}_{22})^2 + K_{23}\bar{v}_{22}\bar{v}_{32} + K_{33}(\bar{v}_{32})^2$. After this step, every term of r.h.s. has one factor depending on the basis components: $e_{1\phi}^2 e_{1\sigma}^2$, $e_{1\phi} e_{1\sigma}(e_{1\sigma}^2 - e_{1\phi}^2)$ or $(e_{1\sigma}^2 - e_{1\phi}^2)^2$. We use the relation $(e_{1\sigma}^2 - e_{1\phi}^2)^2 = 1 - 4e_{1\phi}^2 e_{1\sigma}^2$ coming from the normalization of the basis to eliminate one of the factors. Having terms with these factors permits us to use equations (8.10) and (8.11) to eliminate the slow-roll parameters χ, $\tilde{W}_{221}$ and $\tilde{W}_{222}$. Finally, we obtain:

$$\begin{aligned}
\text{r.h.s.} =& \epsilon \left(\frac{H}{\mathcal{N}}\right)^2 \Big\{ 2(\eta^\perp)^4(\epsilon + 3\eta^\parallel) + e_{1\phi}^2 e_{1\sigma}^2 \Big[(\eta^\perp)^4 \left(-18 - 14\epsilon - 36\eta^\parallel\right) - 2(\eta^\perp)^3 \xi^\perp \\
&+ (\eta^\perp)^2 \left(-3\tilde{W}_{111} - 18\epsilon - 6\epsilon^2 - 24\epsilon\eta^\parallel + 18(\eta^\parallel)^2 + 6\xi^\parallel + 2\epsilon^2\eta^\parallel + 10\epsilon(\eta^\parallel)^2 + 12(\eta^\parallel)^3 \right. \\
&\left. + 2\epsilon\xi^\parallel + 12\eta^\parallel\xi^\parallel \right) + \eta^\perp\xi^\perp \left(6\epsilon - 6\eta^\parallel - 2\epsilon\eta^\parallel - 10(\eta^\parallel)^2 - 2\xi^\parallel\right) + 2\eta^\parallel(\xi^\perp)^2 + 3\eta^\perp\eta^\parallel\tilde{W}_{211} \Big] \\
&+ e_{1\phi} e_{1\sigma}(e_{1\sigma}^2 - e_{1\phi}^2) \Big[-6(\eta^\perp)^5 + (\eta^\perp)^3 \left(-6\epsilon + 18\eta^\parallel + 2\epsilon^2 + 12\epsilon\eta^\parallel + 18(\eta^\parallel)^2 + 6\xi^\parallel\right) \\
&- 4\eta^\parallel(\eta^\perp)^2\xi^\perp \Big] \Big\}.
\end{aligned} \tag{9.11}$$

At first sight, this expression does not look simpler than the original one. However, it has an important new feature which is the ϵ factor in front of the whole expression. In fact, in the computation every term without ϵ cancels. Recalling that the main assumption we made is that ϵ is small during the turn, this indicates that r.h.s. might be negligible during the turn, which means that only the homogeneous solution (which is known) is needed. In the rest of this section we will show that this is indeed the case.

First we have to figure out compared to what r.h.s. has to be negligible. One way to answer this question is to use what we already know about the solution: the slow-roll expression given in (8.15) which we write as $\dot{g}_{\text{int}} = P_{\text{sr}} + h_{\text{sr}}$ with:

$$P_{\text{sr}} = 2\epsilon(\epsilon + \eta^\parallel)(\bar{v}_{22})^2 + 2\epsilon\bar{v}_{22}\bar{v}_{32}, \qquad h_{\text{sr}} = -\frac{e_{1\phi *}^2 \tilde{V}_{\sigma\sigma *} - e_{1\sigma *}^2 \tilde{U}_{\phi\phi *}}{e_{1\phi *} e_{1\sigma *}} \eta^\perp \bar{v}_{22}. \tag{9.12}$$

Here we used that $\bar{v}_{32} = -\chi\bar{v}_{22}$ in the slow-roll regime. P_{sr} corresponds to the particular solution while h_{sr} is the homogeneous part. We will study these two parts of the solution in the two next sections to see how they evolve beyond the slow-roll regime. In section 9.6, we will discuss why they are sufficient to solve the g_{int} equation even beyond the slow-roll approximation. We start by focusing on this homogeneous solution.

9.4 Fate of the slow-roll homogeneous solution

As already discussed at the end of chapter 7, the homogeneous slow-roll solution is also a homogeneous solution of the full second-order equation. Hence, we can use it and substitute it into (7.47). Then we look at each term (order1 $\propto \dot{h}_{\rm sr}$, order2 $\propto \ddot{h}_{\rm sr}$ and order3 $\propto \dddot{h}_{\rm sr}$) individually and not at the total sum because that is obviously zero. We want to show that these terms are large compared to r.h.s., so that, during the turn, r.h.s. is only a small correction which can be neglected to get a good approximation of $g_{\rm int}$. To compute the three left-hand side terms, we use the same steps as in deriving (9.11) to get:

$$\begin{aligned}
\text{order1} =& -\frac{H}{\mathcal{N}}\frac{e_{1\phi*}^2\tilde{V}_{\sigma\sigma*}-e_{1\sigma*}^2\tilde{U}_{\phi\phi*}}{e_{1\phi*}e_{1\sigma*}}\left\{(e_{1\sigma}^2-e_{1\phi}^2)\left[-6(\eta^\perp)^4-2(\eta^\perp)^3\xi^\perp\right]+e_{1\phi}e_{1\sigma}\right.\\
&\left.\times\left[6(\eta^\perp)^5+(\eta^\perp)^3\left(6(\eta^\parallel)^2+2\xi^\parallel\right)-8\eta^\parallel\xi^\perp(\eta^\perp)^2+2\eta^\perp(\xi^\perp)^2+3(\eta^\perp)^2\tilde{W}_{211}\right]\right\}\\
\text{order2} =& \frac{H}{\mathcal{N}}\frac{e_{1\phi*}^2\tilde{V}_{\sigma\sigma*}-e_{1\sigma*}^2\tilde{U}_{\phi\phi*}}{e_{1\phi*}e_{1\sigma*}}\left\{(e_{1\sigma}^2-e_{1\phi}^2)\left[(\eta^\perp)^4\left(-3+\epsilon-6\eta^\parallel\right)+2(\eta^\perp)^3\xi^\perp\right]+e_{1\phi}e_{1\sigma}\right.\\
&\left.\times\left[(\eta^\perp)^3\left(6\eta^\parallel-2\epsilon\eta^\parallel+12(\eta^\parallel)^2\right)+(\eta^\perp)^2\xi^\perp\left(-3+\epsilon-10\eta^\parallel\right)+2\eta^\perp(\xi^\perp)^2\right]\right\}\\
\text{order3} =& \frac{H}{\mathcal{N}}\frac{e_{1\phi*}^2\tilde{V}_{\sigma\sigma*}-e_{1\sigma*}^2\tilde{U}_{\phi\phi*}}{e_{1\phi*}e_{1\sigma*}}\left\{(e_{1\sigma}^2-e_{1\phi}^2)\left[(\eta^\perp)^4\left(-3-\epsilon+6\eta^\parallel\right)-4(\eta^\perp)^3\xi^\perp\right]+e_{1\phi}e_{1\sigma}\right.\\
&\left.\times\left[6(\eta^\perp)^5+(\eta^\perp)^3\left(-6\eta^\parallel+2\epsilon\eta^\parallel-6(\eta^\parallel)^2+2\xi^\parallel\right)+(\eta^\perp)^2\xi^\perp\left(3-\epsilon+2\eta^\parallel\right)+3(\eta^\perp)^2\tilde{W}_{211}\right]\right\}.
\end{aligned} \tag{9.13}$$

We separate our equations into parts easier to compare. We start by comparing the factors in front of the braces of each expression in (9.11) and (9.13) which are:

$$\frac{H}{\mathcal{N}}\frac{e_{1\phi*}^2\tilde{V}_{\sigma\sigma*}-e_{1\sigma*}^2\tilde{U}_{\phi\phi*}}{e_{1\phi*}e_{1\sigma*}} \qquad \text{and} \qquad \epsilon(\frac{H}{\mathcal{N}})^2. \tag{9.14}$$

After simplifying the common factor $H/\mathcal{N}$ and inserting $\mathcal{N}=H_*^2e_{1\phi*}e_{1\sigma*}/H_0$ from (9.9), we use the quasi single-field initial conditions at horizon-crossing to write (9.14) as

$$\tilde{V}_{\sigma\sigma*}\frac{H_*^2}{H^2} \qquad \text{and} \qquad \epsilon. \tag{9.15}$$

The discussion about the spectral index from section 8.2 is still valid, because the only difference from the slow-roll regime is the value of $\bar{v}_{12e}$, but for a large enough value (larger than four) the dependence on $\bar{v}_{12e}$ in (7.39) disappears and (8.26) can be used. Hence, $\tilde{V}_{\sigma\sigma*}$ is typically of order 10^{-2}, or at least not hugely smaller.

As for the size of ϵ and H_*^2/H^2, this depends on the type of turn. For the first type, ϵ is still of order slow-roll but it can be easily larger than $\tilde{V}_{\sigma\sigma*}$ by an order of magnitude. However H_*^2/H^2 is also larger than one. Moreover, if ϵ had enough time to increase since horizon-crossing, the situation is the same for H_*^2/H^2 because H decreases faster if ϵ is larger. During a few dozens of e-folds with ϵ of order slow-roll, it can also increase by an order of magnitude. This means that both terms will be of the same order during the turn in this case, or at least that neither of them is hugely smaller or larger than the other. For the second type of turn, the situation is different. During the turn, ϵ is again of order slow-roll so it is not hugely larger than $\tilde{V}_{\sigma\sigma*}$. However, because of the period of large ϵ, we know that $H_*^2/H^2 \gg 1$ from (9.3). Hence the factor in front of order1, order2 and order3 is large compared to the one in r.h.s. in this case.

Next we focus on the second part of each expression, which is the part inside the braces and which is a complicated expression depending on basis components and slow-roll parameters. We start with some comments on the factors $e_{1\phi}e_{1\sigma}$ and $e_{1\sigma}^2 - e_{1\phi}^2$. By definition of the basis, $e_{1\phi}e_{1\sigma}$ goes from $-\frac{1}{2}$ to $\frac{1}{2}$ and $e_{1\sigma}^2 - e_{1\phi}^2$ from -1 to 1 and when one is at an extremum, the other one vanishes. When one vanishes, the leftover slow-roll parameter terms are similar in the different expressions. It is also not possible to have both of them small compared to one at the same time, hence the term in r.h.s. without a factor depending on the basis is not an issue. Hence, we can forget about these basis component factors which cannot change the conclusion.

The different expressions depend on all the first and second-order slow-roll parameters, except χ, $\tilde{W}_{221}$ and $\tilde{W}_{222}$ which have been eliminated using the relations specific to sum potentials (8.10) and (8.11). The first step is to study the cancellations of the left-hand side terms. An obvious one is when $\eta^\perp$ vanishes because it multiplies every term in (9.13); the homogeneous solution vanishes in that case. It also multiplies every term in r.h.s. except the one term $2\eta^\parallel(\xi^\perp)^2$. However $\xi^\perp$ is also small when $\eta^\perp$ becomes small. During the turn of the field trajectory, it is usual that the slow-roll parameters oscillate, hence $\eta^\perp$ can vanish several times. At those times our hypothesis that r.h.s. is much smaller than the other terms is not valid and we cannot neglect the particular solution. However, we will show in section 9.6 that we have a way of dealing with this. Apart from this vanishing of $\eta^\perp$, there is no other possibility to cancel order1, order2 and order3 simultaneously. Indeed the expressions contain similar terms, but with opposite signs or different numerical constants.

Once we know there are no cancellations in the left-hand side terms (apart from the moments when $\eta^\perp = 0$), we can compare their expressions to r.h.s. and verify they are of the same order. As the expressions contain terms up to order five in slow-roll parameters, two cases have to be differentiated. First, the slow-roll parameters can be of order unity. Then the powers do not matter and most of the terms have to be taken into account. We remark that the terms are similar on each side of the equation, and that the numerical constants are also of the same order, so that r.h.s. cannot be very large compared to the other expressions in this case. However, the slow-roll parameters can also become larger than order unity and this situation requires more discussion. An important remark is that when the slow-roll approximation is broken, the slow-roll cancellations in (7.9) disappear which means that $\xi^\parallel$ and $\xi^\perp$ are of order a few times $\eta^\parallel$ and $\eta^\perp$ respectively, and not of order $(\eta^\parallel)^2$ and $(\eta^\perp)^2$. Using the expressions for $\dot{\eta}^\parallel$ and $\dot{\eta}^\perp$ in (7.12), we can see that when $|\eta^\parallel|$ is at a maximum, $|\eta^\perp|$ has to be of the same order because the only possibility to cancel the largest term $(\eta^\parallel)^2$ in the derivative expression is to have $(\eta^\perp)^2$ of the same order. However, when $|\eta^\perp|$ is at a maximum, we can see in a similar way that $|\eta^\parallel|$ must be of the order of a few at most.

Then we can study what happens if the perpendicular parameters are the largest (near the maximum of $|\eta^\perp|$). If $\eta^\parallel$ is only a few, the dominant terms in r.h.s. and the order1,2,3 are the ones in $(\eta^\perp)^5$ and $(\eta^\perp)^4$ (or the equivalent $(\eta^\perp)^3\xi^\perp$). The same terms exist in all the different expressions meaning the part inside the braces has to be of the same order in general. If, on the other hand, the parallel parameters are the largest, there is a term in $(\eta^\perp)^2(\eta^\parallel)^3$ in r.h.s. which does not exist in the other expressions. However, as discussed a few lines earlier, $\eta^\perp$ is also of the same order as $\eta^\parallel$ at that time. Using this, the dominant terms are actually of order $(\eta^\perp)^5$. Again we find similar terms inside the braces for the different expressions which have to be of the same order. Finally, the only term in r.h.s. that has no equivalent in the other expressions is $(\eta^\perp)^2\tilde{W}_{111}$. This term, which is only of order three, can never be dominant because $\tilde{W}_{111}$ cannot be large enough to make this term a lot larger than the order five ones because this parameter is also in the derivative of $\xi^\parallel$ (see (7.12)).

Hence, we have established that the terms inside the braces are of the same order in the general case for each expression in (9.11) and (9.13). This is exactly the situation for the second type of turn where the only hypothesis not used (9.3) has no consequence for the terms inside

the braces. However, for the first type of turn, the relations (9.2) between the parallel and perpendicular slow-roll parameters of the same order can change the result. To verify this, we substitute them into (9.11) and (9.13). We also introduce the notation with $\{\}$ in subscript, meaning we consider only the terms inside the braces. The computation gives

$$\begin{aligned}
\text{r.h.s.}_{\{\}} &= -e_{1\phi}^2 e_{1\sigma}^2 \left[(\eta^\perp)^2 \left(3\tilde{W}_{111} + 6\epsilon^2 + 18\epsilon\right) - 6\eta^\perp \xi^\perp \epsilon\right] \\
&\quad - e_{1\phi} e_{1\sigma}^3 \left[3(\eta^\perp)^2 \tilde{W}_{211} + (\eta^\perp)^3 \left(-2\epsilon^2 - 12\epsilon\right)\right] - e_{1\phi} e_{1\sigma} (\eta^\perp)^3 \left(2\epsilon^2 - 6\epsilon\right) + 2e_{1\phi}^2 (\eta^\perp)^4 \epsilon, \\
\text{order1}_{\{\}} &= \frac{e_{1\sigma}}{e_{1\phi}} \left[4\eta^\perp (\xi^\perp)^2 + 12(\eta^\perp)^5 + 6(\eta^\perp)^2 \tilde{W}_{211}\right] + \frac{e_{1\sigma}^3}{e_{1\phi}} \left[-4\eta^\perp (\xi^\perp)^2 - 6(\eta^\perp)^2 \tilde{W}_{211}\right] \\
&\quad + e_{1\sigma}^2 \left[4(\eta^\perp)^3 \xi^\perp - 24(\eta^\perp)^4\right] + 4(\eta^\perp)^3 \xi^\perp + 12(\eta^\perp)^4,
\end{aligned}$$

$$\begin{aligned}
\text{order2}_{\{\}} &= 12\frac{e_{1\sigma}}{e_{1\phi}} (\eta^\perp)^5 - 48\frac{e_{1\sigma}^3}{e_{1\phi}} (\eta^\perp)^5 - 2e_{1\phi} e_{1\sigma} \left[2\eta^\perp (\xi^\perp)^2 + (\eta^\perp)^2 \xi^\perp (\epsilon - 3)\right] \\
&\quad - 2e_{1\sigma}^2 \left[14(\eta^\perp)^3 \xi^\perp + (\eta^\perp)^4 (4\epsilon - 12)\right] + 4(\eta^\perp)^3 \xi^\perp - 6(\eta^\perp)^4 + 2(\eta^\perp)^4 \epsilon, \\
\text{order3}_{\{\}} &= \frac{e_{1\sigma}}{e_{1\phi}} \left[(\eta^\perp)^2 (\xi^\perp (2\epsilon - 6) - 6\tilde{W}_{211}) - 24(\eta^\perp)^5\right] \\
&\quad + \frac{e_{1\sigma}^3}{e_{1\phi}} \left[48(\eta^\perp)^5 + (\eta^\perp)^2 (6\tilde{W}_{211} + \xi^\perp (6 - 2\epsilon))\right] \\
&\quad + e_{1\sigma}^2 \left[24(\eta^\perp)^3 \xi^\perp + 8(\eta^\perp)^4 \epsilon\right] - 8(\eta^\perp)^3 \xi^\perp + (\eta^\perp)^4 (-2\epsilon - 6).
\end{aligned} \tag{9.16}$$

We can directly see that the higher order terms in $\text{r.h.s.}_{\{\}}$ have disappeared but are still present in the left-hand side terms. Moreover, most of the remaining terms in $\text{r.h.s.}_{\{\}}$ are now proportional to ϵ, which makes them even smaller. Finally, the divisions by the basis components $e_{1\phi}$ and $e_{1\sigma}$ which are smaller in absolute value than one only appear in $\text{order1}_{\{\}}$, $\text{order2}_{\{\}}$ and $\text{order3}_{\{\}}$. All these observations leads to the conclusion that $\text{r.h.s.}_{\{\}}$ is in fact small compared to left-hand side terms for the first type of turn.

To summarize the results of the section, we have established that r.h.s. is negligible compared to order1, order2 and order3. With the first type of turn, this is due to the cancellations of the dominant terms in r.h.s. due to the relations between the parallel and the perpendicular parameters which exist in that case. For the second type of turn, this is simply due to the factor in front of r.h.s. which is smaller than the one in order1,2,3 because $H^2 \ll H_*^2$. This means that even if the slow-roll approximation is broken, if the initial condition of that period is the slow-roll homogeneous solution, then the right-hand side of (7.47) can be neglected. This is illustrated in figure 92 which displays |r.h.s.|, |order1| and |order2| (obviously order3 is not needed because it is minus the sum of the two others) for the potentials of each type of turn that are studied in chapter 10. This figure (with a logarithmic scale) shows that r.h.s. is always several orders of magnitude smaller than the others during the turn (except at the times where $\eta^\perp$ crosses zero, which will be discussed in section 9.6).

From this section we learn that the homogeneous solution, which is known, is sufficient to solve (7.47) during the turn when the slow-roll approximation is broken (large $\eta^\parallel$ and $\eta^\perp$) as long as ϵ remains small, since the particular solution is negligible.

9.5 Fate of the slow-roll particular solution

In the previous section, we showed that we only need the homogeneous solution of the g_{int} equation during the turn when the slow-roll approximation is broken. However, this does not

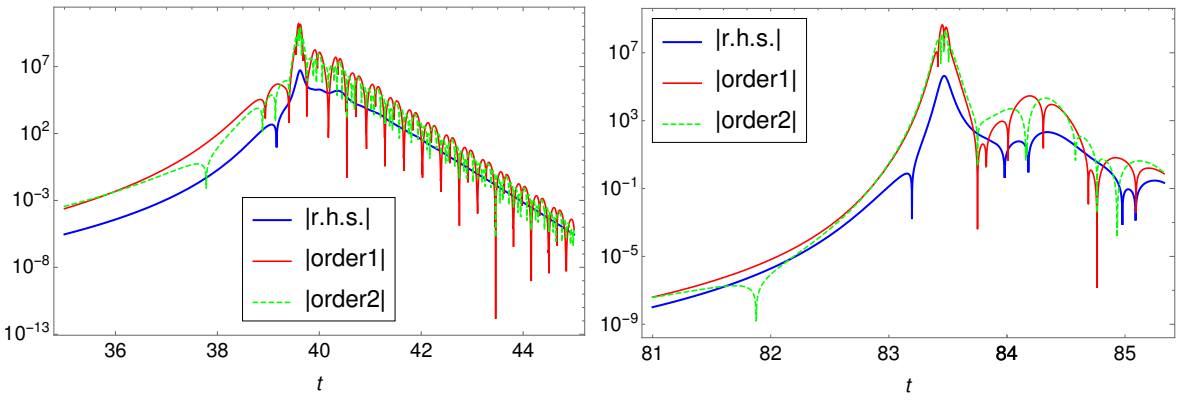

Figure 92: This plot displays |r.h.s.| in blue (thick line), |order1| in red and |order2| in green (dashed) during the turn of the field trajectory for the potentials studied in sections 10.3.1 (on the left) and 10.4.1 (on the right), which correspond to the first and second types of turn, respectively. Note the logarithmic scale.

mean that we can forget about the particular solution completely. It is still required during the slow-roll evolution before and after the turn as we will show explicitly in this section (and potentially during the turn when $\eta^\perp$ crosses zero, see next section) and hence plays a role in principle in the determination of the integration constants in the various regions. In fact, to avoid having to perform an explicit matching at every transition it would be very convenient if we could just add the slow-roll particular solution to the homogeneous solution everywhere. We will come back to this point in the next section. As a preliminary we will in this section investigate the behaviour of the slow-roll particular solution $P_{\rm sr}$ before and during the turn. We start by comparing $P_{\rm sr}$ to the homogeneous solution in the different regimes.

First, we focus on the slow-roll regime using the Green's functions determined in (8.23) when the slow-roll particular solution can be written as:

$$P_{\rm sr} = -2\epsilon\left(e_{1\phi}^2\tilde{V}_{\sigma\sigma} + e_{1\sigma}^2\tilde{U}_{\phi\phi}\right)\frac{H^4 e_{1\phi}^2 e_{1\sigma}^2}{H_*^4 e_{1\phi*}^2 e_{1\sigma*}^2} = \frac{2}{3}\epsilon\left(e_{1\phi}^2 V_{\sigma\sigma} + e_{1\sigma}^2 U_{\phi\phi}\right)e_{1\phi}e_{1\sigma}\frac{H^2 e_{1\phi}e_{1\sigma}}{H_*^4 e_{1\phi*}^2 e_{1\sigma*}^2}. \quad (9.17)$$

Doing the same for the homogeneous part using the quasi single-field initial conditions discussed at the end of section 8.2 and recalled at the beginning of this one, as well as (7.9), we get:

$$h_{\rm sr} = -e_{1\phi*}^2\tilde{V}_{\sigma\sigma*}\eta^\perp\frac{H^2 e_{1\phi}e_{1\sigma}}{H_*^2 e_{1\phi*}^2 e_{1\sigma*}^2} = -e_{1\phi_*}^2\tilde{V}_{\sigma\sigma*}\left(e_{1\phi}e_{1\sigma}(\tilde{V}_{\sigma\sigma} - \tilde{U}_{\phi\phi}) - \frac{1}{3}\xi^\perp\right)H_*^2\frac{H^2 e_{1\phi}e_{1\sigma}}{H_*^4 e_{1\phi*}^2 e_{1\sigma*}^2}. \quad (9.18)$$

In the slow-roll approximation (neglecting the higher-order term $\xi^\perp$ in $h_{\rm sr}$), we end up with $\epsilon\, e_{1\phi}e_{1\sigma}\left(e_{1\phi}^2 V_{\sigma\sigma} + e_{1\sigma}^2 U_{\phi\phi}\right)$ and $\tilde{V}_{\sigma\sigma*}e_{1\phi}e_{1\sigma}\left(V_{\sigma\sigma} - U_{\phi\phi}\right)\frac{H_*^2}{H^2}$ to compare, because $e_{1\phi*}^2 \approx 1$ and by definition $\tilde{V}_{\sigma\sigma} = V_{\sigma\sigma}/(3H^2)$ and $\tilde{U}_{\phi\phi} = U_{\phi\phi}/(3H^2)$. As a reminder, we want to see if $P_{\rm sr}$ can be negligible compared to $h_{\rm sr}$ during the slow-roll regime. First, we look at the terms inside the parentheses which both contain second-order derivatives of the potential. Then, for our models where neither of the derivatives is negligible compared to the other at horizon crossing, we can expect that in general this remains true later, at least up to the turn (it can change during the turn, but at that time the slow-roll approximation is broken and these expressions are not valid as we will discuss later in this section). So we conclude that the terms between parentheses in the two expressions are in general of a comparable order (the basis components in $P_{\rm sr}$ can make it smaller, but not a lot smaller). If there is a difference between the two expressions, it has to come from the remaining factors, which means we have to compare ϵ to

$\tilde{V}_{\sigma\sigma*}\frac{H_*^2}{H^2}$ like in the previous section. As discussed there, these have to be of the same order because in the slow-roll regime H is still of the same order as H_*. There is one exception which corresponds to models where ϵ is extremely small compared to $\eta^{\parallel}$ even in the slow-roll regime (Starobinsky-like inflation for example), so that ϵ is also small compared to $\tilde{V}_{\sigma\sigma*}$ (in that case, there would be a similarity with the beyond-slow-roll situation studied in this section where $\epsilon \ll \eta^{\parallel},\ \eta^{\perp}$ as well). But apart from those specific models, this leads to the conclusion that in general both the particular solution and the homogeneous solution have to be taken into account during the slow-roll regime.

As shown in section 9.2, the slow-roll expressions for the Green's functions are also valid in a region of large ϵ, which occurs just before a turn of the second type. The same expressions as in the previous paragraph can be used, however $\xi^{\perp}$ can no longer be neglected in $h_{\rm sr}$. On the other hand, there is no reason for $\xi^{\perp}$ to become much larger than the other term between the parentheses (which is $\eta^{\perp}$) either, given that we are still before the turn, so that in the end the conclusion about the terms between parentheses from the previous paragraph still holds. As for the other factors, both the homogeneous and the particular solutions will grow because ϵ becomes of order unity, which makes H_*^2/H^2 large compared to 1. However, at the end of this period ϵ will decrease and becomes of order slow roll again, but the ratio H_*^2/H^2 will stay large. This means that the slow-roll particular solution finishes the period of large ϵ being small compared to the slow-roll homogeneous solution. We will show below that this is fully consistent with the result for the second type of turn (the type that has a period of large ϵ right before the turn) that the slow-roll particular solution is negligible during the turn.

We continue by considering the behaviour of the slow-roll particular solution during the different types of turn. Obviously, it is not an actual solution at that time, but we want to know if it would cause any problems if we were to simply add it to the solution. Again, we follow the same method using the Green's function expressions given in (9.9) to write:

$$P_{\rm sr} = \epsilon\frac{H^2H_0^2e_{1\phi}e_{1\sigma}}{H_*^4e_{1\phi*}^2e_{1\sigma*}^2}\left(\eta^{\parallel}e_{1\phi}e_{1\sigma}+\eta^{\perp}(e_{1\sigma}^2-e_{1\phi}^2)\right), \qquad h_{\rm sr} = -e_{1\phi*}^2\tilde{V}_{\sigma\sigma*}\eta^{\perp}\frac{HH_0e_{1\phi}e_{1\sigma}}{H_*^2e_{1\phi*}^2e_{1\sigma*}^2}. \quad (9.19)$$

This time we end up with $\frac{HH_0}{H_*^2}\epsilon\left(\eta^{\parallel}e_{1\phi}e_{1\sigma}+\eta^{\perp}(e_{1\sigma}^2-e_{1\phi}^2)\right)$ and $\tilde{V}_{\sigma\sigma*}\eta^{\perp}$ to compare. Again the two expressions have a similar form, excluding the factor HH_0/H_*^2. As discussed in the previous chapter, $\tilde{V}_{\sigma\sigma*}$ is typically of order 10^{-2} and hence cannot be much smaller than ϵ which is of order slow-roll. During the turn, the terms depending on the η parameters are also of the same order, except in the rare case when $\eta^{\perp}$ vanishes. Finally, the only large difference can come from the factor in front in the slow-roll particular solution. The two types of turn described in section 9.1 give different results. In the first type where ϵ is of order slow-roll since horizon-crossing, H and H_0 are not much smaller than H_*. Then the factor is not much smaller than one. Moreover, the cases where it is the smallest are also the cases where ϵ has increased the most (and can then be larger than $\tilde{V}_{\sigma\sigma*}$ by an order of magnitude), so that these two effects compensate each other. Hence, the slow-roll particular solution is then typically of the same order as the homogeneous solution during the turn. In the second type of turn, the situation is different, indeed H and H_0 are of the same order and we know that $H^2 \ll H_*^2$. This means that this time $P_{\rm sr}$ is small and negligible during the turn compared to $h_{\rm sr}$, fully consistent with the result that $P_{\rm sr}$ has become very small during the period of large ϵ just before the turn, as shown above.

More must be said about the slow-roll particular solution during a turn of the first type and we will now show that it becomes in fact proportional to the homogeneous solution of (7.47). To show this, we substitute $P_{\rm sr}$ in the left-hand side of (7.47), using the Green's function expressions from (9.9), the sum potential relations from (8.10) and (8.11) to eliminate χ, $\tilde{W}_{221}$ and $\tilde{W}_{222}$, and also the relations between parallel and perpendicular parameters (9.2). We

then compare the three terms of the equation corresponding to the three different orders of derivative (called term1, term2 and term3)[1] to their sum (called l.h.s.):

$$\begin{aligned}
\text{l.h.s.}_{\{\}} &= e_{1\phi}^2 e_{1\sigma}^2 \left[(\eta^\perp)^2\left(-6\tilde{W}_{111}-12\epsilon^2\right)+12\epsilon\eta^\perp\xi^\perp\right] \\
&\quad + e_{1\phi}e_{1\sigma}^3\left[(\eta^\perp)^3\left(4\epsilon^2+24\epsilon\right)-6(\eta^\perp)^2\tilde{W}_{211}\right]+e_{1\phi}e_{1\sigma}(\eta^\perp)^3\left(12\epsilon-4\epsilon^2\right)+4e_{1\phi}^2(\eta^\perp)^4\epsilon, \\
\text{term1}_{\{\}} &= -12e_{1\phi}e_{1\sigma}(\eta^\perp)^5+e_{1\phi}^3e_{1\sigma}\left[-4\eta^\perp(\xi^\perp)^2-6(\eta^\perp)^2\tilde{W}_{211}\right]+e_{1\sigma}^4\left[4(\eta^\perp)^3\xi^\perp-24(\eta^\perp)^4\right] \\
&\quad + 36e_{1\sigma}^2(\eta^\perp)^4-4(\eta^\perp)^3\xi^\perp-12(\eta^\perp)^4, \\
\text{term2}_{\{\}} &= -12e_{1\phi}e_{1\sigma}(\eta^\perp)^5+e_{1\phi}^2\left[(\eta^\perp)^4(6-2\epsilon)-4(\eta^\perp)^3\xi^\perp\right]+e_{1\phi}e_{1\sigma}^3\left[48(\eta^\perp)^5+36(\eta^\perp)^3\epsilon\right] \\
&\quad + e_{1\phi}^2e_{1\sigma}^2\left[28(\eta^\perp)^3\xi^\perp+12\eta^\perp\xi^\perp\epsilon+(\eta^\perp)^4(20\epsilon-24)+(\eta^\perp)^2\left(6\epsilon^2-18\epsilon\right)\right] \\
&\quad + e_{1\phi}^3e_{1\sigma}\left[4\eta^\perp(\xi^\perp)^2+(\eta^\perp)^2\xi^\perp(6\epsilon-6)+(\eta^\perp)^3\left(2\epsilon^2-6\epsilon\right)\right], \\
\text{term3}_{\{\}} &= e_{1\phi}e_{1\sigma}^3\left[-48(\eta^\perp)^5+(\eta^\perp)^2(\xi^\perp(6\epsilon-6)-12\tilde{W}_{211})+(\eta^\perp)^3\left(6\epsilon^2-18\epsilon\right)\right] \\
&\quad + e_{1\phi}e_{1\sigma}\left[24(\eta^\perp)^5+(\eta^\perp)^2(6\tilde{W}_{211}+\xi^\perp(6-6\epsilon))+(\eta^\perp)^3\left(18\epsilon-6\epsilon^2\right)\right] \\
&\quad + e_{1\sigma}^2\left[-32(\eta^\perp)^3\xi^\perp+(\eta^\perp)^2\left(-6\tilde{W}_{111}-18\epsilon^2+18\epsilon\right)+(\eta^\perp)^4(-26\epsilon-6)\right] \\
&\quad + e_{1\sigma}^4\left[24(\eta^\perp)^3\xi^\perp+(\eta^\perp)^2\left(6\tilde{W}_{111}+18\epsilon^2-18\epsilon\right)+20(\eta^\perp)^4\epsilon\right] \\
&\quad + 8(\eta^\perp)^3\xi^\perp+(\eta^\perp)^4(6\epsilon+6).
\end{aligned} \tag{9.20}$$

The discussion of these expressions is very similar to the one for (9.11) and (9.13). We use again the subscript $_{\{\}}$ to indicate that we have left out an overall factor (cf. (9.11) and (9.13)), which is here the same for all four expressions. We can see that in l.h.s.$_{\{\}}$ the higher order terms like $(\eta^\perp)^5$ have disappeared. Moreover, most of the terms in l.h.s. have an extra factor of ϵ, which is not the case for the other expressions. This implies that the sum of the three terms is much smaller than the individual terms of (7.47) with the slow-roll particular solution. Hence this function is in fact an approximated solution of the homogeneous equation during a turn of the first type when the slow-roll approximation is broken.

If P_{sr} becomes a homogeneous solution it means that it has to be proportional to a linear combination of the two previously determined exact independent homogeneous solutions $\eta^\perp\bar{v}_{22}$ and $\eta^\perp G_{22*}$. However, using (7.34), these independent solutions have in fact become proportional before the turn. Hence, we simply have that P_{sr} and h_{sr} are proportional. Using (9.19) and (9.2), we rewrite the particular solution as:

$$P_{\text{sr}} = -\epsilon\frac{H^2H_0^2e_{1\phi}e_{1\sigma}}{H_*^4e_{1\phi*}^2e_{1\sigma*}^2}\eta^\perp e_{1\phi}^2. \tag{9.21}$$

We find the same factor $\eta^\perp$ as in the homogeneous solution (9.19), but also another factor $\epsilon He_{1\phi}^2$. Hence, the proportionality is true only if $\epsilon He_{1\phi}^2$ is constant during the turn. This happens if $e_{1\phi}^2\approx 1$, in that case ϕ is dominating meaning that ϵ and H are purely slow-roll and are almost constant during a short turn. At first, the idea of ϕ dominating during the turn might seem odd. However, we recall that this does not have to be during the whole turn, but only when $\eta^\perp$ and $\eta^\parallel$ are large enough to break the slow-roll approximation. Looking at the

[1] These are the same terms we called order1,2,3 before, however now with the particular solution substituted and not the homogeneous one.

form of trajectory in the top left plot of figure 91, the only period when ϕ dominates is in fact at the end of the turn when σ is oscillating around its minimum. This can also be verified with the explicit examples of the next section (see figures 102 and 104). Here, we can observe that $\eta^{\perp}$ becomes large only after the period when $e_{1\sigma}$ was not negligible (the turn).

Different behaviours of the slow-roll particular solution depending on the type of turn have been highlighted in this section. In the next section we will discuss how these results can be used to solve the differential equation (7.47) beyond the slow-roll regime.

9.6 Solution of the $g_{\rm int}$ equation

As usual, we will discuss separately the two types of turn, but we start by reminding the reader about the main result of the previous sections. The solution of (7.47) is known until the end of the slow-roll regime and it is composed of a homogeneous solution and a particular solution that both have to be taken into account. When $\eta^{\parallel}$ and $\eta^{\perp}$ become large, during the turn, only the homogeneous solution (which is exact and does not depend on any slow-roll approximation) is needed to solve the equation. The difficulty is then to ensure the continuity of the solution at the transition between the two regimes. In fact, after the turn, there may also be another period of slow-roll before the end of inflation, and during the turn the slow-roll parameters can oscillate and vanish for a short time, which could lead to a very brief restoration of the slow-roll conditions. So in the end there might be many transitions and it would be very inconvenient if we had to perform an explicit matching of the solutions at each of them. Fortunately, there is another option as we will now show. Finally, we also recall that the slow-roll particular solution evolves differently depending on the type of turn. In the first type, it becomes proportional to the homogeneous solution of (7.47), while in the second type it becomes negligible compared to the homogeneous solution.

It is then easy to see that the case of the first type of turn is most simply treated by keeping the full slow-roll solution at all times. Indeed, at the moment when the slow-roll regime ends and the turn starts, the solution should become only homogeneous, and that is exactly the case because the slow-roll particular solution becomes a homogeneous solution at that time. Continuity at the transition is then automatic, without the need for any explicit matching. Then, if later during the turn or at the end of the turn the slow-roll approximation is re-established, continuity is also ensured since the same solution works on both sides of the transition. Note that if $\eta^{\perp}$ vanishes, from (9.2), $\eta^{\parallel}$ has to be of order slow-roll, meaning that the slow-roll approximation is indeed restored during these brief moments.

The second type of turn deserves a longer discussion. Indeed, we do not know the full particular solution during the period of large ϵ just before the turn but we know two things: the slow-roll particular solution vanishes (but it is not an exact particular solution at that time) and the right-hand side of (7.47) can be neglected once this period has finished, because r.h.s. is negligible at the start of the turn as shown in section 9.4. These two ingredients are sufficient to prove that the particular solution during the period of large ϵ vanishes, even without having its explicit form. To stay general, we write the particular solution P as $P = P_{\rm sr} + Ah + P_{\perp h}$, where A is a constant, h the homogeneous solution, and $P_{\rm sr}$ the slow-roll particular solution. $P_{\perp h}$ is the function that, when inserted into (7.47), gives those right-hand side terms that are not given by $P_{\rm sr}$, and which is zero when these terms vanish (in other words, it does not contain a homogeneous solution). We know that over the course of the period of large ϵ, $P_{\rm sr}$ vanishes (see (9.19)). The right-hand side of (7.47) vanishes during that period too, which means that $P_{\perp h}$ has to vanish by definition. The only remaining term could then be the one proportional to the homogeneous solution, but it has to be zero because of the matching conditions at the start of the period of large ϵ. Indeed at the end of the slow-roll regime, the particular solution

is simply $P_{\rm sr}$ while $P_{\perp h}$ has to be zero, because the terms of higher order in slow-roll are still negligible and will grow only later during that period of large ϵ. The function h is not zero at the transition, hence A has to be. Without knowing the exact formula for P, we can conclude that it vanishes during that period of large ϵ. Hence, at the start of the turn, the solution is simply the slow-roll homogeneous solution.

During the second type of turn, keeping the slow-roll particular solution, even if it is not a particular solution of the exact equation at that time, only induces a negligible error, but it solves any potential issues with matching to later slow-roll periods. When $\eta^{\perp}$ vanishes, $\eta^{\parallel}$ can be larger than order slow-roll in this type of turn. This is not an issue because then the parameters evolve very fast, meaning that a very short time before $\eta^{\perp}$ vanishes, the particular solution is still negligible compared to the homogeneous solution, and the same a very short time after. Moreover, one can verify that at the exact time when $\eta^{\perp} = 0$, the particular solution is $\frac{1}{2}P_{\rm sr}$ and we know that this function is negligible during the rest of the turn. Then it is possible to add this particular solution to the full solution only for these very short periods (without using matching conditions, because at the time of the matchings it it is negligible). It is also important to remember that in the end we are interested in the integrated $g_{\rm int}$, and when $\eta^{\perp}$ vanishes, the right-hand side of (7.47) is also very small compared to its value a short time before or after (because every term contains $\eta^{\perp}$ except one which also becomes small), meaning this particular solution is also small at that time compared to its usual value during the turn. In the integral it is then negligible. In fact, when $\eta^{\perp}$ vanishes, the only thing that happens is that the whole solution almost vanishes (but the particular solution does not vanish at that exact same time), but because the homogeneous solution is zero, it cannot be large compared to the particular solution for once.

To summarize, we have shown that for both types of turn, the slow-roll solution of (7.47) is sufficient to solve this equation even beyond the slow-roll regime, under the condition that ϵ stays of order slow-roll during the turn. Of course, knowing the solution $\dot{g}_{\rm int}$ which is given in (9.12) is not sufficient, we also have to integrate it. But the computation is exactly the same as in the slow-roll case even if the slow-roll approximation is not valid, meaning that $g_{\rm int}$ has again the same form:

$$g_{\rm int} = \epsilon \bar{v}_{22}^2 - \epsilon_* - \frac{e_{1\phi *}^2 \tilde{V}_{\sigma\sigma *} - e_{1\sigma *}^2 \tilde{U}_{\phi\phi *}}{2 e_{1\phi *} e_{1\sigma *}} \bar{v}_{12}. \tag{9.22}$$

9.7 End of inflation and $f_{\rm NL}$

Once the form of $g_{\rm int}$ is known, it is possible to compute $f_{\rm NL}$ at the end of inflation:

$$-\frac{6}{5} f_{\rm NL} = \frac{e_{1\phi *}^2 \tilde{V}_{\sigma\sigma *} - e_{1\sigma *}^2 \tilde{U}_{\phi\phi *}}{e_{1\phi *} e_{1\sigma *}} \frac{(\bar{v}_{12e})^3}{(1 + (\bar{v}_{12e})^2)^2} + \mathcal{O}(10^{-2}). \tag{9.23}$$

This expression has the same form as the slow-roll one (8.16), the difference is hidden in the Green's functions which have been computed in section 9.2. The same discussion of this expression as in section 8.2 holds and the conclusions are the same, see (8.18). Like in that section, we use the limit (8.19) which is a good approximation when $|\bar{v}_{12e}| > 4$. Then the only remaining step is to study the value of $\bar{v}_{12}$ at the end of the turn using (9.10), when the slow-roll approximation is valid again, which is equal to $\bar{v}_{12e}$.

As usual, we need to distinguish the two types of turn because they have different initial and final conditions. In the first case, the turn occurs early which means that $U_0 \gg V_0$ (as defined before, the subscript 0 indicates that the function is evaluated at t_0 when the slow-roll approximation stops to be valid). However because there is a turn, we cannot neglect $e_{1\sigma 0}$

anymore. We can then write $S_0 = e_{1\phi 0}^2 - e_{1\sigma 0}^2 = 1 - 2e_{1\sigma 0}^2$ and $Z_0 \approx -U_0 e_{1\sigma 0}^2$. Moreover, before the turn we are still in slow-roll, meaning that $\epsilon_0 \ll 1$ and we can use the slow-roll expression $H_0^2 = \kappa^2 U_0/3$. At the end of the turn, the situation is similar to single-field inflation in the direction ϕ meaning that $Z \approx 0$ and $S \approx 1$. Inserting this into (9.10), we obtain:

$$\bar{v}_{12e} = \frac{U_0}{W_*} \frac{2e_{1\sigma 0}^2}{4e_{1\phi *}e_{1\sigma *}} + \frac{-U_0 e_{1\sigma_0}^2}{2W_* e_{1\phi *}e_{1\sigma *}} + \frac{-V_*}{W_* e_{1\phi *}e_{1\sigma *}} = \frac{-V_*}{W_* e_{1\phi *}e_{1\sigma *}}. \tag{9.24}$$

This is exactly the same limit as in the slow-roll situation. Hence for this first type of turn, we get the same result:

$$-\frac{6}{5} f_{\mathrm{NL}} = -\frac{V_{\sigma\sigma *}}{\kappa^2 V_*}. \tag{9.25}$$

The implications of this result were already discussed in section 8.2.

In the second type of turn, the situation is slightly different. Firstly, the slow-roll approximation is not valid at the time t_0, at the end of the period of large ϵ. Moreover, at that time we are still in a single-field case (ϕ dominates), hence $S_0 \approx 1$ and $Z_0 \approx -V_0 \approx V_*$ (because even if U_0 is not zero, it cannot be large compared to V_0 because we are near the moment when ϕ reaches the minimum of U). After the turn, the single-field situation is now in the σ direction, hence $S \approx -1$. At the end of inflation, the situation is:

$$\bar{v}_{12e} = -\frac{H_0^2}{2H_*^2 e_{1\phi *}e_{1\sigma *}} + \frac{-Z_*}{2W_* e_{1\phi *}e_{1\sigma *}} = \frac{-\frac{3}{\kappa^2}H_0^2 - Z_*}{2W_* e_{1\phi *}e_{1\sigma *}}. \tag{9.26}$$

Substituting this into f_{NL}, we obtain:

$$-\frac{6}{5} f_{\mathrm{NL}} = -\frac{2V_{\sigma\sigma *}}{3H_0^2 + \kappa^2 V_*}. \tag{9.27}$$

However, we can add that $H_0^2 > \kappa^2 W_0/3$ because ϵ is not negligible (equality in the slow-roll case). Moreover, $W_0 = U_0 + V_0 \approx U_0 + V_* > V_*$. We can then write:

$$|\bar{v}_{12e}| > \left| \frac{-V_*}{W_* e_{1\phi *}e_{1\sigma *}} \right|, \tag{9.28}$$

which has an immediate consequence for f_{NL}:

$$\left| -\frac{6}{5} f_{\mathrm{NL}} \right| < \left| -\frac{V_{\sigma\sigma *}}{\kappa^2 V_*} \right|. \tag{9.29}$$

In this case, the value of f_{NL} is smaller than the slow-roll result. However, it is easily of the same order because U_0 and V_0 are of the same order while even if $\epsilon_0 = 1$, it only changes the factor between H_0^2 and $\kappa^2 W_0$ from 1/3 to 1/2.

So in the end we have derived the rather surprising result that in the class of models considered (two-field sum potentials), the slow-roll expression for f_{NL} gives a very good approximation of the exact result, even in the case where the slow-roll approximation breaks down during the turn. Allowing for the break-down of slow-roll does however increase the region of the parameter space where large non-Gaussianity can occur compared to the results shown in figure 82, because we no longer have the constraint that the turn has to happen before the end of the slow-roll regime.

Chapter 10

Numerical examples

Here, we provide several explicit examples to illustrate the different results of the previous chapters. We also show how to explicitly construct a model that produces $f_{\rm NL}$ of order unity while satisfying all observational constraints.

10.1 Double quadratic potential

The double quadratic potential has the form:

$$W(\phi,\sigma) = \frac{1}{2}m_\phi^2\phi^2 + \frac{1}{2}m_\sigma^2\sigma^2. \tag{10.1}$$

It has been studied and discussed in many papers, see e.g. [195, 164, 191]. However, it is always a good introductory example.

Without taking into account the exact constraints of the monomial potential yet, we keep the main idea that the second field has a negligible effect at the time of horizon-crossing. This can be achieved by taking $m_\phi^2 \gg m_\sigma^2$ and we will use the same values as in [191]: $m_\phi = 20m_\sigma$ and $m_\sigma = 10^{-5}\kappa^{-1}$. As initial conditions, we use $\phi_i = 13\kappa^{-1}$ and $\sigma_i = 13\kappa^{-1}$, while their derivatives $\dot{\phi}_i$ and $\dot{\sigma}_i$ are determined by the slow-roll approximation. In figure 101 we show how the various relevant quantities evolve during the turn of the field trajectory. First, one can see clearly when the turn occurs: $\eta^\perp$ becomes large and $e_{1\sigma}$ becomes of the same order as $e_{1\phi}$. We also see that this example corresponds to the second type of turn where ϕ reaches the minimum of its potential and ϵ is of order unity before the turn. Another remark is that the second-order parameters $\xi^\parallel$ and $\xi^\perp$ do not give new information compared to the first-order parameters $\eta^\parallel$ and $\eta^\perp$, at least not by eye.

However, in this model the two most important constraints and goals, concerning the two observables n_s and $f_{\rm NL}$, are not achieved. The spectral index, which is 0.92, is clearly outside the bounds from the Planck observations. $f_{\rm NL}$ is slow-roll suppressed and far from the goal of $f_{\rm NL}$ of order unity. Moreover, $\bar{v}_{12e}$ is only -1.5 which is smaller in absolute value than the value 4 needed to use the approximations (8.25) and (8.26) for $f_{\rm NL}$ and n_s.

The main result of the previous section was the validity of the slow-roll expressions in cases beyond slow-roll, like this one, at least to give an estimation of the Green's functions. Hence, we can use this approximation to compute $\bar{v}_{12e}$ to see how the situation can be improved. Using dimensionless fields, (8.27), the slow-roll expression for $\bar{v}_{12e}$ given by (8.24) becomes:

$$\bar{v}_{12e} = -\frac{V_*}{W_* e_{1\phi *} e_{1\sigma *}} = -\sqrt{2\epsilon}\frac{V_*}{V_{\sigma *}} = -\frac{\sigma_*}{\phi_*}. \tag{10.2}$$

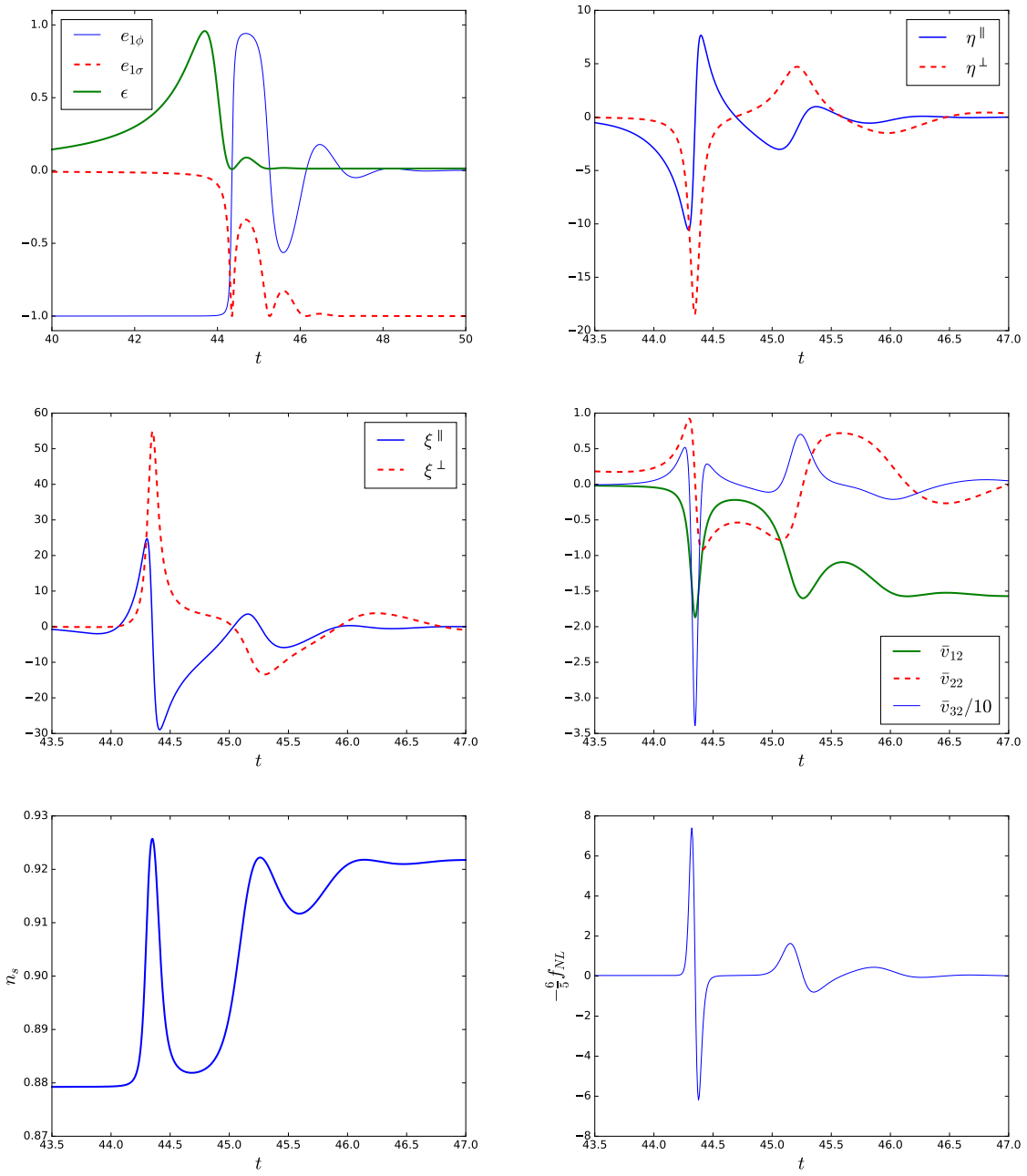

Figure 101: The exact numerical solutions for the different interesting parameters (basis components, slow-roll parameters, Green's functions, the spectral index and f_{NL}) during the turn for the double quadratic potential (10.1).

This shows that $\bar{v}_{12e}$ can be increased only by changing the initial conditions. Assuming that now we have $\bar{v}_{12e}$ large enough, $f_{\rm NL}$ takes the form:

$$-\frac{6}{5}f_{\rm NL} = -\frac{V_{\sigma\sigma *}}{V_*} = \frac{2}{\sigma_*^2}. \tag{10.3}$$

The value of $f_{\rm NL}$ becomes smaller if we increase σ_*. Hence, it is impossible to increase both $\bar{v}_{12e}$ and $f_{\rm NL}$ at the same time. One can also verify there is no optimal value of σ_* where $f_{\rm NL}$ would be larger than order slow-roll, meaning that this potential cannot produce large persistent non-Gaussianity.

Instead of looking directly at $f_{\rm NL}$, we could also have used the conclusion that for a monomial potential $N_\sigma \propto \sigma^2$ has to be of order unity to have $f_{\rm NL}$ large, which requires here to decrease σ_* and $\bar{v}_{12e}$. The solution is then to add an extra parameter in the potential.

10.2 How to build a monomial potential model that produces $f_{\rm NL}$ of order unity

The form of the potentials we are interested in is:

$$W(\phi,\sigma) = \alpha(\kappa\phi)^n + C + \beta(\kappa\sigma)^m\left(+\lambda(\kappa\sigma)^{m'}\right), \tag{10.4}$$

which is the one studied in section 8.4. There is an extra term with $m' > m$ inside the parentheses to complete the model (i.e. make sure it has a minimum) and we will choose it to be negligible until after the turn. Hence this does not change the different expressions determined for a monomial potential.

A first step it to choose the value of m and n using figure 82 to be in the region where $f_{\rm NL}$ of order unity is possible. α can be put as an overall factor of the whole potential, hence it does not count in the number of parameters. ϕ_* is given by $N_{\phi *} \approx 60$ and this also determines ϵ_* because it only depends on ϕ_*. Once ϵ_* is known, it is possible to determine σ_*, β and C using the three constraints we have ($f_{\rm NL}$, n_s and $\bar{v}_{12e}$) as follows.

We can start by choosing the value of $f_{\rm NL}$ and (8.25) takes the following form for a monomial potential:

$$-\frac{6}{5}f_{\rm NL} = -\frac{V_{\sigma\sigma *}}{\kappa^2 C}. \tag{10.5}$$

Using (8.26) and the lower bound on the spectral index $n_s = 0.962$, as this is the easiest way to get a large $f_{\rm NL}$, we have:

$$V_{\sigma\sigma *} = \kappa^2 U_*\left(\frac{n_s - 1}{2} + \epsilon_*\right). \tag{10.6}$$

Finally, we need $\bar{v}_{12e} > 4$. Using the slow-roll expression for $\bar{v}_{12e}$ in (8.24), (8.27) and (8.41), we get:

$$\bar{v}_{12e} = -\frac{V_*}{W_* e_{1\phi *} e_{1\sigma *}} = -\sqrt{2\epsilon_*}\frac{\kappa C}{V_{\sigma *}} = -\sqrt{2\epsilon_*}\frac{m-1}{\sigma_*}\frac{\kappa C}{V_{\sigma\sigma *}}. \tag{10.7}$$

A last step is to determine λ, this is done using the fact that the minimum of the potential has to be zero. Then it is possible to verify if the last term is really negligible at horizon-crossing, if not it is possible to increase m' to decrease it because σ_* is small compared to one. We will now apply this to two different potentials with a turn of the first type.

10.3 First type of turn

10.3.1 First example: $n = 2$ and $m = 4$

This first example corresponds to the case where the turn occurs early enough to have a trajectory with the same direction before and after the turn, see the top right plot of figure 91 for an illustration of the field trajectory. The potential is:

$$W(\phi, \sigma) = \alpha\phi^2 + C + \beta\sigma^4 + \lambda\sigma^6, \tag{10.8}$$

with $\alpha = \frac{1}{2}\kappa^{-2}$, $C = \frac{4}{27}\frac{\beta^3}{\lambda^2}$, $\beta = -12.5$, and $\lambda = -\frac{4}{3}\beta\kappa^2$. The initial conditions are $\phi_i = 16\kappa^{-1}$ and $\sigma_i = 0.09\kappa^{-1}$ and, as usual, $\dot{\phi}_i$ and $\dot{\sigma}_i$ are determined by the slow-roll approximation.

With this, it is possible to obtain an analytical estimate of the observables. First, we need to compute ϕ_* and σ_*, using the solutions of equations (8.44) and (8.54) determined for monomial potentials. These solutions were computed assuming that ϕ_* and σ_* were the initial conditions, one has just to replace them by ϕ_i and σ_i here. This quick computation gives:

$$\phi_* = 15.2\kappa^{-1} \qquad \text{and} \qquad \sigma_* = 0.092\kappa^{-1}. \tag{10.9}$$

Using these values and the different expressions (10.5), (10.6) and (10.7), we obtain:

$$\bar{v}_{12e} = -\frac{2}{\phi_*}\frac{3}{\sigma_*}\frac{\kappa C}{12\beta\sigma_*^2} = 3.52, \quad n_s = 1 - \frac{4}{\phi_*^2} - 2\frac{12\beta\sigma_*^2}{\kappa^2\alpha\phi_*^2} = 0.961, \quad -\frac{6}{5}f_{\mathrm{NL}} = -\frac{12\beta\sigma_*^2}{\kappa^2 C} = 1.2. \tag{10.10}$$

In these calculations, there are different approximations. First we use the monomial expressions to compute ϕ_* and σ_* (we refer the reader to section 8.4 for the details, but they require the slow-roll approximation and a quasi single-field situation, at least until horizon-crossing). Second, we use the limit of large $\bar{v}_{12e}$ to compute the observables, the validity of this limit is explained in detail in section 8.2. Hence, an error of order slow-roll (at horizon-crossing) is expected compared to the exact numerical results, which can be larger here since $\bar{v}_{12e}$ is a little smaller than four. Figure 102 contains the same plots as shown for the double quadratic potential except that we have removed the plot of $\xi^{\parallel}$ and $\xi^{\perp}$ which does not provide any additional information, and added a plot of g_{int}. The different analytical predictions in (10.10) are reasonable estimations of the different parameters but the difference is larger than expected, especially on the new plot concerning g_{int}. This plot displays both the exact numerical $\tilde{g}_{\mathrm{int}}$ and its analytical prediction from (9.22) (more precisely, the analytical form of the approximated solution, with the different parameters determined numerically), using the definition:

$$\tilde{g}_{\mathrm{int}} = -\frac{2(\bar{v}_{12})^2}{\left(1 + (\bar{v}_{12})^2\right)^2} g_{\mathrm{int}}. \tag{10.11}$$

As one can see, both curves have a similar form, but there is a difference of around 15%. The reason is that the turn occurs late with $\epsilon \approx 0.2$ when it starts. This value is already too large to have the slow-roll approximation working perfectly, but not enough for it to totally break down. In fact, this problem is quite general with the monomial potential because the turn has to occur late to get f_{NL} of order unity, as shown in the section 8.4.

However, if we forget momentarily about the observational constraint on the spectral index, only for one example to illustrate the validity of the analytical expressions, it is possible to have the turn occurring earlier. The second set of values is: $\alpha = \frac{1}{2}\kappa^{-2}$, $C = \frac{4}{27}\frac{\beta^3}{\lambda^2}$, $\beta = -2000$, and $\lambda = -\frac{40}{3}\beta\kappa^2$ with the initial conditions $\phi_i = 16\kappa^{-1}$ and $\sigma_i = 0.01\kappa^{-1}$. This time, the analytical predictions are:

$$\phi_* = 15.3\kappa^{-1} \qquad \text{and} \qquad \sigma_* = 0.0106\kappa^{-1}. \tag{10.12}$$

which leads to:

$$\bar{v}_{12e} = 23, \quad n_s = 0.914 \quad \text{and} \quad -\frac{6}{5} f_{\text{NL}} = 1.62. \tag{10.13}$$

Figure 103, which contains the same plots as figure 102 but for the new parameters, shows that ϵ is of order 10^{-2} during the turn, which is in the domain of validity of the main hypothesis $\epsilon \ll 1$. During the turn, $\eta^{\perp}$ is of order 10 at most, which shows that the slow-roll regime is broken. As expected, analytical predictions are now a very good estimation. However, the spectral index is 0.917, which is outside the observational bounds. This example is also used in the previous section in figure 92 to illustrate that r.h.s. is several orders of magnitude smaller than the left-hand side terms of (7.47).

10.3.2 Second example: Axion

The next example is the axion-quartic model originally introduced in [70] and discussed more recently in [61]. The potential is:

$$W(\phi, \sigma) = \frac{1}{4} g \phi^4 + \Lambda^4 \left[1 - \cos\left(\frac{2\pi\sigma}{f} \right) \right], \tag{10.14}$$

with $g = 10^{-10}$, $\Lambda^4 = \left(\frac{25}{2\pi}\right)^2 g\kappa^{-4}$ and $f = \kappa^{-1}$. The initial conditions are $\phi_i = 23.5\kappa^{-1}$ and $\sigma_i = \frac{f}{2} - 10^{-3}\kappa^{-1}$. Defining $\sigma' = \frac{f}{2} - \sigma$, we have $\sigma' \ll \kappa^{-1}$. This will stay true until the turn, hence it is possible to perform an expansion of the potential in terms of this small parameter. At first order, we have $\cos\left(\frac{2\pi\sigma}{f}\right) = -\cos\left(\frac{2\pi\sigma'}{f}\right) = -1 + \frac{1}{2}\left(\frac{2\pi\sigma'}{f}\right)^2$ which substituted into the potential gives:

$$W(\phi, \sigma') = \frac{1}{4} g \phi^4 + 2g \left(\frac{25}{2\pi} \right)^2 \kappa^{-4} - \frac{1}{2} g \left(\frac{25}{f} \right)^2 \kappa^{-4} (\sigma')^2. \tag{10.15}$$

This is a monomial potential with $n = 4$ and $m = 2$, hence in the region of parameters where the spectral index constraints cannot be satisfied. This is verified by computing the analytical predictions like for the previous example. The fields at horizon-crossing are:

$$\phi_* = 21.8\kappa^{-1} \qquad \text{and} \qquad \sigma'_* = -1.1 \times 10^{-3}\kappa^{-1}. \tag{10.16}$$

which leads to:

$$\bar{v}_{12e} = -\frac{8\kappa}{\phi_* \sigma'_*} \left(\frac{f}{2\pi} \right)^2 = -8.4, \quad n_s = 1 - \frac{16}{\phi_*^2} - 8\frac{25^2}{\kappa^2 f^2 \phi_*^4} = 0.944 \quad \text{and} \quad -\frac{6}{5} f_{\text{NL}} = 2\pi^2. \tag{10.17}$$

This model gives f_{NL} of order ten, however the spectral index is lower than the Planck constraints.

Figure 104 confirms these results. Again in this model the turn occurs very late and there is a shift between the prediction and the exact result even if ϵ is still small enough during the turn. Moreover, $\eta^{\parallel}$ and $\eta^{\perp}$ stay smaller than one during the turn, but χ, which is displayed on the same plot, becomes large. This is another regime than the ones studied in section 9.2. This has a direct impact on the Green's functions because χ appears in (7.23) which explains the difference between the slow-roll prediction for $\bar{v}_{12e}$ and the exact value. However, one interesting point is that the analytical form of g_{int} stays valid. This case of large χ when other slow-roll parameters are small is not common and is due here partially to the fact that $\tilde{V}_{\sigma\sigma*}$ is too large to respect the Planck constraint (because as discussed in section 8.2, $\chi_* = \epsilon_* + \eta_*^{\parallel} + \tilde{V}_{\sigma\sigma*}$).

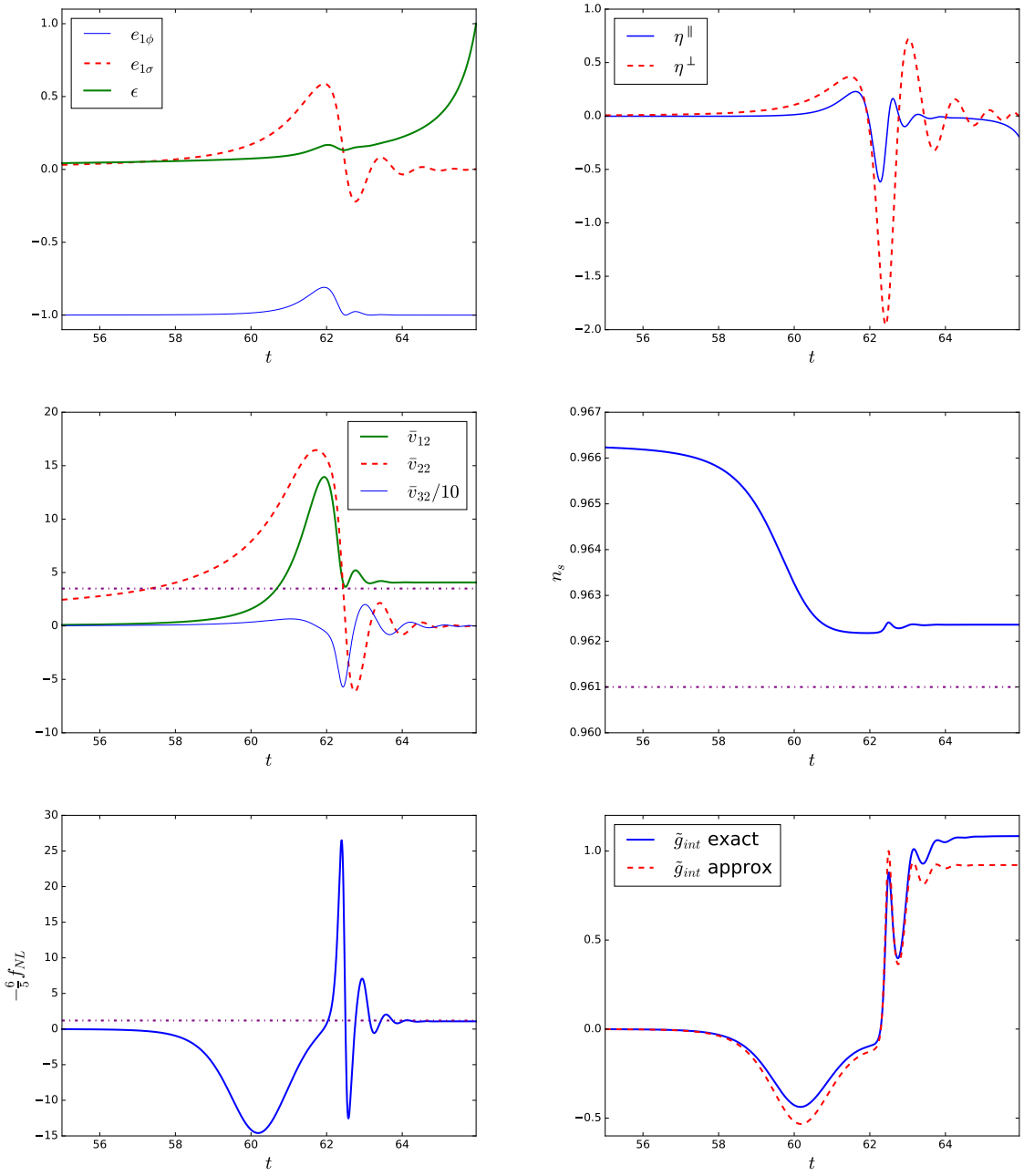

Figure 102: The exact numerical solutions for the different interesting parameters (basis components, slow-roll parameters, Green's functions, the spectral index and f_{NL}) during the turn for the first example of a monomial potential (10.8) with $n = 2$ and $m = 4$. The last figure shows both the exact numerical solution for $\tilde{g}_{\mathrm{int}}$ and its analytical approximation. The horizontal purple dash-dot lines are the analytical predictions for $\bar{v}_{12e}$, n_s and f_{NL}.

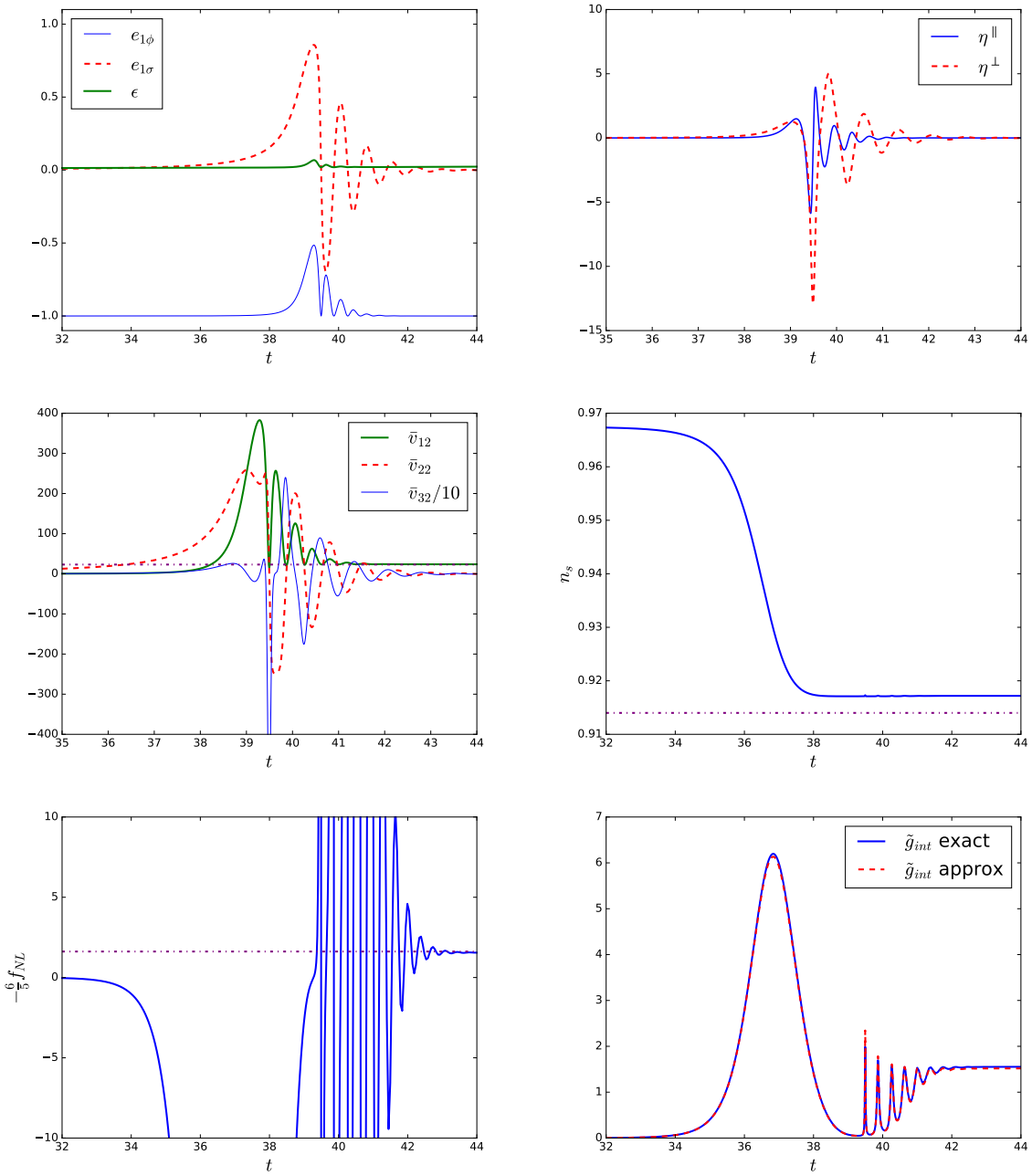

Figure 103: Same as figure 102 but for the second example of monomial potential (10.8) with $n = 2$ and $m = 4$ (with the parameter values given just above (10.12))).

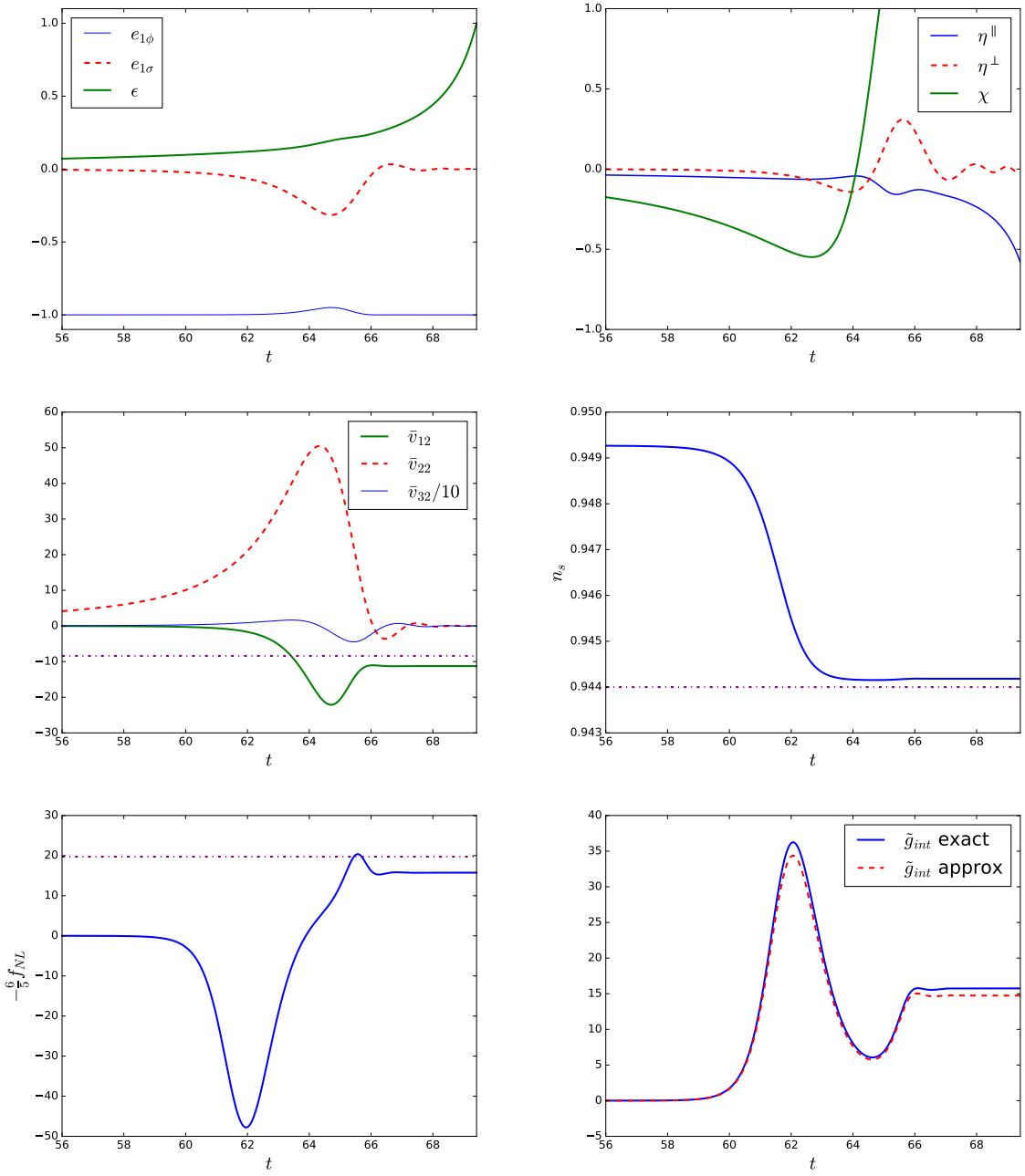

Figure 104: Same as figure 102 but for the quartic-axion potential (10.14).

10.4 Second type of turn

10.4.1 $m = 2$ and $n = 2$

Figure 82 shows that a turn of the first type respecting observational constraints is not possible for a monomial potential with $n = 2$ and $m = 2$. However, if we do not keep the constraint that the turn must start before the end of the slow-roll regime, this model can have a turn of the second type. This example was published originally in [191] and is here adapted to be in agreement with the latest Planck constraints. See the second line of plots in figure 91 for an illustration of the field trajectory. The potential has the form:

$$W(\phi, \sigma) = \alpha\phi^2 + C + \beta\sigma^2 + \lambda\sigma^4, \tag{10.18}$$

with $\alpha = 20\kappa^{-2}$, $C = \frac{\beta^2}{4\lambda}$, $\beta = -9\kappa^{-2}$ and $\lambda = 2$. The initial conditions are $\phi_i = 18\kappa^{-1}$ and $\sigma_i = 0.01\kappa^{-1}$ with $\dot{\phi}_i$ and $\dot{\sigma}_i$ determined by the slow-roll approximation. At horizon-crossing, we have:

$$\phi_* = 14.9\kappa^{-1} \qquad \text{and} \qquad \sigma_* = 0.011 \times 10^{-3}\kappa^{-1}. \tag{10.19}$$

Substituted into (10.5), (10.6) and (10.7) this gives:

$$\bar{v}_{12e} = -\frac{2\kappa}{\phi_*\sigma_*}\frac{C}{2\beta} = 6.9, \quad n_s = 1 - \frac{4}{\phi_*^2} + \frac{4\beta}{\kappa^2\alpha\phi_*^2} = 0.974 \quad \text{and} \quad -\frac{6}{5}f_{\rm NL} = -\frac{2\beta}{\kappa^2 C} = 1.8. \tag{10.20}$$

Figure 105 confirms that in this example the turn occurs after the field ϕ reaches the minimum of its potential. The Green's function $\bar{v}_{12e}$ is larger than the slow-roll value, hence $f_{\rm NL}$ is a little smaller than expected. This is in agreement with the discussion of the second type of turn in section 9.7. However, this does not have any impact on the spectral index because the dependence on $\bar{v}_{12e}$ disappears when it is larger than 4. Hence, this model is allowed by the Planck constraints.

10.4.2 A non-monomial example

This last example is in the vein of the previous one in terms of the form of the field trajectory. However, there are several supplementary terms to show the validity of some analytical results beyond simple monomial potentials. The model has the following potential:

$$W(\phi, \sigma) = \frac{1}{4}\lambda\left(\phi^4 + \sigma^4 + m^4 - 2m^2\phi^2 - 2m^2\sigma^2\right) + \nu(m - \phi)^3 + W_0, \tag{10.21}$$

with $\lambda = 1200$, $\nu = 100\kappa^{-1}$, $m = 2\kappa^{-1}$ and $W_0 = \frac{1}{4}\lambda m^4$. The initial conditions are $\phi_i = 25\kappa^{-1}$ and $\sigma_i = 0.05\kappa^{-1}$. We cannot use the monomial potential equations to determine ϕ_* and σ_*, however the slow-roll estimation of $f_{\rm NL}$ does not require them:

$$-\frac{6}{5}f_{\rm NL} = \frac{4}{\kappa^2 m^2} = 1. \tag{10.22}$$

Figure 106 shows a similar behaviour as for the previous example. Again $f_{\rm NL}$ is smaller than its slow-roll prediction. The reason is still the same, the period of large ϵ makes $\bar{v}_{12e}$ larger by a factor of order unity than in the slow-roll approximation and the direct consequence is that $f_{\rm NL}$ is reduced by the same factor.

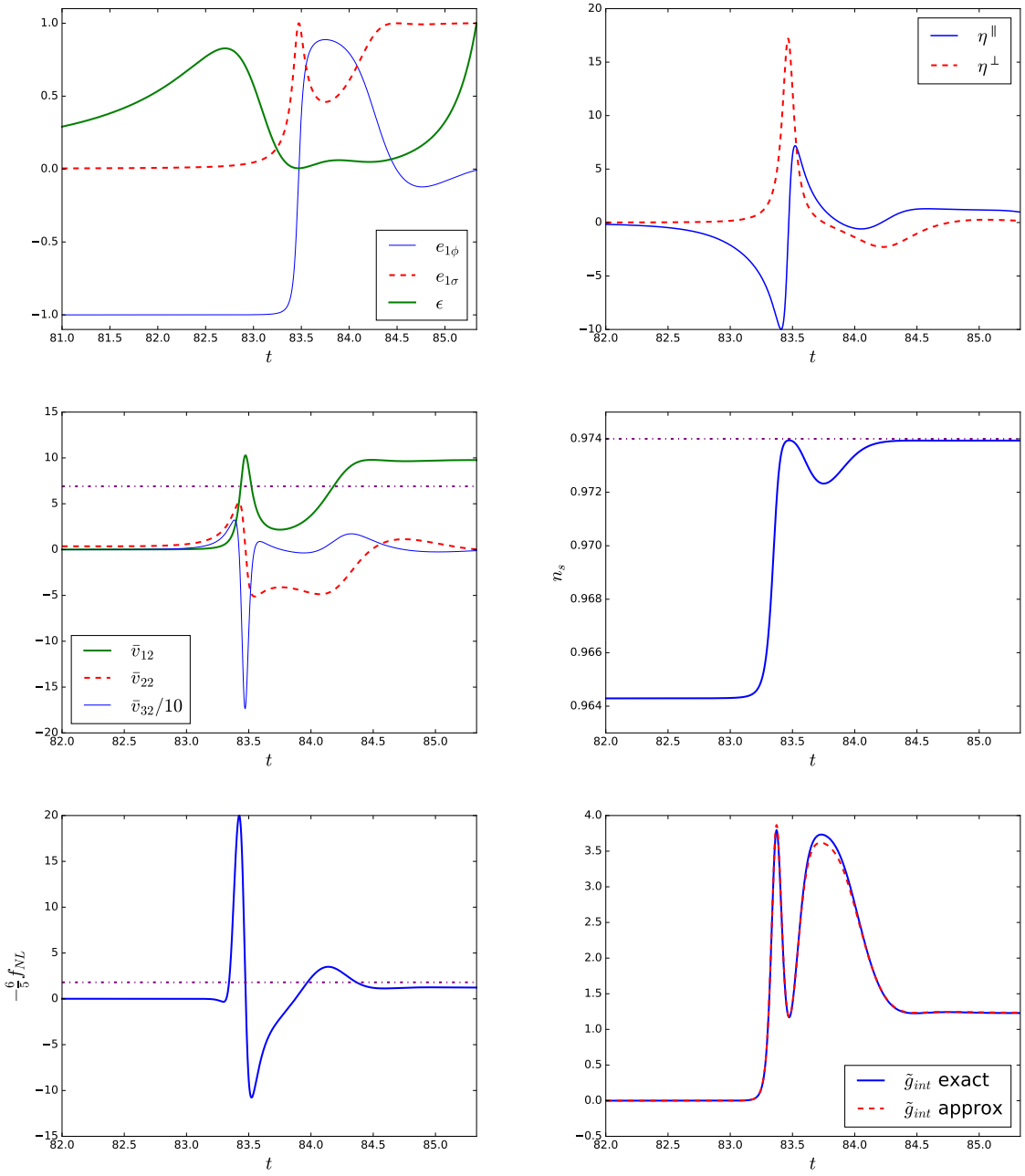

Figure 105: Same as figure 102 but for the monomial potential with $n = 2$ and $m = 2$ (10.18).

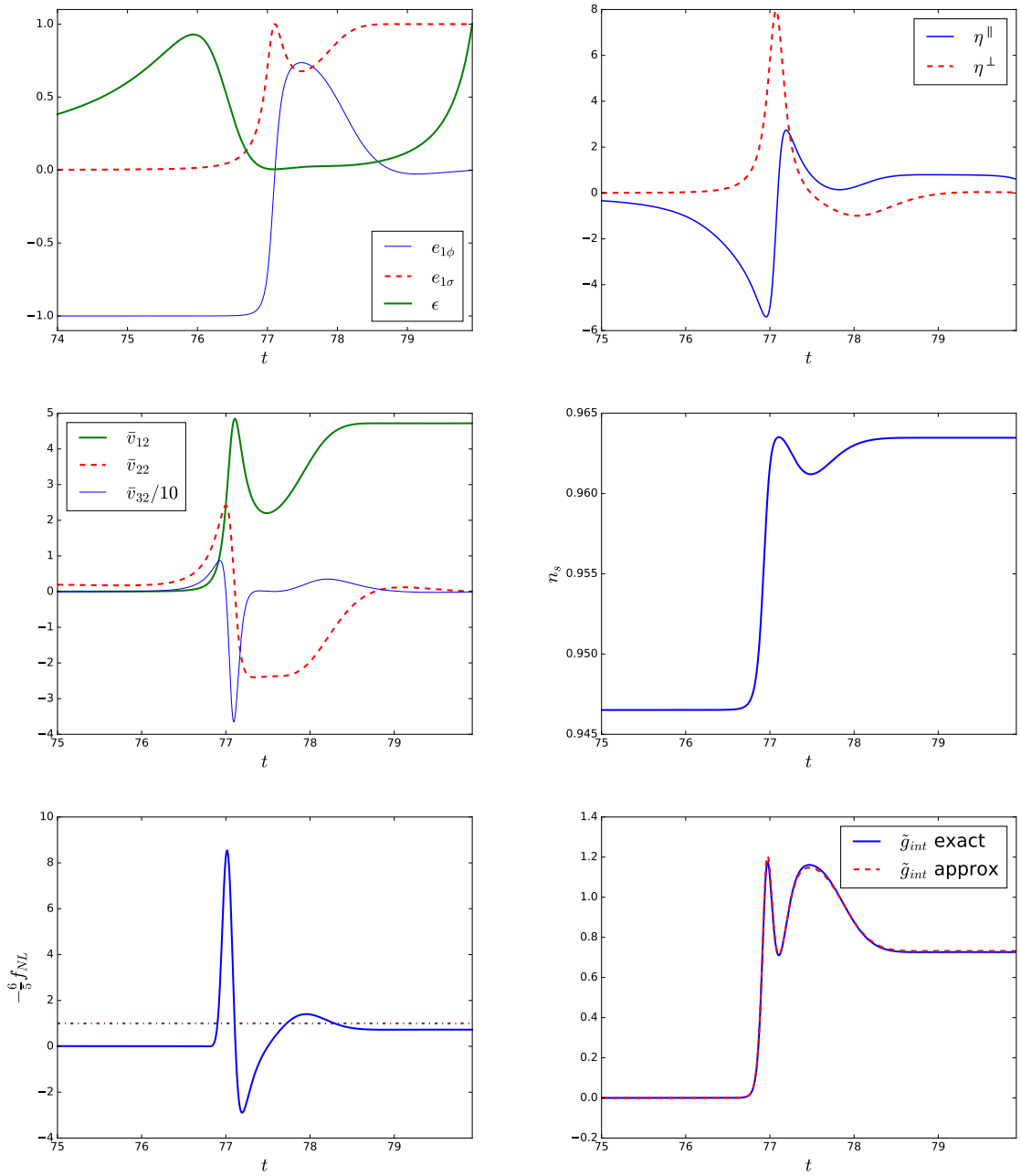

Figure 106: Same as figure 105 but for the non-monomial potential (10.21) (without analytical predictions for n_s and $\bar{v}_{12e}$).

Chapter 11

Conclusion

In this thesis, we worked on the theoretical and observational aspects of primordial non-Gaussianity of the bispectral type. It is an important observable from the point of view of inflation because many models that are today compatible with the observations of the power spectrum (amplitude and scale dependence) predict bispectra with different shapes and amplitude. The Planck satellite has so far not detected any primordial non-Gaussianity but it has tightened the constraints significantly. Hence it is necessary to better understand what regions of inflation model space have been ruled out, as well as prepare for the next generation of experiments. In this thesis, we have worked on the case of two-field inflation where the presence of an isocurvature mode on super-horizon scales can cause the adiabatic mode to evolve, while it would be frozen on these scales if there were only one field. One of the main consequences is the presence of a bispectrum of the local type.

For the moment, the main constraints on primordial quantities come from the observations of the CMB anisotropies. Estimating the amount of primordial non-Gaussianity from the data is not an easy task as they have been contaminated by many effects. Some, like the intrinsic bispectrum arising when taking into account second-order terms in the equations describing the evolution of the primordial fluctuations after horizon re-entry before recombination, have a small influence compared to the current constraints, but might be an issue later. Others, due to the presence of many structures along the path of the CMB photons (extra-galactic foregrounds, ISW-lensing), are strong enough to be detected but are also well understood. The most non-Gaussian ones are the closest to us: the galactic foregrounds. Many techniques have been developed to separate them from the rest of the sky observations in the microwave range. We used temperature maps of several galactic foregrounds (dust, synchrotron, free-free, AME) which are the results of one of these techniques (Commander).

There are different methods to determine the values of the bispectrum amplitude parameters $f_{\rm NL}$. Here we worked with the binned bispectrum estimator, a method well adapted for relatively smooth bispectra. It has several advantages, among them is the fact that it can compute explicitly the binned bispectrum of any data map. Then in principle, it is possible to use the numerical binned bispectrum of a map as a theoretical template for which we want to determine a parameter $f_{\rm NL}$ in any other maps. This possibility was mentioned in the original paper of the binned bispectrum estimator [43] and was indeed one of the motivations for developing it, but had until now never been worked out. A large part of the work was to implement it explicitly in the binned bispectrum estimator code. Moreover, that was the basic idea of the data analysis part of this thesis, where the galactic foregrounds played the role of numerical templates we applied to the CMB maps. The first step of the procedure was to determine the binned bispectra of the galactic foregrounds. We found that the dust, the free-free and the anomalous microwave emissions have very squeezed bispectra (similar to the local shape, but with an opposite sign). The small-scale fluctuations of the dust radiation are biggest in the

large-scale dust clouds, so small-scale and large-scale fluctuations are correlated (and a similar explanation is valid for the other foregrounds). The synchrotron map as provided is different, as its bispectrum is more similar to the equilateral shape, but we were able to show that at least a large part of this effect is due to a residual contamination by unresolved extra-galactic point sources. At 143 GHz (the most important Planck frequency for CMB analysis), only the dust really contaminates the CMB signal, the other foregrounds giving contributions orders of magnitude smaller. An issue with the numerical templates we determined is that they also depend on the mask applied to the foregrounds and contain the characteristics of the experiment like the beam and the noise. We showed that the choice of the mask is very important because the foregrounds are localized in the galactic plane like the largest part of the mask, so a small change of mask could give a large difference of bispectrum. This means the same mask should be used for determining the template as for the final analysis.

We then used these templates on different CMB maps (simulations and observational data). We performed several tests to confirm the validity of this new usage of the binned bispectrum estimator. These tests were based on Gaussian realizations of the CMB to which we added noise simulations and a known amount of dust. We showed that both with an isotropic and anisotropic noise, we managed to detect the expected amount of dust in our maps. However, to do a joint analysis with the primordial and the dust shapes, the usual choice of bins, while acceptable, can be improved. More bins are required at low ℓ to better discriminate between the templates that peak in the squeezed configuration (local and dust especially). We also discussed the effects of the (small) breakdown of the weak non-Gaussianity approximation that occurs when we add the full dust map to the CMB simulations (so the expected amount of dust in raw sky observations). The main consequence is that the real error bars become several times larger than the Fisher forecasts. We then used the numerical templates on the cleaned CMB SMICA map of the 2015 Planck release. As expected, we did not detect any residual of the dust. The error bars for the dust and local shapes increase in a joint analysis with the usual binning, again because of the choice of bins that is not optimal to differentiate them. Finally, we applied the foreground templates to the raw sky map at 143 GHz and the binned bispectrum estimator succeeded in detecting the dust in it (the intensities of other foregrounds at 143 GHz being too small to detect even if they were present in the map).

While the data we analyzed consisted only of temperature maps in this thesis, the additions to the binned bispectrum estimator code are also compatible with E-polarization. Moreover, the emissions from several galactic foregrounds like the dust and the synchrotron is also polarized. Therefore, it would be interesting to perform a similar study on the polarization to determine full templates (temperature + polarization) of the galactic foregrounds and to analyze jointly the CMB temperature and polarization anisotropies. Moreover, a new release from Planck with a better understanding of the polarization systematics is planned in the coming months (see [18] for recent results on the dust polarization). Other uses of this new ability of the binned bispectrum estimator are also envisaged. Instead of determining the numerical templates from observational data, it would be important to examine the simulations of the galactic foregrounds that already exist. It could also become a test of the validity of the simulations to verify that they are consistent with the real foregrounds at the bispectral level. Building analytical heuristic models of the foreground shapes from the numerical binned bispectra would also be interesting for future analyses, including those using other estimators of f_{NL}.

In this thesis, we also discussed the levels of non-Gaussianity produced in two-field inflation with a sum potential $W(\phi, \sigma) = U(\phi) + V(\sigma)$ and standard kinetic terms. We looked both at the case where the (strong) slow-roll approximation is valid throughout inflation (meaning that all slow-roll parameters, even the perpendicular ones, are small), and at the case where slow roll is broken during the turn of the field trajectory. For comparison we also examined

the case of a product potential, but as was shown before, in that case one cannot get large non-Gaussianity at all in the slow-roll approximation and with a vanishing isocurvature mode at the end of inflation. An important assumption in our models is that we impose that the isocurvature mode that is present during inflation (and whose interaction with the adiabatic mode on super-Hubble scales generates the non-Gaussianity) has disappeared by the end of inflation. In that case the super-Hubble adiabatic mode is constant after inflation and we can extrapolate the results at the end of inflation directly to the time of recombination and observations of the CMB without knowing any details about the evolution of the universe in between. Without this assumption it would be much easier to create large non-Gaussianity, simply by ending inflation in the middle of the turn, but the result at the end of inflation would be meaningless from the point of view of CMB observations without a proper treatment of the transition at the end of inflation and the consecutive period of (p)reheating.

We use the long-wavelength formalism for our computations of non-Gaussianity. In this formalism [191], under the assumption mentioned above, any large (meaning order unity or more, so not slow-roll suppressed) contribution to $f_{\rm NL}$ can only come from an integral expression called $g_{\rm int}$. The original formulation of this expression contains an integral over Green's functions, which depend on two different times, making it hard to interpret the expression and see which types of potentials will lead to large non-Gaussianity. In this thesis we have found another expression for $g_{\rm int}$, as the solution (7.49) of a differential equation (7.47), which can be written as the sum of a homogeneous and a particular solution. This expression is very useful, since for the homogeneous solution we have an exact analytic expression that does not require any slow-roll approximation, while for the particular solution we have seen (within the context of the class of models studied) that we can either compute it explicitly, or show that it is negligible. We also derived some relations of proportionality between the different Green's functions which are useful in the computations.

We have highlighted the tension between a large $f_{\rm NL}$ of order unity or more and the current observational bounds on the spectral index n_s, both being linked to the second derivative of the potential $V_{\sigma\sigma}$, where σ is the sub-dominant field at horizon crossing and until the turn of the field trajectory. We evaluated these tensions within the slow-roll approximation for monomial potentials, where it would otherwise be easy, with some fine-tuning, to reach the requirements for a large $f_{\rm NL}$. We have shown that a large part of the parameter space for $f_{\rm NL}$ of order unity is simply forbidden because of the constraints on n_s. We have found that these constraints are very sensitive to the value of n_s: if the lower bound were only smaller by 0.02 ($n_s \approx 0.94$), the situation would be very different and most of the parameter space would be allowed. This analysis of the monomial potential also revealed that the duration of inflation after horizon-crossing is important: a value around fifty e-folds is much more constraining than the usual sixty e-folds. This also indicates that in the rare working models, the turn of the field trajectory occurs near the end of inflation. This raises several issues, the main one being that at that time, slow-roll parameters generally stop to be small compared to one and the slow-roll approximation does not work anymore. Moreover, if the turn occurs too close to the end of inflation, the isocurvature mode may not have time to vanish. By studying turns where the slow-roll parameter ϵ is still small compared to one we avoid this last problem: the time ϵ needs to increase to one and end inflation can give enough time for the isocurvature mode to vanish.

The natural continuation of this study was to consider what would happen if we abandoned the slow-roll approximation during the turn and allowed the slow-roll parameters $\eta^{\parallel}$ and $\eta^{\perp}$ to become large there. On the other hand, we still assume that ϵ remains small during the turn, for several reasons: because of the issue regarding the vanishing of the isocurvature mode mentioned above, because we saw numerically in the models we looked at that this was a good approximation, and because this approximation allowed us to derive some very interesting

analytical results (a potential period of large ϵ right before the turn was taken into account though). We identified two different types of models where such a turn can happen, shown in figure 91. Substituting the slow-roll expression for $\dot{g}_{\rm int}$ into (7.47), we were able to show (using simple comparisons of the different terms of the differential equation) that it is also a very good approximation even if the slow-roll parameters $\eta^{\parallel}$ and $\eta^{\perp}$ become large during the turn. The main idea is the one mentioned above: as long as the slow-roll approximation is valid, we can compute the particular solution explicitly, while when it is broken, we can show that the particular solution becomes negligible, even though we cannot compute an analytic expression for it in that case (the fact that ϵ remains small is a crucial ingredient in this proof). For the homogeneous solution we have an analytic expression that is valid everywhere. We were also able to show that adding the slow-roll particular solution to the homogeneous solution in the regions where the exact particular solution is negligible does not introduce a significant error, which means that we do not have to perform an explicit matching of the solutions at each transition between a slow-roll and a non-slow-roll region.

This led us to the conclusion that, within the context of the models studied and the assumptions mentioned above, the slow-roll expression for $f_{\rm NL}$ is a very good approximation for the exact value, even in models where $\eta^{\parallel}$ and $\eta^{\perp}$ become large during the turn of the field trajectory and break slow roll. Hence the implications of this expression for having large non-Gaussianity, discussed in the context of the slow-roll approximation, mostly apply to this case as well. In particular, the constraints due to the spectral index n_s remain very important. A two-field sum potential with large $f_{\rm NL}$ requires a lot of fine-tuning (and we showed explicitly in the section with numerical examples how to construct such a model). Reducing the error bars on the measurements of the spectral index could even shrink the parameter region of these models where $f_{\rm NL}$ is of order unity more than reducing the error bars on $f_{\rm NL}$ itself.

A large part of the work presented in this thesis is devoted to the treatment of sum potentials, but it would be interesting to examine other classes of potentials. We investigated the question numerically for other two-field potentials (keeping standard kinetic terms). We observed that in fact it was also difficult to obtain large non-Gaussianity with more complicated models with the important assumption of a vanishing isocurvature mode at the end of inflation. More importantly, the few examples we got obeyed the conditions of large non-Gaussianity for sum potentials. In other words, the few examples we had were always easy to transform into sum potentials by eliminating the interaction terms, which gave similar (but not exactly the same) non-Gaussianity predictions. However, we do not yet have enough evidence to state that this is a general result. Moreover, the question would also have to be studied analytically, using (7.47) and (7.49) which are general results. The situation is different if inflation ends during a turn of the field trajectory or soon after because the isocurvature mode does not have the time to vanish and large non-Gaussianity is easy to obtain. However, in that case the main contribution does not come from the integral term $g_{\rm int}$ but from the term $g_{\rm iso}$ defined in (7.45). The extrapolation of the inflationary prediction to the CMB anisotropies becomes a lot more complicated because the adiabatic mode could continue to evolve on super-horizon scales after inflation. The proper treatment of perturbations during (p)reheating, a complicated topic from the theoretical and numerical points of view, then becomes necessary.

We conclude this thesis by a brief overview of the future cosmological observations which will improve our knowledge about the primordial universe. The measurements of the temperature anisotropies of the CMB are so precise since Planck that they are close to the cosmic variance, the limit due to the fact we only have one realization of the CMB to observe. However, there is still a lot of information to recover from the CMB by observing more precisely its polarization. There is still room for improvements of the measurements of E-polarization, but the main focus of CMB surveys in the near future is the detection of primordial B-modes. Observing the tensor modes of the primordial fluctuations, instead of having only an upper

bound, would give us the energy scale of inflation. The current limit (where $r < \mathcal{O}(10^{-1})$) is already constraining for classic single-field models. But many inflationary models, like the two-field models with large non-Gaussianity we discussed in this thesis, predict a tensor-to-scalar ratio several orders of magnitude smaller. Ground experiments like BICEP and Keck Array are already underway and improving their accuracy regularly (see [12] for the current best constraints), and new results are expected in the coming months. For the future ground experiments, we can cite the ambitious CMB-S4 [1]. Satellite missions are also envisaged, we mentioned earlier LiteBIRD [145] and CORE [40], this last one being the successor of Planck. A detection of r down to a value of 0.001 is realistic for the next generation experiments. An experiment like CORE would also reduce significantly the error bars on the different $f_{\rm NL}$ parameters, at least by a factor 2 compared to Planck. Moreover, other sources of information than the CMB anisotropies are now conceivable. Large-scale structure surveys like Euclid [120] will help to answer major questions of the field of cosmology like the nature of dark energy. They can also be constraining for primordial non-Gaussianity despite all the non-linear effects arising during structure formation. It has been shown that reaching the important milestone of $\Delta f_{\rm NL}^{\rm local} = 1$ is realistic (see [199] and references therein). This same amplitude for the local primordial bispectrum can also be detected using precise measurements of the angular power spectrum of the CIB and a better mapping of the galactic dust [188]. The era of precision cosmology that started fifteen years ago is still only in its initial stages. The whole field of cosmology can expect major results and a better understanding of the evolution of our universe in the coming years. This is especially the case for the early universe and inflation, where our increasing knowledge of the primordial perturbations and their non-Gaussianity is more and more constraining, leading to many theoretical challenges.

Appendices

Appendix A

Weights of bispectral shapes

In this appendix, we give another representation of the different bispectra discussed in section 4.2 (primordial shapes, ISW-lensing and extra-galactic foregrounds) and chapter 5 (galactic foregrounds) well-suited to understand the correlation coefficients given in tables 41, 51 and 52.

The weight of a single multipole configuration (ℓ_1, ℓ_2, ℓ_3) of a bispectral shape $B_{\ell_1\ell_2\ell_3}$ is defined by [43]

$$w_{\ell_1\ell_2\ell_3} = \frac{1}{\langle B, B\rangle} \frac{(B_{\ell_1\ell_2\ell_3})^2}{V_{\ell_1\ell_2\ell_3}}. \tag{A.1}$$

It is the inverse of the variance of the ratio of the observed and theoretical bispectra divided by $\langle B, B\rangle$ which is the denominator of the estimator for $f_{\rm NL}$ and normalizes the sum of the weights to one. In other words,

$$\hat{f}_{\rm NL} = \sum_{\ell_1\ell_2\ell_3} w_{\ell_1\ell_2\ell_3} \frac{B^{\rm obs}_{\ell_1\ell_2\ell_3}}{B_{\ell_1\ell_2\ell_3}}, \tag{A.2}$$

where $B^{\rm obs}/B$ can be viewed as an $f_{\rm NL}$ estimator based on just a single ℓ-triplet. These equations are the same for bin-triplets (i_1, i_2, i_3). Figures A1, A2, and A3 show the weights of the different theoretical and numerical shapes discussed in this thesis at both high and low resolution, with the usual choice of 57 bins. Instead of using a few slices of ℓ_3 like in chapter 5, we summed over ℓ_3. It has the advantage that now the whole bispectrum is used in one figure, but of course we lose the information about the variation of the bispectrum as a function of ℓ_3. A larger weight means that the region of multipole space is more important for the template. Conversely, a large observed non-Gaussianity in that region of multipole space means that it is more likely to be that particular shape.

In this kind of plot, shapes that peak in squeezed configurations will have a colored band/line at the bottom of the figure (low ℓ_1). As expected it is present for the different foregrounds for very low ℓ_1 ($< \mathcal{O}(20)$), including synchrotron (which was not visible in figure 58). As expected, the characteristic line of a squeezed bispectrum can be seen for the local and the ISW-lensing shapes, but also for the orthogonal shape (which explains why it is somewhat correlated to the foregrounds).

Shapes that peak in equilateral configurations have a large weight along the diagonal black line of these plots, when the three ℓ's are of the same order. The primordial equilateral shape is the strongest for three low ℓ's, while the point sources and the CIB are more non-Gaussian at higher multipoles. It is easy to see the correlation between the point sources and the synchrotron bispectra which peak when the three ℓ's are over 150. An additional remark is necessary about the orthogonal shape. Indeed by definition it is orthogonal to the equilateral shape

(uncorrelated), which is not visible in these figures because they both have similar acoustic peaks. It is an effect of the sum over ℓ_3 which hides the differences of these bispectra.

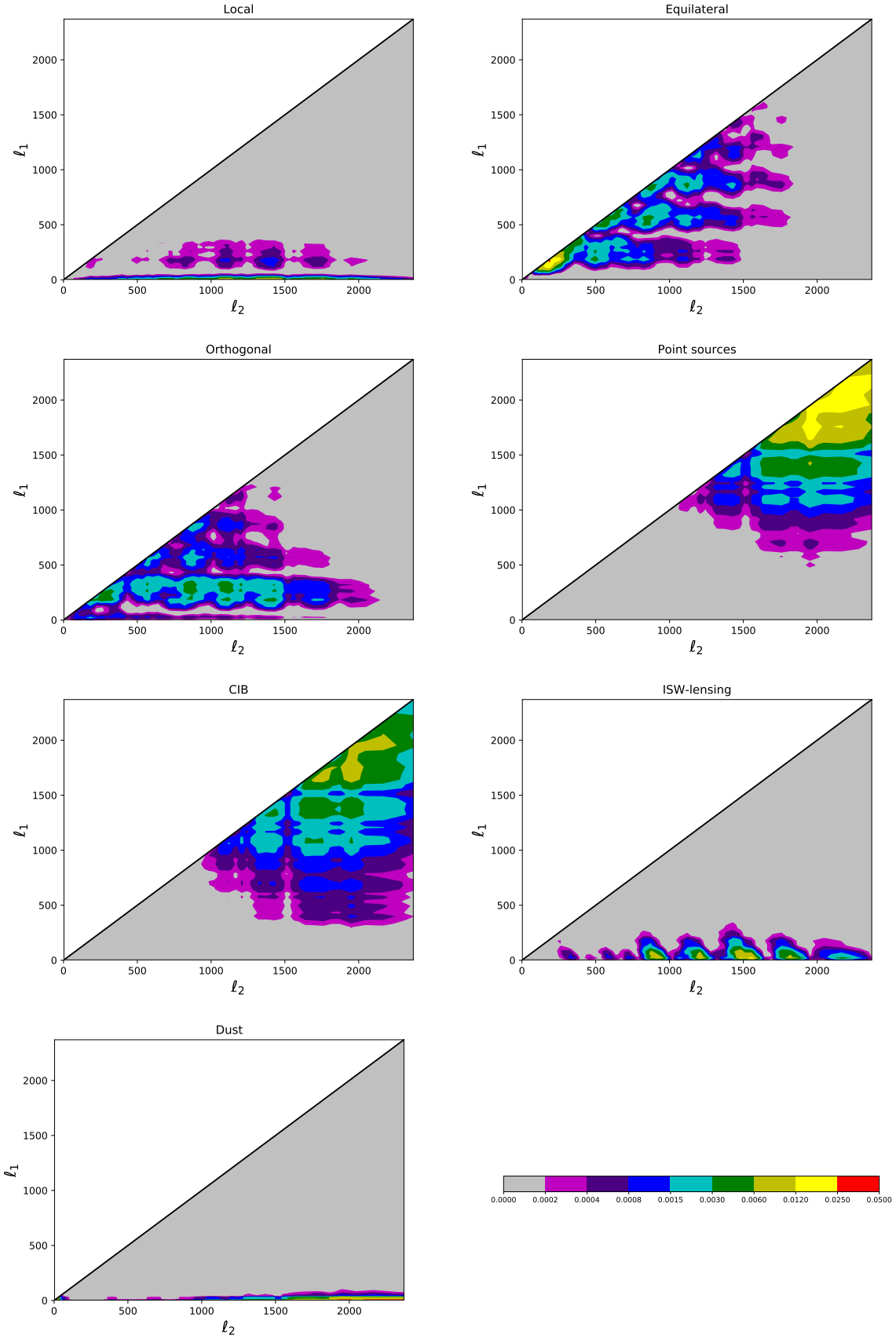

Figure A1: Weights of the bispectral shapes discussed in section 4.2 and chapter 5 at high resolution. Note that the colour scale is logarithmic.

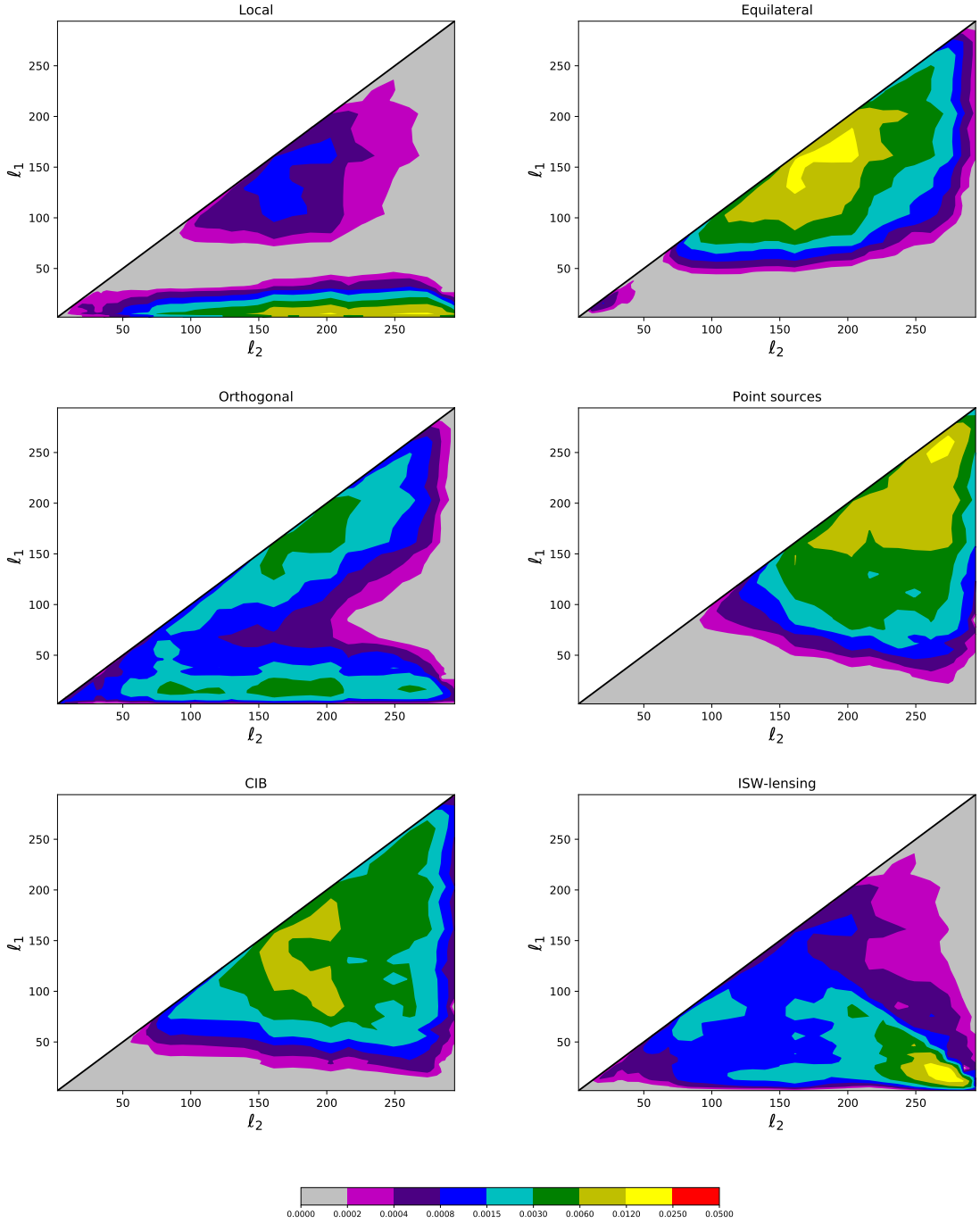

Figure A2: Weights of the bispectral shapes discussed in section 4.2 and chapter 5 at low resolution. Note the difference on the axes with the previous figure. The colour scale is the same, but the weights are normalized to one here over a much reduced region of multipole space with $\ell < 300$.

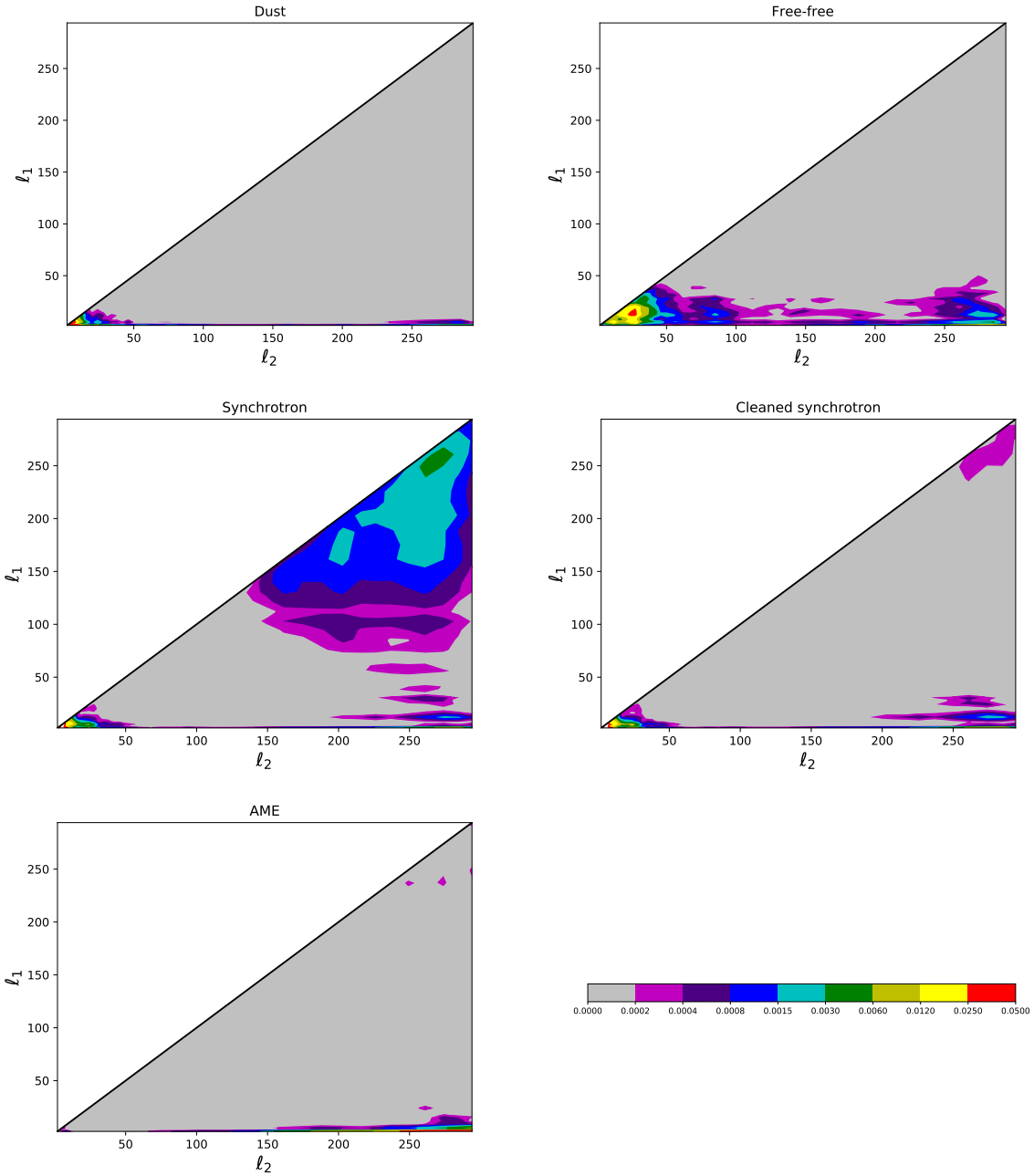

Figure A3: Weights of the foreground bispectral shapes discussed in this thesis at low resolution.

Appendix B

Long-wavelength formalism

In this appendix, we give the expressions of several quantities used in the derivation of second-order perturbations in the long-wavelength formalism (7.15). First, we need the first-order perturbation of the matrix $\mathbf{A}$. It is given by $A^{(1)}_{ab} = \bar{A}^{(0)}_{abc} v^{(1)}_c(t, \boldsymbol{x})$ where the matrix elements of $\bar{A}_{abc}$ are zero except [164]

$$\begin{aligned}
\bar{A}_{121} &= 2\epsilon\eta^{\perp} - 4\eta^{\parallel}\eta^{\perp} + 2\xi^{\perp}, \\
\bar{A}_{122} &= -6\chi - 2\epsilon\eta^{\parallel} - 2(\eta^{\parallel})^2 - 2(\eta^{\perp})^2, \\
\bar{A}_{123} &= -6 - 2\eta^{\parallel}, \\
\bar{A}_{321} &= -12\epsilon\eta^{\parallel} - 12(\eta^{\perp})^2 - 6\epsilon\chi - 8\epsilon^3 - 20\epsilon^2\eta^{\parallel} - 4\epsilon(\eta^{\parallel})^2 - 12\epsilon(\eta^{\perp})^2 \\
&\quad + 16\eta^{\parallel}(\eta^{\perp})^2 - 6\epsilon\xi^{\parallel} - 12\eta^{\perp}\xi^{\perp} + 3(\tilde{W}_{111} - \tilde{W}_{221}), \\
\bar{A}_{322} &= -24\epsilon\eta^{\perp} - 12\eta^{\parallel}\eta^{\perp} + 24\eta^{\perp}\chi - 12\epsilon^2\eta^{\perp} + 8(\eta^{\parallel})^2\eta^{\perp} + 8(\eta^{\perp})^3 \\
&\quad - 8\epsilon\xi^{\perp} - 4\eta^{\parallel}\xi^{\perp} + 3(\tilde{W}_{211} - \tilde{W}_{222}), \\
\bar{A}_{323} &= 12\eta^{\perp} - 4\epsilon\eta^{\perp} + 8\eta^{\parallel}\eta^{\perp} - 4\xi^{\perp}, \\
\bar{A}_{331} &= -2\epsilon^2 - 4\epsilon\eta^{\parallel} + 2(\eta^{\parallel})^2 - 2(\eta^{\perp})^2 - 2\xi^{\parallel}, \\
\bar{A}_{332} &= -4\epsilon\eta^{\perp} - 2\xi^{\perp}, \\
\bar{A}_{333} &= -2\eta^{\perp}.
\end{aligned} \tag{B.1}$$

We also need the second-order source term $b^{(2)}$ which was computed in [191] and is constructed similarly to the first-order term (7.19)

$$\begin{aligned}
b^{(2)}_{ia} = \int \frac{\mathrm{d}^3\boldsymbol{k}}{(2\pi)^{3/2}} \int \frac{\mathrm{d}^3\boldsymbol{k'}}{(2\pi)^{3/2}} \dot{W}(\max(k', k)) \\
\times [L_{abc}(t) X^{(1)}_{bm}(k', t) X^{(1)}_{cn}(k, t) \hat{a}^{\dagger}_m(\boldsymbol{k'}) \hat{a}^{\dagger}_n(\boldsymbol{k}) \mathrm{i}(k'_i + k_i) \mathrm{e}^{i(\boldsymbol{k'}+\boldsymbol{k}).\boldsymbol{x}} \\
+ N_{abc}(t) X^{(1)}_{bm}(k', t) X^{(1)}_{cn}(k, t) \hat{a}^{\dagger}_m(\boldsymbol{k'}) \hat{a}^{\dagger}_n(\boldsymbol{k}) \mathrm{i} k_i \mathrm{e}^{i(\boldsymbol{k'}+\boldsymbol{k}).\boldsymbol{x}} + \text{c.c.}],
\end{aligned} \tag{B.2}$$

where the matrices L_{abc} and N_{abc} are determined at horizon crossing with a slow-roll approximation. Their only non-zero elements obey the relations:

$$\begin{aligned}
L_{111*} &= \epsilon_* + \eta^{\parallel}_*, & L_{122*} &= -\left(\epsilon_* + \eta^{\parallel}_* - \chi_*\right), \\
L_{211*} &= \eta^{\perp}_*, & L_{222*} &= \eta^{\perp}_*, \\
L_{112*} + L_{121*} &= 2\eta^{\perp}_*, & N_{112*} + N_{121*} &= -2\eta^{\perp}_*, \\
L_{212*} + L_{221*} &= 2\left(\epsilon_* + \eta^{\parallel}_* - \chi_*\right), & N_{212*} + N_{221*} &= \chi_*.
\end{aligned} \tag{B.3}$$

Appendix C

Derivation of the g_{int} equation

In this appendix we present the derivation of the differential equation (7.47) for $\dot{g}_{\text{int}}$. A direct computation of the first, second, and third derivatives of the definition of g_{int} in (7.45) with respect to t using (7.12) and (7.20) gives:

$$
\begin{aligned}
\dot{g}_{\text{int}} =& -2(\eta^{\perp})^2(\bar{v}_{22})^2 - (\epsilon+\eta^{\parallel})\bar{v}_{22}\bar{v}_{32} - (\bar{v}_{32})^2 + 2\eta^{\perp}\int_{t_*}^{t} \mathrm{d}t'\, \bar{v}_{22}G_{23}\left(\Xi\bar{v}_{22} + 9\eta^{\perp}\bar{v}_{32}\right),\\
\ddot{g}_{\text{int}} =& 2\left(\xi^{\perp} + \eta^{\perp}(\epsilon - 2\eta^{\parallel})\right)\int_{t_*}^{t} \mathrm{d}t'\, \bar{v}_{22}G_{23}\left(\Xi\bar{v}_{22} + 9\eta^{\perp}\bar{v}_{32}\right)\\
&+ 2\eta^{\perp}\int_{t_*}^{t} \mathrm{d}t'\, \bar{v}_{22}G_{33}\left(\Xi\bar{v}_{22} + 9\eta^{\perp}\bar{v}_{32}\right)\\
&+ (\bar{v}_{22})^2\Big(3(\epsilon+\eta^{\parallel})\chi + 2\epsilon^3 + 6\epsilon^2\eta^{\parallel} + 4\epsilon(\eta^{\parallel})^2 + 12\eta^{\parallel}(\eta^{\perp})^2 + (\epsilon+\eta^{\parallel})\xi^{\parallel} - 4\eta^{\perp}\xi^{\perp}\Big)\\
&+ \bar{v}_{22}\bar{v}_{32}\Big(3\epsilon + 3\eta^{\parallel} + 6\chi + 3\epsilon^2 + 8\epsilon\eta^{\parallel} + 3(\eta^{\parallel})^2 + 3(\eta^{\perp})^2 + \xi^{\parallel}\Big) + (\bar{v}_{32})^2\Big(6 + \epsilon + 3\eta^{\parallel}\Big),\\
\dddot{g}_{\text{int}} =& -(3\eta^{\perp} - \epsilon\eta^{\perp} + 6\eta^{\parallel}\eta^{\perp} - 2\xi^{\perp})\int_{t_*}^{t} \mathrm{d}t'\, \bar{v}_{22}G_{33}\left(\Xi\bar{v}_{22} + 9\eta^{\perp}\bar{v}_{32}\right)\\
&+ \Big(9\epsilon\eta^{\perp} + 6\eta^{\parallel}\eta^{\perp} - 6\eta^{\perp}\chi - 3\xi^{\perp} - 3\tilde{W}_{211} + \epsilon^2\eta^{\perp} - 8\epsilon\eta^{\parallel}\eta^{\perp} + 6(\eta^{\parallel})^2\eta^{\perp} - 6(\eta^{\perp})^3\\
&\quad - 4\eta^{\perp}\xi^{\parallel} + (3\epsilon - 2\eta^{\parallel})\xi^{\perp}\Big)\int_{t_*}^{t} \mathrm{d}t'\, \bar{v}_{22}G_{23}\left(\Xi\bar{v}_{22} + 9\eta^{\perp}\bar{v}_{32}\right)\Big)\\
&+ (\bar{v}_{22})^2\Big(32\eta^{\parallel}\eta^{\perp}\xi^{\perp} - 60(\eta^{\parallel})^2(\eta^{\perp})^2 - 36\eta^{\parallel}(\eta^{\perp})^2 - 4(\eta^{\parallel})^2\xi^{\parallel} - 3\eta^{\parallel}\xi^{\parallel} - 12(\eta^{\parallel})^2\chi - 9\eta^{\parallel}\chi\\
&+ 6(\eta^{\perp})^2\xi^{\parallel} + 12\eta^{\perp}\xi^{\perp} + 6(\eta^{\perp})^2\chi + 12(\eta^{\perp})^4 - 6\xi^{\parallel}\chi - 4(\xi^{\perp})^2 - 18\chi^2 - 3\eta^{\parallel}\tilde{W}_{111} - 3\epsilon\tilde{W}_{111}\\
&+ 9\eta^{\perp}\tilde{W}_{211} + 3\eta^{\parallel}\tilde{W}_{221} + 3\epsilon\tilde{W}_{221} - 3\eta^{\perp}\tilde{W}_{222} + \eta^{\parallel}\xi^{\parallel}\epsilon - 33\eta^{\parallel}\chi\epsilon + 14\eta^{\parallel}\epsilon^3 - 4(\eta^{\parallel})^2\epsilon^2 - 6\eta^{\parallel}\epsilon^2\\
&- 12(\eta^{\parallel})^3\epsilon - 8\eta^{\perp}\xi^{\perp}\epsilon - 12(\eta^{\perp})^2\epsilon^2 - 36(\eta^{\perp})^2\epsilon + 5\xi^{\parallel}\epsilon^2 - 3\xi^{\parallel}\epsilon - 9\chi\epsilon^2 - 9\chi\epsilon + 6\epsilon^4 - 6\epsilon^3\Big)\\
&+ \bar{v}_{22}\bar{v}_{32}\Big(-12\eta^{\parallel}(\eta^{\perp})^2 - 24\eta^{\parallel}\chi - 12(\eta^{\parallel})^3 - 21(\eta^{\parallel})^2 - 9\eta^{\parallel} + 4\eta^{\perp}\xi^{\perp} - 15(\eta^{\perp})^2 - 9\xi^{\parallel} - 54\chi\\
&- 3\tilde{W}_{111} + 6\tilde{W}_{221} + 14\eta^{\parallel}\epsilon^2 - 21(\eta^{\parallel})^2\epsilon - 57\eta^{\parallel}\epsilon + 3(\eta^{\perp})^2\epsilon + 9\xi^{\parallel}\epsilon + 6\chi\epsilon + 9\epsilon^3 - 30\epsilon^2 - 9\epsilon\Big)\\
&+ (\bar{v}_{32})^2\Big(-12(\eta^{\parallel})^2 - 39\eta^{\parallel} + 6(\eta^{\perp})^2 + 4\xi^{\parallel} + 6\chi + 3\eta^{\parallel}\epsilon + 3\epsilon^2 - 15\epsilon - 36\Big).
\end{aligned}
\tag{C.1}
$$

Taking the specific combination of the three expressions above that eliminates all the terms with integrals then gives the differential equation (7.47), with K_{22}, K_{23}, K_{33} given by

$$\begin{aligned}
K_{22} =& -18(\eta^\perp)^2\chi^2 + 2(\eta^\parallel)^2(\eta^\perp)^2\xi^\parallel - 6\eta^\parallel\eta^\perp\xi^\perp\chi + 6(\eta^\parallel)^2(\eta^\perp)^2\chi - 6(\eta^\perp)^2\chi\xi^\parallel - 2(\eta^\perp)^4\xi^\parallel \\
&- 6(\eta^\perp)^4\chi - 18\epsilon\eta^\parallel(\eta^\perp)^2\chi + 12\epsilon^2\eta^\parallel(\eta^\perp)^2 + 12\epsilon(\eta^\parallel)^2(\eta^\perp)^2 - 6\epsilon\eta^\perp\xi^\perp\chi - 12\epsilon^2(\eta^\perp)^2\chi \\
&- 12\epsilon(\eta^\perp)^4 - 3\eta^\parallel(\eta^\perp)^2\tilde{W}_{111} - 3\epsilon(\eta^\perp)^2\tilde{W}_{111} + 3(\eta^\perp)^3\tilde{W}_{211} + 3\eta^\parallel(\eta^\perp)^2\tilde{W}_{221} \\
&+ 3\epsilon(\eta^\perp)^2\tilde{W}_{221} - 3(\eta^\perp)^3\tilde{W}_{222} - 2\eta^\parallel\eta^\perp\xi^\parallel\xi^\perp + 6\epsilon\eta^\parallel(\eta^\perp)^2\xi^\parallel - 12\epsilon^2\eta^\parallel\eta^\perp\xi^\perp \\
&+ 20\epsilon^3\eta^\parallel(\eta^\perp)^2 + 28\epsilon^2(\eta^\parallel)^2(\eta^\perp)^2 - 12\epsilon\eta^\parallel(\eta^\perp)^4 + 12\epsilon(\eta^\parallel)^3(\eta^\perp)^2 - 2\epsilon\eta^\perp\xi^\parallel\xi^\perp \\
&- 8\epsilon(\eta^\parallel)^2\eta^\perp\xi^\perp + 4\epsilon^2(\eta^\perp)^2\xi^\parallel - 4\epsilon^3\eta^\perp\xi^\perp - 4\epsilon(\eta^\perp)^3\xi^\perp + 4\epsilon^4(\eta^\perp)^2 - 12\epsilon^2(\eta^\perp)^4, \\
K_{23} =& -36(\eta^\perp)^2\chi - 6\epsilon\eta^\parallel(\eta^\perp)^2 - 12\epsilon^2(\eta^\perp)^2 - 6(\eta^\perp)^4 - 6\epsilon(\eta^\perp)^2\chi + 6(\eta^\parallel)^2(\eta^\perp)^2 - 6\eta^\parallel\eta^\perp\xi^\perp \\
&+ 6\eta^\parallel(\eta^\perp)^2\chi - 6(\eta^\perp)^2\xi^\parallel - 6\epsilon\eta^\perp\xi^\perp - 12\eta^\perp\chi\xi^\perp - 3(\eta^\perp)^2\tilde{W}_{111} - 3\eta^\parallel\eta^\perp\tilde{W}_{211} \\
&- 3\eta^\perp\epsilon\tilde{W}_{211} + 6(\eta^\perp)^2\tilde{W}_{221} - 2\eta^\perp\xi^\parallel\xi^\perp - 2\eta^\parallel(\xi^\perp)^2 + 2(\eta^\parallel)^2\eta^\perp\xi^\perp + 2\eta^\parallel(\eta^\perp)^2\xi^\parallel \\
&- 2(\eta^\perp)^3\xi^\perp - 8\epsilon\eta^\parallel\eta^\perp\xi^\perp + 18\epsilon(\eta^\parallel)^2(\eta^\perp)^2 + 24\epsilon^2\eta^\parallel(\eta^\perp)^2 + 4\epsilon(\eta^\perp)^2\xi^\parallel - 6\epsilon^2\eta^\perp\xi^\perp \\
&- 6(\eta^\perp)^4\epsilon + 6\epsilon^3(\eta^\perp)^2 - 2\epsilon(\xi^\perp)^2, \\
K_{33} =& -18(\eta^\perp)^2 - 6\epsilon(\eta^\perp)^2 + 6\eta^\parallel(\eta^\perp)^2 - 12\eta^\perp\xi^\perp - 3\eta^\perp\tilde{W}_{211} + 6\epsilon\eta^\parallel(\eta^\perp)^2 + 2\epsilon^2(\eta^\perp)^2 \\
&+ 2\eta^\parallel\eta^\perp\xi^\perp - 2\epsilon\eta^\perp\xi^\perp - 2(\xi^\perp)^2.
\end{aligned} \tag{C.2}$$

To obtain (8.6), the slow-roll approximation of (7.47), several steps have to be followed. First, on the right-hand side of the equation, one can use (8.3) to eliminate $\bar{v}_{32}$. Then one sees that the lowest-order terms (the first of each K in (C.2)) cancel each other. The remaining terms are one or two orders higher than the ones which cancel, so that in the leading-order slow-roll aproximation we only have to keep those one order higher. On the left-hand side of the equation, we also use the fact that a time derivative adds an order in slow roll, so that $\dddot{g}_{\rm int}$ is one order higher in slow-rol than $\ddot{g}_{\rm int}$. Hence, we see that the $\dddot{g}_{\rm int}$ term disappears completely from the equation. Finally, it is possible to substitute the second line of (8.1) into the two sides of (7.47) to eliminate $\tilde{W}_{111}$ and $\tilde{W}_{211}$, and after simplifying the common factor $3\eta^\perp$ the result is given in (8.6).

Appendix D

Influence of the choice of the value of $f_{\rm NL}$ on the start of a turn of the second type

In the second type of turn, we supposed that at horizon-crossing the situation was so close to single-field inflation that it is still quasi single-field at the time when ϵ becomes large and the slow-roll approximation breaks down for the first time. That time would have been the end of inflation in a purely single-field situation, the only difference being that here the potential goes to $W = V_*$ instead of $W = 0$. As we have seen, ϵ becomes small again soon after, but the remaining question is how much time is needed to break the quasi single-field situation and have the turn start? In other words, how much time is there typically between the moment when ϵ becomes small again and the start of the turn? We will see that is in particular related to the value of $f_{\rm NL}$.

First, for this argument we do not need to know the potential U as it is already supposed to be almost zero because ϕ is near the minimum. For σ, we will keep the simple monomial potential V (8.38) because, as already discussed, it is quite general when seen as an expansion in terms of σ around its local extremum. As discussed, ϕ is near the minimum of its potential while σ has not evolved much since horizon-crossing, hence W is simply C. Moreover, ϵ decreases again just before the turn, meaning that the slow-roll regime is back (see figure 91), with only one exception: $\eta^{\parallel}$ can be large (order unity or more). However, this concerns only the field ϕ and the only possible effect on σ is through ϵ which is small. Then, the field equation for σ is:

$$\frac{\mathrm{d}\sigma}{\sigma^{m-1}} = -\frac{m\beta}{C}\mathrm{d}t. \tag{D.1}$$

For $m = 2$, we have:

$$\sigma = \sigma_1 \exp\left[-\frac{2\beta}{C}(t-t_1)\right], \qquad \epsilon \approx \frac{1}{2}\dot{\sigma}^2 = 2\left(\frac{\sigma_1\beta}{C}\right)^2 \exp\left[-\frac{4\beta}{C}(t-t_1)\right], \tag{D.2}$$

where t_1 is the time when ϵ has become small compared to one again. The factor $-\frac{2\beta}{C}$ in the exponential is in fact $-\frac{6}{5}f_{\rm NL}$ in slow-roll (8.25). As we supposed that it is of the same order as the real value of $f_{\rm NL}$, it is of order unity and positive because of the form of the potential. The parameter ϵ increases exponentially and unless the initial value σ_* is ridiculously small compared to one, a very small number of e-folds after t_1 will be needed to reach $\epsilon = 1$, which is the end of inflation. However, in general the slow-roll regime will be broken again before that time. But here we are interested in the time when the turn starts, that is to say when $\dot{\phi}$ and $\dot{\sigma}$ are of the same order. As $\frac{1}{2}\dot{\phi}^2 \ll 1$ (because $\epsilon \ll 1$ and ϕ dominates at t_1), this will

occur before the end of inflation when $\epsilon = 1$. Hence, this period of quasi single-field inflation between t_1 and the start of the turn will only last a very few e-folds at most, because $f_{\rm NL}$ is of order unity.

For $m \neq 2$, the solution is

$$\sigma = \sigma_1 \left[1 - \frac{(2-m)m\beta}{C\sigma_1^{2-m}}(t-t_1)\right]^{\frac{1}{2-m}}. \tag{D.3}$$

Then, we obtain:

$$\epsilon = \frac{1}{2}\left(\frac{m\beta}{C}\right)^2 \sigma_1^{2m-2}\left[1 - \frac{(2-m)m\beta}{C\sigma_1^{2-m}}(t-t_1)\right]^{\frac{2m-2}{2-m}}. \tag{D.4}$$

When $m > 2$ and $m-2$ not small compared to 1, the end of inflation will be reached when $\frac{(2-m)m\beta}{C\sigma_1^{2-m}}(t-t_1) \approx 1$ which implies that

$$t_e - t_1 = \frac{C\sigma_1^{2-m}}{(2-m)m\beta} = \left(\frac{V_{\sigma\sigma *}}{V_*}\right)^{-1}\left(\frac{\sigma_1}{\sigma_*}\right)^{2-m}\frac{(m-1)}{(m-2)}. \tag{D.5}$$

The first factor is the inverse of $-\frac{6}{5}f_{\rm NL}$ in slow-roll, hence this is of order unity. The two ratios σ_1/σ_* and $(m-1)/(m-2)$ are also of order unity. Hence, $t_e - t_1$ is small and is of order one. When m is close to 2, we do an expansion at first order using the small parameter $m-2$ to obtain:

$$\begin{aligned}\epsilon &= \frac{1}{2}\left(\frac{m\beta}{C}\right)^2 \sigma_1^{2m-2}\exp\left[-2\frac{m(m-1)\beta\sigma^{m-2}}{C}\left(\frac{\sigma_1}{\sigma_*}\right)^{m-2}(t-t_1)\right] \\ &= \frac{1}{2}\left(\frac{m\beta}{C}\right)^2 \sigma_1^{2m-2}\exp\left[-2\left(\frac{V_{\sigma\sigma *}}{V_*}\right)\left(\frac{\sigma_1}{\sigma_*}\right)^{m-2}(t-t_1)\right].\end{aligned} \tag{D.6}$$

This gives back the formula for the $m = 2$ case. Again, we can see the factor $-\frac{V_{\sigma\sigma *}}{V_*}$ which is the slow-roll expression for $-\frac{6}{5}f_{\rm NL}$, while the whole expression in the exponential is positive because of the sign of β. It is of order one, for the same reason as in the other cases. Hence, in a matter of a few e-folds ϵ is large enough to say that $\dot\sigma$ is at least of the same order as $\dot\phi$ and that the turn has started.

A last important remark is that if $f_{\rm NL}$ is too large (more than order unity), inflation will end even faster. One has to verify that the turn has enough time to finish so that the isocurvature mode can vanish before the end of inflation.

Résumé en français

Contexte général

Lors du dernier siècle, de multiples observations ainsi que de nombreux travaux théoriques ont permis de construire et d'affiner le modèle standard de la cosmologie qui décrit l'histoire de notre univers. Dans l'univers primordial, il y a une période d'expansion rapide et accélérée appelée inflation [179, 96, 132]. Elle résout plusieurs problèmes importants de la théorie du Big Bang chaud (par exemple les problèmes de l'horizon et de la platitude). De façon encore plus remarquable, l'inflation explique d'où viennent les perturbations cosmologiques primordiales qui sont à l'origine des structures à grande échelle présentes dans l'univers observable actuel.

Il existe une fenêtre observationnelle presque directe sur ces petites fluctuations primordiales : les anisotropies de température et de polarisation du fond diffus cosmologique (CMB). Ce rayonnement électromagnétique a été émis lorsque le plasma primordial est devenu transparent, environ 380000 ans après le Big Bang. De nombreuses missions ont observé le ciel dans le domaine des micro-ondes et les résultats les plus récents proviennent de la mission Planck [13, 15]. Comme ses prédécesseurs, Planck n'a trouvé aucun désaccord avec les prédictions basiques de l'inflation : la distribution des perturbations primordiales est cohérente avec la loi gaussienne et est presque (mais pas exactement) invariante d'échelle. De plus, le satellite Planck a considérablement amélioré les contraintes sur tout écart potentiel par rapport à une distribution gaussienne (i.e. les non-gaussianités) [14].

Lors de la détermination des paramètres cosmologiques d'origine primordiale à l'aide de mesures précises du CMB, l'un des principaux problèmes est que plusieurs avant-plans d'origine galactique (comme la poussière interstellaire) ou extra-galactique (par exemple les sources ponctuelles) émettent également dans le domaine des micro-ondes. Cela a nécessité le développement de nombreuses techniques (voir [8, 9, 9, 16] et les références qui s'y trouvent) pour nettoyer les données observationnelles de ces différentes sources de contamination.

Si le CMB était gaussien, toutes les informations seraient contenues dans le spectre de puissance, qui est lié à la fonction de corrélation à deux points des fluctuations de température (ou de polarisation) du CMB. Le spectre de puissance est paramétrisé par deux observables importantes du point de vue de l'inflation : son amplitude A_s et l'indice spectral n_s qui décrit sa pente, c'est-à-dire l'écart par rapport à l'invariance d'échelle exacte. Les non-gaussianités primordiales sont généralement décrites par les paramètres d'amplitude $f_{\rm NL}$ d'un certain nombre de formes bispectrales spécifiques qui sont produites dans des classes génériques de modèles d'inflation. Le bispectre est lié à la fonction de corrélation à trois points des anisotropies du CMB. Il est connu pour être inobservablement petit [141] pour le modèle d'inflation le plus simple : l'inflation à un champ à roulement lent. Toutefois, ce résultat n'est pas général, ce qui signifie que les observations actuelles peuvent en principe être utilisées pour contraindre des modèles d'inflation plus complexes. Une extension populaire de l'inflation qui peut produire des non-gaussianités est l'inflation à plusieurs champs, où l'expansion est due à plusieurs champs scalaires.

Objectifs de la thèse et plan du manuscrit

Dans cette thèse, le sujet des non-gaussianités primordiales est étudié de deux points de vue différents. Le premier est l'estimation des non-gaussianités bispectrales dans les données d'observation des anisotropies du CMB (Planck). Il s'agit de la suite des travaux sur l'estimateur du bispectre binné [43, 42], utilisé pour l'analyse officielle Planck [11, 14]. Nous sommes intéressés par l'étude de la contamination du signal primordial due à plusieurs avant-plans galactiques (principalement la poussière) et à la détermination (numérique) de modèles pour leurs bispectres. Même si le bispectre n'est pas idéal pour décrire les non-gaussianités des avant-plans galactiques parce qu'ils sont très anisotropes (il vaudrait mieux travailler dans l'espace des pixels plutôt que dans l'espace harmonique), c'est exactement ce dont nous avons besoin pour comprendre leur impact sur la détermination des formes primordiales. L'objectif principal est de vérifier si il était possible de détecter ces avant-plans dans les observations de ciel brut ou certains résidus de ceux-ci sur des cartes nettoyées du CMB.

Le deuxième travail concerne l'inflation à plusieurs champs, où des non-gaussianités de forme locale peuvent être produites sur des échelles super-horizon. Son objectif est triple. Le premier est la suite du travail sur le formalisme *long-wavelength* (grande longueur d'onde) [163, 162, 164, 191, 192, 189], utilisé pour calculer le paramètre non-gaussien $f_{\rm NL}$. Nous en déduisons une nouvelle formulation de l'expression de $f_{\rm NL}$ et discutons de ses conséquences pour certaines classes de potentiels. Puisque Planck a exclu la possibilité de grandes non-gaussianités locales (d'ordre 10), le lecteur pourrait se demander quel est l'intérêt de chercher des modèles à grandes non-gaussianités. Cependant, il est très important de comprendre si Planck a effectivement exclu des parties significatives de l'espace des modèles d'inflation à plusieurs champs, ou si ces modèles prédisent en général de faibles non-gaussianités. De plus, un $f_{\rm NL}$ d'ordre 1, que nous considérerons comme grand, n'a pas encore été exclu par Planck mais pourrait être observable par la prochaine génération d'expériences.

Le deuxième objectif est de comprendre si il est possible d'avoir des non-gaussianités importantes tout en restant dans les limites de l'approximation de roulement lent. Nous avons également pris en compte les contraintes de Planck sur les autres observables de l'inflation, en particulier n_s. Et il s'avère qu'il est très difficile de satisfaire les contraintes observationnelles sur n_s tout en ayant un grand $f_{\rm NL}$ et en restant dans l'approximation de roulement lent. Dans le cas d'une somme de deux potentiels monomiaux et d'une constante, nous calculons explicitement la région de l'espace de paramètres (en termes de puissance des deux potentiels) où cela est possible. Notez que nous supposons partout que le mode isocourbure a disparu à la fin de l'inflation. Sinon, il serait facile d'obtenir des non-gaussianités importantes en mettant la fin de l'inflation au milieu d'un virage de la trajectoire des champs, mais nous pensons que dans ce cas les résultats à la fin de l'inflation n'auraient aucun sens, puisqu'ils ne pourraient pas être extrapolés au moment de la recombinaison et de l'émission du CMB sans traiter correctement la fin de l'inflation et la période consécutive de (p)réchauffement.

Enfin, le troisième objectif est de comprendre l'observation numérique, à première vue très surprenante, que même dans le cas où l'approximation de roulement lent n'est plus valide pendant le virage de la trajectoire des champs, l'expression analytique issue du roulement lent pour $f_{\rm NL}$ est souvent encore une très bonne approximation du résultat final exact. Nous avons pu le comprendre en utilisant la nouvelle formulation mentionnée ci-dessus. Dans cette formulation, $f_{\rm NL}$ est donné par une équation différentielle et la solution peut être écrite comme la somme d'une solution homogène et d'une solution particulière. La solution homogène peut être donnée analytiquement sous une forme exacte (sans avoir besoin de l'approximation de roulement lent), alors que la solution particulière est négligeable exactement dans les régions où le roulement lent ne fonctionne pas et où elle ne peut pas être calculée analytiquement.

Ce manuscrit de thèse est divisée en trois parties principales. La première partie présente

les concepts cosmologiques nécessaires à cette thèse. Dans le chapitre 2, nous passons en revue le modèle standard de la cosmologie, en discutant de l'histoire thermique de notre univers dans le contexte de la théorie du Big Bang. Les motivations historiques pour une période d'inflation dans l'univers primordial sont discutées et enfin les équations de base décrivant l'inflation sont données. Dans le chapitre 3, de petites fluctuations sont ajoutées à ce fond homogène. Nous rappelons quelques concepts statistiques de base et nous les appliquons à la distribution gaussienne des anisotropies du CMB (valide au premier ordre) décomposées en harmoniques sphériques. Nous rappelons ensuite les principaux résultats de la théorie des perturbations de premier ordre appliquée à l'inflation et nous les relions aux observations du CMB.

La deuxième partie se concentre sur l'estimation des non-gaussianités bispectrales à l'aide des données observationnelles de Planck. Le chapitre 4 est une introduction au sujet. Les quantités importantes comme le bispectre y sont définies. La dérivation de la densité de probabilité faiblement non-gaussienne est discutée à l'aide de l'expansion d'Edgeworth. La méthode de l'estimateur du bispectre binné est également examinée. Dans les chapitres 5 et 6, nos résultats d'analyses des données de Planck (2015) à l'aide de l'estimateur du bispectre binné sont présentés. Dans le chapitre 5, plusieurs avant-plans galactiques sont étudiés au niveau bispectral. Les nouveaux modèles déterminés à partir de ces avant-plans sont ensuite appliqués à plusieurs cartes du CMB (simulations gaussiennes et données réelles) dans le chapitre 6.

La troisième partie de cette thèse concerne la génération de non-gaussianités dans l'inflation à deux champs. Dans le chapitre 7 nous définissons les paramètres de roulement lent et d'autres grandeurs utilisées dans le reste de la thèse. Nous rappellons aussi les principales étapes du formalisme *long-wavelength*, en particulier les expressions des différentes observables. C'est également dans ce chapitre que nous dérivons la nouvelle formulation de $f_{\rm NL}$ mentionnée précédemment. Dans le chapitre 8, nous traitons les résultats dans le cas du roulement lent qui sont mentionnés ci-dessus dans le deuxième objectif. Nous avons utilisé différents niveaux d'approximation. Tout d'abord, nous travaillons dans le cadre de l'approximation de roulement lent. Nous ajoutons ensuite l'hypothèse que le potentiel est séparable en deux sommes pour résoudre les équations de fonction de Green et obtenir des expressions simples pour les observables. Ils sont ensuite appliqués à la classe spécifique des potentiels monomiaux, où les effets des contraintes observationnelles sur l'indice spectral sur la région de l'espace de paramètres où $f_{\rm NL}$ est grand sont calculés. Dans le chapitre 9, nous conservons l'hypothèse du potentiel séparable en somme pour calculer $f_{\rm NL}$ au-delà de l'approximation de roulement lent. Deux types génériques et différents de trajectoires des champs avec un virage sont discutés. Nous montrons qu'à la fin l'expression de roulement lent de la section précédente donne également une très bonne approximation du résultat exact pour $f_{\rm NL}$ dans ce cas. Le chapitre 10 contient plusieurs exemples spécifiques pour illustrer les différents résultats de cette partie de la thèse. La méthode pour construire un potentiel monomial qui produit un grand $f_{\rm NL}$ tout en satisfaisant toutes les contraintes est détaillée, tandis que quelques exemples tirés de la littérature sont également discutés. Chaque fois, nous comparons les résultats numériques exacts dans le formalisme *long-wavelength* aux expressions analytiques approximatives dérivées de cette thèse. Enfin, nous concluons dans le chapitre 11, tandis que certains détails supplémentaires sont traités dans les annexes.

Principaux résultats

Il existe différentes méthodes pour déterminer les valeurs des paramètres d'amplitude du bispectre $f_{\rm NL}$. Ici, nous avons travaillé avec l'estimateur du bispectre binné. Cette méthode a plusieurs avantages, dont le fait qu'elle peut calculer explicitement le bispectre binné de n'importe quelle carte de données. Ensuite, en principe, il est possible d'utiliser le bispectre binné

numérique d'une carte comme modèle théorique pour lequel nous voulons déterminer un paramètre $f_{\rm NL}$ dans n'importe quelle autre carte. Cette possibilité a été mentionnée dans l'article original de l'estimateur du bispectre binné [43] et était en effet l'une des motivations pour la développer, ce qui n'avait jamais été fait. Une grande partie du travail consistait à l'implémenter explicitement dans le code (Python/C) de l'estimateur du bispectre binné. De plus, cela était la base de la partie de cette thèse consacrée à l'analyse de données, où les avant-plans galactiques ont joué le rôle de modèles numériques ensuite appliqués à des cartes du CMB. La première étape de la procédure consistait à déterminer le bispectre binné des avant-plans galactiques. Nous avons constaté que la poussière, l'émission *free-free* et l'émission anormale ont un bispectre de type *squeezed* (semblable à la forme locale, mais avec un signe opposé). Les fluctuations à petite échelle de ces avant-plans sont plus importantes dans les nuages de poussière (grande échelle), de sorte que les fluctuations à petite échelle et à grande échelle sont corrélées. Le synchrotron est différent, car son bispectre est plus proche de la forme équilatérale, mais nous n'excluons pas la possibilité d'une contamination par des sources ponctuelles non résolues. À 143 GHz (la fréquence que nous avons étudiée), seule la poussière contamine réellement le signal du CMB. Un problème avec les modèles numériques que nous avons déterminés est qu'ils dépendent aussi du masque appliqué aux avant-plans et qu'ils contiennent les caractéristiques de l'expérience comme le faisceau et le bruit. Nous avons montré que le choix du masque est très important car les avant-plans sont localisés dans le plan galactique comme la plus grande partie du masque, donc un petit changement de masque pourrait donner une grande différence de bispectre. Cela signifie qu'il faut utiliser le même masque pour déterminer le modèle que pour l'analyse finale.

Nous avons ensuite utilisé ces modèles sur différentes cartes CMB (simulations et données observationnelles). Nous avons effectué plusieurs tests pour confirmer la validité de cette nouvelle utilisation de l'estimateur du bispectre binné. Ces tests étaient basés sur des réalisations gaussiennes du CMB auxquelles nous avons ajouté des simulations de bruit et une quantité connue de poussière. Nous avons montré qu'avec un bruit isotrope et anisotrope, nous avons réussi à détecter la quantité de poussière attendue sur nos cartes. Cependant, pour faire une analyse jointe avec les formes primordiales et les formes de poussière, le choix habituel des bins n'est pas suffisant. Plus de bins sont nécessaires à faible ℓ pour mieux différencier les bispectres théoriques qui ont une configuration *squeezed* (local et poussière en particulier). Nous avons également discuté des effets de la (petite) brisure de l'approximation de faible non-gaussianités qui se produit lorsque nous avons ajouté la carte complète de la poussière aux simulations du CMB (donc la quantité de poussière attendue dans les observations du ciel brut). La principale conséquence est que les barres d'erreur réelles deviennent plusieurs fois plus grandes que les prévisions de Fisher. Nous avons ensuite utilisé les modèles numériques sur la carte CMB SMICA nettoyée de Planck (2015). Comme prévu, nous n'avons détecté aucun résidu de poussière (les intensités des autres avant-plans à 143 GHz étant trop faibles pour qu'ils soient détectés, même si ils étaient présents sur la carte). Les barres d'erreur pour la poussière et la forme locale augmentent beaucoup dans une analyse jointe avec le binning habituel, encore une fois à cause du choix des bins qui n'est pas adapté pour les différencier. Enfin, nous avons appliqué les modèles de avant-plans à la carte du ciel brut à 143 GHz et l'estimateur du bispectre binné a réussi à détecter la poussière qu'elle contient.

Dans cette thèse, nous avons également discuté du niveau de non-gaussianités produit dans l'inflation à deux champs avec un potentiel séparable en somme $W(\phi, \sigma) = U(\phi) + V(\sigma)$ et des termes cinétiques standards. Nous avons examiné à la fois le cas où l'approximation de roulement lent (forte) est valable tout au long de l'inflation (ce qui signifie que tous les paramètres de roulement lent, même les paramètres perpendiculaires, sont petits), et le cas où le roulement lent est cassé pendant le virage de la trajectoire des champs. À titre de comparaison, nous avons également examiné le cas d'un potentiel séparable en produit, mais comme montré

précédemment, il n'est pas possible d'obtenir des non-gaussianités importantes dans ce cas dans l'approximation de roulement lent avec un mode isocourbure qui disparaît à la fin de l'inflation.

Nous utilisons le formalisme *long-wavelength* pour nos calculs des non-gaussianités. Dans ce formalisme [191] et dans le cadre de l'hypothèse mentionnée ci-dessus, toute large (ce qui signifie d'ordre un ou plus) contribution à $f_{\rm NL}$ ne peut provenir que d'une expression intégrale appelée $g_{\rm int}$. La formulation originale de cette expression contient une intégrale sur des fonctions de Green dépendant de deux temps différents, ce qui rend difficile d'interpréter l'équation et de voir quels types de potentiels peuvent conduire à des non-gaussianités importantes. Dans cette thèse, nous avons trouvé une autre expression pour $g_{\rm int}$, c'est la solution (7.49) d'une équation différentielle (7.47), qui peut être écrite comme la somme d'une solution homogène et d'une solution particulière. Cette formulation est très utile, puisque nous avons une expression analytique exacte de la solution homogène qui ne nécessite pas d'approximation. Pour la solution particulière, nous avons vu (dans le contexte de la classe de modèles étudiés) que nous pouvons soit la calculer explicitement, soit montrer qu'elle est négligeable. Nous avons également dérivé quelques relations de proportionnalité entre les différentes fonctions de Green qui sont utiles dans les calculs.

Nous avons mis en évidence les tensions entre un grand $f_{\rm NL}$ d'ordre un ou plus et les contraintes observationnelles actuelles sur l'indice spectral n_s, les deux étant liés à la dérivée de deuxième ordre du potentiel $V_{\sigma\sigma}$, où σ est le champ sous-dominant du franchissement de l'horizon au virage de la trajectoire des champs. Nous avons évalué ces tensions dans le cadre de l'approximation de roulement lent pour les potentiels monomiaux, où il serait autrement facile, avec quelques ajustements, d'atteindre les exigences pour un grand $f_{\rm NL}$. Nous avons montré qu'une grande partie de l'espace des paramètres donnant $f_{\rm NL}$ d'ordre un est simplement interdit à cause des contraintes sur n_s. Nous avons constaté que ces contraintes sont très sensibles à la valeur de n_s : si la limite inférieure était plus petite de 0,02 ($n_s \approx 0,94$), la situation serait très différente et la plupart des paramètres seraient autorisés. Cette analyse du potentiel monomial a également révélé que la durée de l'inflation après le franchissement de l'horizon est importante : une valeur autour de cinquante e-folds est beaucoup plus contraignante que les soixante e-folds habituels. Cela indique également que dans les rares modèles qui fonctionnent, le virage de la trajectoire des champs se produit vers la fin de l'inflation. Cela soulève plusieurs questions, la principale étant qu'à ce moment-là, les paramètres de roulement lent s'arrêtent généralement d'être petits par rapport à un et donc que l'approximation de roulement lent ne fonctionne plus. De plus, si le virage se produit trop près de la fin de l'inflation, le mode isocourbure peut ne pas avoir le temps de disparaître. En étudiant les virages où le paramètre de roulement lent ϵ est encore petit par rapport à un, nous évitons ce dernier problème : le temps que ϵ met à devenir un et donc terminer l'inflation peut être assez long pour que le mode isocourbure disparaisse.

La suite naturelle de cette étude était de considérer ce qui se passerait en abandonnant l'approximation de roulement lent pendant le virage et en permettant aux paramètres de roulement lent $\eta^{\parallel}$ et $\eta^{\perp}$ (décrivant l'accélération des champs) de devenir grands. D'autre part, nous supposons toujours que ϵ reste petit pendant le virage, pour plusieurs raisons : à cause du problème concernant la disparition du mode isocourbure mentionné ci-dessus, parce que nous avons vu numériquement dans plusieurs modèles que c'était une bonne approximation, ebt parce que cette approximation nous a permis d'obtenir des résultats analytiques très intéressants. Nous avons identifié deux types différents de modèles où un tel virage peut se produire, comme le montre la figure 91. En substituant l'expression de roulement lent à $\dot{g}_{\rm int}$ dans (7.47), nous avons pu montrer (en utilisant des comparaisons simples des différents termes de l'équation différentielle) que c'est aussi une très bonne approximation même si les paramètres de roulement lent $\eta^{\parallel}$ et $\eta^{\perp}$ deviennent grands pendant le virage. L'idée principale est celle mentionnée ci-dessus : tant que l'approximation au ralenti est valide, nous pouvons calculer explicitement

la solution particulière, tandis que lorsqu'elle est cassée, nous pouvons montrer que la solution particulière devient négligeable, même si nous ne pouvons pas calculer une expression analytique pour elle dans ce cas (le fait que ϵ reste petit est un ingrédient crucial dans cette preuve). Pour la solution homogène, nous avons une expression analytique valable partout. Nous avons également pu montrer que l'ajout de la solution particulière à roulement lent à la solution homogène dans les régions où la solution particulière exacte est négligeable n'introduit pas d'erreur significative, ce qui signifie que nous n'avons pas à effectuer un appariement explicite des solutions à chaque transition entre une région à roulement lent et une région à roulement non lent.

Ceci nous a conduit à la conclusion que, dans le contexte des modèles étudiés et des hypothèses mentionnées ci-dessus, l'expression à faible roulement lent pour $f_{\rm NL}$ est une très bonne approximation pour la valeur exacte, même dans les modèles où $\eta^{\parallel}$ et $\eta^{\perp}$ deviennent grands pendant le virage de la trajectoire des champs et cassent le roulement lent. Par conséquent, les implications de cette expression pour avoir des non-gaussianités larges, discutées dans le contexte de l'approximation de roulement lent, s'appliquent dans un cadre beaucoup plus général. En particulier, les contraintes dues à l'indice spectral n_s restent très importantes. Un potentiel somme de deux champs avec un grand $f_{\rm NL}$ nécessite beaucoup de *fine-tuning* (et nous avons montré explicitement dans la section avec des exemples numériques comment construire un tel modèle). Réduire les barres d'erreur sur les mesures de l'indice spectral pourrait même être plus efficace pour contraindre les non-gaussianités dans certaines régions de l'espace des paramètres des potentiels que de réduire les barres d'erreur sur $f_{\rm NL}$ lui-même.

Ce travail qui a répondu a des questions importantes et ambitieuses sur différents aspects des non-gaussianités, en apporte également de nouvelles qui mériteraient d'être étudiées lors de futurs projets. Concernant l'inflation, il serait très important de regarder d'autres classes de modèles que ceux séparables en somme pour comprendre l'influence d'un terme d'interaction entre les deux champs sur les conditions de large non-gaussianités. Une continuation directe de la partie consacrée à l'analyse des observations du CMB serait d'étudier les nouvelles données de polarisation de Planck, avec une meilleure compréhension des erreurs systématiques, qui devraient être disponibles dans les mois qui viennent (alors qu'ici seule la température était considérée). D'un point de vue beaucoup plus général, l'ère de la cosmologie de précision entamée il y a une quinzaine d'années n'en est encore qu'à ses débuts. Une nouvelle génération d'expériences va observer le CMB (CMB-S4, LiteBIRD, CORE, etc.), mais d'autres sources d'informations sur l'univers primordial sont maintenant envisageables comme l'étude de la structure à grande échelle de l'univers (Euclid). Nous pouvons donc nous attendre à une meilleure compréhension de l'évolution de notre univers dans les années qui viennent, et en particulier de l'univers primordial et de l'inflation. Cette connaissance croissante des perturbations primodiales et de leurs non-gaussianités entraînera également de nombreux défis théoriques.

Bibliography

[1] CMB-S4 collaboration, K. N. Abazajian et al., *CMB-S4 Science Book, First Edition*, 1610.02743.

[2] Planck collaboration, A. Abergel et al., *Planck intermediate results*, *Astron. Astrophys.* **5**66 (2014) A55, [1312.5446].

[3] A. Achucarro, V. Atal, B. Hu, P. Ortiz and J. Torrado, *Inflation with moderately sharp features in the speed of sound: Generalized slow roll and in-in formalism for power spectrum and bispectrum*, *Phys. Rev.* **D**90 (2014) 023511, [1404.7522].

[4] A. Achucarro, J.-O. Gong, S. Hardeman, G. A. Palma and S. P. Patil, *Features of heavy physics in the CMB power spectrum*, *JCAP* **1**101 (2011) 030, [1010.3693].

[5] A. Achucarro, J.-O. Gong, G. A. Palma and S. P. Patil, *Correlating features in the primordial spectra*, *Phys. Rev.* **D**87 (2013) 121301, [1211.5619].

[6] V. Acquaviva, N. Bartolo, S. Matarrese and A. Riotto, *Second order cosmological perturbations from inflation*, *Nucl. Phys.* **B**667 (2003) 119–148, [astro-ph/0209156].

[7] Planck collaboration, R. Adam et al., *Planck 2015 results. I. Overview of products and scientific results*, *Astron. Astrophys.* **5**94 (2016) A1, [1502.01582].

[8] Planck collaboration, R. Adam et al., *Planck 2015 results. IX. Diffuse component separation: CMB maps*, *Astron. Astrophys.* **5**94 (2016) A9, [1502.05956].

[9] Planck collaboration, R. Adam et al., *Planck 2015 results. X. Diffuse component separation: Foreground maps*, *Astron. Astrophys.* **5**94 (2016) A10, [1502.01588].

[10] Planck collaboration, P. A. R. Ade et al., *Planck 2013 results. XII. Diffuse component separation*, *Astron. Astrophys.* **5**71 (2014) A12, [1303.5072].

[11] Planck collaboration, P. A. R. Ade et al., *Planck 2013 Results. XXIV. Constraints on primordial non-Gaussianity*, *Astron. Astrophys.* **5**71 (2014) A24, [1303.5084].

[12] BICEP2, Keck Array collaboration, P. A. R. Ade et al., *Improved Constraints on Cosmology and Foregrounds from BICEP2 and Keck Array Cosmic Microwave Background Data with Inclusion of 95 GHz Band*, *Phys. Rev. Lett.* **1**16 (2016) 031302, [1510.09217].

[13] Planck collaboration, P. A. R. Ade et al., *Planck 2015 results. XIII. Cosmological parameters*, *Astron. Astrophys.* **5**94 (2016) A13, [1502.01589].

[14] Planck collaboration, P. A. R. Ade et al., *Planck 2015 results. XVII. Constraints on primordial non-Gaussianity*, *Astron. Astrophys.* **5**94 (2016) A17, [1502.01592].

[15] Planck collaboration, P. A. R. Ade et al., *Planck 2015 results. XX. Constraints on inflation*, *Astron. Astrophys.* **5**94 (2016) A20, [1502.02114].

[16] Planck collaboration, P. A. R. Ade et al., *Planck 2015 results. XXV. Diffuse low-frequency Galactic foregrounds*, *Astron. Astrophys.* **5**94 (2016) A25, [1506.06660].

[17] Planck collaboration, N. Aghanim et al., *Planck 2015 results. XI. CMB power spectra, likelihoods, and robustness of parameters*, *Astron. Astrophys.* **5**94 (2016) A11, [1507.02704].

[18] Planck collaboration, Y. Akrami et al., *Planck intermediate results. LIV. Polarized dust foregrounds*, 1801.04945.

[19] A. Albrecht and P. J. Steinhardt, *Cosmology for Grand Unified Theories with Radiatively Induced Symmetry Breaking*, *Phys. Rev. Lett.* **4**8 (1982) 1220–1223.

[20] M. Alishahiha, E. Silverstein and D. Tong, *DBI in the sky*, *Phys. Rev.* **D**70 (2004) 123505, [hep-th/0404084].

[21] R. A. Alpher and R. Herman, *Evolution of the universe*, *Nature* **1**62 (1948) 774.

[22] H. W. Babcock, *The rotation of the Andromeda Nebula*, *Lick Observatory Bulletin* **1**9 (1939) 41–51.

[23] D. Babich, *Optimal estimation of non-Gaussianity*, *Phys. Rev.* **D**72 (2005) 043003, [astro-ph/0503375].

[24] D. Babich, P. Creminelli and M. Zaldarriaga, *The Shape of non-Gaussianities*, *JCAP* **0**408 (2004) 009, [astro-ph/0405356].

[25] J. M. Bardeen, *Gauge Invariant Cosmological Perturbations*, *Phys. Rev.* **D**22 (1980) 1882–1905.

[26] J. M. Bardeen, J. Bond, N. Kaiser and A. Szalay, *The statistics of peaks of gaussian random fields*, *The Astrophysical Journal* **3**04 (1986) 15–61.

[27] J. M. Bardeen, P. J. Steinhardt and M. S. Turner, *Spontaneous Creation of Almost Scale - Free Density Perturbations in an Inflationary Universe*, *Phys. Rev.* **D**28 (1983) 679.

[28] N. Barnaby and J. M. Cline, *Nongaussianity from Tachyonic Preheating in Hybrid Inflation*, *Phys. Rev.* **D**75 (2007) 086004, [astro-ph/0611750].

[29] N. Bartolo, E. Komatsu, S. Matarrese and A. Riotto, *Non-Gaussianity from inflation: Theory and observations*, *Phys. Rept.* **4**02 (2004) 103–266, [astro-ph/0406398].

[30] N. Bartolo, S. Matarrese and A. Riotto, *On non-Gaussianity in the curvaton scenario*, *Phys. Rev.* **D**69 (2004) 043503, [hep-ph/0309033].

[31] T. Battefeld and R. Easther, *Non-Gaussianities in Multi-field Inflation*, *JCAP* **0**703 (2007) 020, [astro-ph/0610296].

[32] D. Baumann, *Inflation*, in *Physics of the large and the small, TASI 09, proceedings of the Theoretical Advanced Study Institute in Elementary Particle Physics, Boulder, Colorado, USA, 1-26 June 2009*, pp. 523–686, 2011. 0907.5424. DOI.

[33] J. Baur, *Determining the mass of cosmological neutrinos using Lyman-alpha forests*. Theses, Université Paris-Saclay, Sept., 2017.

[34] WMAP collaboration, C. L. Bennett et al., *Nine-Year Wilkinson Microwave Anisotropy Probe (WMAP) Observations: Final Maps and Results*, *Astrophys. J. Suppl.* **2**08 (2013) 20, [1212.5225].

[35] C. Bennett, D. Larson, J. Weiland, N. Jarosik, G. Hinshaw, N. Odegard et al., *Nine-year wilkinson microwave anisotropy probe (wmap) observations: final maps and results*, *The Astrophysical Journal Supplement Series* **2**08 (2013) 20.

[36] F. Bernardeau and L. Kofman, *Properties of the cosmological density distribution function*, *Astrophys. J.* **4**43 (1995) 479–498, [astro-ph/9403028].

[37] F. Bernardeau, L. Kofman and J.-P. Uzan, *Modulated fluctuations from hybrid inflation*, *Phys. Rev.* **D**70 (2004) 083004, [astro-ph/0403315].

[38] D. Blas, J. Lesgourgues and T. Tram, *The Cosmic Linear Anisotropy Solving System (CLASS) II: Approximation schemes*, *JCAP* **1**107 (2011) 034, [1104.2933].

[39] J. R. Bond and A. S. Szalay, *The Collisionless Damping of Density Fluctuations in an Expanding Universe*, *Astrophys. J.* **2**74 (1983) 443–468.

[40] F. R. Bouchet et al., *COrE: Cosmic Origins Explorer - A White Paper*, .

[41] M. Bucher, *Physics of the cosmic microwave background anisotropy*, *Int. J. Mod. Phys.* **D**24 (2015) 1530004, [1501.04288].

[42] M. Bucher, B. Racine and B. van Tent, *The binned bispectrum estimator: template-based and non-parametric CMB non-Gaussianity searches*, *JCAP* **1**605 (2016) 055, [1509.08107].

[43] M. Bucher, B. Van Tent and C. S. Carvalho, *Detecting Bispectral Acoustic Oscillations from Inflation Using a New Flexible Estimator*, *Mon. Not. Roy. Astron. Soc.* **4**07 (2010) 2193, [0911.1642].

[44] C. T. Byrnes, *Lecture notes on non-Gaussianity*, *Astrophys. Space Sci. Proc.* **4**5 (2016) 135–165, [1411.7002].

[45] C. T. Byrnes, K.-Y. Choi and L. M. H. Hall, *Conditions for large non-Gaussianity in two-field slow-roll inflation*, *JCAP* **0**810 (2008) 008, [0807.1101].

[46] C. T. Byrnes, M. Cortês and A. R. Liddle, *Comprehensive analysis of the simplest curvaton model*, *Phys. Rev.* **D**90 (2014) 023523, [1403.4591].

[47] C. T. Byrnes, M. Gerstenlauer, S. Nurmi, G. Tasinato and D. Wands, *Scale-dependent non-Gaussianity probes inflationary physics*, *JCAP* **1**010 (2010) 004, [1007.4277].

[48] C. T. Byrnes and J.-O. Gong, *General formula for the running of fNL*, *Phys. Lett.* **B**718 (2013) 718–721, [1210.1851].

[49] C. T. Byrnes, D. Regan, D. Seery and E. R. M. Tarrant, *The hemispherical asymmetry from a scale-dependent inflationary bispectrum*, *JCAP* **1**606 (2016) 025, [1511.03129].

[50] C. T. Byrnes and G. Tasinato, *Non-Gaussianity beyond slow roll in multi-field inflation*, *JCAP* **0**908 (2009) 016, [0906.0767].

[51] J.-F. Cardoso, M. Martin, J. Delabrouille, M. Betoule and G. Patanchon, *Component separation with flexible models. Application to the separation of astrophysical emissions*, 0803.1814.

[52] X. Chen, *Primordial Non-Gaussianities from Inflation Models*, *Adv. Astron.* **2**010 (2010) 638979, [1002.1416].

[53] X. Chen, R. Easther and E. A. Lim, *Generation and Characterization of Large Non-Gaussianities in Single Field Inflation*, *JCAP* **0**804 (2008) 010, [0801.3295].

[54] J. Chluba, J. Hamann and S. P. Patil, *Features and New Physical Scales in Primordial Observables: Theory and Observation*, *Int. J. Mod. Phys.* **D**24 (2015) 1530023, [1505.01834].

[55] K.-Y. Choi, L. M. H. Hall and C. van de Bruck, *Spectral Running and Non-Gaussianity from Slow-Roll Inflation in Generalised Two-Field Models*, *JCAP* **0**702 (2007) 029, [astro-ph/0701247].

[56] T. Clifton, P. G. Ferreira, A. Padilla and C. Skordis, *Modified Gravity and Cosmology*, *Phys. Rept.* **5**13 (2012) 1–189, [1106.2476].

[57] S. R. Coleman and E. J. Weinberg, *Radiative Corrections as the Origin of Spontaneous Symmetry Breaking*, *Phys. Rev.* **D**7 (1973) 1888–1910.

[58] E. J. Copeland, E. W. Kolb, A. R. Liddle and J. E. Lidsey, *Reconstructing the inflation potential, in principle and in practice*, *Phys. Rev.* **D**48 (1993) 2529–2547, [hep-ph/9303288].

[59] P. Creminelli, A. Nicolis, L. Senatore, M. Tegmark and M. Zaldarriaga, *Limits on non-gaussianities from wmap data*, *JCAP* **0**605 (2006) 004, [astro-ph/0509029].

[60] A. Curto, M. Tucci, M. Kunz and E. Martinez-Gonzalez, *The CIB-lensing bispectrum: impact on primordial non-Gaussianity and detectability for the Planck mission*, *Mon. Not. Roy. Astron. Soc.* **4**50 (2015) 3778–3801, [1405.7029].

[61] M. Dias, J. Frazer, D. J. Mulryne and D. Seery, *Numerical evaluation of the bispectrum in multiple field inflation — the transport approach with code*, *JCAP* **1**612 (2016) 033, [1609.00379].

[62] R. H. Dicke, P. J. E. Peebles, P. G. Roll and D. T. Wilkinson, *Cosmic Black-Body Radiation*, *Astrophys. J.* **1**42 (1965) 414–419.

[63] C. Dickinson, R. D. Davies and R. J. Davis, *Towards a free-free template for CMB foregrounds*, *Mon. Not. Roy. Astron. Soc.* **3**41 (2003) 369, [astro-ph/0302024].

[64] S. Dodelson, *Modern Cosmology*. Academic Press, Amsterdam, 2003.

[65] S. Donzelli, F. K. Hansen, M. Liguori, D. Marinucci and S. Matarrese, *On the linear term correction for needlets/wavelets non-Gaussianity estimators*, *Astrophys. J.* **7**55 (2012) 19, [1202.1478].

[66] B. T. Draine and A. Lazarian, *Electric dipole radiation from spinning dust grains*, *Astrophys. J.* **5**08 (1998) 157–179, [astro-ph/9802239].

[67] B. T. Draine, *Physics of the interstellar and intergalactic medium*. Princeton University Press, 2010.

[68] A. Einstein, *Die feldgleichungen der gravitation*. Wiley Online Library, 1913.

[69] A. Einstein, *Die grundlage der allgemeinen relativitätstheorie*, *Annalen der Physik* **3**54 (1916) 769–822.

[70] J. Elliston, L. Alabidi, I. Huston, D. Mulryne and R. Tavakol, *Large trispectrum in two-field slow-roll inflation*, *JCAP* **1**209 (2012) 001, [1203.6844].

[71] J. Elliston, D. Mulryne, D. Seery and R. Tavakol, *Evolution of non-Gaussianity in multi-scalar field models*, *Int. J. Mod. Phys.* **A**26 (2011) 3821–3832, [1107.2270].

[72] J. Elliston, D. J. Mulryne, D. Seery and R. Tavakol, *Evolution of fNL to the adiabatic limit*, *JCAP* **1**111 (2011) 005, [1106.2153].

[73] J. Elliston, S. Orani and D. J. Mulryne, *General analytic predictions of two-field inflation and perturbative reheating*, *Phys. Rev.* **D**89 (2014) 103532, [1402.4800].

[74] F. Elsner and B. D. Wandelt, *Efficient Wiener filtering without preconditioning*, *Astron. Astrophys.* **5**49 (2013) A111, [1210.4931].

[75] K. Enqvist, A. Jokinen, A. Mazumdar, T. Multamaki and A. Vaihkonen, *Non-Gaussianity from preheating*, *Phys. Rev. Lett.* **9**4 (2005) 161301, [astro-ph/0411394].

[76] K. Enqvist and T. Takahashi, *Mixed Inflaton and Spectator Field Models after Planck*, *JCAP* **1**310 (2013) 034, [1306.5958].

[77] H. K. Eriksen, J. B. Jewell, C. Dickinson, A. J. Banday, K. M. Gorski and C. R. Lawrence, *Joint Bayesian component separation and CMB power spectrum estimation*, *Astrophys. J.* **6**76 (2008) 10–32, [0709.1058].

[78] H. K. Eriksen, I. J. O'Dwyer, J. B. Jewell, B. D. Wandelt, D. L. Larson, K. M. Gorski et al., *Power spectrum estimation from high-resolution maps by Gibbs sampling*, *Astrophys. J. Suppl.* **1**55 (2004) 227–241, [astro-ph/0407028].

[79] J. R. Fergusson, *Efficient optimal non-Gaussian CMB estimators with polarisation*, *Phys. Rev.* **D**90 (2014) 043533, [1403.7949].

[80] J. R. Fergusson, M. Liguori and E. P. S. Shellard, *General CMB and Primordial Bispectrum Estimation I: Mode Expansion, Map-Making and Measures of fNL*, *Phys. Rev.* **D**82 (2010) 023502, [0912.5516].

[81] J. R. Fergusson, M. Liguori and E. P. S. Shellard, *The CMB Bispectrum*, *JCAP* **1**212 (2012) 032, [1006.1642].

[82] J. R. Fergusson and E. P. S. Shellard, *The shape of primordial non-Gaussianity and the CMB bispectrum*, *Phys. Rev.* **D**80 (2009) 043510, [0812.3413].

[83] CORE collaboration, F. Finelli et al., *Exploring Cosmic Origins with CORE: Inflation*, 1612.08270.

[84] R. Flauger, M. Mirbabayi, L. Senatore and E. Silverstein, *Productive Interactions: heavy particles and non-Gaussianity*, 1606.00513.

[85] P. J. Fox, G. Jung, P. Sorensen and N. Weiner, *Dark Matter in Light of the LUX Results*, *Phys. Rev.* **D**89 (2014) 103526, [1401.0216].

[86] K. Freese, J. A. Frieman and A. V. Olinto, *Natural inflation with pseudo - Nambu-Goldstone bosons*, *Phys. Rev. Lett.* **65** (1990) 3233–3236.

[87] A. Friedman, *Über die krümmung des raumes*, *Zeitschrift für Physik* **10** (1922) 377–386.

[88] A. Friedmann, *Über die möglichkeit einer welt mit konstanter negativer krümmung des raumes*, *Zeitschrift für Physik* **21** (1924) 326–332.

[89] G. Gamow, *Expanding universe and the origin of elements*, *Phys. Rev.* **70** (1946) 572–573.

[90] D. M. Goldberg and D. N. Spergel, *Microwave background bispectrum. 2. A probe of the low redshift universe*, *Phys. Rev.* **D59** (1999) 103002, [astro-ph/9811251].

[91] C. Gordon, D. Wands, B. A. Bassett and R. Maartens, *Adiabatic and entropy perturbations from inflation*, *Phys. Rev.* **D63** (2001) 023506, [astro-ph/0009131].

[92] K. M. Gorski, E. Hivon, A. J. Banday, B. D. Wandelt, F. K. Hansen, M. Reinecke et al., *HEALPix - A Framework for high resolution discretization, and fast analysis of data distributed on the sphere*, *Astrophys. J.* **622** (2005) 759–771, [astro-ph/0409513].

[93] S. Groot Nibbelink and B. J. W. van Tent, *Density perturbations arising from multiple field slow roll inflation*, hep-ph/0011325.

[94] S. Groot Nibbelink and B. J. W. van Tent, *Scalar perturbations during multiple field slow-roll inflation*, *Class. Quant. Grav.* **19** (2002) 613–640, [hep-ph/0107272].

[95] H. F. Gruetjen, J. R. Fergusson, M. Liguori and E. P. S. Shellard, *Using inpainting to construct accurate cut-sky CMB estimators*, *Phys. Rev.* **D95** (2017) 043532, [1510.03103].

[96] A. H. Guth, *The Inflationary Universe: A Possible Solution to the Horizon and Flatness Problems*, *Phys. Rev.* **D23** (1981) 347–356.

[97] A. H. Guth and S. Y. Pi, *Fluctuations in the New Inflationary Universe*, *Phys. Rev. Lett.* **49** (1982) 1110–1113.

[98] R. J. Hardwick, V. Vennin, K. Koyama and D. Wands, *Constraining Curvatonic Reheating*, *JCAP* **1608** (2016) 042, [1606.01223].

[99] C. Haslam, C. Salter, H. Stoffel and W. Wilson, *A 408 mhz all-sky continuum survey. ii-the atlas of contour maps*, *Astronomy and Astrophysics Supplement Series* **47** (1982) 1.

[100] S. W. Hawking, *The Development of Irregularities in a Single Bubble Inflationary Universe*, *Phys. Lett.* **115B** (1982) 295.

[101] S. Hotchkiss and S. Sarkar, *Non-Gaussianity from violation of slow-roll in multiple inflation*, *JCAP* **1005** (2010) 024, [0910.3373].

[102] C. Howlett, A. Lewis, A. Hall and A. Challinor, *CMB power spectrum parameter degeneracies in the era of precision cosmology*, *JCAP* **1204** (2012) 027, [1201.3654].

[103] W. Hu and S. Dodelson, *Cosmic microwave background anisotropies*, *Ann. Rev. Astron. Astrophys.* **40** (2002) 171–216, [astro-ph/0110414].

[104] W. Hu and N. Sugiyama, *Toward understanding CMB anisotropies and their implications*, *Phys. Rev.* **D**51 (1995) 2599–2630, [astro-ph/9411008].

[105] E. Hubble, *A relation between distance and radial velocity among extra-galactic nebulae*, *Proceedings of the National Academy of Sciences* **1**5 (1929) 168–173.

[106] A. Jokinen and A. Mazumdar, *Very large primordial non-gaussianity from multi-field: application to massless preheating*, *JCAP* **0**604 (2006) 003, [astro-ph/0512368].

[107] G. Jung, B. Racine and B. van Tent, *The bispectra of galactic CMB foregrounds and their impact on primordial non-Gaussianity estimation*, 1810.01727.

[108] G. Jung and B. van Tent, *Non-Gaussianity in two-field inflation beyond the slow-roll approximation*, *JCAP* **1**705 (2017) 019, [1611.09233].

[109] R. Juszkiewicz, D. H. Weinberg, P. Amsterdamski, M. Chodorowski and F. Bouchet, *Weakly nonlinear Gaussian fluctuations and the Edgeworth expansion*, *Astrophys. J.* **4**42 (1995) 39, [astro-ph/9308012].

[110] M. Kamionkowski, A. Kosowsky and A. Stebbins, *A Probe of primordial gravity waves and vorticity*, *Phys. Rev. Lett.* **7**8 (1997) 2058–2061, [astro-ph/9609132].

[111] Z. Kenton and D. J. Mulryne, *The squeezed limit of the bispectrum in multi-field inflation*, *JCAP* **1**510 (2015) 018, [1507.08629].

[112] Z. Kenton and D. J. Mulryne, *The Separate Universe Approach to Soft Limits*, *JCAP* **1**610 (2016) 035, [1605.03435].

[113] T. Kobayashi, F. Takahashi, T. Takahashi and M. Yamaguchi, *Spectator field models in light of spectral index after Planck*, *JCAP* **1**310 (2013) 042, [1303.6255].

[114] L. Kofman, A. D. Linde and A. A. Starobinsky, *Reheating after inflation*, *Phys. Rev. Lett.* **7**3 (1994) 3195–3198, [hep-th/9405187].

[115] E. Komatsu and D. N. Spergel, *Acoustic signatures in the primary microwave background bispectrum*, *Phys. Rev.* **D**63 (2001) 063002, [astro-ph/0005036].

[116] E. Komatsu, D. N. Spergel and B. D. Wandelt, *Measuring primordial non-Gaussianity in the cosmic microwave background*, *Astrophys. J.* **6**34 (2005) 14–19, [astro-ph/0305189].

[117] E. Komatsu, B. D. Wandelt, D. N. Spergel, A. J. Banday and K. M. Gorski, *Measurement of the cosmic microwave background bispectrum on the COBE DMR sky maps*, *Astrophys. J.* **5**66 (2002) 19–29, [astro-ph/0107605].

[118] F. Lacasa, A. Pénin and N. Aghanim, *Non-Gaussianity of the cosmic infrared background anisotropies – I. Diagrammatic formalism and application to the angular bispectrum*, *Mon. Not. Roy. Astron. Soc.* **4**39 (2014) 123–142, [1312.1251].

[119] D. Langlois and F. Vernizzi, *Conserved non-linear quantities in cosmology*, *Phys. Rev.* **D**72 (2005) 103501, [astro-ph/0509078].

[120] EUCLID collaboration, R. Laureijs et al., *Euclid Definition Study Report*, 1110.3193.

[121] E. M. Leitch, A. C. S. Readhead, T. J. Pearson and S. T. Myers, *An Anomalous component of galactic emission*, *Astrophys. J.* **4**86 (1997) L23, [astro-ph/9705241].

[122] G. Lemaître, *Un Univers homogène de masse constante et de rayon croissant rendant compte de la vitesse radiale des nébuleuses extra-galactiques*, *Annales de la Société Scientifique de Bruxelles* **47** (1927) 49–59.

[123] J. Lesgourgues, *Inflationary cosmology*, .

[124] J. Lesgourgues, *The Cosmic Linear Anisotropy Solving System (CLASS) I: Overview*, 1104.2932.

[125] J. Lesgourgues and S. Pastor, *Massive neutrinos and cosmology*, *Phys. Rept.* **429** (2006) 307–379, [astro-ph/0603494].

[126] A. Lewis, A. Challinor and D. Hanson, *The shape of the CMB lensing bispectrum*, *JCAP* **1103** (2011) 018, [1101.2234].

[127] A. Lewis, A. Challinor and A. Lasenby, *Efficient computation of CMB anisotropies in closed FRW models*, *Astrophys. J.* **538** (2000) 473–476, [astro-ph/9911177].

[128] A. Liddle, *An introduction to modern cosmology*. John Wiley & Sons, 2015.

[129] A. R. Liddle and D. H. Lyth, *Cosmological inflation and large scale structure*. Cambridge University Press, 2000.

[130] A. R. Liddle and D. H. Lyth, *The Cold dark matter density perturbation*, *Phys. Rept.* **231** (1993) 1–105, [astro-ph/9303019].

[131] A. D. Linde, *A New Inflationary Universe Scenario: A Possible Solution of the Horizon, Flatness, Homogeneity, Isotropy and Primordial Monopole Problems*, *Phys. Lett.* **108B** (1982) 389–393.

[132] A. D. Linde, *Chaotic Inflation*, *Phys. Lett.* **129B** (1983) 177–181.

[133] A. D. Linde, *Hybrid inflation*, *Phys. Rev.* **D49** (1994) 748–754, [astro-ph/9307002].

[134] F. Lucchin and S. Matarrese, *Power Law Inflation*, *Phys. Rev.* **D32** (1985) 1316.

[135] X.-c. Luo, *The Angular bispectrum of the cosmic microwave background*, *Astrophys. J.* **427** (1994) L71, [astro-ph/9312004].

[136] X.-c. Luo and D. N. Schramm, *Kurtosis, skewness, and nonGaussian cosmological density perturbations*, *Astrophys. J.* **408** (1993) 33–42.

[137] R. Lupton, *Statistics in theory and practice*. Princeton University Press, Princeton, N.J, 1993.

[138] D. H. Lyth, *Generating the curvature perturbation at the end of inflation*, *JCAP* **0511** (2005) 006, [astro-ph/0510443].

[139] D. H. Lyth and Y. Rodriguez, *The Inflationary prediction for primordial non-Gaussianity*, *Phys. Rev. Lett.* **95** (2005) 121302, [astro-ph/0504045].

[140] D. H. Lyth and D. Wands, *Generating the curvature perturbation without an inflaton*, *Phys. Lett.* **B524** (2002) 5–14, [hep-ph/0110002].

[141] J. M. Maldacena, *Non-Gaussian features of primordial fluctuations in single field inflationary models*, *JHEP* **05** (2003) 013, [astro-ph/0210603].

[142] K. A. Malik and D. Wands, *Evolution of second-order cosmological perturbations*, *Class. Quant. Grav.* **21** (2004) L65–L72, [astro-ph/0307055].

[143] J. Martin and D. J. Schwarz, *The Precision of slow roll predictions for the CMBR anisotropies*, *Phys. Rev.* **D62** (2000) 103520, [astro-ph/9911225].

[144] J. C. Mather et al., *Measurement of the Cosmic Microwave Background spectrum by the COBE FIRAS instrument*, *Astrophys. J.* **420** (1994) 439–444.

[145] T. Matsumura et al., *Mission design of LiteBIRD*, 1311.2847.

[146] M. A. Miville-Deschenes, G. Lagache, F. Boulanger and J. L. Puget, *Statistical properties of dust far-infrared emission*, *Astron. Astrophys.* **469** (2007) 595, [0704.2175].

[147] S. Mizuno, F. Arroja, K. Koyama and T. Tanaka, *Lorentz boost and non-Gaussianity in multi-field DBI-inflation*, *Phys. Rev.* **D80** (2009) 023530, [0905.4557].

[148] S. Mizuno and K. Koyama, *Primordial non-Gaussianity from the DBI Galileons*, *Phys. Rev.* **D82** (2010) 103518, [1009.0677].

[149] V. Mukhanov, *Physical Foundations of Cosmology*. Cambridge University Press, Oxford, 2005.

[150] V. Mukhanov, *Vf mukhanov, sov. phys. jetp 67, 1297 (1988).*, *Sov. Phys. JETP* **67** (1988) 1297.

[151] V. F. Mukhanov, H. A. Feldman and R. H. Brandenberger, *Theory of cosmological perturbations. Part 1. Classical perturbations. Part 2. Quantum theory of perturbations. Part 3. Extensions*, *Phys. Rept.* **215** (1992) 203–333.

[152] D. Munshi and A. Heavens, *A New Approach to Probing Primordial Non-Gaussianity*, *Mon. Not. Roy. Astron. Soc.* **401** (2010) 2406, [0904.4478].

[153] E. Pajer, F. Schmidt and M. Zaldarriaga, *The Observed Squeezed Limit of Cosmological Three-Point Functions*, *Phys. Rev.* **D88** (2013) 083502, [1305.0824].

[154] Particle Data Group collaboration, C. Patrignani et al., *Review of Particle Physics*, *Chin. Phys.* **C40** (2016) 100001.

[155] A. A. Penzias and R. W. Wilson, *A Measurement of excess antenna temperature at 4080-Mc/s*, *Astrophys. J.* **142** (1965) 419–421.

[156] Supernova Cosmology Project collaboration, S. Perlmutter et al., *Measurements of Omega and Lambda from 42 high redshift supernovae*, *Astrophys. J.* **517** (1999) 565–586, [astro-ph/9812133].

[157] P. Peter and J.-P. Uzan, *Primordial Cosmology*. Oxford Graduate Texts. Oxford University Press, 2013.

[158] G. W. Pettinari, *The intrinsic bispectrum of the Cosmic Microwave Background*. PhD thesis, Portsmouth U., ICG, 2013-09. 1405.2280. 10.1007/978-3-319-21882-3.

[159] D. Polarski and A. A. Starobinsky, *Semiclassicality and decoherence of cosmological perturbations*, *Class. Quant. Grav.* **13** (1996) 377–392, [gr-qc/9504030].

[160] Supernova Search Team collaboration, A. G. Riess et al., *Observational evidence from supernovae for an accelerating universe and a cosmological constant*, *Astron. J.* **116** (1998) 1009–1038, [astro-ph/9805201].

[161] G. I. Rigopoulos and E. P. S. Shellard, *The separate universe approach and the evolution of nonlinear superhorizon cosmological perturbations*, *Phys. Rev.* **D68** (2003) 123518, [astro-ph/0306620].

[162] G. I. Rigopoulos, E. P. S. Shellard and B. J. W. van Tent, *Large non-Gaussianity in multiple-field inflation*, *Phys. Rev.* **D73** (2006) 083522, [astro-ph/0506704].

[163] G. I. Rigopoulos, E. P. S. Shellard and B. J. W. van Tent, *Non-linear perturbations in multiple-field inflation*, *Phys. Rev.* **D73** (2006) 083521, [astro-ph/0504508].

[164] G. I. Rigopoulos, E. P. S. Shellard and B. J. W. van Tent, *Quantitative bispectra from multifield inflation*, *Phys. Rev.* **D76** (2007) 083512, [astro-ph/0511041].

[165] A. Riotto, *Inflation and the theory of cosmological perturbations*, *ICTP Lect. Notes Ser.* **14** (2003) 317–413, [hep-ph/0210162].

[166] H. P. Robertson, *Kinematics and World-Structure*, *Astrophys. J.* **82** (1935) 284–301.

[167] V. C. Rubin and W. K. Ford Jr, *Rotation of the andromeda nebula from a spectroscopic survey of emission regions*, *The Astrophysical Journal* **159** (1970) 379.

[168] R. K. Sachs and A. M. Wolfe, *Perturbations of a cosmological model and angular variations of the microwave background*, *Astrophys. J.* **147** (1967) 73–90.

[169] M. Sasaki, *Large Scale Quantum Fluctuations in the Inflationary Universe*, *Prog. Theor. Phys.* **76** (1986) 1036.

[170] M. Sasaki and E. D. Stewart, *A General analytic formula for the spectral index of the density perturbations produced during inflation*, *Prog. Theor. Phys.* **95** (1996) 71–78, [astro-ph/9507001].

[171] D. J. Schwarz, C. A. Terrero-Escalante and A. A. Garcia, *Higher order corrections to primordial spectra from cosmological inflation*, *Phys. Lett.* **B517** (2001) 243–249, [astro-ph/0106020].

[172] U. Seljak and M. Zaldarriaga, *A Line of sight integration approach to cosmic microwave background anisotropies*, *Astrophys. J.* **469** (1996) 437–444, [astro-ph/9603033].

[173] L. Senatore, *Lectures on Inflation*, in *Proceedings, Theoretical Advanced Study Institute in Elementary Particle Physics: New Frontiers in Fields and Strings (TASI 2015): Boulder, CO, USA, June 1-26, 2015*, pp. 447–543, 2017. 1609.00716. DOI.

[174] L. Senatore, K. M. Smith and M. Zaldarriaga, *Non-Gaussianities in Single Field Inflation and their Optimal Limits from the WMAP 5-year Data*, *JCAP* **1001** (2010) 028, [0905.3746].

[175] J. Silk, *Cosmic black body radiation and galaxy formation*, *Astrophys. J.* **151** (1968) 459–471.

[176] E. Silverstein and D. Tong, *Scalar speed limits and cosmology: Acceleration from D-cceleration*, *Phys. Rev.* **D70** (2004) 103505, [hep-th/0310221].

[177] K. M. Smith and M. Zaldarriaga, *Algorithms for bispectra: Forecasting, optimal analysis, and simulation*, *Mon. Not. Roy. Astron. Soc.* **417** (2011) 2–19, [astro-ph/0612571].

[178] COBE collaboration, G. F. Smoot et al., *Structure in the COBE differential microwave radiometer first year maps*, *Astrophys. J.* **396** (1992) L1–L5.

[179] A. A. Starobinsky, *A New Type of Isotropic Cosmological Models Without Singularity*, *Phys. Lett.* **91B** (1980) 99–102.

[180] A. A. Starobinsky, *Dynamics of Phase Transition in the New Inflationary Universe Scenario and Generation of Perturbations*, *Phys. Lett.* **117B** (1982) 175–178.

[181] A. A. Starobinsky, *Multicomponent de Sitter (Inflationary) Stages and the Generation of Perturbations*, *JETP Lett.* **42** (1985) 152–155.

[182] E. D. Stewart and D. H. Lyth, *A More accurate analytic calculation of the spectrum of cosmological perturbations produced during inflation*, *Phys. Lett.* **B302** (1993) 171–175, [gr-qc/9302019].

[183] Y. Tada and V. Vennin, *Squeezed Bispectrum in the δN Formalism: Local Observer Effect in Field Space*, *JCAP* **1702** (2017) 021, [1609.08876].

[184] T. Tanaka and Y. Urakawa, *Dominance of gauge artifact in the consistency relation for the primordial bispectrum*, *JCAP* **1105** (2011) 014, [1103.1251].

[185] Planck collaboration, J. Tauber, M. Bersanelli, J. M. Lamarre, G. Efstathiou, C. Lawrence, F. Bouchet et al., *The Scientific programme of Planck*, astro-ph/0604069.

[186] A. Taylor and P. Watts, *Parameter information from nonlinear cosmological fields*, *Mon. Not. Roy. Astron. Soc.* **328** (2001) 1027, [astro-ph/0010014].

[187] J. Torrado, B. Hu and A. Achucarro, *Robust predictions for an oscillatory bispectrum in Planck 2015 data from transient reductions in the speed of sound of the inflaton*, *Phys. Rev.* **D96** (2017) 083515, [1611.10350].

[188] M. Tucci, V. Desjacques and M. Kunz, *Cosmic Infrared Background anisotropies as a window into primordial non-Gaussianity*, *Mon. Not. Roy. Astron. Soc.* **463** (2016) 2046–2063, [1606.02323].

[189] E. Tzavara, *Second-order cosmological perturbations in two-field inflation and predictions for non-Gaussianity*. PhD thesis, Orsay, LPT, 2013. 1312.0126.

[190] E. Tzavara, S. Mizuno and B. van Tent, *Covariant second-order perturbations in generalized two-field inflation*, *JCAP* **1407** (2014) 027, [1312.6139].

[191] E. Tzavara and B. van Tent, *Bispectra from two-field inflation using the long-wavelength formalism*, *JCAP* **1106** (2011) 026, [1012.6027].

[192] E. Tzavara and B. van Tent, *Gauge-invariant perturbations at second order in two-field inflation*, *JCAP* **1208** (2012) 023, [1111.5838].

[193] E. Tzavara and B. van Tent, *Momentum dependence of the bispectrum in two-field inflation*, *JCAP* **1306** (2013) 001, [1211.6325].

[194] V. Vennin, K. Koyama and D. Wands, *Inflation with an extra light scalar field after Planck*, *JCAP* **1**603 (2016) 024, [1512.03403].

[195] F. Vernizzi and D. Wands, *Non-gaussianities in two-field inflation*, *JCAP* **0**605 (2006) 019, [astro-ph/0603799].

[196] A. G. Walker, *On milne's theory of world-structure*, *Proceedings of the London Mathematical Society* **2** (1937) 90–127.

[197] D. Wands, *Multiple field inflation*, *Lect. Notes Phys.* **7**38 (2008) 275–304, [astro-ph/0702187].

[198] S. Weinberg, *Cosmology*. Oxford University Press, 2008.

[199] Y. Welling, D. van der Woude and E. Pajer, *Lifting Primordial Non-Gaussianity Above the Noise*, *JCAP* **1**608 (2016) 044, [1605.06426].

[200] M. J. White and W. Hu, *The Sachs-Wolfe effect*, *Astron. Astrophys.* **3**21 (1997) 8–9, [astro-ph/9609105].

[201] A. P. S. Yadav, E. Komatsu and B. D. Wandelt, *Fast Estimator of Primordial Non-Gaussianity from Temperature and Polarization Anisotropies in the Cosmic Microwave Background*, *Astrophys. J.* **6**64 (2007) 680–686, [astro-ph/0701921].

[202] A. P. S. Yadav, E. Komatsu, B. D. Wandelt, M. Liguori, F. K. Hansen and S. Matarrese, *Fast Estimator of Primordial Non-Gaussianity from Temperature and Polarization Anisotropies in the Cosmic Microwave Background II: Partial Sky Coverage and Inhomogeneous Noise*, *Astrophys. J.* **6**78 (2008) 578–582, [0711.4933].

[203] A. P. S. Yadav and B. D. Wandelt, *Evidence of Primordial Non-Gaussianity (f(NL)) in the Wilkinson Microwave Anisotropy Probe 3-Year Data at 2.8sigma*, *Phys. Rev. Lett.* **1**00 (2008) 181301, [0712.1148].

[204] M. Zaldarriaga, *Non-Gaussianities in models with a varying inflaton decay rate*, *Phys. Rev.* **D**69 (2004) 043508, [astro-ph/0306006].

[205] M. Zaldarriaga, U. Seljak and E. Bertschinger, *Integral solution for the microwave background anisotropies in non-flat universes*, *Astrophys.J.* **4**94 (1998) 491–502, [astro-ph/9704265].

[206] F. Zwicky, *Die Rotverschiebung von extragalaktischen Nebeln*, *Helvetica Physica Acta* **6** (1933) 110–127.

université PARIS-SACLAY
ÉCOLE DOCTORALE
Physique en île-de-France (EDPIF)

Titre : Non-gaussianités inflationnaires : prévisions théoriques et conséquences observationnelles

Mots clefs : Inflation à plusieurs champs, Fond diffus cosmologique, non-gaussianités

Résumé : Le fond diffus cosmologique (CMB) permet d'étudier la physique à l'œuvre dans l'univers primordial. Ses anisotropies ont été mesurées récemment avec une haute précision par le satellite Planck. Ces mesures sont en accord avec les prédictions de l'inflation, la théorie décrivant une période d'expansion rapide et accélérée de l'univers primordial. Pour distinguer les différents modèles d'inflation, il est important de chercher des déviations de la distribution gaussienne des anisotropies du CMB, appelées non-gaussianités. Cette thèse est consacrée à l'étude, à la fois des points de vue observationnels et théoriques, des non-gaussianités du type bispectral (liées aux fonctions de corrélations à trois points), caractérisées par les paramètres d'amplitude $f_{\rm NL}$.
Après une partie introductive sur le modèle standard de la cosmologie et la théorie des perturbations cosmologiques, la deuxième partie de ce manuscrit décrit la méthode de l'estimateur de bispectre binné, utilisée pour extraire de l'information sur les non-gaussianités à partir des mesures du CMB. Pour obtenir des informations sur l'univers primordial, les données doivent être nettoyées de la contamination dûe aux avant-plans galactiques. Nous vérifions les résultats au niveau du bispectre. Des modèles numériques de plusieurs avant-plans galactiques sont déterminés à partir des données de Planck. Ces modèles ont été utilisés dans des analyses des cartes de la température du CMB et du ciel brut, afin d'améliorer la détermination de la quantité de non-gaussianités primordiales.
La troisième partie de ce manuscrit porte sur l'étude des non-gaussianités bispectrales produites dans des modèles d'inflation à deux champs avec des termes cinétiques standards. Il est important de mieux comprendre quelles régions de l'espace des modèles d'inflation ont été éliminées par les résultats de Planck. Nous appliquons une nouvelle expression de $f_{\rm NL}$ au cas d'un potentiel somme et nous montrons qu'il est très difficile de satisfaire en même temps aux conditions permettant $f_{\rm NL}$ grand et la contrainte observationnelle sur l'indice spectral n_s. Pour le cas de la somme de deux potentiels monomiaux et d'une constante, nous montrons explicitement dans quelles régions de l'espace des paramètres cela est posible et comment construire un tel modèle. Finalement, nous utilisons la nouvelle expression pour $f_{\rm NL}$ pour montrer que dans le cas du potentiel somme, les résultats analytiques restent valides au-delà de l'approximation de roulement lent.

Title: Inflationary non-Gaussianity: theoretical predictions and observational consequences

Keywords: Multiple-field inflation, Cosmic Microwave Background, non-Gaussianity

Abstract: A powerful probe of the physics at play in the early universe is the Cosmic Microwave Background (CMB). Its anisotropies have been measured recently with high precision by the Planck satellite. These measurements are in agreement with the predictions of inflation, a theory describing a period of fast and accelerated expansion in the early universe. To discriminate between the different inflation models, it is important to look for deviations from Gaussianity of the CMB anisotropies (i.e. non-Gaussianity). This thesis is devoted to the study of non-Gaussianity of the bispectral type (related to the three-point correlation functions) parametrized by its amplitude parameters $f_{\rm NL}$, both from the theoretical and observational points of view.
After an introductory part on standard cosmology, the second part of the thesis describes the method of the binned bispectrum estimator, used to extract information about non-Gaussianity from CMB measurements. In order to recover information about the primordial universe, one has to clean observational data from the contamination caused by galactic foregrounds. We verify the results at the bispectral level. Numerical templates for the temperature bispectra of several galactic foregrounds are determined using data from the 2015 Planck release. These templates are then used to perform joint analyses on raw sky and CMB temperature data maps, to improve the determination of the amount of primordial non-Gaussianity.
In the third part, the level of bispectral non-Gaussianity produced in two-field inflation models with standard kinetic terms is investigated using the long-wavelength formalism. It is important to better understand what regions of inflation model space have been ruled out by Planck. We apply a newly derived expression for $f_{\rm NL}$ to the case of a sum potential and show that it is very difficult to satisfy simultaneously the conditions for a large $f_{\rm NL}$ and the observational constraints on the spectral index n_s. In the case of the sum of two monomial potentials and a constant we explicitly show in which small region of parameter space this is possible, and we show how to construct such a model. Finally, we also use the new expression for $f_{\rm NL}$ to show that for the sum potential, the explicit expressions remain valid even beyond the slow-roll approximation.

Université Paris-Saclay
Espace Technologique / Immeuble Discovery
Route de l'Orme aux Merisiers RD 128 / 91190 Saint-Aubin, France